STUDIA UNIVERSITATIS
BABEŞ-BOLYAI

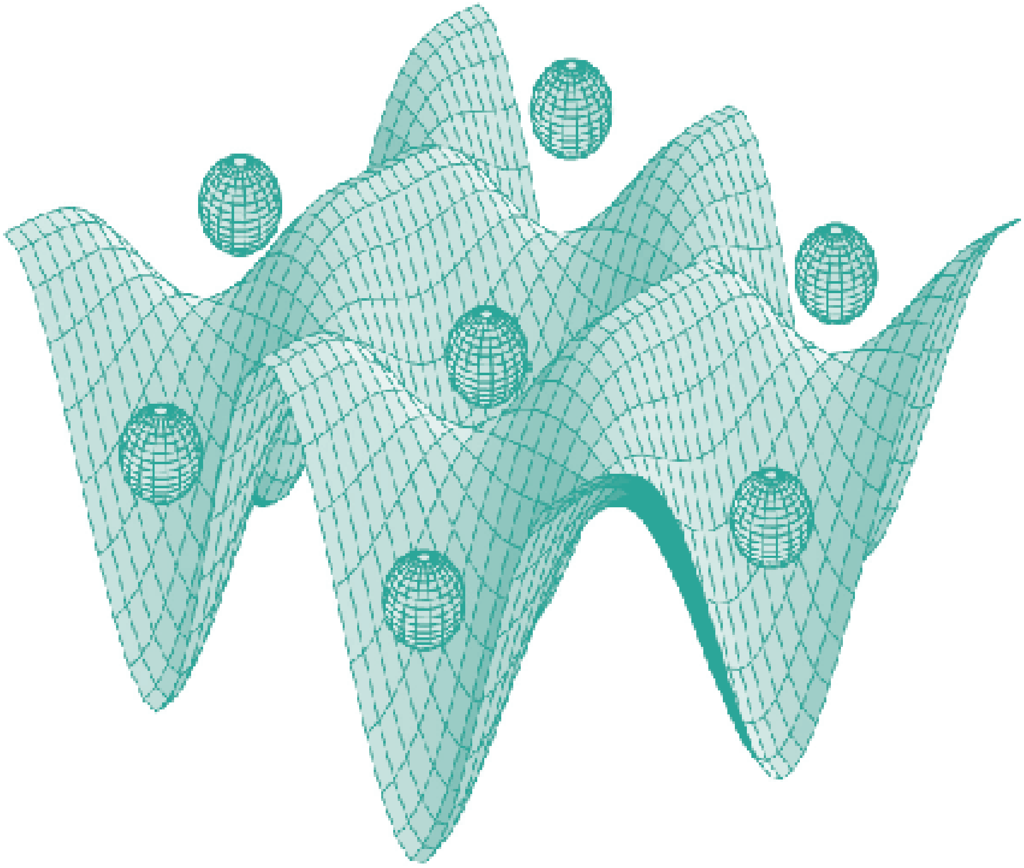

# PHYSICA

2/2011

YEAR Volume 56 (LVI) 2011
MONTH DECEMBER
ISSUE 2

# S T U D I A
# UNIVERSITATIS BABEŞ–BOLYAI

# PHYSICA

## 2

**Desktop Editing Office:** 51ST B.P. Hasdeu, Cluj-Napoca, Romania, Phone + 40 264-40.53.52

## CUPRINS – CONTENT – SOMMAIRE – INHALT

STUDIA UBB PHYSICA, LVI, 2, 2011

# CALIBRATION TECHNIQUES FOR MEASURING THE RADIOACTIVITY OF SOIL SAMPLES BY GAMMA SPECTROMETRY

**R. BARITCHI**[1], **L. DARABAN**[1]

**ABSTRACT.** In the present paper we studied a method of calibration of a gamma spectrometer for measuring the radioactivity of environmental samples, using the $ThO_2$ in secular equilibrium. A HPGe spectrometer type Canberra and a analysis software Genie 2000 were used in order to aquire the gamma spectra. The gamma spectrum for a sample of artificial soil added with $ThO_2$ was obtained and the efficiency curve was drawn. This measurement method was then applied to a sample of radioactive soil from the uranium mines zone, where radionuclides from the uranium family were identified and the total activity of the samples was determined giving a value of 390.9 Bq/kg.

***Keywords:*** *gamma spectrometry, calibration, efficiency curve, natural soil gamma-activity, Marinelli beaker.*

## INTRODUCTION

The effects of the radiation produced by natural or artificial sources on persons or groups of persons [1, 2] impose the knowledge and study of the environmental radioactivity. This activity is very important in order to establish the moment and way of intervention in the case of some unwanted events or to avoid the radioactive contamination of the environment [3]. On the earth surface the radioactive substances are found spread all over in a concentration which is in function of the nature of the soil and the origin of the component rocks. The main natural radionuclides are $^{238}U$, $^{235}U$ and $^{232}Th$, generators of the three radioactive natural families and their descendants, the radioisotope $^{40}K$ which accompanies natural potasium in all its combinations (0,118 %). In the total radiation of the soil it can be considered that the rubidium contributes with 2 %, the uranium family with about 20 %, the thorium family with about 28 % and the potasium with about 40 % [4].

Therefore, even in the regions without radioactive ores, the concentration of the radioactive elements from the superior lithosphere, including the soil, determines the activities presented in Table 1.

---

[1] *Babeş-Bolyai University, Faculty of Physics, 1 Kogălniceanu str., 400084 Cluj-Napoca, Romania*

**Table 1.** Radioisotopic concentrations the lithosphere in regions without radioactive ores

| Radioelement | Half-life [years] | [Bq/kg] | Grams of radioelement at 1 ton of soil [ppm] |
|---|---|---|---|
| Uranium 238 | $4.5\ 10^9$ | 25 | 2 |
| Radium 226 | 1622 | 40 | $10^{-6}$ |
| Thorium 232 | $1.4\ 10^{10}$ | 25 | 6 |
| Potasium 40 | $1.2\ 10^9$ | 500 | 0.3 |

There is a close connection between the contamination of cultures and the grade of contaminations of the soil. The external irradiation outside the buildings is own to the radiation emitted by natural radioelements from the soil and building materials, especially by uranium, radium and thorium. These elements give an average dose of 0,5 mGy/year [4]. Also, the internal irradiation, a component of the natural irradiation, is caused by the inhalation of air and ingestion of water and aliments (in the human body). In lungs these disintegrates cca 30.000 atoms of radon per hour, with emission of $\alpha$, $\beta$ and $\gamma$ radiation, to which it is added the one from the deposit resulted from $^{212,214}$Pb and $^{212,214}$Bi, being descendants from the families of U and Th. The most important natural radioactivity is due to the $^{40}$K, which is found in proportion of 120 parts per million parts of stable potassium.

## EXPERIMENTAL

### *Methodology of the calibration in energy and efficiency of the equipment*

A gamma spectrometer with a HPGe semiconductor detector type Canberra was used, operated under a voltage of 3.5 kV, equiped with a multichannel analyzer with 4096 channels working with the software Genie 2000. The detector is sorrounded by a Pb shield type NZ 138, designed to prevent gamma fotons from environment to reach the detector, so the radionuclides activity from the soil at a natural level can be measured.

These semiconductor detectors have a high resolution determining the energies of the gamma radiation emitted by the radioisotopes [5]. For the natural samples with a very low activity, it is difficult to separate the recorded signal from the background radiation, especially in the laboratory environment. In these conditions, measurements can be performed only using the Pb shielding (Fig.1). In this situation it must be taken into account the fact that this can introduce itself some peaks, such as the one at 73 keV corresponding to the $k_X$ radiation of the Pb and an annihilation peak at 511 keV.

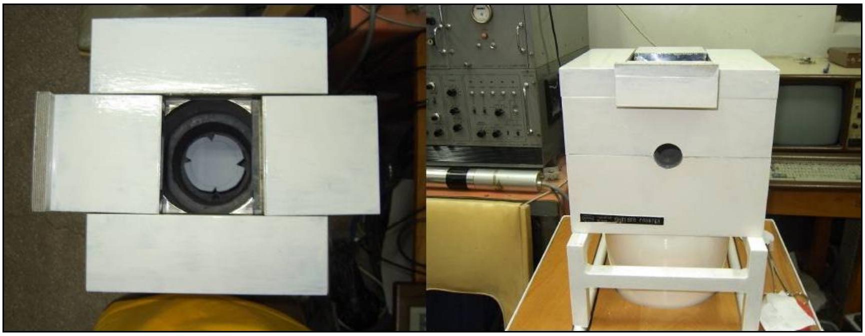

**Fig. 1.** View of a Pb shield NZ 138 of the HPGe detector

### *Efficiency calibration of the analyzer channels using standard sources*

This is a procedure periodically performed for the HPGe detector, as in [5], establishing the connection between the energy of the gamma radiation and the number of the channel. After the identification of the energy using standard sources, the efficiency value is calculated taking into account the probability of disintegration for each energy, as presented in references [5]. This data is necessary for the calibration of the detector in efficiency, as in the formula:

$$\varepsilon = N/(\varepsilon_g \cdot t \cdot \Lambda \cdot p) \qquad (1)$$

where: $\varepsilon$ – the detector efficiency;

N – the peak area in number of counts at that energy;

$\Lambda$ –the absolute activity of the standard [Bq];

t – the measurement time;

p – the probability of disintegration of the radionuclide

$\varepsilon_g$- geometric efficiency

By applying the formula (1), the peak areas N for each peak with energy can be deduced and by taking into account the scheme factor (p), the efficiency is calculated [ 6- 8].

The first tests were made by using small sources with known activity, type Leybold Germany. These can be sources of $^{241}$Am, $^{137}$Cs and $^{60}$Co, which energies are presented in Table 2, have a circular area of $\Phi$ = 3 mm.

**Table 2.** Efficiency values using standard sources

| E(keV) | ε(%) | Radioisotope |
|---|---|---|
| 60 | 6.4 | $^{241}$Am |
| 662 | 3.8 | $^{137}$Cs |
| 1172 | 2.62 | $^{60}$Co |
| 1330 | 2.34 | $^{60}$Co |

By making the calculation using the formula (1) in a $2\pi$ geometry, the characteristic curve is obtained as presented in Fig.2.

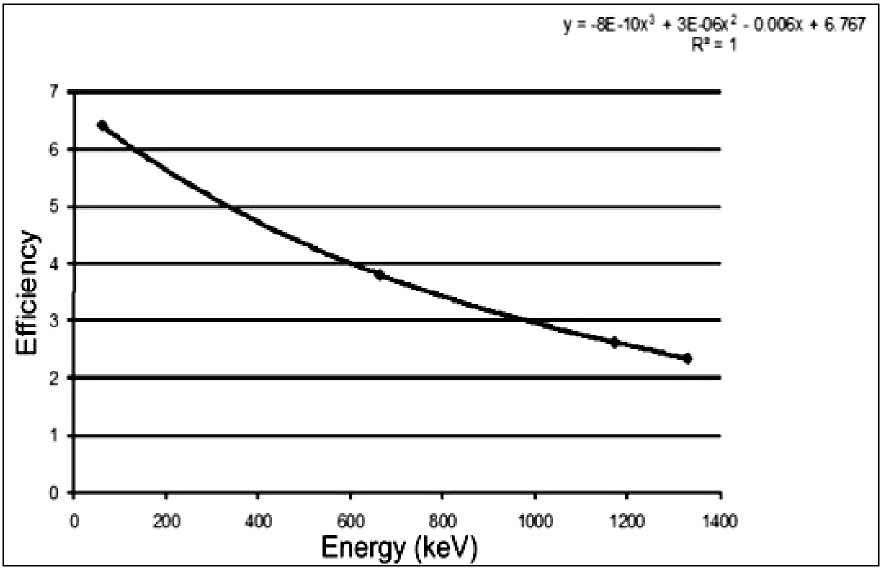

**Fig. 2.** Efficiency curve of a gamma spectrometer using standard sources

It can be noticed that on the graphic are too less points, therefore we used another source of known activity of 3.33 kBq of $^{226}$Ra, which emits many energies, as in the spectrum presented in Fig.3, where $^{226}$Ra is in secular equilibrium with its descendents [9]. The efficiency is calculated again with the same formula and the obtained results are presented in Table 3 and Fig.4.

**Table 3.** Detector efficiency calculation using a source of $^{226}$Ra

| Energy (keV) | Peak area | Scheme factor (p) | ε (efficiency) | Eff (%) |
|---|---|---|---|---|
| 243.7 | 171868 | 0.074 | 0.1955 | 19.5 |
| 296.8 | 364903 | 0.19 | 0.1616618 | 16.2 |
| 353.4 | 589516 | 0.37 | 0.134115 | 13.4 |
| 609.8 | 363348 | 0.46 | 0.0664888 | 6.6 |
| 769 | 21707 | 0.049 | 0.0372896 | 3.7 |
| 934.7 | 12566 | 0.03 | 0.0352581 | 3.5 |
| 1120.9 | 62058 | 0.15 | 0.0348249 | 3.5 |
| 1239.6 | 17966 | 0.057 | 0.0265314 | 2.6 |
| 1378.4 | 14570 | 0.04 | 0.0306608 | 3.1 |

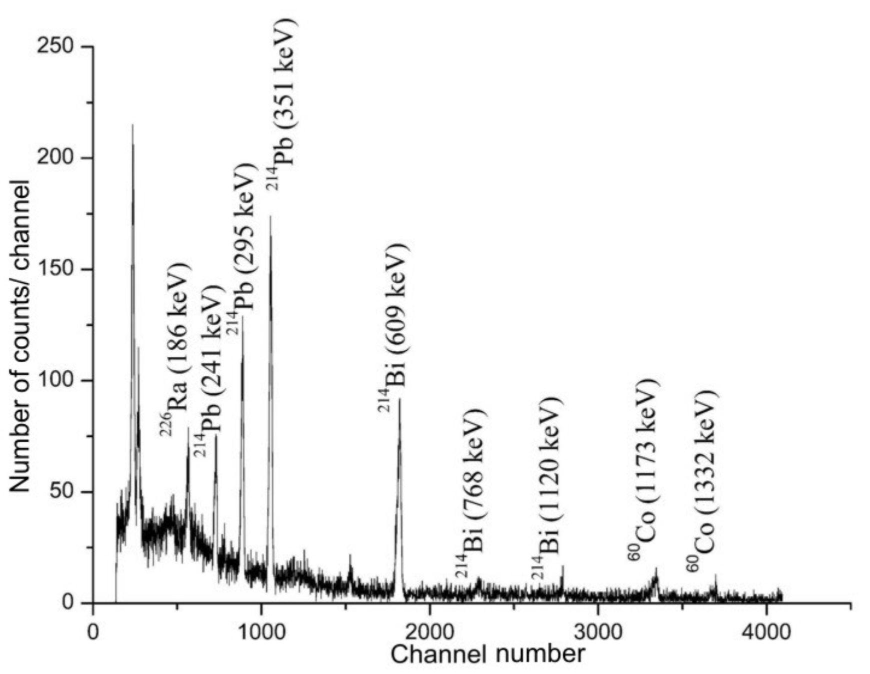

**Fig. 3.** Characteristic spectrum of $^{226}$Ra and its descendants

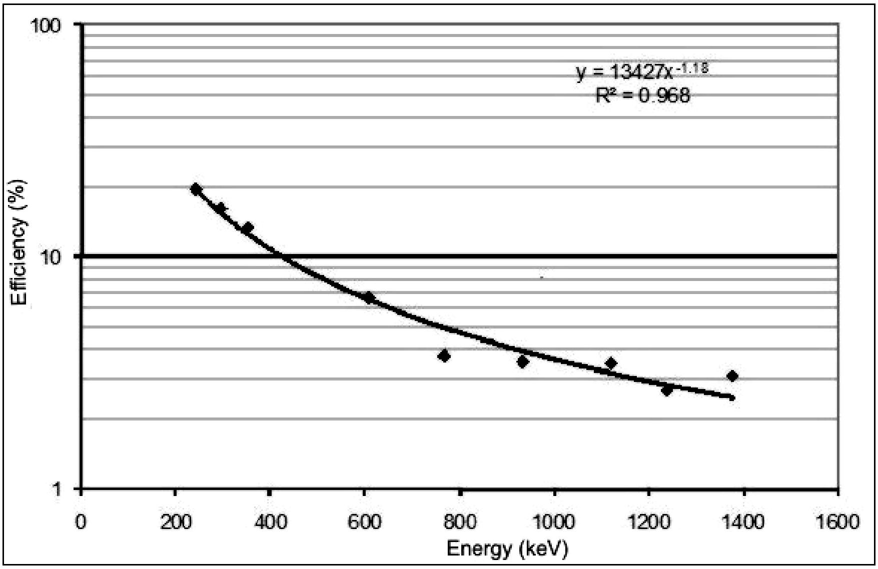

**Fig. 4.** Detector efficiency curve using a source of $^{226}$Ra

It can be noticed a better agreement of the shape of the curve of known efficiency from the literature with the curve for this type of detector.

*Efficiency calibration of volum samples with $ThO_2$ in secular equilibrium*

Further, the dimension of the source was increased to a cylindrical shape of 8x20 mm, containing oxide of Th older than 30 years [10], which can be used as a calibration source in efficiency, as in [11- 14], where the absolute activity per gram of $ThO_2$ is of 3565 ± 15 Bq/g. The geometrical factor was included in equation by using a beaker with the same geometry as the sample. Therefore, this efficiency can be referred only to this type of beaker and only in this geometry, the source being placed at 10 cm from the detector. The geometry can be calculated at $\varepsilon_g = 0.035$.

**Table 4.** Efficiency calculation of a source of $ThO_2$ of 0.52 g

| E (keV) | ε | Radioisotope |
|---|---|---|
| 273 | 0.165 | $^{228}$Ac |
| 338 | 0.121 | $^{228}$Ac |
| 461 | 0.081 | $^{228}$Ac |
| 911 | 0.04 | $^{228}$Ac |
| 968 | 0.043 | $^{228}$Ac |

In this case the efficiency is calculated from each peak area, presented in Fig. 5.

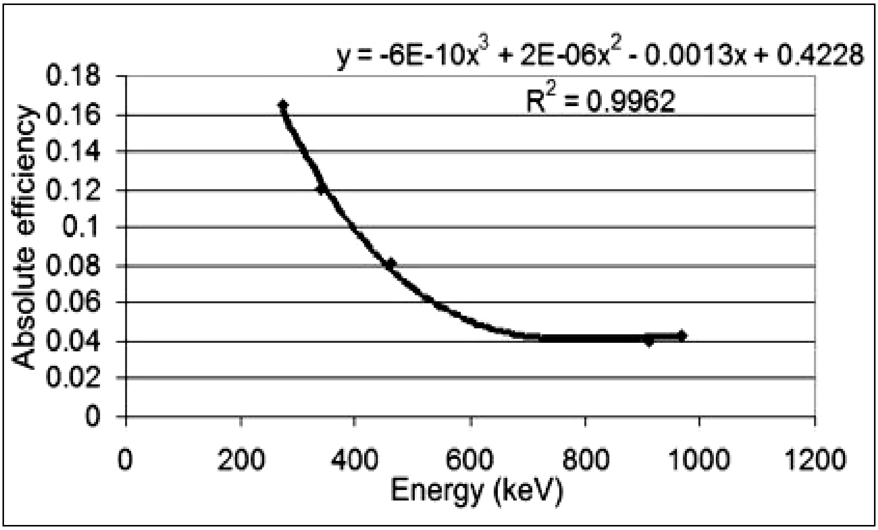

**Fig. 5.** Detector efficiency curve using a cylindrical source of $ThO_2$

In order to measure the radioactivity of the soil (and other samples with low activity), it is important to use samples in high volumes. The sample must be placed in a Marinelli beaker, with a special geometry to allow the disposition of the material to be analyzed in such a way that this will sorround the detector of radiation, to collect gamma photons from a large solid angle. In our laboratory we concieved and executed some Marinelli beakers made of recycled materials, cheap and widely available, which are aliments packing made of poly(chloroethanediyl) (PVC). The reason we made this was the necessity of adapting the Marinelli beakers to the shape of the shielding in the laboratory.

The calibration of Marinelli beakers can be made locally in each laboratory by using mixtures of soil-radionuclides for the calibration using old Th (in equilibrium with its daughter nuclei), in the shape of $ThO_2$ or $Th(NO_3)_4$, in a mixture with a matrix of $CaCO_3$, $SiO_2$, $Al_2O_3$ or other compounds with the density close to that of the samples that are about to be analyzed. For this step, we followed the calibration procedures described in [12].

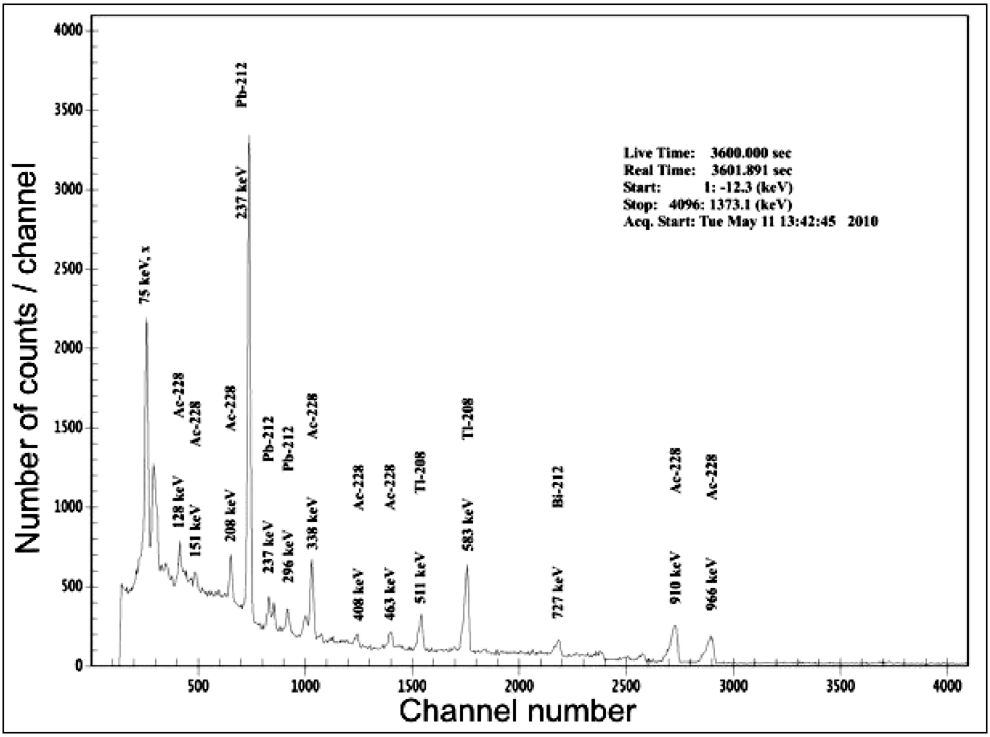

**Fig. 6.** Characteristic gamma spectrum for the artificial ( $SiO_2$ $Al_2O_3$·CaSO4) soil, impurified with 0.32g of $ThO_2$ with an absolute activity of $\Lambda$ =1239 Bq

In order to calibrate the Marinelli beaker is necessary to prepare a standard mixture (artificial soil) in a beaker containing $SiO_2$ with 2% $Al_2O_3$, with a total mass of 260 g, to which we added a quantity of 218 g $CaSO_4 \cdot 2H_2O$ (gypsum). We measured a quantity of 0.32g $ThO_2$ (Carlo Erba, Italy) on the electronic scale and added it to the matrix. In order to obtain an uniform dispersion of $ThO_2$ in the artificial soil is necessary to mix them using a special procedure described in [13]. The half-life of $ThO_2$ of an order to tenth of years was enough in order to establish a secular equilibrium. The Marinelli beaker was filled with a mixture of a total mass of 541g, from which 0.32g of $ThO_2$ was homogeneously dispersed in the entire volume of the sample.

From [13] we know the absolute activity of $ThO_2$ in secular equilibrium with the daughter nuclei, has a value of 3872 Bq/g. Further, we proceeded to the calibration in energy of the analyzer channels and we could therefore measure the artificial sample of soil. The measurement time was about 1 hour and the result is presented in Fig.6. The recorded spectrum will then yield to the calibration curve, which can be later used to determine the γ-absolute activity of a well-known sample, but only using the same geometry (the same Marinelli beaker) and at the same density.

**Table 5.** Data from the calibration spectrum using $ThO_2$

| **Energy** | **Ni (peak area)** | **Error** | **$p_i$ (Scheme factor)** | **$\Lambda_i$( Absolut activity)** | **$\varepsilon_i$(efficiency)** | **Radionuclide** |
|---|---|---|---|---|---|---|
| **keV** | **Counts/hour** | **%** | **(%)** | **Bq/0.32g** | **-** | **-** |
| 207 | 3598 | 4 | | 1239.04 | | Ac-228 |
| 237.4 | 47718 | 0.6 | 43.1 | | 0.89 | Pb-212 |
| 267 | 5494 | 4 | | | | Ac-228 |
| 336.5 | 7388 | 2 | 12 | | 0.5 | Ac-228 |
| 581.8 | 12407 | 1 | 86 | | 0.12 | Tl-208 |
| 725 | 2732 | 5 | 11 | | 0.19 | Bi-212 |
| 910 | 8420 | 2 | 29 | | 0.23 | Ac-228 |
| 966.4 | 6057 | 2 | 17.46 | | 0.28 | Ac-228 |

## Aplications for the measurement of soil samples

The soil samples analysis is a method often used to supervise the environment radioactivity, the estimation of the doses in the concentrations of radionuclides is complex and sometimes uncertain, due to the variation induced by the redistribution of the isotopes because of the retain in vegetation and of the rainfalls.

A sample of soil is characterized by defining its structure, the agricultural state and the vegetative bed. In order to determine the natural radioactivity, characteristic to a certain area, the superficial layer is removed and the samples are taken from 25 cm deep. The place of harvest must be isolated, unmodified and without water leakages. Before the harvest of the samples, the chosen surface is being cleaned by vegetation, or if it covered by ice of snow, this is being removed as well. With the help of a metalic scafe a sample of 1 kg is harvested and inserted in plastic bags. The samples are also cleaned of the rests of vegetation and stones.

Was measured the gamma spectrum of a sample of mosses (*Sphagnum sp.)* with soil from Baita river, an area with uranium ore. From the Fig.7 spectra results the presence of the following nuclides from Uranium family: $^{226}$Ra, $^{214}$Pb and $^{214}$Bi.

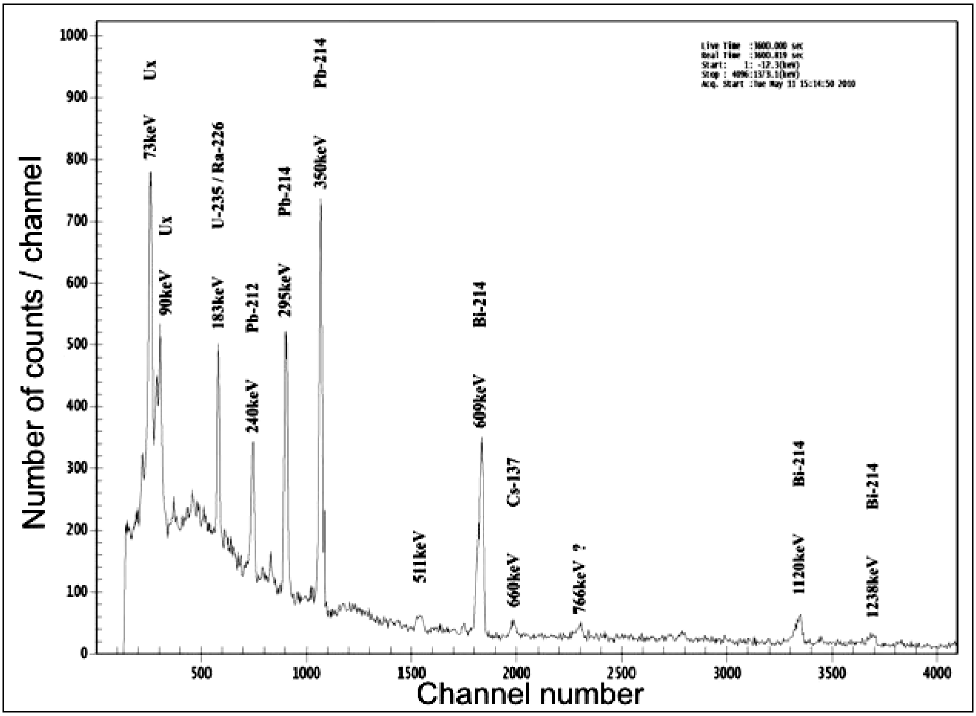

**Fig. 7.** Characteristic gamma spectrum of a sample of mosses (*Sphagnum sp.)* with soil from Baita river, with a total activity of 544 Bq (without the contribution of $^{40}$K and the presence of $^{137}$Cs), measured for 1 hour

We therefore achieved to process the samples of soil according to regulations [4]. The 6 samples with a mass of about 1 kg were dried in an oven at 110°C for 24 h. Then, they were sieved with a sieve of a diameter of the holes of 0.5 mm and submitted to roast at 450°C for 5 h, being then prepared for the transfer into the Marinelli beaker.

The annual average of the $\gamma$-global activity for the samples of uncultivated soil was about 311.5 Bq/kg and the maxium value was of 390.9 Bq/kg recorded on the date of 28.04.2009. The recorded values are situated in the range of variation of the natural background in the area [14-16]. Our performace was to measure the activity of a natural soil from the Faget forest and its spectrum is presented in Fig.8. Lower limit of detection was calculated at 2 Bq/samples. The activities of the radionuclides from natural samples are in this range.

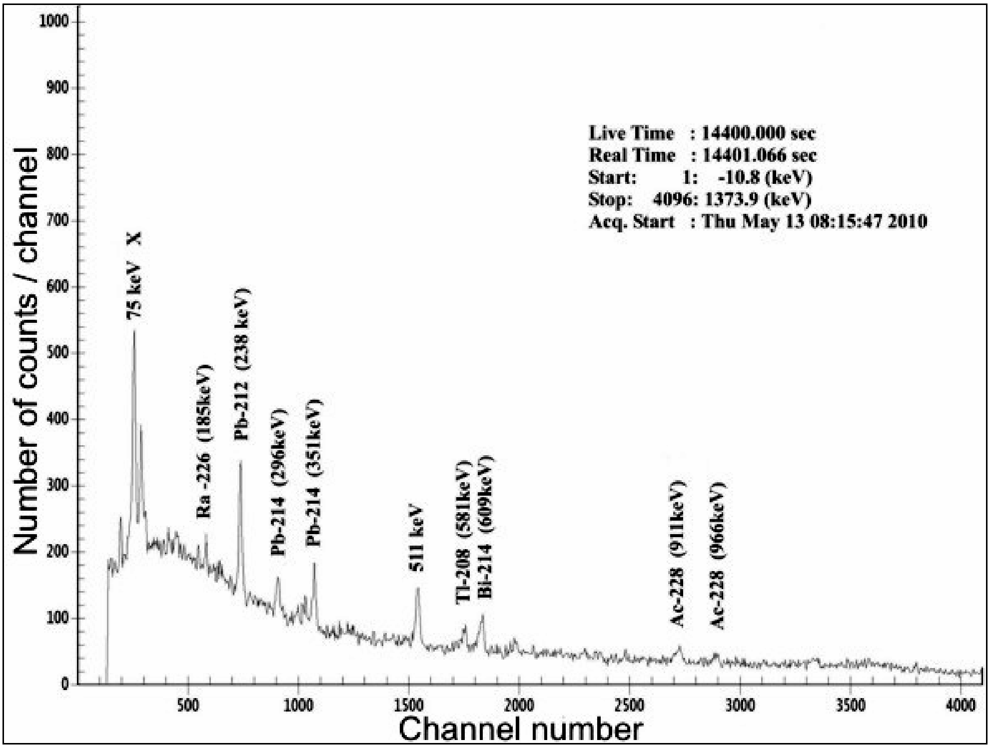

**Fig.8.** Characteristic gamma spectrum of a sample of natural soil from the Faget forest

## CONCLUSIONS

A shielding made of low level background Pb was set and the measurements were performed with a HPGe gamma spectrometer in order to aquire the gamma spectra for the measured samples.

First we made an energy calibration of the spectrometer and then a calibration in efficiency using standard samples with two small samples and other type Marinelli beaker containing $ThO_2$ in secular equilibrium. The characteristic gamma spectrum of the pure $ThO_2$ was therefore obtained, knowing the scheme factors and the descendent radionuclides. The calibration in efficiency was also made for samples of artificial soil containg $ThO_2$.

This method was then applied to a sample of soil from the area with mines of uranium, obtaining a spectrum in which we identified the radionuclides from the uranium family and we determined a total activity of 390.9 Bq/kg. The obtained results were placed under the level of warning, fiting into the limits of variation of the natural background in the area, measured on natural soil samples from the Faget area as well.

## REFERENCES

1. UNSCEAR, *Sources and Effects of Ionizing Radiation*, 2010, page 339, retrieved 2011-6-29.
2. V. Simon, Introducere în Fizica Mediului, pp. 5-21, Ed. Presa Universitară Clujeană, 2001.
3. G. Damian, Surse de Radiatii Nucleare, pp.37-48, 195-208, Ed. Casa Cărtii de Stiintă, Cluj-Napoca, 2005.
4. C. Cosma, T. Jurcut – Radonul si mediul inconjurator, p. 7-9, **1996**, Ed. Dacia, Cluj-Napoca, 1996.
5. O. Cozar – Detectori de Radia□ii. Spectroscopie gama. pp.126-131, 183-199, Ed. Presa Universitara Clujeana, Cluj-Napoca, **2007**.
6. C.A. Adesanmi, F.A. Balogun, M.K. Fasasi, I.A. Tubosun, A.A. Oladipo, *A semi-empirical formula for HPGe detector efficiency calibration*, Journal of Radioanalytical and Nuclear Chemistry, **249***,* No. 3, pp. 607– 611, 2001.
7. Mahmoud I. Abbas, *Validation of analytical formulae for the efficiency calibration of gamma detectors used in laboratory and in-situ measurements,* Applied Radiation and Isotopes **64**, 1661–1664, 2006.
8. Dirk Arnolda, Octavian Sima, *Extension of the efficiency calibration of germanium detectors using the GESPECOR software*, Applied Radiation and Isotopes **61**, 117–121, 2004.
9. D. Sardari, T.D. MacMahon, *Gamma-ray probabilities in the decay of 226Ra and its daughters,* Journal of Radioanalytical and Nuclear Chemistry, **244**, 2, 463-469, 2000.
10. N. Antovic, N. Svrkota, *Development of a method for activity measurements of* $^{232}$*Th daughters with a multidetector gamma-ray coincidence spectrometer*, Applied Radiation and Isotopes **67**, 1133–1138, 2009.

11. N. Lavi, Z.B. Alfassib, N. Drndarski, *Calibration of Marinelli vessels for measurement of radioactive environmental samples,* Nuclear Instruments and Methods in Physics Research A **385**, pp.376-380, 1997.
12. N. Lavi, Z.B. Alfassi, *Development and application of Marinelli beaker standards for monitoring radioactivity in Dairy-Products by gamma-ray spectrometry*, Applied Radiation and Isotopes **61,** 1437–1441, 2004.
13. N. Lavi, Z.B. Alfassi , *Development of Marinelli beaker standards containing thorium oxide and application for measurements of radioactive environmental samples*, Radiation Measurements, **39**, 15-19, 2005.
14. J. Saegusaa, K. Kawasakia, A. Miharaa, M. Itob, M. Yoshida, *Determination of detection efficiency curves of HPGe detectors on radioactivity measurement of volume samples*, Applied Radiation and Isotopes **61**, 1383–1390, 2004.
15. N. Antovic, N. Svrkota, *Measuring the radium-226 activity using a multidetector* $\gamma$*-ray coincidence spectrometer*, Journal of Environmental Radioactivity **100**, 823–830, 2009.
16. G. Jia, G. Torri, *Estimation of radiation doses to members of the public in Italy from intakes of some important naturally occurring radionuclides, (*$^{238}U$*,* $^{234}U$*,* $^{235}U$*,* $^{226}Ra$*,* $^{228}Ra$*,* $^{224}Ra$ *and* $^{210}Po$*) in drinking water,* Applied Radiation and Isotopes **65**, 849–857, 2007.

STUDIA UBB PHYSICA, LVI, 2, 2011

# TETRACYCLINE LOADING AND RELEASE FROM BIOACTIVE GLASS MICROSPHERES

**Z. BENYEY[1], E. VANEA[1], T. SIMON[1], S. CAVALU[2], V. SIMON[1]**

**ABSTRACT.** Bioactive glass microspheres loaded with tetracycline for possible biomedical applications were synthesized and characterized in this work. A sol-gel derived glass matrix with the composition $45SiO_2{\cdot}24.5CaO{\cdot}24.5Na_2O{\cdot}6P_2O_5$ including 1mg/ml tetracycline was spray dried to produce microspheres. Scanning Electron Microscopy (SEM) images evidenced the spherical form of the spray dried particles. Particle size analysis showed a maximum distribution in the 8-10 µm range. The zeta potential of the microspheres dispersed in water was -12 mV at neutral pH. X-ray Photoelectron Spectroscopy (XPS) confirmed the occurrence of the antibiotic on the surface of the glass. A release study of the tetracycline loaded microspheres in simulated body fluid for 48 hours was performed using UV-Vis and fluorescence spectroscopy.

***Keywords:*** bioactive glass; microspheres; spray drying; antibiotics release.

## INTRODUCTION

In the last years a great deal of effort has been expended in the engineering of biomaterials. Bioactive glasses are largely applied in orthopedic surgery and dentistry [1]. Bacterial colonization of medical devices or implants [2,3] frequently leads to infection of the bone or bone marrow, known as osteomyelitis [4], and represents a serious hazard despite the aseptic surgical techniques. These infections may compromise the implants leading to complex revision processes or the removal of the implants [5]. The susceptibility of the implants to infection depends to a large extent on the patients immune system, which is less effective because the lack of blood circulation in bone defect sites. Another risk factor is due to the ability of the microorganisms to form biofilms [6], because the biofilm protects the microorganisms from stressful environmental conditions and prevents the entrance of antibiotics and antimicrobial substances [7]. In order to reduce the biofilm formation on the implants, antimicrobial drugs must be delivered to the affected regions [8]. Locally administered antibiotic drugs enhance the concentration the antibiotics reaching the target area [1]. For

---

[1] *Babes-Bolyai University, Faculty of Physics & Institute of Interdisciplinary Research in Bio-Nano-Sciences, Cluj-Napoca, Romania*

[2] *University of Oradea, Faculty of Medicine and Pharmacy, Oradea, Romania*

this purpose was tried to include antibiotics with large antimicrobial spectrum in the implant material itself [9-11]. The tetracycline antibiotic was chosen because of its antimicrobial activity against a wide range of gram-positive and gram-negative bacteria, as well as the absence of major side effects [12].

The purpose of this study is to characterize bioactive glass microspheres obtained by spray drying and to evaluate their ability as a controlled release system of tetracycline. For this purpose we used Scanning Electron Microscopy (SEM), particle size distribution analysis, zeta potential measurements, X-ray Photoelectron Spectroscopy (XPS), UV-Vis and fluorescence spectroscopy.

## MATERIALS AND METHODS

The samples were prepared by means of sol-gel method using as starting materials tetraetoxisilan (TEOS), $Ca(NO_3)_2{\cdot}4H_2O$, $(NH_4)_2{\cdot}HPO_4$ and $Na_2CO_3$ as SiO, CaO, $P_2O_5$ and $Na_2O$ precursors to form the glass matrix with the composition $45SiO_2{\cdot}24.5CaO{\cdot}24.5Na_2O{\cdot}6P_2O_5$ (mol %). Tetracycline (purchased from Sigma-Aldrich) dissolved in phosphate buffered saline (PBS) solution (1mg/ml) was added to the final sol, homogenised and then spray dried with a Mini Spray Dryer B-290 in order to obtain tetracycline loaded bioactive glass (BG-TCL) microspheres. After preparation SEM images were recorded using a JEOL JSM 7000F Scanning Electron Microscope to determine the morphology of the samples. For this purpose the sample was mounted on aluminium SEM pins and coated with Au/Pd.

The average diameter and size distributions of the bioactive glass microspheres were determined using a SALD-7101 particle size analyzer. In order to determine the stability of particles suspension, the zeta potential of the microspheres was measured in water, using a Nano Series (ZS 90) Malvern instrument.

For delivery assays, spray dried glass (BG-TCL) (35 mg) was immersed in 5 ml simulated body fluid (SBF) prepared according to Kokubo protocol [13], pH 7.4, and kept at 37°C for 2, 5, 24 and 48 hours in Falcon tubes, with continuous stirring. After each period, the SBF solution was completely removed from the tube for analysis and replaced by another freshly prepared one.

The removed SBF was analysed by fluorescence spectroscopy, as well as UV-VIS spectroscopy. Fluorescence measurements were performed on a Jasco spectrofluorometer FP-6300. The excitation wavelength was 280 nm, and fluorescence spectra were recorded from 380 to 700 nm. The UV-VIS measurements were performed on a Jasco V-670 UV-Vis-NIR spectrometer with a slit width of 2 nm and 1 nm spectral resolution.

The incorporation of tetracycline in the glass matrix was proved by XPS measurements performed after preparation and after the different release periods on the microspheres using a SPECS PHOIBOS 150 MCD system equipped with monochromatic Al-$K_\alpha$ source (250 W, hν=1486.6 eV), hemispherical analyser and multichannel detector. The vacuum in the analysis chamber during the measurements was in the range of $10^{-9}$-$10^{-10}$ mbar. The binding energy scale was charge referenced to the C 1s at 284.6 eV.

## RESULTS AND DISCUSSION

The SEM micrograph taken from the sample after preparation (Fig 1.) shows that after spray dying we obtained microspheres with two size ranges, the majority of the microspheres are in the range of 5-10 μm, but there are also smaller particles in the range of 0.1-0.3 μm. The particle size distribution was also determined by the laser particle size analyser SALD-7101. The data indicate that the average diameter occurring as a maximum in the size distribution curve of the bioactive glass microspheres is around 10 μm (Fig 2), but also a smaller peak in the 0.1 μm region is evidenced. A good bioactivity is expected [15] for glass microspheres in this size range.

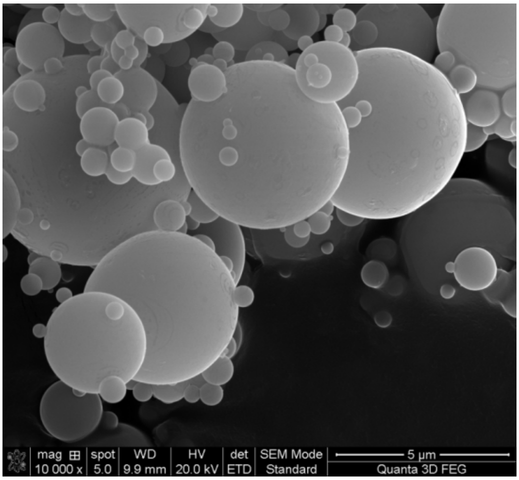

**Fig. 1.** Surface morphology of the tetracycline loaded microspheres according to SEM image; magnification 10000 X.

The zeta potential of the microspheres suspended in water shows the difference in the electrical potential between the stationary layer of fluid attached to the particles and the rest of the fluid. The main significance of the zeta potential in a colloidal suspension is the determination of its stability, the higher the value of the module of zeta potential is the more stable the particle dispersion becomes. This is caused by repulsion forces between the dispersed particles that prevent aggregation. It is accepted that a lower threshold for stability can be set to a value of ±25mV [14]. Besides particle stability, the zeta potential of BG-TCL particles offers information about the materials biocompatibility. It was reported [16, 17] that negative zeta potential is beneficial for attachment and proliferation of bone cells. The value obtained by our measurements was -12.1 ± 1.5 mV at neutral pH (Fig. 3), i.e. under the stability threshold, which suggests that the spheres could aggregate, that is actually observed in the SEM image (Fig. 1).

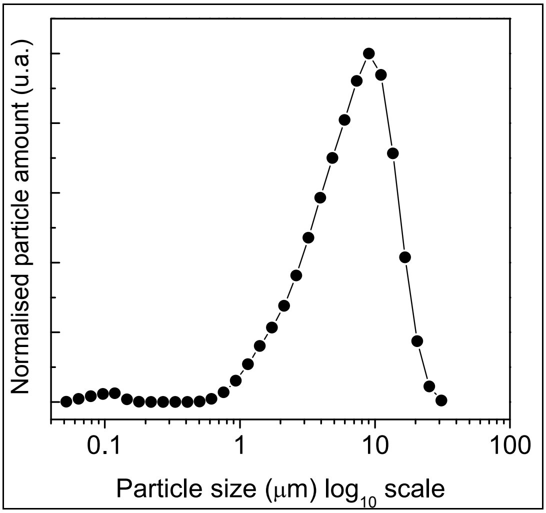

**Fig. 2.** Particle size distribution of the microspheres.

As already mentioned, the antibiotic that is incorporated in the glass to be effective, it needs to be on the surface of the material.

Because XPS measurements give results from only the top 5-10 nm of the investigated materials [15] they can be used to determine the amount of tetracycline available on the surface of the spheres. As seen in the XPS survey spectra, pure tetracycline (Fig. 4a) is composed mostly of carbon, oxygen and nitrogen ($C_{22}H_{24}N_2O_8$), and the occurrence of these elements was used to prove the existence of the antibiotic on the surface of the spheres. Although the bioactive glass matrix has neither carbon nor nitrogen in its structure, carbon can be observed in most XPS spectra in small quantities as contamination. This is clearly not the case here. The atomic concentrations (Table 1) of over 20 % carbon, as well as nitrogen concentrations nearing pure tetracycline, clearly show the available antibiotic on the surface of the glass. The amount of carbon doesn't decrease even after the release study, which shows that part of the antibiotic is strongly attached to the glass matrix, and will be only released gradually with the bioabsorption of the matrix.

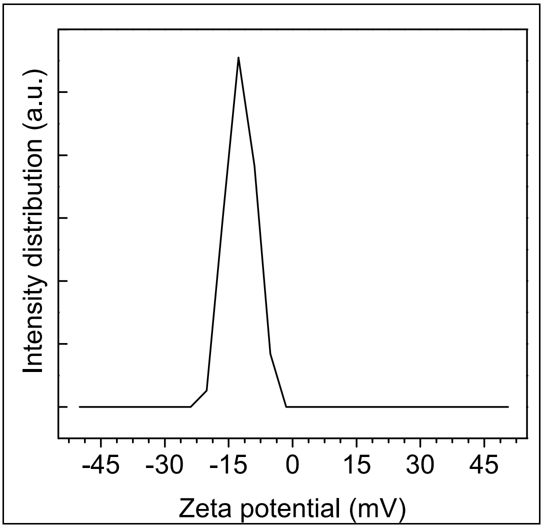

**Fig. 3.** Zeta potential at neutral pH of microspheres.

**Table 1.** Surface chemical composition of pure tetracycline (TCL) and of the BG-TCL microsphere before and after 48 hours release.

| **Sample** | **Elemental composition (at %)** | | | | | | |
|---|---|---|---|---|---|---|---|
| | **C** | **N** | **O** | **Si** | **Ca** | **P** | **Na** |
| TCL | 72.9 | 5.4 | 21.6 | - | - | - | - |
| BG-TCL | 21.0 | 8.4 | 48.0 | 11.7 | 5.5 | 3.9 | 1.1 |
| BG-TCL (after 48 hours release in SBF) | 26.4 | 3.4 | 43.7 | 15.3 | 4.9 | 5.0 | 0.9 |

To determine the release rate of tetracycline from the glass matrix, fluorescence spectroscopy has been used on the SBF extracted from the microspheres after different immersion times. Tetracycline is a natural fluorophore with excitation frequency around 280 nm and emission around 450 nm, thereby was no need to use fluorescent dies. As can be seen from the spectra (Fig. 5) the emission peak around 480 nm shows a stronger release in the first two hours followed by gradually decreasing release with increasing immersion time. This result was also supported by the UV-VIS study of the withdrawn SBF (Fig. 6) that shows the same tendency. For a better understanding of the release, the tendency was plotted in one graph containing both florescence and UV-VIS results (Fig. 7). Both techniques show a similar, almost linear decrease of the tetracycline concentration in the SBF solution.

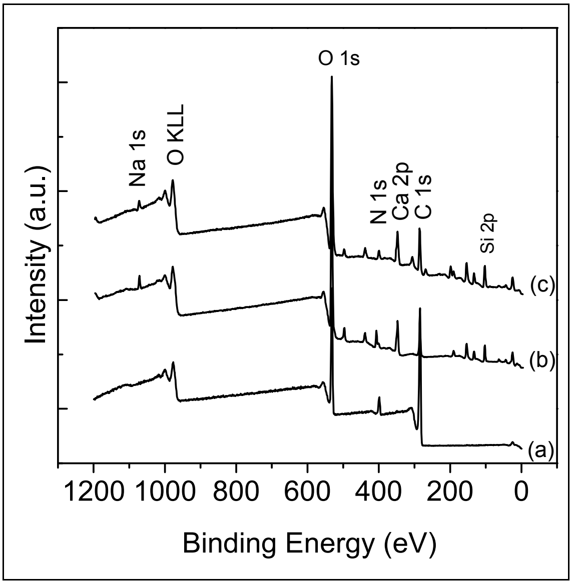

**Fig. 4.** XPS survey spectra of (a) pure tetracycline, (b) BG-TCL before release and (c) BG-TCL 48 hours after release.

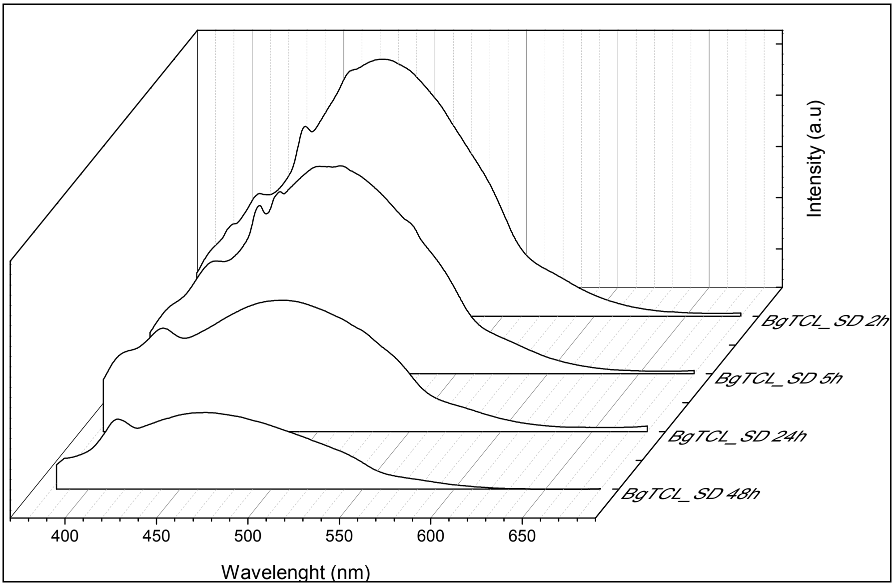

**Fig. 5.** Fluorescence spectra of tetracycline released from the spray dried bioactive glass after 2, 5, 24 and 48 hours.

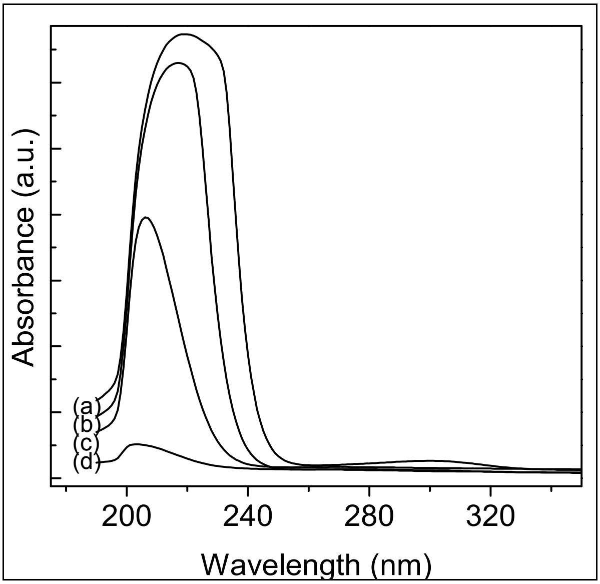

**Fig. 6.** UV-Vis absorbance spectra of tetracycline released from the spray dried bioactive glass after 2 (a), 5 (b), 24 (c) and 48 (d) hours.

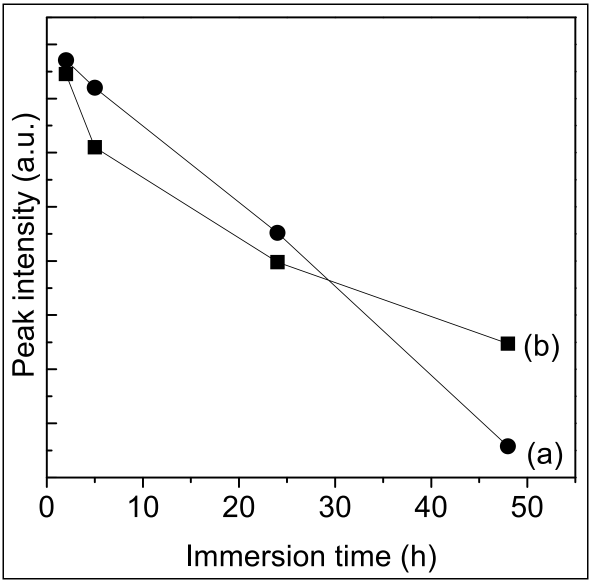

**Fig. 7.** Time dependence of tetracycline UV- VIS (a) and fluorescence (b)peak intensities.

## CONCLUSIONS

The tetracycline loaded spray dried BG microspheres with diameters close to 10 µm are expected to own good bioactivity. The negative zeta potential of -12 mV determined for the BG microspheres dispersed in water is favourable for attachment and proliferation of bone cells. The release of the antibiotic in simulate body fluid is maximum during first two hours and decreases over time. Although the release of the antibiotic after 48 hours is slowed compared to the first hours, the XPS study shows that a great amount of antibiotic is still incorporated within the glass matrix and could act for longer time as antimicrobial agent. The strong release in the first hours followed by an almost linear diminution of the antibiotic concentration in SBF, make the microspheres potential candidates for bone regenerative medicine combined with drug delivery applications.

## ACKNOWLEDGMENTS

The research was accomplished in the framework of PNII Idei PCCE-248/2008 project granted by the Romanian National University Research Council. E.V., and Z.B. and T.S. authors wish to thank for the financial support provided from contract POSDRU/89/1.5/S/60189 and POSDRU/107/1.5/S/76841 respectively.

## REFERENCES

[1]. A.L. Andrade, D.M. Souza, W.A. Vasconcellos, R.V. Ferreira, R.Z. Domingues, J. Non-Cryst. Solids (2009) 355, 811.

[2]. J. Vila, A. Soriano, J. Mensa, Erm. Infec. Micr. Cl. (2008) 26, 48.

[3]. E.M. Hetrick, M.H. Schoenfisch, Chem. Soc. Rev. (2006) 35, 780.

[4]. G. Wei, Y Kotoura, M Oka, T Yamamuro, R Wada, SH Hyon, Y Ikada, J. Bone Joint Surg. BR (1991) 73, 246.

[5]. L. Zhao, P.K Chu, Y. Zhang, Z. Wu. J. Biomed. Mater. Res. B (2009) 91,470.

[6]. P.D. Fey, M.E. Olson, Future Microbiol. (2010) 5, 917.

[7]. C.C. de Carvalho, Recent Pat. Biotechnol (2007) 1, 49.

[8]. A.L Andrade, D. Manzi, R.Z. Domingues, J. Non-Cryst. Solids (2006) 352, 3502.

[9]. Z.R. Domingues, M.E. Cortes, T.A. Gomesa, H.F. Diniz, C.S. Freitas, J.B. Gomes, A.M.C. Fariac, R.D Sinisterra, Biomaterials (2004) 25, 327.

[10]. U.M.E. Wikesjo, P.J. Baker, L.A. Christersson, R.J. Genco, R.M. Lyall, S. Hic, R.M. Diflorio, V.P. Terranova, J. Periodontal Res. (1986) 21, 322.

[11]. B.N.A. Vandekerckhove, M. Quirynen, D. van Steenberghe, J. Periodontol. (1997) 68, 353.

[12]. I. Chopra, P.M. Hawkey, M. Hinton. J. Antimicrob. Chemother. (1992) 29, 245.

[13]. T. Kokubo, H. Kushitani, S. Sakka, T. Kitsugi, T. Yamamuro, J. Biomed. Mater. Res. (1990) 24, 721.

[14]. A. Doostmohammadi, A. Monshi, R. Salehi, M. H. Fathi, Z. Golniya, A.U. Daniels, Ceram. Int. (2011) 37, 2311.

[15]. B. Lei, X. Chen, Y. Wang, N. Zhao, Mater. Lett. (2009) 63, 1719.

[16]. E. Vanea, V. Simon, Appl. Surf. Sci. (2011) 257, 2346.

[17]. J.J. Cooper, J.A. Hunt, J.J. Cooper, J.A. Hunt, communication at Society for Biomaterials 2006 Annual Meeting, Pennsylvania, USA.

STUDIA UBB PHYSICA, LVI, 2, 2011

# BEHAVIOURS IN THERMAL EXPANSION OF NICKEL-BASED, COBALT-BASED AND IRON-BASED ALLOYS CONTAINING VERY HIGH CARBON CONTENTS

**PATRICE BERTHOD**[1,*], **LIONEL ARANDA**[1]

**ABSTRACT.** Nine model ternary alloys, (Bal. Ni, Co or Fe) - 30Cr - (4, 4.5 or 5C) were elaborated by foundry and subjected to microstructure examinations and dilatometry experiments up to 1200°C, in order to examine the thermal expansion behaviours of alloys used for applications requiring high hardness and wear-resistance. All of these alloys are of a hyper-eutectic type with presence of coarse acicular proeutectic carbides in addition to a (matrix+carbides) - eutectic compound. Graphite is also present in the nickel alloys and in the carbon-richest cobalt alloy. Hardness is high (nickel alloys, about 300Hv) and even very high (cobalt alloys, about 600Kv), and maximal (about 700Hv) with the graphite-free iron alloys in which the volume carbide fraction can be higher than 50%. The great difference of thermal expansion coefficient between matrix and carbides leads to curious dimensional variations during temperature changes as well as during the isothermal stage following the heating up to 1200°C, consequently to intense interactions at the microstructure scale. This reveals the progressive stress accumulation during heating, due to both the great difference of thermal expansion between matrix and carbides and the especially high quantities of the latter in such alloys.

***Keywords:*** *nickel alloys, cobalt alloys, iron alloys, high chromium, very high carbon, thermal expansion, chromium carbides, graphite*

## INTRODUCTION

Significant quantities of carbides can be encountered in some alloys used in high temperature applications [1-2], as nickel-based / cobalt-based superalloys or heat-resistant steels. Many of these carbides-strengthened alloys are elaborated by foundry practice and contain several tens of weight percents of chromium, an element which promotes the formation of $Cr_7C_3$ or $Cr_{23}C_6$ carbides in presence of carbon.

Chromium-rich cast nickel-based alloys are in some cases used for aeronautic (jet engines) or terrestrial (energy production) turbine blades to which

---

[1] *Institut Jean Lamour (UMR 7198), Department of Chemistry and Physics of Solids and Surfaces, Faculty of Sciences and Technologies, Postal Box 70239, 54506 Vandoeuvre-lès-Nancy, France, * Patrice.Berthod@lcsm.uhp-nancy.fr*

high chromium contents give a good resistance against high temperature oxidation [3-4], as well as for other applications for which the required hardness is achieved by addition, to the (Ni, Cr)-base, of more carbon [5-8]. Cr-rich cobalt-based alloys rich in chromium can be also considered for turbines blades or disks, as well as for some industrial applications as the fiberizing tools used in the glass industry for glass wool production [9]. In their case too, the addition of several tens of weight percent of chromium allows the alloy resisting oxidation by hot gases and high temperature corrosion by various molten substances (salts, glasses ...). The role of chromium can be also the development of carbides for mechanically strengthening the alloys at high temperature. High levels of hardness can be also expected with carbon-rich cobalt-based alloys but the hard cobalt alloys generally contain other types of carbides, as dispersed WC carbides in the cases of cutting tools [10] or coatings deposited by thermal spray on steels [11]. Concerning the iron-based alloys, the possible presence of large quantities of cementite or pearlite (and martensite in quenched structures allow them to offer high hardness without other carbide-forming elements. However, in their cases too, chromium can be added to enhance mechanical resistance or hardness of bulk alloys [12] or of hardfacing coatings [13] by forming chromium carbides.

Thus, some nickel-based, cobalt-based and iron-based alloys can contain great quantities of chromium carbides to obtain high mechanical properties at low and high temperature (medium amounts of carbon and fractions of carbides) or for achieving wear-resistance (high carbon contents and carbides fractions). A common point of the use of such carbides-rich alloys is the possibility of severe increase in temperature during their use, in case of friction/abrasion, and then the difference of thermal expansion coefficient existing between matrix (15-20 $\times 10^{-6}$ $K^{-1}$) and carbides ($10 \times 10^{-6}$ $K^{-1}$) [14] may lead to particular global thermal expansion behaviours for the whole alloys.

The aim of this paper is to explore the thermal expansion of several carbides-rich nickel-based, cobalt-based and iron-based alloys to predict the possible dimensional phenomena resulting from the matrix-carbides mechanical interactions during heating and cooling. For this purpose several model nickel-based alloys, cobalt-based alloys and iron-based alloys, all containing the same high quantity of chromium and, for each family, three different high levels in carbon, were elaborated by fusion/solidification and their thermal expansion behaviours were explored up to very high temperatures.

## EXPERIMENTAL SECTION

Nine high-carbon 30wt.%Cr-containing ternary alloys were synthesized by foundry from pure elements: three Ni-30Cr-xC alloys, three Co-30Cr-xC alloys and three Fe-30Cr-xC alloys with x = 4.0, 4.5 or 5.0 wt.%. The ingots, all displaying a mass equal to about 30g, were obtained by solidification in the water-cooled copper crucible of a High Frequency induction furnace (CELES), under an inert atmosphere of 300 millibars of pure argon, from pure elements melted together in the same location (purity of elements higher than 99% in mass): Co, Ni, Fe and Cr coming from Alfa Aesar, and C added as pure graphite.

All ingots were cut using a Buehler Isomet 5000 precision saw. Per ingot one part was embedded in a cold resin (Escil CY230 + HY956). Polishing was achieved using SiC papers from 120 to 1200 grit under water, and finished with a 1µm–diamond paste. The metallographic observations were performed using a Philips XL30 Scanning Electron Microscope (SEM), essentially in the Back Scattered Electrons mode (BSE) and with an acceleration voltage of 20kV. The chemical composition of each alloy was controlled using a Cameca SX microprobe (defocalized mode at × 400) on several locations in the bulk. A Bruker XPERT-Pro diffractometer was also used to complete the metallographic characterization.

The hardness of the nine alloys were measured using a Testwell Wolpert device. At least three Vickers indentations per alloy were performed with a load of 30kg.

The dilatometry runs were performed using a TMA 92-16.18 Setaram apparatus on parallelepipedic samples cut in each ingot (samples' dimensions: about 4mm × 4mm (square main faces) × 2mm (direction of the observed expansion). The samples were heated from room temperature up to 1200°C with a rate of 10 K min$^{-1}$, kept at this temperature during a 1 hour – stage, and cooled down to room temperature with a rate of -10K min$^{-1}$. Three parts of the obtained dilatometry curves were characterized: the expansion during the heating part, the isothermal thickness evolution during the 1200°C-stage, and the contraction during the cooling part.

To help the interpretation of the obtained results, calculations of successive thermodynamic stable states were carried out using the Thermo-Calc software [15] and a data base containing the descriptions of:
* the Cr-C system [16] for the three alloys' families,
* the Ni-C, Ni-Cr and Ni-Cr-C [17-19] systems for the nickel alloys,
* the Co-C, Co-Cr and Co-Cr-C systems for the cobalt alloys [20-23],
* the Fe-C, Fe-Cr and Fe-Cr-C systems [24-27] for the iron alloys.

In addition, Differential Thermal Analysis (DTA) experiments were run using a Setaram TGA 92-16.18 device, to correct/complete the previous calculated results with experimental ones to better know the fusion start temperatures of some of the studied alloys.

## RESULTS AND DISCUSSION

The embedded samples were all subjected to microstructure examinations using the SEM in BSE mode. Illustrating micrographs are given in Fig. 1 for the nickel-based alloys, Fig. 2 for the cobalt-based alloys and Fig. 3 for the iron-based alloys.

The nickel-based alloys present as-cast microstructures which are obviously all of the hyper-eutectic type. Indeed, in addition to the eutectic {matrix + carbides} compound there are coarse acicular carbides probably formed early during solidification, as suggested by their typical pro-eutectic shapes. The X-Ray Diffraction experiments show that both $Cr_7C_3$ and $Cr_3C_2$ carbides are present in the three alloys, with surface fractions varying over the [26-28%] range (all carbides counted together). The three alloys also contain graphite as dispersed particles. The latter, of a lamellar type, is more present when the alloy is richer in carbon (from about 1-2% to almost 5% in surface fraction). Due to the very high hardness of the present carbides (1336 $Hv_{50g}$ for $Cr_7C_3$ and 1350$Hv_{50g}$ for $Cr_3C_2$ [28]) compared to the less hard nickel matrix, the hardness of these alloys is rather high, with values comprised between 320 and 350Hv.

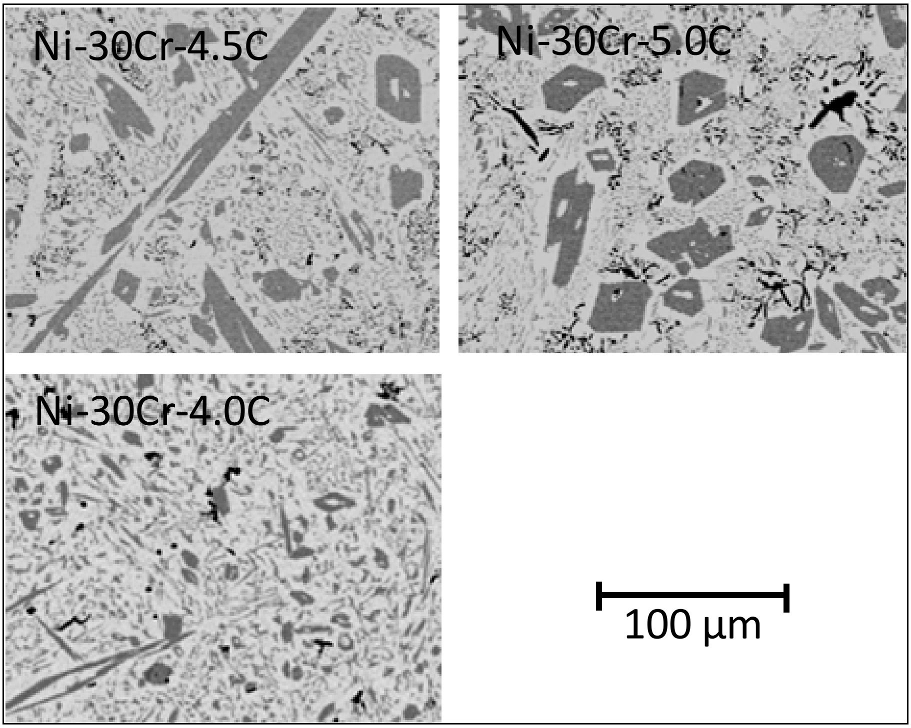

**Fig. 1.** As-cast microstructures of the three nickel alloys (SEM/BSE)

The cobalt-based alloys too are of the hyper-eutectic type, with also an eutectic {matrix + carbides} compound and coarse acicular pro-eutectic carbides, which are $Cr_7C_3$ as revealed by XRD results. Graphite also appears, but only in the Co-30Cr-5.0C alloy. The carbides surface fraction is situated between

40 and 50 % (with about 2% for graphite in the alloy with 5wt.%C), and the hardness is higher than for the nickel alloys, since values between 580 and 650Hv were found for the three alloys.

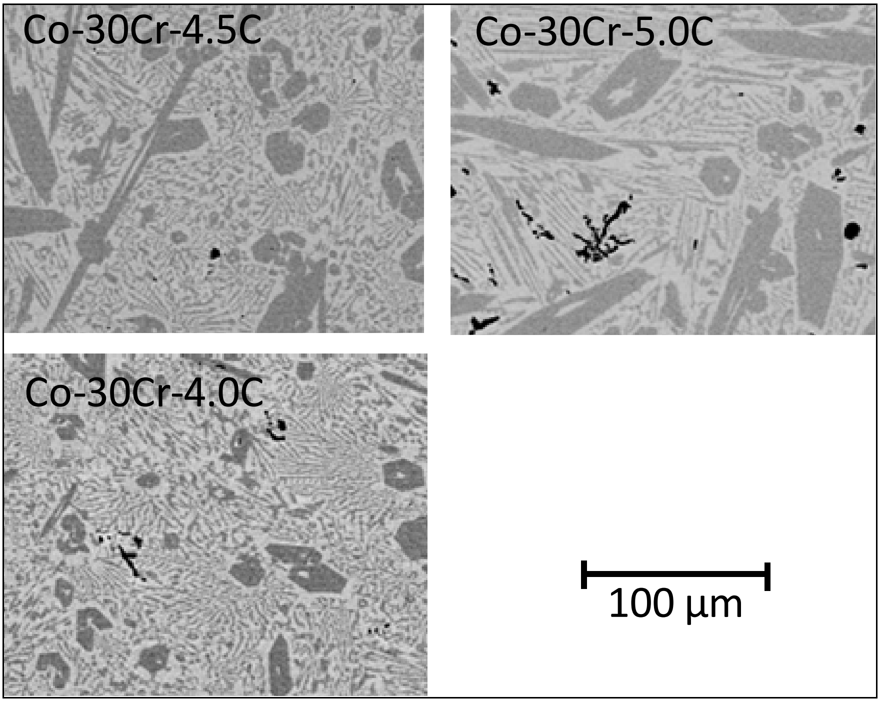

**Fig. 2.** As-cast microstructures of the three cobalt alloys (SEM/BSE)

The iron-based alloys microstructures also present the hyper-eutectic character, with again an eutectic {matrix + $Cr_7C_3$ carbides} compound and coarse acicular $Cr_7C_3$ carbides (here too identified by X-Ray Diffraction), but none of them contains any graphite. The obtained carbides surface fractions are then especially high and the value clearly increases with the carbon content (from about 35% up to about 60%). With such high carbides fractions, the obtained hardness are logically of a very high level (from 600 to 750Hv).

The dilatometry curves obtained are given with a first presentation (heating + cooling, versus temperature) and with a second presentation (heating and 1200°C-stage, versus time), for the nickel alloys in Figure 4 and Figure 5 respectively, for the cobalt-based alloys in Figure 6 and Figure 7, and for the iron-based alloys in Figure 8 and Figure 9. Figures are accompanied by Tables recapitulating the numerical results red on the curves: Table 1 for the nickel alloys, Table 2 for the cobalt alloys and Table 3 for the iron alloys.

**Table 1.** Ni alloys: thermal expansion coefficients measured on the dilatometry curves, deformation at T reaching 1200°C, deformation and total deformation values after the 1200°C stage ($\Delta\varepsilon_{1200}$%) and after return to 100°C ($\Delta\varepsilon_{100}$%)

| **temperature (°C)** | **average linear thermal expansion coefficient ($\times 10^{-6}$°C$^{-1}$)** | | |
|---|---|---|---|
| | **Ni-30Cr-4.0C** | **Ni-30Cr-4.5C** | **Ni-30Cr-5.0C** |
| **Average $\alpha$ ($10^{-6}$ K$^{-1}$)** | **18.2** | **16.0** | **18.1** |
| T range for $\alpha$ | 100-1200°C | 100-1200°C | 200-1100°C |
| **$\varepsilon_{1200}$%** end heating | 1.959 | 1.821 | 1.522 |
| **$\varepsilon_{1200}$%** start cooling | 2.013 | 1.924 | 1.818 |
| Total **$\Delta\varepsilon_{1200}$%** | +0.054 | +0.103 | +0.296 |
| Total **$\Delta\varepsilon_{100}$%** | +0.400 | +0.334 | +0.343 |

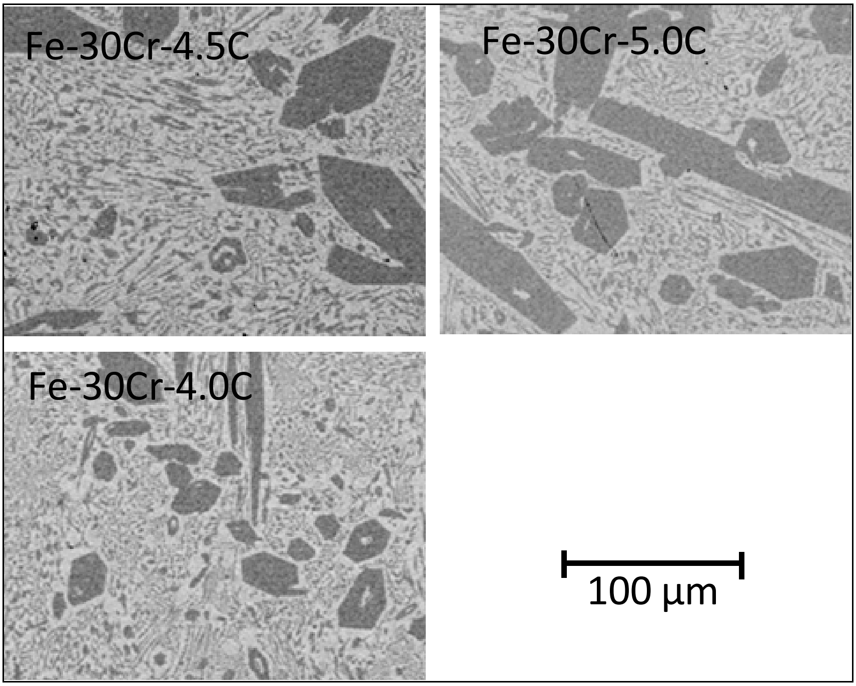

**Figure 3.** As-cast microstructures of the three iron alloys (SEM/BSE)

If cyclic dilatometry runs generally lead, for metallic alloys, to thermal expansion and thermal contraction curves regular and almost superposed, the presence of high quantities of carbides obviously leads to perturbations in the thermal expansion of the alloys.

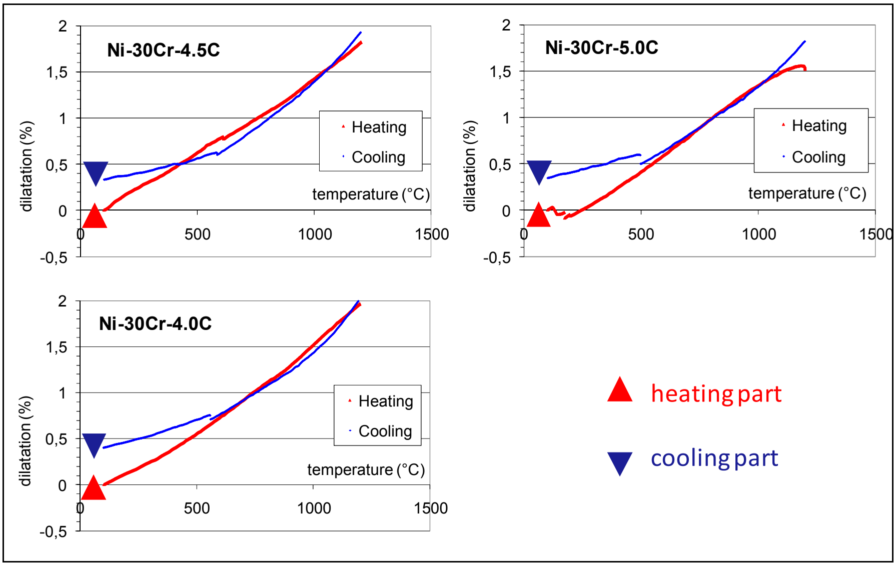

**Figure 4.** Ni alloys: heating & cooling parts of the dilatometry curves (vs. T)

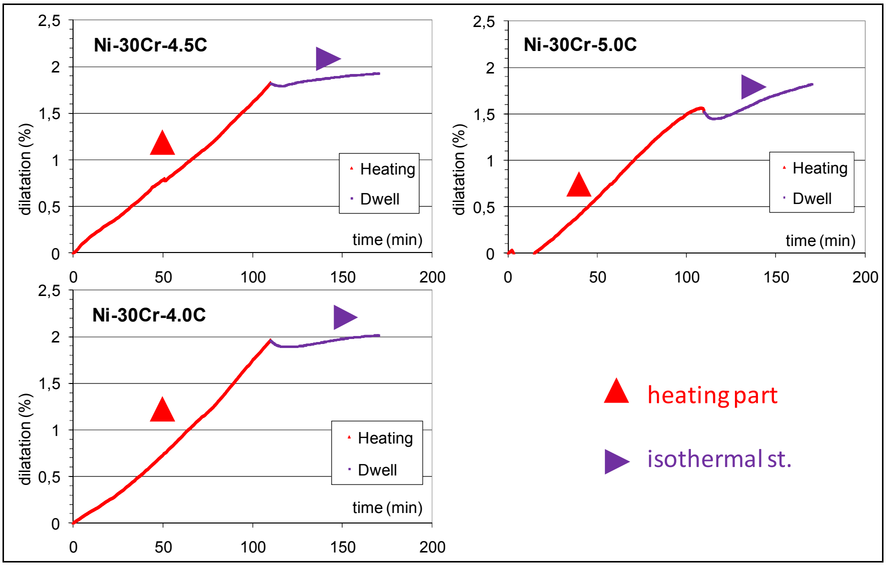

**Figure 5.** Ni alloys: heating & stage parts of the dilatometry curves (vs. t)

This is already a little visible for the nickel-based alloys for which the beginning of the isothermal stage (and also the end of heating for the Ni-30Cr-5.0C alloy) is accompanied by a small contraction. Indeed, after a heating without any particular phenomenon (Thermo-Calc calculations indicating no matrix change over the 100-1200°C temperature range, as logically expected for a nickel-based matrix), the 30% of carbides (in volume) obviously compress the matrix weakened by the high temperature [29]. However, this contraction is soon replaced by a new, still isothermal, expansion which results in a global expansion for the whole isothermal stage.

The initial isothermal contraction seems being more accentuated for the Ni-30Cr-5.0C than for the two other C-poorer nickel alloys, but the following isothermal expansion tends to be higher for the Ni-30Cr-5.0C again. The first of the two latter observations can be attributed to the higher carbides fraction in the Ni-30Cr-5.0C alloy. The second one may be explained by the presence of more graphite in the Ni-30Cr-5.0C, as is to say more possible growing sites for graphitization at 1200°C, and which may promotes the development of a little more graphite (participating to expansion due to its low density) at the expense of the carbides quantity (with a little releasing of the compressed matrix).

The thermal expansion of the cobalt alloys during heating is not perturbed by the allotropic change of matrix (Hexagonal Compact → Face Centred Cubic) which must occur near 400-500°C according to Thermo-Calc calculations. The contraction due to the compression of matrix by the carbides is more significant than for the nickel alloys because of the quantities of carbides which are greater in the cobalt alloys than in the nickel ones. This contraction starts before the end of heating even for the Co-30Cr-4.0C for which a severe contraction goes on during the isothermal stage. This seems more complex for the Co-30Cr-4.5C alloy which seemingly behaves as the previous cobalt alloys, but thereafter as the nickel alloys with possibly an isothermal expansion maybe due to a graphite growth. In the case of the Co-30Cr-5.0C, there is in addition a drastic isothermal thickness decrease, which let think to a partial melting of the alloy: even if Thermo-Calc calculations show that the solidus temperature of the three cobalt alloys is slightly higher than 1200°C, it is true that the refractoriness of the Co-30Cr-xC alloys effectively decreases when carbon increases in a high values range. It is possible that the Co-30Cr-4.5C alloy itself began to melt, as suggested by the high temperature parts of its two dilatation curves (versus temperature and versus time). DTA experiments were done to verify this hypothesis of partial melting at 1200°C of the carbon-richest cobalt alloys, and the obtained results effectively show that the fusion start temperatures of Co-30Cr-4.5C and Co-30Cr-5.0C alloys are around 1190°C, while they are over 1200°C for all the other alloys of this study. New solidification during cooling seemingly induces a perturbed expansion for these two carbon-richest cobalt alloys.

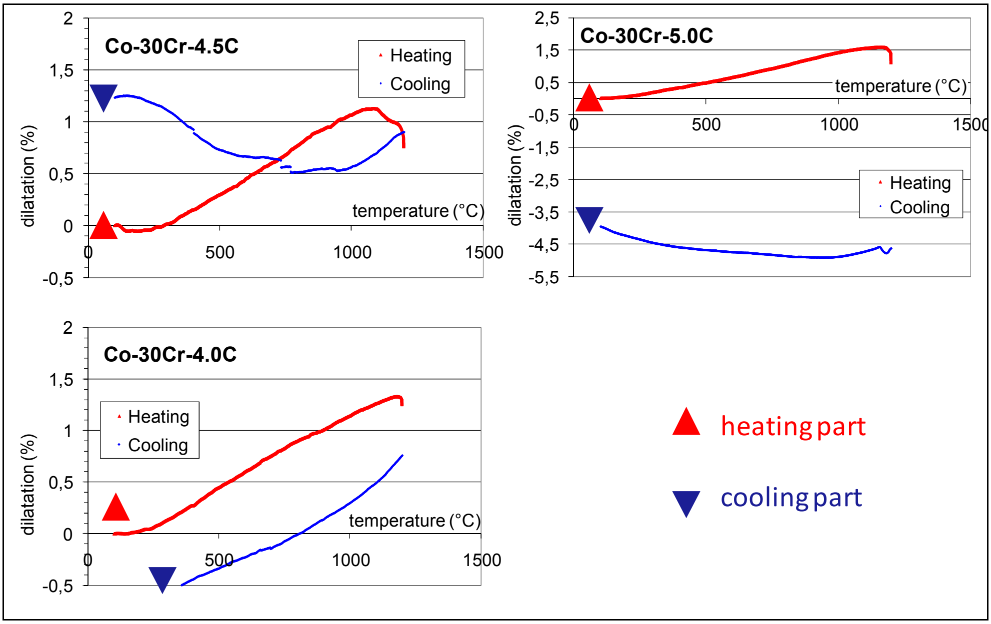

**Figure 6.** Co alloys: heating & cooling parts of the dilatometry curves (vs. T)

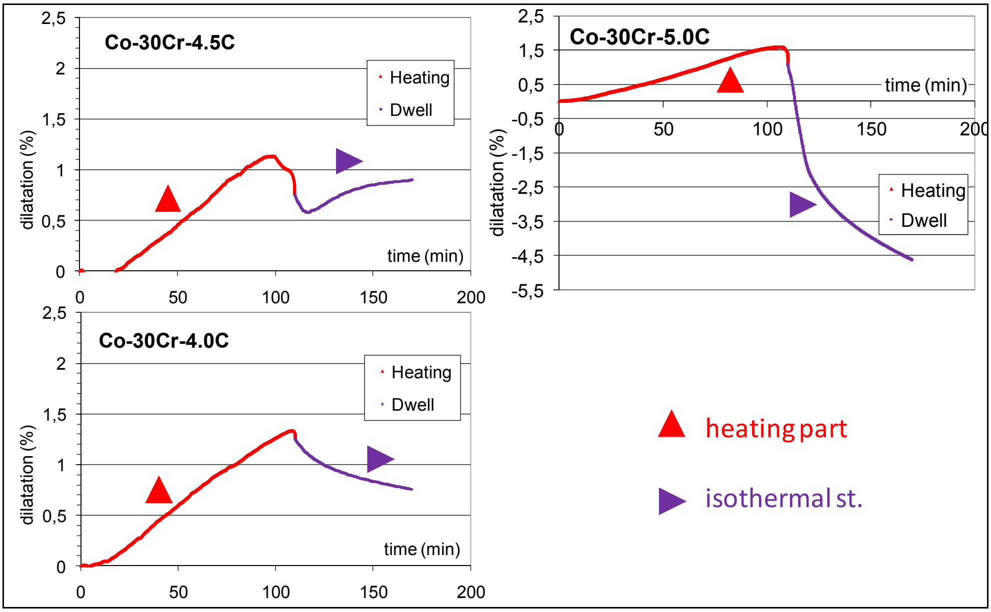

**Figure 7.** Co alloys: heating & stage parts of the dilatometry curves (vs. t)

**Table 2.** Co alloys: thermal expansion coefficients measured on the dilatometry curves, deformation at T reaching 1200°C, deformation and total deformation values after the 1200°C stage ($\Delta\varepsilon_{1200}\%$) and after return to 100°C ($\Delta\varepsilon_{100}\%$)

| **temperature (°C)** | **average linear thermal expansion coefficient ($\times 10^{-6} {}^\circ C^{-1}$)** | | |
|---|---|---|---|
| | **Co-30Cr-4.0C** | **Co-30Cr-4.5C** | **Co-30Cr-5.0C** |
| **Average α ($10^{-6}$ $K^{-1}$)** | **14.4** | **15.2** | **17.5** |
| T range for α | 200-1100°C | 230-1040°C | 200-1100°C |
| $\varepsilon_{1200}\%$ end heating | 1.254 | 0.761 | 1.108 |
| $\varepsilon_{1200}\%$ start cooling | 0.755 | 0.903 | -4.633 |
| Total $\Delta\varepsilon_{1200}\%$ | -0.499 | +0.142 | -5.741 |
| Total $\Delta\varepsilon_{100}\%$ | -0.746 | +1.234 | -3.966 |

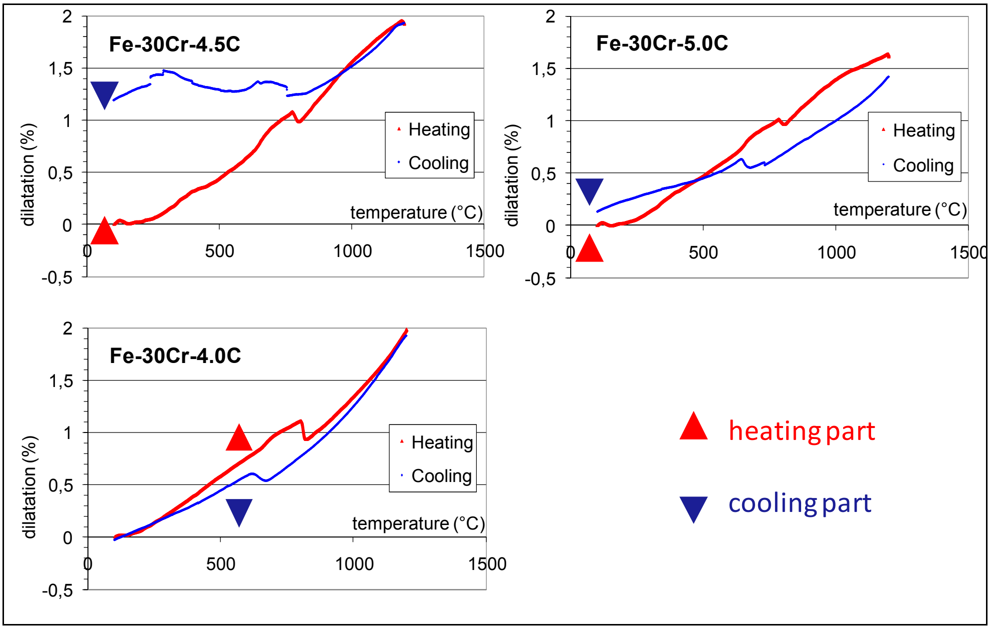

**Figure 8.** Fe alloys: heating & cooling parts of the dilatometry curves (vs. T)

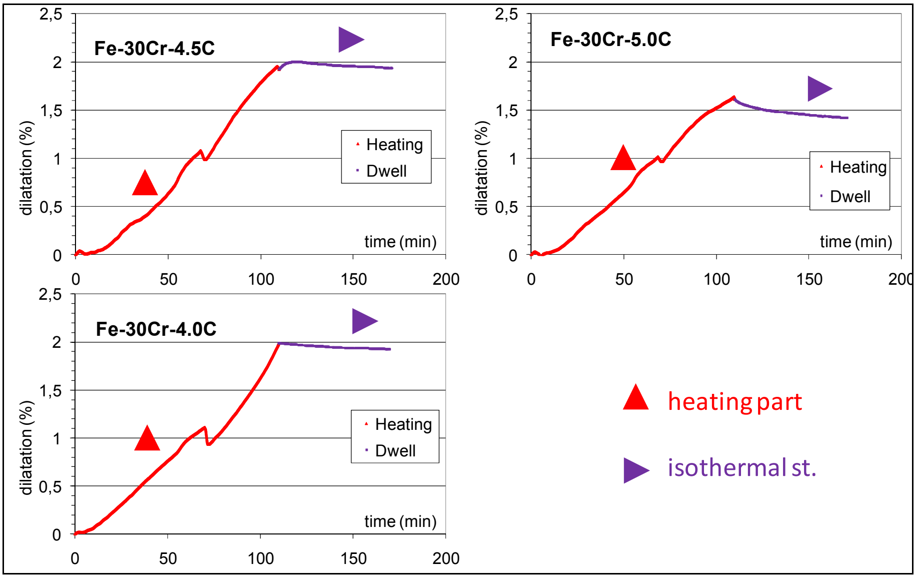

**Figure 9.** Fe alloys: heating & stage parts of the dilatometry curves (vs. t)

**Table 3.** Fe alloys: thermal expansion coefficients measured on the dilatometry curves, deformation at T reaching 1200°C, deformation and total deformation values after the 1200°C stage ($\Delta\varepsilon_{1200}$%) and after return to 100°C ($\Delta\varepsilon_{100}$%)

| **temperature (°C)** | **average linear thermal expansion coefficient ($\times 10^{-6}$°C$^{-1}$)** | | |
|---|---|---|---|
| | **Fe-30Cr-4.0C** | **Fe-30Cr-4.5C** | **Fe-30Cr-5.0C** |
| **Average $\alpha$ 1 ($10^{-6}$ K$^{-1}$)** | **17.3** | **16.3** | **16.0** |
| $\alpha \rightarrow \gamma$ *contraction T range* | 782-814°C | 756-798°C | 768-796°C |
| **Average $\alpha$ 2 ($10^{-6}$ K$^{-1}$)** | **28.9** | **25.0** | **22.5** |
| **$\varepsilon_{1200}$%** end heating | 1.986 | 1.925 | 1.614 |
| **$\varepsilon_{1200}$%** start cooling | 1.926 | 1.935 | 1.419 |
| Total **$\Delta\varepsilon_{1200}$%** | -0.060 | +0.010 | -0.195 |
| Total **$\Delta\varepsilon_{100}$%** | -0.026 | +1.193 | +0.130 |

The iron alloys present a thermal expansion at heating which is rather regular, except near 800°C where the allotropic transformation of matrix, Centred Cubic → Face Centred Cubic, induces an increase in network compacity which cannot be obstructed by the matrix interaction with the numerous carbides. For such high carbon contents, the precipitation of a high quantity of chromium carbides has greatly impoverished the matrix in chromium which cannot stay anymore ferritic over the whole temperature range of the study, despite the 30wt.%Cr contained by the alloys. By looking at the cooling parts of the dilatometry curves one can see the inverse FCC → CC transformation, obviously delayed to lower temperatures.Considering again the heating parts of the curve one can find that austenite presents a higher thermal expansion coefficient than the ferritic one, as usually shown by low carbon unalloyed steels. But these coefficients both tend to decrease when the carbon increases, then the carbide fraction increases. These iron alloys are not really affected by a contraction due to the action of carbides at the end of heating but such contraction occurs during the isothermal stage. Further, one can notice that the contraction is the most severe for the highest carbon content or carbide fraction (Fe-30Cr-5.0C).

## CONCLUSIONS

In this study different curious phenomena occurred during the dilatometry tests for these high-carbon chromium-rich nickel-based, cobalt-based and iron based alloys. If some of these dimensional phenomena may be attributed to phase transformations ($\alpha \leftrightarrow \gamma$ for iron alloys at moderate temperatures, and possibly melting start and graphitization at high temperature for the cobalt and nickel alloys), most of them are directly related to the matrix ↔ carbides interactions, especially intense in the case of these alloys which are very rich in carbon then in carbides. These interactions obviously induce dimensional deformation at high and constant or not temperatures, with as consequence irreversible and uncontrolled residual shape changes, which can represent some problems in use. This was seen here because heating was pursued until very high temperatures in these tests. The phenomena may be less problematic for heating up to not so high temperatures, which will be studied later with new dilatometry tests, for example up to only 1000°C or 800°C, with again one hour stage too at the maximal temperature.

## REFERENCES

1. E.F. Bradley, "Superalloys : A Technical Guide", ASM International, Metals Park, **1988**.
2. C.T. Sims, W.C. Hagel, “The Superalloys”, John Wiley & Sons, New-York, **1972**.
3. P. Kofstad, “High Temperature Corrosion”, Elsevier, London, **1988**.
4. D. Young, “High Temperature Oxidation and Corrosion of Metals, Elsevier, Amsterdam, **2008**.
5. A. Klimpel, L.A. Dobrzanski, A. Lisiecki, D. Janicki, *Journal of Materials Processing Technology*, **2005,** 164-165,1068.
6. Z.T. Wang, H.H. Chen, *Mocaxue Xuebao Tribology*, **2005,** 25, 203.
7. H. Han, S. Baba, H. Kitagawa, S.A. Suilik, K. Hasezaki, T. Kato, K. Arakawa, Y. Noda, *Vacuum*, **2005,** 78, 27.
8. D. Zhang, X. Zhang, *Surface and Coating Technology*, **2005,** 190, 212.
9. P. Berthod, J.L. Bernard, C. Liébaut; Patent WO99/16919.
10. B. Roebuck, E.A. Almond, *Int. Mater. Rev.,* **1988,** 33, 90.
11. A. Klimpel, L.A. Dobrzanski, A. Lisiecki, D. Janicki, *J. Mater. Process. Tech.*, **2005**,164-165, 1068.
12. H.E.N. Stone, *J. Mater. Sci.*, **1979,** 14, 2781.
13. B.V. Cockeram, *Met. Mater. Trans. A: Phys. Met. Mater. Sci.,* **2002,** 33, 3403.
14. T.B. Shaffer, “Handbooks of High-Temperature materials N°1. Materials Index”, Plenum Press, New York,**1964**.
15. Thermo-Calc version N: “Foundation for Computational Thermodynamics” Stockholm, Sweden, Copyright **(1993, 2000)**, www.thermocalc.com
16. J.O. Andersson, *Calphad*, **1987,** 11, 271.
17. A. Gabriel, C. Chatillon, I. Ansara, *High Temp. Sci.,* ***1988,*** 25, 17.
18. A. Dinsdale, T. Chart, MTDS NPL, unpublished work, **1986**.
19. NPL, unpublished work, **1989**.
20. A. Fernandez Guillermet, *Int. J. Thermophys.*, **1987**, **8**, 481.
21. A. Fernandez Guillermet, *Z. Metallkde*, **1987**, 78, 700.
22. J.O. Anderson, *Calphad*, **1987,** 11, 271.
23. A. Fernandez Guillermet, *Z. Metallkde,* **1988,** 79, 317.
24. A. Fernandez Guillermet, P. Gustafson, *High Temp. High Press.*, **1984,** 16, 591.
25. J.O. Andersson, B. Sundman, Calphad, **1987,** 11, 83.
26. P. Gustafson, *Scan. J. Metall.,* **1985,** 14, 259.
27. J.O. Andersson, *Met. Trans. A*, **1988,** 19A, 627.
28. G.V. Samsonov, “Handbooks of High-Temperature materials N°2. Properties Index”, Plenum Press, New York,**1964**.
29. P. Berthod, *Int. J. Mat. Res. (formerly Z. Metallkd.),* **2008,** 99(3), 265.

STUDIA UBB PHYSICA, LVI, 2, 2011

# MAGNETIC PROPERTIES AND MAGNETOCALORIC EFFECT IN $Tb_8Co_{16-X}Cu_X$ COMPOUNDS

**A. BEZERGHEANU[1], R. GRASIN[1], R. TETEAN[1*]**

**ABSTRACT.** The $Tb_8Co_{16-X}Cu_X$ compounds crystallize in a cubic Laves phase structure of C15 type for $x \leq 4$. The magnetic properties and magnetocaloric effect in these compounds are reported. The compounds are ferrimagnetically ordered. The Curie temperature decrease while the magnetic moments are little affected by substitution of cobalt atoms by cooper ones. The cobalt behavior is analyzed in spin fluctuation model. The potential use of these materials in magnetic refrigeration is discussed.

***Keywords:*** *Magnetocaloric effect; Magnetization; Rare-earth-transition metal compounds; Susceptibility*.

## INTRODUCTION

Magnetic materials showing a large magnetocaloric effect (MCE) have attracted considerable attention for their potential application in magnetic refrigeration technology [1-3]. MCE is an isothermal magnetic entropy change or an adiabatic temperature change of a magnetic material upon application of a magnetic field. The compounds which undergo temperature driven paramagnetic to ferromagnetic transitions show relatively large "negative" MCE, in which the isothermal magnetic entropy change, $\Delta S_m = S(H,T) - S(0,T)$ is negative [4]. Generally, due to their high magnetic moments, heavy rare earths elements and their compounds are considered as best candidate materials for finding a large MCE [5].

Several Laves phase compounds have been investigated for magnetocaloric effect because of simply crystal structure [6-8]. The $RCo_2$ intermetallic compounds (R= rare earth metal) were intensively studied due to the metamagnetic character of its cobalt sublattice [9,10]. When R is nonmagnetic there are necessary high fields (> 70 T in $YCo_2$) in order to induce magnetic moments on cobalt atoms and giving rise to metamagnetic transitions. If R is a magnetic atom the internal field is high enough to induce and polarize the cobalt moments. It was reported that in the compounds with R = Dy, Ho or

---

[1] *Babes-Bolyai University, Faculty of Physics, RO-400084, Cluj-Napoca, Romania*
[*] *Corresponding author. Tel.: +4-0264-594315; fax: +4-0264-591906;*
*e-mail: romulus.tetean@phys.ubbcluj.ro*

Er the ferrimagnetic state is coupled to a structural transition, leading to a first order transition at the critical temperature [11-13]. Due to the high value of the R magnetic moment a large entropy changes at the transition temperature were reported [14,15].

The physical properties of the $RM_2$ intermetallic compounds, where R is a rare earth or yttrium and M a transition metal, were intensively investigated [16]. The f electrons of R elements have a small spatial extent, and generally one can assume that they are well localized. The 3d electrons give rise to a wide range of behaviors from well established magnetism with high ordering temperatures to paramagnetism by crossing the situation in which magnetism is close to an onset or a collapse.

The $RCo_2$ compounds crystallize in a cubic Laves phase structure of C15 type. In this structure the R and M atoms, respectively, occupy each one type of site only. Because of the high symmetry of this lattice, the study of these compounds may give useful information on the magnetic behavior of the constituent atoms [16,17]. The $TbCo_2$ compound was reported to be ferrimagnetically ordered, the Tb magnetization being antiparallel oriented to that of cobalt. In the paramagnetic region a non-linear temperature dependence of the reciprocal susceptibility was reported.

Previously, we have studied the magnetic properties in $TbCo_{3-X}Cu_X$ compounds in the region where a rhombohedral structure having $R\bar{3}m$ space group is formed [18**]**. It was shown that the cobalt magnetic moment is sensitive to the local environment. In order to obtain additional information on transition metals behavior in pseudobinary compounds we study the magnetic properties of cobalt in $Tb_8Co_{16-X}Cu_X$ system in the range with rich cobalt content. In all cases the magnetic entropy changes around transition temperatures were evaluated.

## EXPERIMENTAL

The $Tb_8Co_{16-X}Cu_X$ compounds were prepared by arc melting in a purified argon atmosphere from high purity Co (99.9%), Cu (99.999%) and Tb (99.95%) ingots (Alfa Aesar, Jonson & Matthey, Karlsruhe, Germany). A small excess of rare earth element was used in order to compensate for losses during melting. The ingots were remelted several times in order to ensure a good homogeneity. The samples were heat treated in vacuum at 1000 ºC for 5 days. The crystal structure was checked by X-ray Diffraction using a Bruker 8 XD diffractometer.

The magnetic measurements were performed in the temperature range 4.2-650 K and external fields up to 12T using a close cycle 12 T Vibrating Sample Magnetometer (VSM) from Cryogenics. The spontaneous magnetizations, $M_s$, were determined from magnetization isotherms according to approach to saturation law, $M = M_s(1 - b/H) + \chi_o H$. We denoted by *b* the coefficient of magnetic hardness and $\chi_o$ is a Pauli-type contribution. In order to avoid any possible alteration of magnetic susceptibilities as result of the presence of small quantities of magnetic ordered impurities, the susceptibilities, $\chi$, were determined from Honda-Arrott plots according to the relation $\chi_m = \chi + dM_s^{'}H^{-1}$ by extrapolation to $H^{-1} \to 0$ [19]. By d we denoted presumed impurity content and $M_s^{'}$ is their saturation magnetization.

The entropy changes were determined from magnetization isotherms, between zero field and a maximum field ($H_0$) using the thermodynamic relation:

$$\Delta S_m(T,H_0) = S_m(T,H_0) - S_m(T,0) = \frac{1}{\Delta T}\int_0^{H_0}[M(T+\Delta T,H) - M(T,H)]dH$$

where $\Delta T$ is the temperature increment between measured magnetization isotherms ($\Delta T = 5K$ for our data).

## RESULTS AND DISCUSSION

The X-ray analysis shows, in the limit of experimental errors, the presence of one phase only, for x ≤ 4, of C15 type. The lattice parameters decrease slightly when Cu content increases, fact attributed to smaller radius of Cu ion compared with Co one.

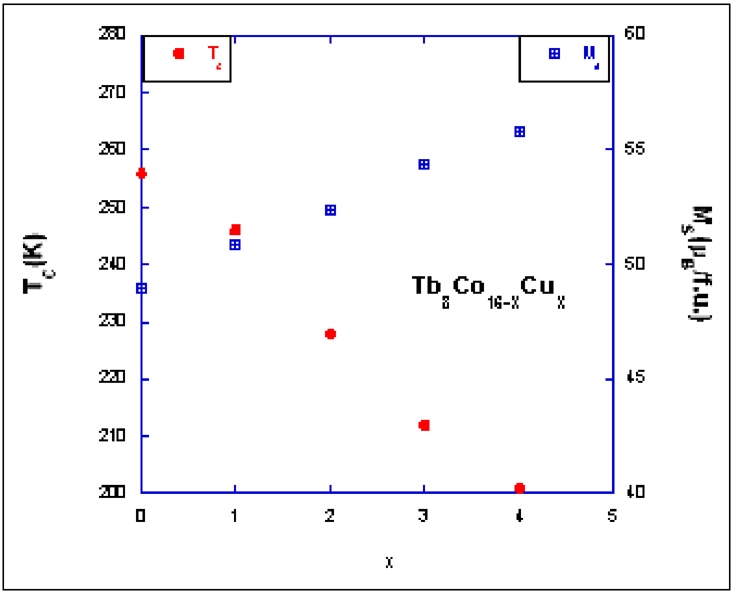

**Fig. 1.** The composition dependences Of the Curie temperatures and spontaneous magnetizations measured at 4.2 K.

The magnetization isotherms measured in magnetic fields up to 12 T shows that the saturation is not attended. The magnetizations, at 4.2 K, increase from 48.96 $\mu_B$/f.u. at x = 0 to 55.76 $\mu_B$/f.u. at x = 4 –see Fig.1. The above behavior is in agreement with the presence of a ferrimagnetic type ordering, the cobalt and terbium magnetic moments being antiparallely oriented. Assuming that the terbium mean magnetic moment, at 4.2 K, is the same like that determined on $TbCo_2$ compound by neutron diffraction study [20] the cobalt contributions to magnetizations were determined. The cobalt moments are little dependent on Cu content having values in the range 1.1±0.09 $\mu_B$/atom. The Curie temperatures decrease when copper content increase – Fig.1.

The temperature dependences of reciprocal susceptibilities, $\chi^{-1}$, follow a hyperbolic law of Néel- type, characteristic for ferrimagnetic ordering. At high temperatures, the $\chi^{-1}$ vs. T plots shows linear dependences. The Curie constants, determined in the above temperature ranges, are higher than the characteristic values for $Tb^{3+}$ ion suggesting the presence of contributions from the cobalt atoms. According to addition law of susceptibilities and supposing that the Curie constant of terbium is the same as that of $Tb^{3+}$ ion, we determined the contributions of Co, to the Curie constants and the effective cobalt moments, $M_{eff}$(Co), respectively. The $M_{eff}$(Co) values are only slightly composition dependent being 2.81±0.12 $\mu_B$/atom. The ratio $r=S_P/S_0$ between the number of spins obtained from effective cobalt moments, $S_P$, and saturation moments, $S_0$, is quite constant having values around 1.73±0.07. In the local moment limit we have r=1.0. For a weak ferromagnet the r values increase considerably. In our compounds the r value suggests that cobalt have rather high degree of itinerancy.

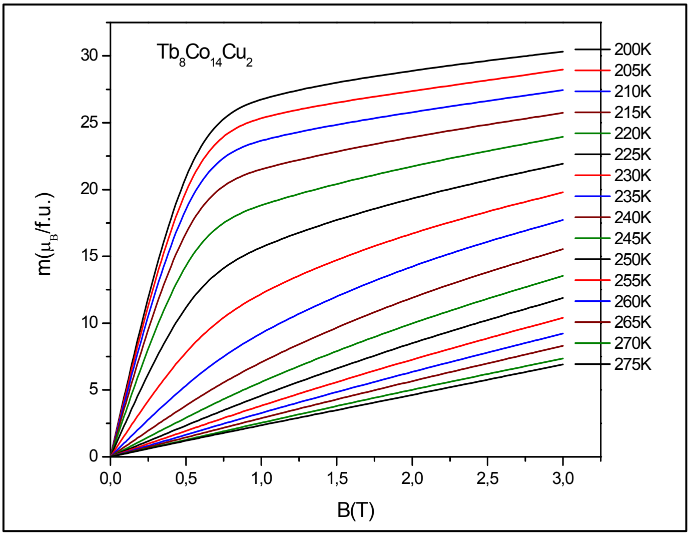

**Fig. 2.** The magnetization isotherms around the Curie temperature for the compound with x=2.

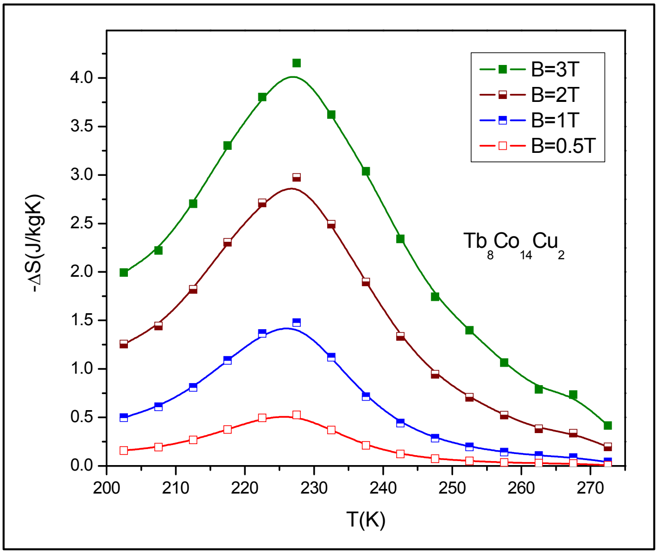

**Fig. 3.** The temperature dependence of the magnetic entropy change for the compound with x=2.

The above behaviour can be analyzed in spin fluctuation model [21,22]. When the amplitude of local spin fluctuations (LSF) is large and fixed, there is a local moment limit, where only the transverse components of LSF are important. As the amplitude of LSF is small, there is the weakly ferromagnet limit, where the longitudinal components of LSF or temperature variation of amplitude of LSF play an important role. From the r values in $Tb_8Co_{16-X}Cu_X$ system we conclude that there are significant contributions from longitudinal components of LSF. The cobalt behavior in these compounds can be described as a weak ferromagnet. The effective cobalt moments determined in $Tb_8Co_{16-X}Cu_X$ system are smaller than in $YCo_2$ compound. This fact may be attributed to partial quenching of spin fluctuation by internal field [23]. If the exchange field is sufficiently large so that the Zeeman splitting energy of opposite spin states is comparable or larger than the characteristic spin fluctuation energy, the paramagnons no longer have sufficient energy to flip spins and therefore the inelastic spin flip scattering is quenched. A magnetic field of the order of the characteristic spin fluctuation temperature is needed to quench the spin fluctuation enhancement [24-26]. Similar behavior was reported on $GdCo_{2-X}Si_X$ and $GdCo_{2-X}Cu_X$ compounds [27,28].

The magnetization isotherms in magnetic fields up to 3T around the transition temperature for the $Tb_8Co_{14}Cu_2$ compound are presented in Fig.2. From this dependences the magnetic entropy change in 0.5T, 1T, 2T and 3T external applied field for the compound with x = 2 were calculated and are plotted in Fig.3. The maximum values of entropy change occur almost at the Curie temperature. Similar behaviour was found for all the compounds. The maximum value is around 4 J/kgK in a 3T respectively 3 J/kgK in 2 T magnetic field for the compound with x = 2. The values of the magnetic entropy change obtained for the doped compound are smaller than that obtained for the parent compound, $Tb_8Co_{16}$, where a value of 3.75 J/kgK in 2 T magnetic field was obtained. One can see that the variation of the magnetic entropy change is symmetric around the transition temperature, suggesting that the transitions are of second order. The determined ΔS values in $Tb_8Co_{16-X}Cu_X$ are rather high for compounds showing a second order type transition. Around 63 % of the heat is absorbed in a temperature range ±12 K, centered at the Curie point.

A parameter characteristic for magnetocaloric materials is the relative cooling power $RCP(\Delta S)=|\Delta S_m|\delta T_m$, defined as a product of the maximum value of the entropy change $|\Delta S|$ and the full-width at half-maximum $\delta T_m$. A large RCP(ΔS) corresponds to a better magnetocaloric material. As an example, for compounds with x=0.0 and 2 values of the order of 99.5 J/kg respectively 111 J/kg for RCP(ΔS) were obtained. These rather high values of the relative cooling power suggest the possibility to use these materials in magnetic refrigeration. We note that the determined $|\Delta S|$ values are only approximate. These are inflenced by the rate of increase in magnetic field, during the measurements as well as by the approximation used in determining $|\Delta S|$ values from a discrete set of magnetizations data [29,30]. The entropy changes are also sensitive to the magnetic hardness of the material.

## CONCLUSIONS

We have studied the magnetic properties and the magnetocaloric effect in $Tb_8Co_{16-X}Cu_X$ compounds with Laves phase structure. The cobalt behavior in these compounds can be described as a weak ferromagnet. Partial quenching of spin fluctuation by internal field was observed. Large magnetic entropy changes have been observed for all concentrations. The transition temperature can be tuned via Cu concentration. These suggest that $Tb_8Co_{16-X}Cu_X$ has a potential application as a working substance of magnetic refrigeration in the temperature range 190-270 K.

## ACKNOWLEDGEMENTS

This work was supported by the grant ID-2578 nr.565/2008 with CNCSIS Romania. A.B. and R.G would like to acknowledge support from contract POSDRU 6/1.5/S/3-"Doctoral studies: through science towards society".

## REFERENCES

[1] K.A.Gschneider, Jr and V.K.Pecharsky, Annu. Rev. Mater. Sci. **30**, 387 (2000).

[2] V.K.Pecharsky and K.A.Gschneider, Jr, Phys. Rev Lett. **78**, 4494 (1997).

[3] V.K.Pecharsky and K.A.Gschneider, Appl. Phys. Lett. **70**, 3299 (1997).

[4] H. Wada and Y. Tanabe, Appl. Phys. Lett., **79**, 3302 (2001).

[5] E. Bruck, O.Tegus, X.W.Li, F.R. de Boer, K.H.J. Buschow, Physica B, **327**, 431 (2003).

[6] H.D. Liu, D.H. Wang, S.L. Tang, Q.Q. Cao, T. Tang, B.X. Gu, Y.W. Du, J. Alloy Compd., **346**, 314, (2002).

[7] H. Wada, S. Tomekawa, M. Shiga, J. Magn. Magn. Mater., **196/197**, 689 (1999).

[8] D.H. Wang, S.L. Tang, H.D. Liu, W.L. Gao and Y.W. Du, Intermetallics, **10**, 819 (2002).

[9] E. Gratz and A.S. Markosyan, J. Phys: Condens. Matter, **13**, R385 (2001).

[10] T. Goto, K. Fukamichi, T. Sakakibara and H. Komatsu, Solid State Commun., **72**, 945 (1989).

[11] R. Moon, W.C. Koehler and J. Farrel, J. Appl. Phys., **36**, 978 (1965).

[12] P. Hendy and E.W. Lee, Phys. Status Solidi a, **50**, 101 (1978).

[13] W. Ross and J. Crangle, Phys. Rev. **133** A509 (1964).

[14] A.M. Tishin, in *Handbook of Magnetic Materials*, edited by K.H.J. Buschow, Elsevier Science, New York, Vol. **12** (1999).

[15] A.M. Tishin and Y.I. Spichkin, *The Magnetocaloric effect and its Applications*, 1st ed., Institute of Physics, New York (2003).

[16] E. Burzo, A. Chelkovski and H. R. Kirchmayr, Landolt Bornstein Handbook, Springer, Berlin, vol **III/19d2** (1990).

[17] K.H.J. Buschow, Rep. Progr. Phys. **40**, 1179 (1977).

[18] R.Tetean, E. Burzo, I.G. Deac, J. Alloy. Compd., **442**, 206 (2007).

[19] L.F.Bates, Modern Magnetism, p.133, Cambridge University Press, Cambridge, England (1951).

[20] T. Moriya, J. Magn. Magn. Mat., **14**, 1 (1979).

[21] T.Moriya, J. Magn. Magn. Mat., **100**, 201 (1991).

[22] E. Burzo and R. Lemaire, Solid State Commun., **84**, 1145 (1992).

[23] W.F. Brinkman, S. Engelsberg, Phys. Rev. B, **169**, 417 (1968).

[24] M.T. Beal-Monod, S.K. Ma, D.R. Fredkin, Phys. Rev. Lett., **22**, 928 (1968).

[25] K. Ikeda, k.A. Gschneidner, R.J. Stiermann, J.W.E. Tsang, O.D.Mc Masters, Phys. Rev. B, **29**, 5039 (1984).

[27] E. Burzo, R. Tetean, Zs. Sarkozi, L. Chioncel, M. Neumann, J. Alloy. Compd., **323-324**, 490 (2001).

[28] R. Tetean, E. Burzo, L. Chioncel, T. Crainic, Phys. Status Solidi (a), **19**6, 301 (2003).

[29] A.M. Tishin, A.V. Derkach, Y.I. Spichkin, V.D. Kuzmin, A.S. Chernyshov K.A. Gschneider Jr., V.K. Pecharsky, J. Magn. Magn. Mater. **310**, 2800 (2007).

[30] E. Brück, M. Ilyn, A.M. Tishin, O. Tegus, J. Magn. Magn. Mater. **290–291,** 8 (2005).

STUDIA UBB PHYSICA, LVI, 2, 2011

# CORRELATION CLUSTERING APPROACH TO LOGICAL LEARNING

CSEH GY[1], NÉDA Z.[1,2], D. DAVID[3,4]

**ABSTRACT**. The relation between the level of logical learning and intelligence quotient (IQ) of an individual is investigated in view of a complex clustering model. A useful analogy between the learning process of a material with logically interconnected parts and the correlation clustering problem suggest a phase-transition like trend: the Logical Learning Rate of individuals should increase sharply above some IQ level. Psychological tests are conducted and analyzed for a sample of 177 high-school students. The measured IQ and LLR values confirm the conjecture.

***Keywords:*** *correlation clustering, phase-transition, logical learning, networks*

## INTRODUCTION

Basic models and methods of statistical physics proved to be useful in understanding several complex phenomena in biology, economy or sociology [1]. Critical phenomena, pattern formation and selection, self-organized criticality, small-world networks, nonlinear and disordered systems, non-equilibrium processes and combinatorial optimizations are only a few known examples in such sense. In the present work we consider the recently introduced correlation clustering problem [2-5] and an interesting application of it in psychology.

Correlation Clustering (CC) can be formulated simply in laymen terms: given a set of elements interconnected globally through positive and negative links, find an optimal clustering of them which maximizes the number of positive links within the clusters and the number of negative links between the clusters. Based on our daily-life experience a simpler sociological formulation can be also given. Let us consider a group of people that know each other and have fixed and reciprocal (symmetric) propensities towards the group members. These propensities can be either positive (they sympathize each other) or negative ones (they consider antipathetic the other). The CC problem is to find an optimal grouping of them, so that the given propensities are optimally satisfied. This

---

[1] *Babeş-Bolyai University, Department of Physics, Cluj-Napoca, Romania*
[2] *Interdisciplinary Computer Simulation Research Group, KMEI, Cluj-Napoca, Romania*
[3] *Babeş-Bolyai University, Department of Clinical Psychology, Cluj-Napoca, Romania*
[4] *Mount Sinai School of Medicine, New York, USA*

means that persons connected with positive propensities (persons that “like” each other) should be in the same group while persons connected by negative propensities (agents that “hate” each other) should be in different groups.

It is easy to realize that the CC problem is relevant to many other practical situations in different domains of sciences. It was originally motivated by a research at Whizbang Labs, where learning algorithms were trained to help various clustering tasks [1]. CC is also related to agnostic learning [6], which is an emerging approach to efficient data mining and artificial intelligence. Important applications can be in medicine and pharmaceutics, where one needs to divide drugs in compatibility groups. Closely related problems were considered also while studying coalition formation phenomena in sociological systems [7-9]. It also resembles the infinite-range Potts-glass [10-12] system. From statistical physics point of view it is especially interesting because it exhibits a non-trivial phase transition-like phenomena [3].

In the present work we apply results of the correlation clustering problem for explaining experimentally obtained connections between the Logical Learning Rate (LLR) and Intelligence Quotient (IQ) of a person. The relationship between learning and intelligence is one of the major topics in psychology [13]. There are hundreds of studies investigating this relationship, showing that explicit learning (e.g., logical learning) strongly correlates with what we traditionally call intelligence quotient. Indeed, Reber et al. [14] showed that IQ accounted for almost 50% of the variance in the explicit (logical) learning performance.

The structure of the paper is as follows: first, we will review those major results for CC that are used for explaining the experimental data, than we discuss the connection between CC and logical learning and finally we present our experimental results for the relation between LLR and IQ which confirm our conjecture.

## THE CORRELATION CLUSTERING PROBLEM

Solving the CC problem is a rather complex task. A perfect solution for a general situation is usually not possible because there is no grouping so that all connections are optimally satisfied. A simple example for this is when there is a “frustrated triangle”: three agents interconnected with two positive links and one negative link. If one would put all three agents in one cluster the negative link becomes frustrated, putting them in two different clusters will frustrate one of the positive links. There are of course a few simple cases when a perfect solution can be achieved. An immediate example for the three agent situation is when all propensities are positive, which means that everybody likes each other. In this case the ideal clustering is to put all agents in one cluster. Another simple case is when all propensities are negative (everybody hate each other). The solution is again straightforward: all agents have to be in separate clusters. For a general system however the problem becomes an NP hard optimization. This means that the computational time necessary for finding the optimal clustering increases as a function of the system size faster than any polynomial function. This is the reason why an exact solution by exhaustive search is impossible for moderately large systems. As an example, for a group formed by N=15 individuals and an arbitrary propensity distribution among the group members, it is not possible to obtain an exact solution in reasonable computational time even on the fastest supercomputer.

The CC problem can be formulated mathematically. For this we quantify the positive links as +1 and the negative links as -1 and introduce a K cost-function [3] which increases by 1 whenever two conflicting agents are in the same cluster or when two agents with positive propensities between them are in different clusters. The mathematical problem is then to get a clustering which minimizes the value of K:

$$K = -\sum_{i<j} \delta_{\sigma(i)\sigma(j)} J_{ij} + \frac{1}{2}\sum_{i<j}(J_{ij} + |J_{ij}|)\,, \tag{1}$$

In Eq. 1 $\sigma(i)$ denotes the cluster to which agent i belongs, the sums are for all possible pairs, $\delta$ is the Kronecker-delta symbol ($\delta_{ij} = 1$ for $i = j$ and $\delta_{ij} = 0$ for $i \neq j$) and $J_{ij} = \pm 1$ is the link (propensity) between agent i and j. Solving the CC problem is equivalent with finding the $\sigma(i)$ values that minimizes the K cost-function. Although perspectives for a simple and exact solution are quite gloomy due to the NP hard complexity of the problem, surprisingly the solution in the thermodynamic limit (infinitely large system, $N \to \infty$) is simple! Based on analogies with thermodynamic systems and the Potts glass problem in physics, it has been shown [3-5] that for an infinitely large system, statistically the optimal clustering is the following: whenever there are more positive propensities than negative ones put all agents in one big cluster, whenever there are more negative propensities than positive ones put each agent in a separate cluster. The term, “statistically”, means here that the above solution is true for the majority of the cases, neglecting a few special situations. Before getting too excited about this, let us remember that all practically interesting cases are for finite N values, where the problem remains NP hard [15]. In such cases the best we can do is to consider some numerical optimization techniques to cluster the system. Various methods are known, the ones which have been already considered for this problem are the simulated annealing, analytical or numerical renormalization approach or a Molecular Dynamics motivated optimization trick [3-5].

The CC problem leads to a phase-transition like behavior in the thermodynamic limit [3]. In order to understand this we will introduce some relevant quantities. Let us denote by *q* the density of the positive propensities in the system:

$$q = \frac{W_+}{W_t} \tag{3}$$

(W₊ denotes the number of +1 links and $W_t = N(N-1)/2$ is the total number of links in the system). Naturally, many different distributions of the propensities are possible for a fixed *q* density. We denote with *r* the relative size of the largest cluster in the optimal clustering, and we consider this parameter as order parameter for the CC problem. Mathematically, this order parameter is defined as

$$r(q) = \left\langle \left\langle \max_{(j)} \left\{ \frac{C_x\{j,q\}}{N} \right\} \right\rangle_{\deg} \right\rangle_x , \tag{3}$$

where $C_x\{k,q\}$ denotes the number of agents in cluster *j,* for an *x* realization of the propensities (distribution of the $J_{ij}$ interactions) with a given *q* density of the positive links. Since the ground-state might be degenerated (different clustering gives the same minimum *K* value), first an average over all these degenerated states are considered, then a second average over the disorder *x* is performed. For finite system sizes, *N,* one can compute the *r(q)* curves using different numerical or analytical approximation techniques. As an example on Figure 1 we present the results of a simulated annealing approach done in [3].

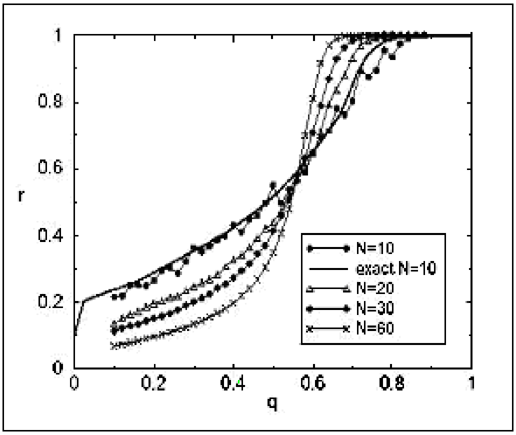

**Fig. 1.** Simulated annealing results for r(q) in the case of globally coupled system. Results from [3]. The “exact” results are obtained with a total enumeration of all the possible states.

The r(q) curves plotted in Figure 1 suggest a phase-transition like behavior near the $q_c = 0.5$ critical density. This result is in agreement with the predictions discussed in [3] for the thermodynamic limit. For $q < q_c = 0.5$, when there are more negative propensities than positive ones, the order parameter is $r = 0$, suggesting that the relative size of the largest cluster is 0. This corresponds to the case when all elements are in different clusters ($r = 1/N$, which for $N \to \infty$ yields r=0). For $q > q_c = 0.5$ there are more positive links than negative ones. The predicted order parameter is $r = 1$, suggesting that the relative size of the largest cluster is 1. This means that all agents are in the same cluster. The $r(q)$ curves for finite system sizes will have a sharp increase in the neighborhood of the $q_c = 0.5$ critical point. As it is expected for a real phase-transition like phenomena the curves for increasing system sizes are converging to a step-like form in the neighborhood of $q_c$.

Another clue suggesting that we deal with a phase-transition like phenomenon is from the fluctuation of the order parameter, quantified by the value of its standard deviation:

$$\Delta r(q) = \sqrt{\left\langle r^2(q) \right\rangle_{\deg,x} - \left\langle r(q) \right\rangle_{\deg,x}^2} . \tag{4}$$

The average $\langle \ \rangle_{\deg,x}$ is taken for all the performed numerical optimization experiments when an *x* realization of the $J_{ij}$ propensities is given and several *x* realizations (of the order of hundreds) of the links with fixed *q* value. In Figure 2 we present the simulated annealing results for $\Delta r(q)$ taken from [3], considering various system sizes, N. As it is expected for real phase-transitions, a clear maximum is obtained in the vicinity of $q_c = 0.5$, suggesting an increase of the fluctuations at the transition point. The maximum becomes sharper and its position converges towards the $q_c = 0.5$ critical point as the system size is increased.

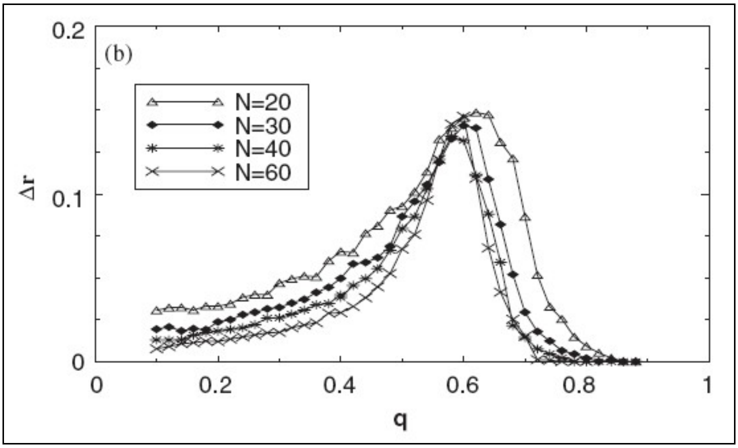

**Fig. 2.** Standard deviation, $\Delta r(q)$ of the order parameter for different system sizes. Simulated annealing results from [3].

Globally coupled networks (complete graphs) are however rarely relevant to natural and sociological systems [16-18]. Links between the agents in a real natural or sociological system has a quite complex topology, and leads to several non-trivial network structures [18]. A natural question arising then is to consider the CC problem on such random graphs and see how the results discussed up to now will modify. Without entering in details (for a detailed discussion see our recent work [5]) we mention here the basic result for the CC problem on such networks. We will limit the overview only on single component networks in which each node can be reached from each other node by following the existing links. Moreover, we consider the case of randomly diluted Erdos-Renyi type networks with a fixed finite dilution rate (dilution rate is defined here as the number of existing links in the network over the number of possible links). The main results are the following:

1. The *r(q)* curves exhibit a similar trend with the one obtained on complete graphs. There is the same critical proportion of the positive links, $q_c = 0.5$, where the *r(q)* curves have a sharp increase and an inflexion point.

2. The $\Delta r(q)$ curves exhibit a similar trend with the one obtained on complete graphs. At the critical $q_c$ value there is a clear maximum, which increases with the system size and its position is converging for $q_c = 0.5$ as in the case of the globally connected networks.

3. For an infinite size network with a fixed dilution rate ($N \to \infty$), we get the same step-like transition as in the case of globally connected graphs.

In the present study we consider finite graph structures. The results mentioned in items 1.-2. are of importance hereafter.

## CORRELATION CLUSTERING AND LOGICAL LEARNING

Any study subject can be represented with a complex graph-like structure. The syllabus can be divided into basic components (parts) which are logically inter-connected in a graph-like manner. Learning logically the subject of study means, that these links are revealed and transformed in positive connections. The positive connection suggests in such case that those parts are logically connected in the students mind. Contrary, a non-logical learning means that the student is assimilating the components without revealing the underlying connections. The link in such cases can be considered negative, since parts of the syllabus are conflicting, and the desired logical relation is not revealed. As an example, in Figure 3a we have considered an idealized study subject composed of 8 parts, interconnected in the depicted graph-like manner. Connections are considered without direction, implication from any node is a link. Depending on the learning style some of the connections are understood and parts of the syllabus becomes connected. If the student uncovers all connections between parts of the material (Figure 3b) the whole syllabus is merged and the learning style is logical. On the other hand if none of the existing connections are revealed the material falls in parts and learning is non-logical (Figure 3c). In general, a situation between these two extremes will occur: some links are revealed (positive in the CC problem) and some links are unexplored (negatives in the CC problem), this is illustrated in Figure 3d. The logical learning rate is a measurable psychological quantity [19], characterizing how logically one assimilates a given material. There are several tests available for quantifying this aspect of learning. Using the graph picture shown on Figure 3 one could interpret the Logical Learning Rate (LLR) as the largest relative size of the syllabus in which the parts are mostly non-conflicting. This is however nothing else but the relative size of the largest cluster in the correlation clustering problem. One can construct thus a useful analogy between the CC problem and logical learning of a material. In the view of this analogy the order parameter, *r*, defined in CC will characterize the LLR of the give subject of study. For continuing the analogy with the CC problem one has to quantify in psychological terms the ratio of positive links, which is the *q* parameter in CC. Our basic hypothesis is that the well quantifiable IQ of students is a good candidate for this. As the intelligence level is higher, existing logical connections between parts of the syllabus are easier to reveal. This means that the ratio of positive links in the graph should depend on IQ and the simplest assumption is: $q \sim IQ$. Since theoretically there is no upper limit for IQ, the proportionality constant is unknown.

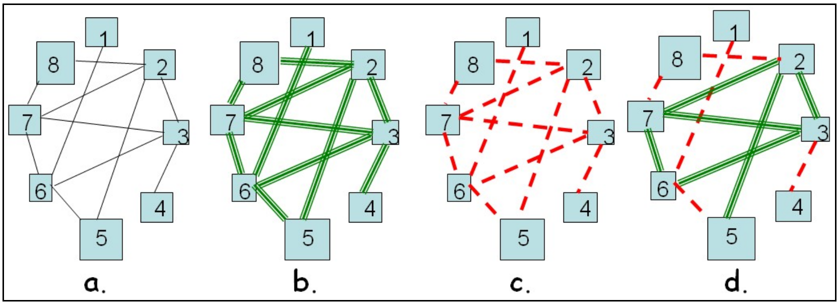

**Fig. 3.** (a) Graph-like representation for the logically connected parts of a subject of study. (b) When all links are positive (revealed) learning is completely logical and the syllabus is understood as a whole. (c) When all links are negative learning is non-logical and the study material falls in parts. (d) A general situation.

Assuming that the analogy discussed above is justified, one would expect that LLR as a function of IQ should have a similar trend as the *r(q)* curves in the CC problem. This means that the value of LLR should increase sharply at a critical IQ level. Based on conjectures from psychology, this point is expected around an IQ of 120-130, which corresponds to the level of superior intelligence ("gifted" persons) [20]. The variance of LLR as a function of IQ should also exhibit a maximum at this critical IQ value. In the following psychological test measurement results for LLR and IQ for the same control set will be presented and discussed.

## MEASUREMENTS AND RESULTS

With the help of a psychologist team we have considered test measurements on a sample of N=177 high-school students. IQ was measured by means of the classical standardized Raven test [21]. The Raven Progressive Matrices (RPM) tests are made up of a series of diagrams or designs with a missing component. Individuals taking the tests are expected to select the correct element to complete the designs from a number of options printed beneath. The instrument has been adapted for Romanian population and has very good psychometric properties. The value of LLR was quantified with the help of the MEMLETICS [22]. The MEMLETICS test is a questionnaire which, based on an evaluation, gives a reasonable estimate of the learning styles relevant for an individual. These learning styles are categorized as: Social, Solitary, Visual, Aural, Verbal, Physical and Logical. We were primarily interested in the results concerning the rate of logical learning (for details see [14]). Results of both tests were summarized and the desired $LLR(IQ)$ and $\Delta LLR(IQ)$ curves were plotted.

First the considered sampling, its correctness and significance level were tested. For this the distribution of the measured IQ values in form of a normalized histogram with bin sizes $d(IQ)=10$ was considered. From the experimental results it was possible to determine the mean IQ value and standard deviation: $\langle IQ \rangle = 112.92; \Delta(IQ) = 14.94$ . The normalized histogram was then plotted together with the normal distribution expected with these parameters (Fig. 4):

$$G(y) = W \cdot d \frac{1}{\sqrt{2\pi \cdot \Delta(IQ)}} \exp\left( - \frac{y^2}{2 \cdot \Delta(IQ)} \right) \tag{6}$$

The reasonable agreement of the experimental results with the normal distribution suggests that our sampling is an acceptable one.

The measured LLR values as a function of the IQ values are shown in Figure 5.

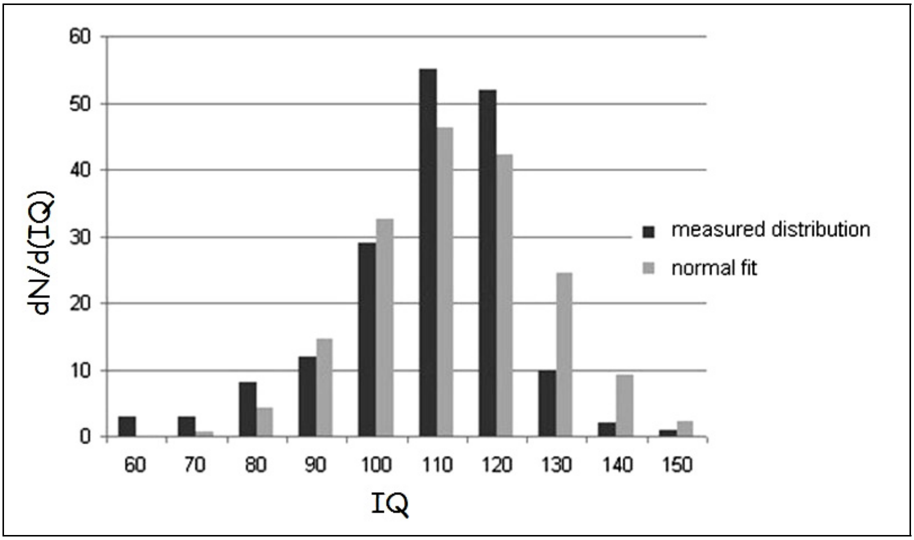

**Fig. 4.** Distribution in form of a histogram of the measured IQ values. The grey bars indicate the fitted normal distribution.

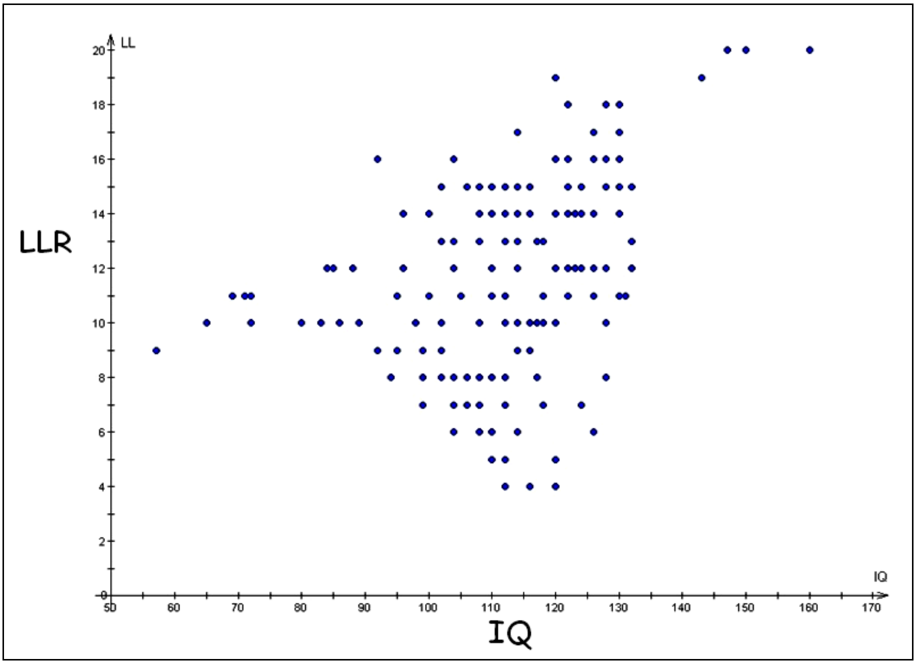

**Fig. 5.** Plot of experimentally obtained LLR values as a function of IQ.

A simple qualitative view on the set of points suggests that the standard deviation of the LLR values has a maximum somewhere in the $100 \leq IQ \leq 130$ interval. The dispersion of the experimental points is too high however to get any hint from here on the nature of the $LLR(IQ)$ and $\Delta LLR(IQ)$ curves. An averaging was performed, which resulted in a much smoother and easier interpretable curve. The averaging was done by considering IQ intervals (bins) of size 10 for $IQ < 100$ and $IQ > 130$ and bins of size 5 for $100 \leq IQ \leq 130$. The non-uniform binning is motivated by the fact that the results are less abundant for $IQ < 100$ and $IQ > 130$ then for $100 \leq IQ \leq 130$ and so in order to obtain a reasonable average several experimental points are needed. The averaged results are plotted in Figure 6. The trend illustrated by the continuous line resembles well the conjectured shape. In the vicinity of $IQ = 120$ a sharp increase in the LLR level is detectable.

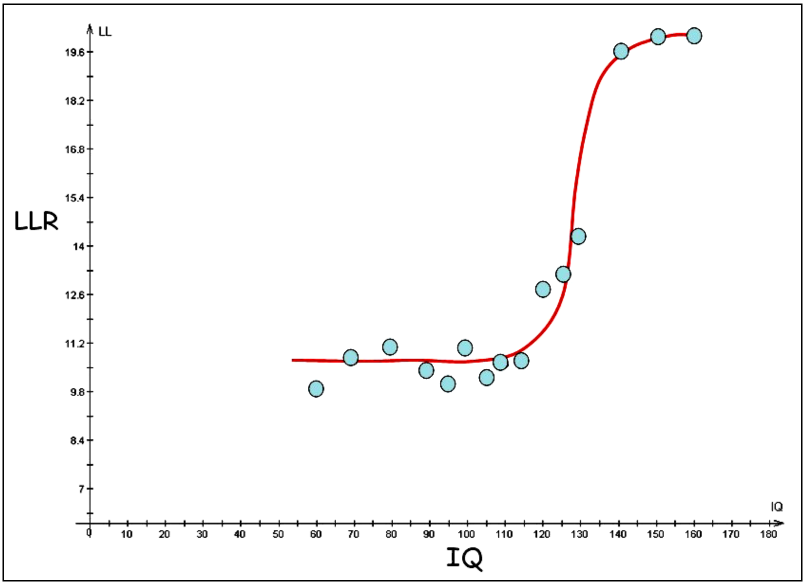

**Fig. 6.** Bin-averaged results for LLR as a function of IQ. The continuous line illustrates the trend.

For plotting the experimental $\Delta LLR(IQ)$ curve, the standard deviation of the LLR values for individuals with IQ values in the considered bin were calculated and plotted as a function of the average IQ in the bin. Results are given in Figure 7. Similarly with Figure 6, the trend is illustrated by a continuous line. The clear maximum in the vicinity of $IQ = 120$ supports again our conjecture and the applicability of the CC problem for logical learning.

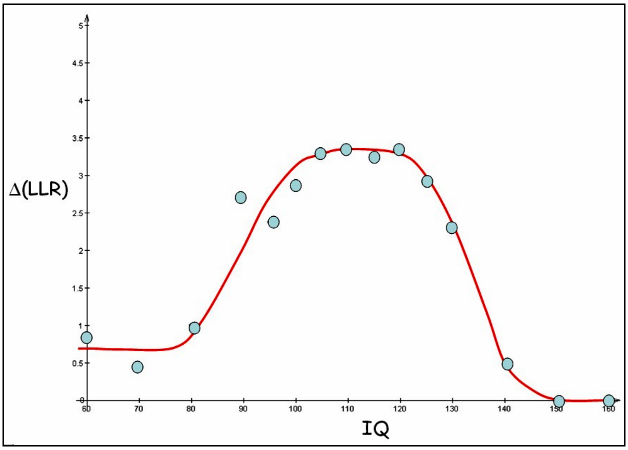

**Fig. 7.** Averaged experimental results for the standard variation of LLR as a function of IQ. The continuous line illustrates the trend.

## CONCLUSIONS

A simple analogy between the Correlation Clustering (CC) problem and logical learning of a subject of study was formulated. The main conclusion which resulted from this analogy is that the Logical Learning Rate (LLR) as a function of the Intelligence Quotient (IQ) should present a sharp increase at a critical IQ level. One would also expect that the standard deviation of LLR as a function of IQ presents a clear maximum at the critical IQ value. Experiments were designed to prove this conjecture. IQ was measured by a standardized Raven test and LLR was quantified with the help of the Memletics test. The obtained results revealed that the conjectured analogy holds for a random sample of individuals and LLR as a function of IQ varies as predicted by CC. From a psychological point of view we replicated previous results concerning connections between logical learning and IQ, by using new measures and models. Additionally, the modeling process, revealed a novel critical transition point, corresponding to the IQ shift from high intelligence to superior intelligence (120-130), with an impact on logical learning performance. This is a new discovery revealed by modeling psychological data in a statistical physics paradigm, with impact on applied psychology (e.g., different teaching styles for people of different IQ categories).

## ACKNOWLEDGMENTS

Research supported by a Romanian PN2II Idei 2369/2008 research grant. Financial support for Gy. Cseh was provided by the Sectoral Operational Programme Human Resources Development, Contract POSDRU 6/1.5/S/3 Doctoral Studies: "Through science towards society".

# REFERENCES

1. Applications of Statistical Physics, Editors: A. Gadomski, J, Kertész, H.E. Stanley and N. Vandewalle, Proceedings of the NATO Advanced Research Workshop, Technical Universitz of Budapest, 19-22 May, 1999 (North Holland, 2000).
2. N. Bansal, A. Blum and S. Chawla, Machine Learning, vol. 56, pp. 89-113 (2004).
3. Z. Neda, R. Florian, M. Ravasz, A. Libal, and G. Gyorgyi, Physica A, **vol.** 362, **pp.** 357-369 (2006).
4. R. Sumi, and Z. Neda, International Journal of Modern Physics C, **Vol.** 19, **pp.** 1349-1358 (2008).
5. Z. Neda, R. Sumi, M. Ercsey-Ravasz, M. Varga and B. Molnar. Journal of Physics A: Mathematical and Theoretical, vol. 42, pp. 345003-345017 (2009)
6. M.J. Kearns, R.E. Schapire, L.M. Sellie, Machine Learning, vol. 17, pp. 115-141 (1994).
7. R. Axelrod, and S. Bennett, British Journal of Political Science, 23, **pp.** 211-233 (1993).
8. S. Galam, Physica A, **vol.** 230, **pp.** 174-188 (1996).
9. S. Galam, Physica A, vol. 238, **pp.** 66-88 (1997).
10. D. Elderfield, and D. Sherrington, J. Physics C: Solid State Physics, **vol.** 16, **pp.** L497-L503 (1983).
11. A. Erzan, and E.J.S. Lage, J. Physics C: Solid State Physics, **vol.** 16, pp. L555-L560 (1983).
12. T.R. Kirkpatrick and D. Thirumalai, Physical Review B, vol. 37, **pp.** 5342-5350 (1988).
13. P. McGeorge, J.R. Crawford, and S.W. Kelly, Journal of Experimental Psychology: Learning, Memory, and Cognition, vol. 23, pp. 239-245 (1997).
14. A.S. Reber, F.F. Walkenfeld and R. Hernstadt, Journal of Experimental Psychology: Learning, Memory, and Cognition, vol. 17, pp. 888-896 (1991).
15. M.R. Garey, and D.S. Johnson, Computers and Intractability. A Guide to the Theory of NP-Completeness (New York: W. H. Freeman and Company, 1979).
16. R. Albert and A.L. Barabasi, Rev. Mod. Phys. **Vol.** 74, **pp.** 47-97 (2002).
17. A.L. Barabasi and E. Bonabeau, E., Scientific American, **vol.** 288, 60-69 (2003).
18. A.L. Barabasi et. al, Physica A, **vol.** 311, **pp.** 590-614 (2002).
19. J. Anderson, Cognitive psychology and its implications (6th ed.) (New York: Worth Publisher, 2004).
20. D. Wechsler, The Measurement of Adult Intelligence. Baltimore (The Williams & Wilkins Company, 1944)
21. J. Raven, Cognitive Psychology, vol. 41, pp. 1-48 (2000).
22. MEMLETICS test: http://www.memletics.com/

STUDIA UBB PHYSICA, LVI, 2, 2011

# ENHANCED EXTRINSIC MAGNETORESISTANCE IN $La_{0.8}Pb_{0.2}MnO_3/Pb(Zr_{0.52}Ti_{0.48})O_3$ CERAMIC COMPOSITES

**O. FLOREA**[1], **I. BALASZ**[1], **I. G. DEAC**[1,*]

**ABSTRACT.** We report the electrical and magnetic properties of the ferromagnet/ferroelectric-type composite $0.8La_{0.8}Pb_{0.2}MnO_3 – 0.2Pb(Zr_{0.52}Ti_{0.48})O_3$. The x-ray analysis indicated that the two component phases exist independently in the composite, without any sign of a new phase. Compared with pure $La_{0.8}Pb_{0.2}MnO_3$ (LPMO), the magnetic measurements did not show significant changes in the Curie temperature ($T_C$ = 320 K), in the coercivity ($H_c$ = 0.05 T, at 5 K) and in the magnetic moment ($m$ = 3.56 $\mu_B$/Mn), suggesting the absence of interdiffusion between the LPMO and $Pb(Zr_{0.52}Ti_{0.48})O_3$ (PZT) phases. Both the pure LPMO and the composite sample show magnetoresistance effect. The LPMO sample has a metal – insulator transition at a temperature close to $T_p$ ~ 250 K were $\rho(T)$ curve has a maximum. In composite, this maximum is replaced by a change of slope in the temperature dependence of resistivity at about 80 K, and $\rho(T)$ curve indicates a semiconductor-like behavior. The highest magnetoresitance (*MR*) value in 7 T was found to increase from 48% for LPMO (at 8 K) to 76% for the composite (at 50 K). The magnetotransport properties of the composite were analyzed in a strain-mediated magnetoelectric coupling scenario, between the LPMO and PZT phases.

***Keywords:*** *Ferromagnetic–ferroelectric composite; Colossal magnetoresistance; Magnetoelectric coupling*

## INTRODUCTION

Among the multiferroic materials, ceramic composites have stimulated much scientific and technological interest because the multiferroic properties are expected to be easily obtained by combining the individual ferroic phases [1-6]. The search for large grain-boundary extrinsic magnetoresistance (*MR*) in polycrystalline magnetic oxides with high spin polarization has been of great interest in recent years because of possible sensor applications. For perovskite manganites $La_{1-x}A_xMnO_3$ (A = Ca, Sr, Pb), single-crystal and epitaxial films, magnetoresistance *MR* is maximum near $T_C$ and almost zero at low temperatures [7, 8]. In polycrystalline compounds, *MR* has a maximum value at low

---

[1] *Universitatea Babeş-Bolyai, Facultatea de Fizică, Str. Kogălniceanu, Nr. 1, RO-400084 Cluj-Napoca, Romania,* [*] *iosif.deac@phys.ubbcluj.ro*

temperatures. In this case, *MR* effect is characterized by an initial, rapid drop of resistance with applied magnetic field, followed by a slow decrease at higher fields [7-11]. The crucial points in this problem are the spin polarized scattering at grain boundaries together with the magnetic state of their surface. At low temperatures the negative *MR* of the polycrystalline manganite samples is dominated by spin-polarized tunneling/scattering between grains, and is associated with magnetic domain rotation at the grain boundaries at very low magnetic field. At higher magnetic fields, the spins are aligned, the magnetization approaches saturation, and external magnetic field has weak effect on the transport properties: the magnetoresistance increase rate substantially reduces (usually, linearly) [7-9].

Several groups have tried to merge the high degree of spin polarization present in manganites with the advantages of a heterogeneous granular structure [12, 13]. By diluting ferromagnetic (FM) metallic grains in an insulating matrix, one may expect an enhancement of magnetoresistance due to the “disorder-driven amplification of spin-dependent transport at the structural boundaries of the mixture” [13]. The main conclusion of these studies was that the low field magnetoresistance (LFMR) of manganites can be enhanced by composites with a proper insulator phase, near the percolation threshold [12, 13]. The high field magnetoresistance (HFMR) arise as a consequence of the noncollinear spins in surface layer of manganites grains [7, 8], and it remains nearly unchanged in composites. Studies done on bulk polycrystalline and thin film manganites LCMO, LPMO, $La_{0.775}Sr_{0.225}MnO_3$ (LSMO) revealed linear or small to medium deviation from linear magnetoconductance in high magnetic fields [10, 11]. A very interesting situation occurs when the composites consist of a mixture between a ferromagnetic manganite and a ferroelectric/ piezoelectric insulator. It was expected that the ferroelectric/piezoelectric material to produce an additional strain at the grain boundary of the manganite matrix, and to influence magnetic and other physical properties too. This problem was analyzed in bulk composite LCMO/BTO [20, 21], LSMO/BTO [22], LCMO/$SrTiO_3$ [13] and in $La_{0.775}Sr_{0.225}MnO_3$ (LSMO) thin films on $Ba_{0.996}Y_{0.004}TiO_3$ and $BaTi_{0.85}Sn_{0.15}O_3$ substrates [11]. The main conclusion of these studies was that the magnetoresistance (especially LFMR) of these material systems can be enhanced (compared to the mother compounds) by using this method.

We have found that the ceramic composite obtained from $0.2Pb(Zr_{0.52}Ti_{0.48})O_3$ and 0.8 $La_{0.8}Pb_{0.2}MnO_3$ shows high magnetoresistance effects. While in the low field region (below 1 T) there is no significant difference between the behavior of the *MR*’s of the LPMO sample and the composite, HFMR of the composite is greatly enhanced, at 50 K and 7 T reaching 76 % compared to 42% for LPMO. We attributed these properties to the boundary layer strain and to the associated magnetoelectric coupling between LPMO and PZT.

## EXPERIMENTAL

The composite $0.8La_{0.8}Pb_{0.2}MnO_3 – 0.2Pb(Zr_{0.52}Ti_{0.48})O_3$ was prepared by mixing LPMO and PZT powders. LPMO was separately prepared by a conventional solid state reaction method [23]. PZT was prepared by high-energy ball milling (for 12 hours) from $PbTiO_3$ and $PbZrO_3$ powders. The obtained powder was checked by x-ray diffraction, and it was found that the compound is mainly clean PZT single phase, within the limit of experimental errors. Stoichiometric quantities of PZT and LPMO powders were mixed, pressed and sintered 12 h in air at 1100 $^0$C, to prepare the samples. The X-ray powder diffraction (XRPD) patterns were recorded at room temperature using a Brucker Advance D8 AXS diffractometer.

A cryogen free VSM magnetometer (Cryogenic Ltd.) was used for magnetization measurements in the temperature range 5 - 300 K and up to 12 T. The resistivities measurements were performed (using Keithley equipment) in another cryogen free magnet cryostat CFM-7 T (Cryogenic Ltd.) by the four-probe technique, in the temperature range from 5 to 300 K and in magnetic fields up to 7 T. To avoid the Joule heating, the magnitude of the applied current in the composite was set to10 $\mu$A.

## RESULTS AND DISCUSSION

The x-ray analysis indicated that PZT and LPMO phases exist independently in the samples, without any sign from another phase. Fig. 1 shows the XRD patterns of the PZT, LPMO and of the composite. The XRD patterns of the composites show two different sets of diffraction peaks, corresponding to trigonal LPMO and tetragonal PZT phases ($a$ =4.049 Å, $c$ = 4.074 Å), respectively, which clearly indicates the coexistence of the two phases. X-ray diffraction pattern analysis show that the reflection peaks of LPMO do not shift. The pure LPMO sample crystallizes in trigonal symmetry with lattice parameters: $a$ = 5.526 Å; $b$ = 5.526 Å; $c$ = 13.400 Å. The lattice parameters of LPMO in the LPMO/PZT composite do not change within the accuracy of diffractometer. This shows that LPMO maintains its identity, without any interdiffusion of ions from PZT into LPMO phase during the heat treatment.

The magnetic measurements also suggest the absence of interdiffusion between the two phases. The magnetic field dependence of magnetization at 5 K for our samples is described in Fig. 2, and it can be seen that in high field region the magnetizations are almost saturated. The general behavior of magnetization versus temperature indicates a long-range ferromagnetism. The Curie temperatures $T_C$'s, estimated as the inflection points in $M(T)$ curves, remain practically unchanged around 320 K, as shown in Fig.2.

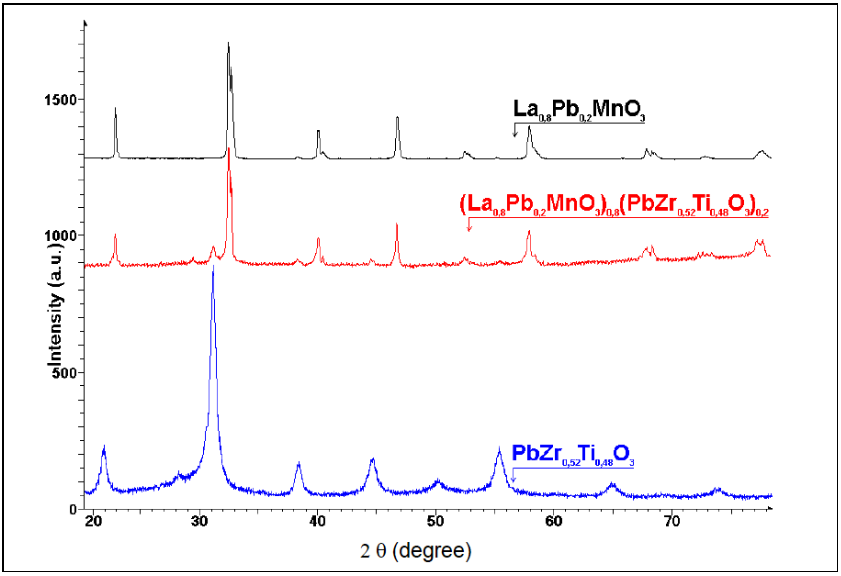

**Fig. 1.** X-ray diffraction diagrams of the LPMO sample (the upper curve), composite (middle) and that of $Pb(Zr_{0.52}Ti_{0.48})O_3$ (the lower curve).

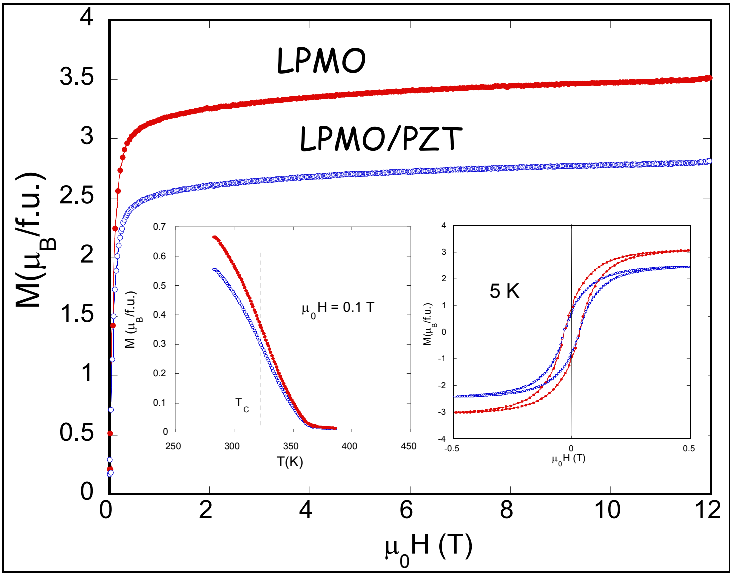

**Fig. 2.** The magnetic field dependence of magnetization at 5 K for LPMO sample (solid symbol) and of the composite (open symbol). The insets show the high temperature dependence of magnetization in 0.1 T and the magnetic hysteresis loops, taken at 5 K

As can be seen, the decrease of the high-field magnetization is due only to the PZT percentage present in the sample. The magnetic contribution is reduced by the same amount as the PZT percentage, and the magnetic moment per Mn ion reaches 3.56 $\mu_B$/Mn. The hysteresis loops taken at 5 K, shown in the other inset of Fig.2, indicate no change in the coercivity ($H_c$ = 0.05 T), suggesting a weak influence of the surface magnetic disorder on the domains rotation. This is an additional indication that no reaction between the two compounds occurred.

The physical properties of the pure LPMO sample are well-known [24]. It has ferromagnetic behavior below $T_C$ = 320 K and it is metallic at low temperatures. The temperature dependencies of the resistivity for this sample, in 0, 1, 2 and 4 T magnetic fields, are shown in Fig. 3. The peak corresponding to the metal-insulator transition, usually close to $T_C$, is shifted at $T_{MI}$ ~ 250 K due to the grain boundary (GB) effects [19]. $T_{MI}$ is an extrinsic property, which strongly depends on the synthesis conditions and microstructure, while $T_C$ is an intrinsic characteristic, i.e. it does not show significant change as a function of the granularity. The sample shows negative magnetoresistance $MR = [(\rho(H)-\rho(0))/\rho(0)]$, and the variation of *MR* with the magnetic field at different temperatures is depicted in Fig. 4. The maximum magnetoresitivity *MR* ~ 48 % occurs at 8 K and 7 T, much lower than $T_C$ suggesting that a substantial part of the magnetoresistance effect at low temperatures is not intrinsic but it arises from the GB effects [19].

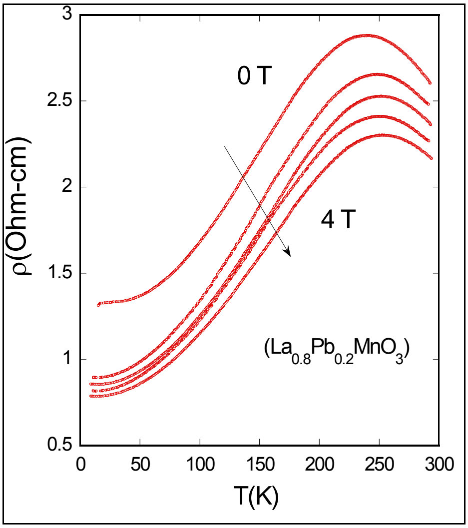

**Fig. 3.** The temperature dependence of resistivity for the LPMO sample taken in the range from 0 to 4 T.

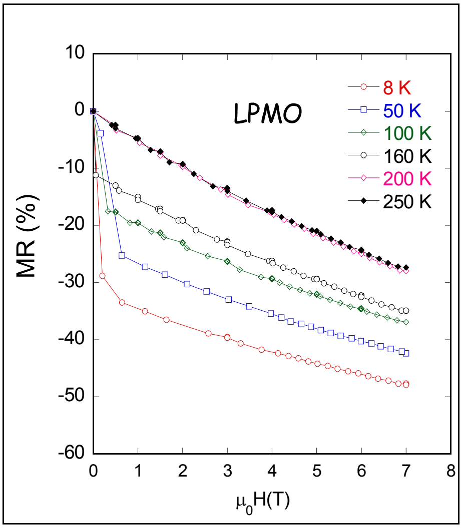

**Fig. 4.** The field dependence of magnetoresistance *MR* at 8, 50, 100, 160, 200 and 250 K for the LPMO sample.

Dilution with insulating PZT powder changes the shape of the ρ(*T*) curve to a semiconductor-like behaviour (dρ/d*T* < 0) as shown in Fig.5, indicating that the metal-insulator transition is suppressed in the composite. The conductivity was reduced by 3 orders of magnitude, but the high field magnetoresistance ratio was enhanced, and reached 76% at 50 K and 7 T (Fig. 6), while it was 42 % in the LPMO sample. At 100 K, MR became 73% in composite while in the LPMO it was 37 %. The maximum in ρ(*T*) curve for the LPMO sample is replaced by a change of slope in the temperature dependence of resistivity below about 100 K, in the case of the composite. As it can be seen from Fig. 6, the low field ($\mu_0$H < 1 T) magnetoresistance (LFMR) does not change significantly for the composite. For a 1 T magnetic field MR reaches ~ 35 % at 8 K in LPMO and ~36 % in the composite.

In the case of sintered granular manganite/insulator composites, previous reports indicated a high increase in the LFMR, as compare with pure manganite [13, 20-22].

The large drop of *MR* in the low-field region is associated with a rotation of magnetic domains (coercivity is about 0.05 T) which are defined by grains boundaries. Since the LPMO grains have the same average sizes in the two samples (since they are formed from the same LPMO powder), no great changes are expected in the magnetoresistance of the composite. The domains are successively oriented in the increasing field, until all of them are switched parallel to the magnetic field, thereby reducing scattering of polarized electrons, and this process is not affected by the presence of non magnetic PZT at grain boundaries. The barrier and the connectivity between the LPMO grains is greatly change in the composite. The electrical resistance of these boundaries increase dramatically (more than 3 orders of magnitude) at lower temperatures due to the insulating behavior of PZT (dρ/d*T* < 0) in a percolative system [19].

In the case of polycrystalline materials grain boundaries provide defect sites that can become strong pinning centers for the disordered spins. At the grain surface, Mn spins can be blocked, for example because their environment is unbalanced or because of magnetic anisotropy. At low temperatures and in increasing high magnetic fields the magnetoresistivity continues to increase slowly due to polarization of electrons in magnetically disordered regions near grain boundaries [7-11]. The alignment of electron spins in higher magnetic field leads to a reduction of the resistivity, as it can be seen in Fig. 4. Magnetic measurements are not sensitive to these disordered Mn spins because their fraction is very small, as we have found in our magnetic measurements (Fig.2).

For LPMO/PZT composite a pronounced increase of HFMR arises for *T* < 160 K, while LFMR do not change significantly as compare with LPMO.

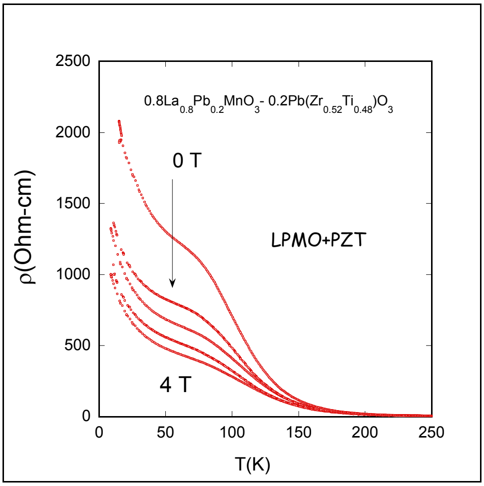

**Fig. 5.** The temperature dependence of resistivity for the LPMO/PZT composite taken in the range from 0 to 4 T.

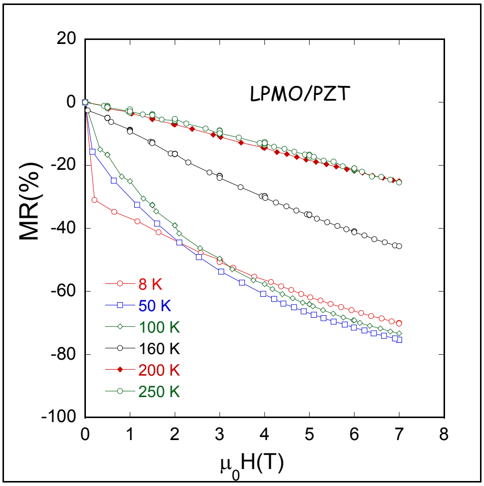

**Fig. 6.** The field dependence of magnetoresistance *MR* at 8, 50, 100, 160, 200 and 250 K for the LPMO/PZT composite.

We expect a strain-mediated magnetoelectric coupling to occur, since the system consists of two single-phase compounds, LPMO and PZT with large magnetic and respectively, ferroelectric/piezoelectric responses [25]. We are faced here with a percolative/filamentary electrical conduction. Because of the vast resistivity contrast between LPMO and PZT phases, current transports through filaments, which are basically, connected LPMO domains [26] in contact with PTZ grains. The PZT interfacial polarization can generate stress on the LPMO grains. The manganites are known to be very sensitive to strains. As known, the hydrostatic pressure leads to the enhancement of ferromagnetic order in manganites [27, 28]. A natural, naïve, explanation of the increase of the high field magnetoresistance resides in the fact that this enhanced ferromagnetism amplifies the effect of the magnetic field in rotating the disordered grain surface spins. At lower temperatures, 8 K in our case, the spins are frozen in their strained condition, the conduction mechanism changes [29], and the increase rate of MR is reduced. This explains why *MR* is higher at 50 K and 100 K than at 8 K, as illustrated in Fig. 6.

## CONCLUSIONS

We have investigated the transport properties of the $0.8La_{0.8}Pb_{0.2}MnO_3 – 0.2Pb(Zr_{0.52}Ti_{0.48})O_3$composite in the temperature range from 5 to 300 K and in magnetic field up to 7 T. The x-ray and magnetic measurements do not show evidence of interdiffusion between the LPMO and PZT phases. Compared to pure $La_{0.8}Pb_{0.2}MnO_3$, the magnetic measurements did not reveal significant changes in the Curie temperature, in the coercivity, and in the magnetic moment/Mn, in the composite. Both LPMO and the composite show high negative magnetoresistance. In the range of low magnetic fields ($\mu_0H < 1$ T) there are no significant differences between the behavior of their magnetoresistances that reach about 35 % at 8 K and 1T. For higher magnetic fields and below 160 K the magnetoresistance in the composite increases consistently to 76% at 50 K and 7 T, while the maximum value of MR in LPMO is 48% at 8 K and 7 T. This behavior can be explained in the frame of a scenario based on a strain-mediated magnetoelectric coupling between the ferromagnetic LPMO and ferroelectric/piezoelectric PZT. This work provides a promising method for enhancing the magnetoresistance effect in manganites by composites with a proper ferroelectric/piezoelectric insulator phase.

### ACKNOWLEDGMENTS

This work was supported by the Romanian CNCS-UEFISCDI Project PNII IDEI 2590 (Contract No.481/2009).

## REFERENCES

1. H. Schmid, Ferroelectrics 162 (1994) 317-338.
2. N.A. Hill, J. Phys. Chem. B 104 (2000) 6694-6709.
3. M. Fiebig, J. Phys. D: Appl. Phys. **38** (2005) R123–R152.
4. W. Eerenstein, N. D. Mathur, J. F. Scott, Nature 442 (2006) 759-765.
5. K.F. Wang, J.-M. Liuab, Z.F. Renc, Adv. Phys. 58, (2009) 321–448.
6. C.A. F. Vaz, J. Hoffman, C.H. Ahn, R. Ramesh, Adv. Mater 22 (2010) 2900–2918.
7. H.Y. Hwang, S-W. Cheong, N.P. Ong, and B. Batlogg, Phys. Rev. Lett. 77 (1996) 2041-2044.
8. M. Ziese, Phys. Rev. B 60 (1999) R738-R741.
9. P.K. Siwach, H.K. Singh, O.N. Srivastava, J. Phys. Condens. Matter 20 (2008) 273201.

10. R.B. Gangineni, K. Dörr, N. Kozlova, K. Nenkov, K.-H. Müller, L. Schultz, J. Appl. Phys.99 (2006) 053904.
11. N. Kozlova, K. Dörr, D. Eckert, T. Walter, K.-H. Müller, J. Magn. Magn. Mater.261 (2003) 48–55.
12. Ll. Balcells, A.E. Carrillo, B. Martınez, J. Fontcuberta, Appl. Phys.Lett. 74, (1999) 4014-4016.
13. D.K. Petrov, L. Krusin-Elbaum, J.Z. Sun, C. Feild, P.R. Duncombe, Appl. Phys. Lett. 75, (1999) 995-997.
14. A. de Andrés, M. Garcia-Hernandez, J.L. Martinez, C. Prieto, Appl. Phys. Lett. 74 (1999) 3884-3886.
15. S.L. Cheng, J.G. Lina J. Appl. Phys. 98 (2005) 114318.
16. K. Dörr, K.-H. Müller, N. Kozlova, P. Reutler, R. Klingeler, B. Büchner, J. Magn. Magn. Mater. 290–291 (2005) 416–419.
17. A. Singh, D.K. Aswal, P. Chowdhury, N. Padma, C.S. Viswanadham, Santosh Kumar, S.K. Gupta, J.V. Yakhmi, J. Magn. Magn. Mater. 313 (2007) 115–121.
18. S.A. Solopan, O.I. V'yunov, A.G. Belous, A.I. Tovstolytkin, L.L. Kovalenko, J. Europ. Ceram. Soc. 30 (2010) 259–263.
19. M. Ziese, Rep. Prog. Phys. 65 (2002) 143–249.
20. E. Bose, S. Taran, S. Karmakar, B.K. Chaudhuri, S. Pal, C.P. Sun, H.D. Yang, J. Magn. Magn. Mater. 314 (2007) 30–36.
21. G.M. Ren, S.L. Yuan, G.Q. Yu, J.H. Miao, X. Xiao, H. G. Guan, Y.Q. Wang, S. Y. Yin, J. Phys. D: Appl. Phys. 39 (2006) 4867–4871.
22. Y.P. Lee, S.Y. Park, Y.H. Hyun, J.B. Kim, V.G. Prokhorov,V.A. Komashko, V.L. Svetchnikov, Phys. Rev. B 73 (2006) 224413.
23. E. Burzo, I. Balasz, I. G. Deac, M. Neumann, R. Tetean, Physica B, 400 (2008) 1601-1602.
24. L. Ghivelder, R.S. Freitas, R.E. Rapp, F.A.B. Chaves, M. Gospodinov M.A. Gusmão, J. Magn. Magn. Mater. 226-230 (2001) 845-846; S. G. Min, K. S. Kim, S. C Yu,H. S. Suh, S.W. Lee, IEEE Trans. Magn. 41 (2005) 2760 – 2762.
25. K. Dörr, J. Phys. D: Appl. Phys. 39 (2006) 125-150.
26. D.S. Jeong, B.J. Choi, C.S. Hwang, J. Appl. Phys. 100 (2006) 113724.
27. H.Y. Hwang, T.T.M. Palstra, S-W. Cheong, B. Batlogg, Phys. Rev. B52 (1995) 15046−15049.
28. J.J. Neumeier, M.F. Hundley, J.D. Thompson, R.H. Heffner, Phys. Rev. B 52 (1995) R7006-R7009.
29. S. Lee, H.Y. Hwang, Boris I. Shraiman, W.D. Ratcliff II, S-W. Cheong, Phys. Rev. Lett.82 (1999) 4508-4511.

STUDIA UBB PHYSICA, LVI, 2, 2011

# EFFECT OF THE TEMPERATURE AND THE HEATING TIME ON THE COMPOSITION OF AN ILLITE-RICH CLAY: AN XRPD STUDY

C. IONESCU[1], V. HOECK[1,2], V. SIMON[3]

**ABSTRACT.** The study focuses on the effect of heating on the composition of an illite-rich clay used to produce black ceramic, by applying several distinct time intervals and temperature ranges. Density measurements and X-ray powder diffraction (XRPD) analysis were carried out on raw and thermally-treated clay samples. The density of the fired samples shows a decrease for lower heating temperatures but increases significantly with heating time at 1100°C. Changes of the intensity of the XRPD lines of illite + muscovite, calcite, feldspar and chlorite occur at different temperatures, depending of the length of the heating time. XRPD proves the presence of newly-formed feldspar, hematite, magnetite, possibly maghemite, as well as some amorphous/vitreous phases.

***Key words:*** Clays; high temperature; density; XRPD.

## INTRODUCTION

In the last decades the clays attracted interest due to their involvement in preservation of cultural heritage, e.g. ancient ceramics [1]. Besides, a special attention is given to the clays because of their wide abundance, implicitly low cost, and in particular because to the high adsorption and ion exchange properties [2].

Clays are naturally-occurring materials consisting mostly of very fine-grained (less than 4 micrometres in size) clay minerals. Besides clay minerals, the clays contain various amounts of quartz, feldspars, micas (muscovite), as well as Fe oxides and hydroxides, sometimes calcite and organic material. The Fe-rich phases usually consist of goethite, lepidocrocite or/and hematite. The clay minerals have a composite layered structure consisting of "components with tetrahedrally and octahedrally coordinated cations" [3]. The clay minerals are hydrous silicates which upon heating loose not only the adsorbed water but also the structural $OH^-$. The clay minerals are classified [3] in: kaolinites (kaolinite, dickite, nacrite, halloysite), illites (illite, hydrous micas, phengite, glauconite, celadonite), smectites (montmorillonite, beidellite, saponite), vermiculites and

---

[1] *Department of Geology, Babeş-Bolyai University, 1 Kogalniceanu Str., RO-400084 Cluj-Napoca, Romania; Email: corina.ionescu@ubbcluj.ro*

[2] *Department of Geography and Geology, Paris Lodron University, 34 Hellbrunner Str., A-5020 Salzburg, Austria; Email: volker.hoeck@sbg.ac.at*

[3] *Faculty of Physics & Institute for Interdisciplinary Research on Bio-Nano-Sciences, Babeş-Bolyai University, 1 Kogalniceanu Str., RO-400084 Cluj-Napoca, Romania; Email: viorica.simon@phys.ubbcluj.ro*

palygorskite (palygorskite and sepiolite). Their capacity to adsorb both inorganic and organic molecules is largely applied to diminish the effects of the pollution [4-7].

Due to their clay minerals content, the clays have plastic properties and therefore are used for obtaining common ceramic materials by heating in general between 600 and 1100°C. The high temperature treatment of clays leads to the destruction of the crystalline structure of the clay minerals but affects also the other compounds of the clays, e.g. calcite, micas, feldspars and less quartz. Goethite and lepidocrocite may change into hematite, magnetite or maghemite.

The present study continues our previous investigation on clays [8]. We report here the results regarding the effect of time of heating on the mineral components of an illite-rich clay used as raw material for the black ceramics produced nowadays in Northern Moldavia (Marginea village).

## EXPERIMENTAL PROCEDURES

The clay samples were obtained from greenish-grayish clays of Miocene age [9] occurring in a quarry operating nearby the Cristuru Secuiesc village, in the eastern part of the Transylvanian Basin (Romania). The samples were air-dried, modeled as small disks [8] and heated in a Naberthem furnace, at 1 atm pressure. The rate of heating from room temperature up to the desired temperature was 10°C/minute. The samples were maintained at the soaking temperatures of 700, 800, 900, 1000, 1100 and 1200°C, for 2, 4 and 8 hours respectively. After the heating, the samples were left to cool down to room temperature. The density of the samples was determined by Archimedes principle using a pan balance. For the structural and compositional investigation, few grams of raw clay and heated disks were powdered in an agate mortar and analyzed with a Shimatzu 6000 X-ray diffractometer, using $Cu_{K\alpha}$ radiation ($\lambda$=1.5418 Å) and Ni filter and operating at 40 kV and 30 mA. The samples were measured from 5 to 80°2θ, with a scan speed of 2°/min.

## RESULTS AND DISCUSSION

The original light grey, slightly greenish colour of the not heated (raw) clay changes already to light brown by 2h heating at 700°C. The colour becomes brighter as the temperature increases and finally turns into black at 1200°C. The increase of the heating time from 2 to 8 hours, for each soaking temperature, results in only a very slight colour change.

The changes of the density after the thermal treatment are displayed in Fig. 1. For the heating at 700°C, a slight decrease of the density is noticed after 2 hours but a more significant change occurs after 8 hours. The same density is achieved at 800°C and remains constant without any relation to the heating time. The decrease in density is probably due to the formation of small pores when the adsorbed water and the structural OH⁻ are released. The density increases between 800°C and 1000°C, but shows no correlation with the heating time. For example, the sample heated for 4 hours shows a higher density than the sample heated for 2 and 8 hours (Fig. 1). For the highest temperatures of thermal treatment, i.e. 1100 to 1200°C, the samples display a strong positive correlation between the density and the heating time. These variations in the density of the heated samples are most likely due to the formation of a liquid phase.

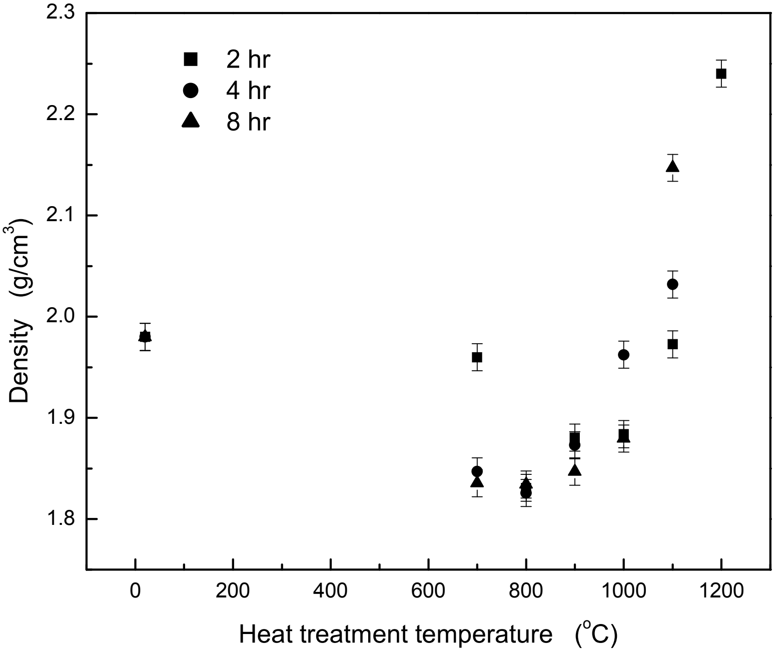

**Fig. 1.** Variation diagram of the density of the raw clay and heated clay samples vs. temperature.

The X-ray diffraction patterns recorded from the not treated raw clay and from samples heated at different temperatures for 2, 4 and 8 hours respectively, are displayed in Figs. 2 to 7. The raw clay shows the lines of quartz, calcite, some feldspar and illite + muscovite. The latter is the predominant clay mineral and has the characteristic peaks at 8.67, 17.87, 27.83, 36, 37.5 and 45.3° 2θ [10]. The weak line at 12.65° 2θ might be assigned to some chlorite or/and kaolinite. No lines assigned to Fe-rich minerals could be identified, although the ICP-MS chemical analyses (*unpublished data*) show a high amount of $Fe_2O_3$, up to 6-7 wt.% in the raw clay sample.

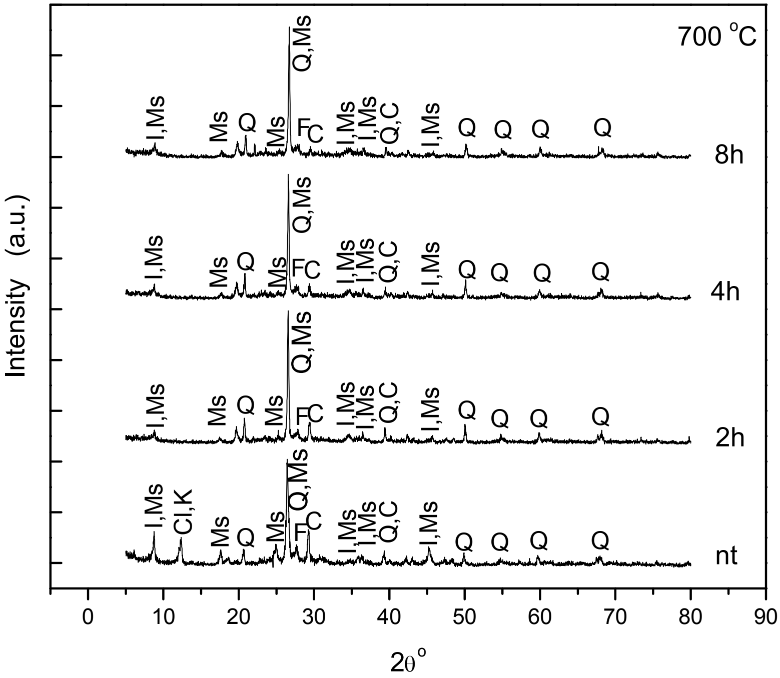

**Fig. 2.** XRD patterns of the not treated raw clay (nt) and the 700°C-heated samples. Abbreviations: I – Illite, Ms – Muscovite, Cl – Chlorite, K – Kaolinite, Q – Quartz, F – Feldspar, C – Calcite.

The XRPDs of the heated samples reveal the disappearance of the primary minerals and the formation of new phases. The most obvious thermal change regards calcite – a mineral well known for the sensitivity to temperature [11-13]. Its diffraction lines start to diminish already after 2 hours of heating at 700°C and become smaller after 4 and 8 hours of heating. At temperatures higher than 800°C, the calcite lines disappear completely after 2 hours of heating.

Up the 900°C, quartz shows only few changes. i.e. a relative increase as the one of the few crystalline phases surviving upon heating. Chlorite and/or kaolinite main diffraction line disappears after 2 hours at each temperature.

The diffraction lines of the main clay component, which is illite (± muscovite) show the most dramatically changes. They start to diminish already after 2 hours at 700°C, independent of the heating time. They completely disappear at 900°C. In the literature, the destruction of illite structure is in general reported to occur at higher temperatures, over 850-900°C [13-16], but only rare at lower temperatures [17], as shown by our results.

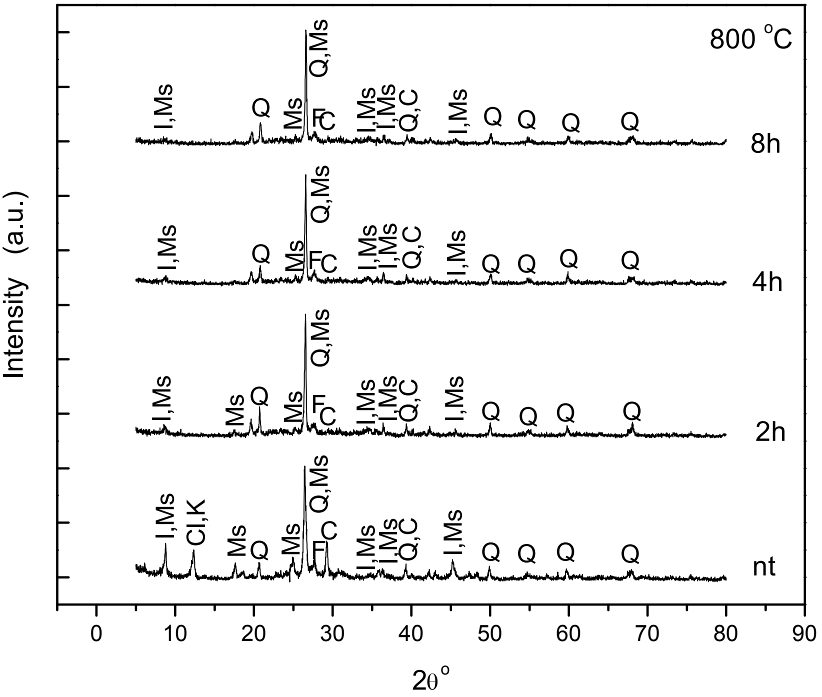

**Fig. 3.** XRD patterns of the not treated raw clay (nt) and the 800°C-heated samples. Abbreviations: I – Illite, Ms – Muscovite, Cl – Chlorite, K – Kaolinite, Q – Quartz, F – Feldspar, C – Calcite.

Feldspar is present in the raw clay and its lines remain unchanged at 700 and 800°C. Only a small increase is observed after 2 hours heating at 900°C, when probably new feldspars start to form [14, 15, 18]. At 1000°C the increase of the feldspar amount is obvious already at 2 hours whereas the heating up to 1100°C shows large-scale formation of feldspar. At 1200°C, feldspar disappears [see also 13] by melting.

The hump occurring at temperature of 1100°C and higher (Figs. 6 and 7) in the range of 20-30° 2θ indicates the diminishing of sample crystallinity or even an amorphous/vitreous phase, the latter resulting most likely from a melt. The presence of the melt is proved also by the glassy surface of the disk heated to 1100°C. The formation of a melt in ceramics generally starts above 900°C [19].

The weak lines around 30-30.4° 2θ occurring at 1100 and 1200°C after 2 hours of heating might be assigned to the formation of a pyroxene (Figs. 6 and 7).

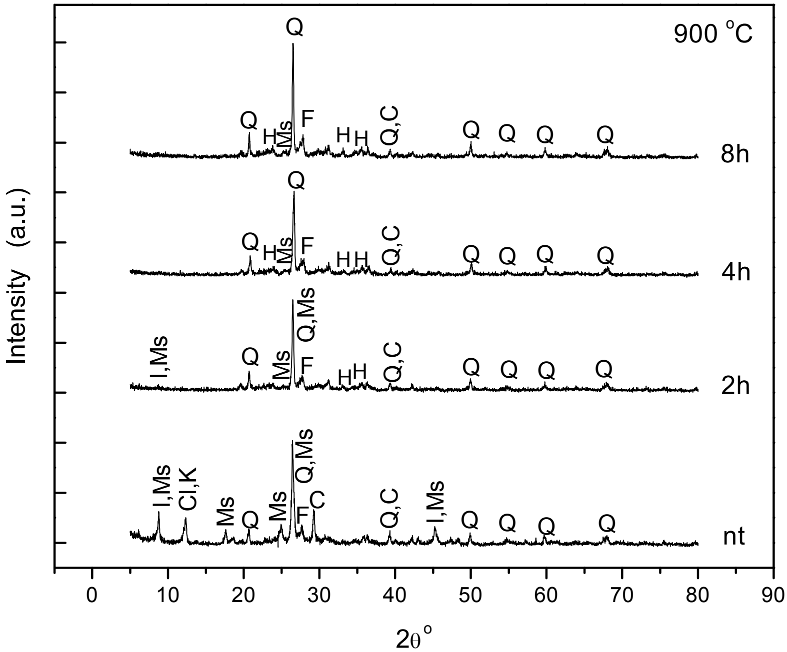

**Fig. 4.** XRD patterns of the not treated raw clay (nt) and the 900°C-heated samples. Abbreviations: I – Illite, Ms – Muscovite, Cl – Chlorite, K – Kaolinite, Q – Quartz, F – Feldspar, C – Calcite, H - Hematite.

The 2 hours heating at 900°C (Fig. 4) already induces the formation of small amount of hematite. The amount of hematite increases with increasing temperature and heating time (Figs. 5 and 6). At 1100°C the formation of hematite is accompanied by some magnetite (maghemite is not excluded) (Fig. 7), whereas at 1200°C the latter predominates. The most characteristic diffraction lines are at 33.2° 2θ (for hematite) and 30.2 and 35.6° 2θ (for magnetite). These minerals formed most likely on the expense of Fe oxides and hydroxides originating from the raw clay. The diffraction patterns for the raw clay do not show any crystallized Fe-rich phases (Figs. 2 to 7) but this can be due to their small amount (<5 wt.%) or/and to a low crystalline/amorphous state. The intensity of the diffraction peaks indicates the prevalence of magnetite compared to hematite. Magnetite and maghemite have similar structures and produce similar XRPD patterns, thus their diffraction peaks nearly overlap. The slight difference in their unit cell parameters results in a slight shift of all peaks of maghemite towards higher angles with respect to the peaks of magnetite [20]. When magnetite and maghemite occur together, the diffraction peak intensity and the peak shape will change in their proportions and it is difficult to discriminate among these minerals only by means of XRPD.

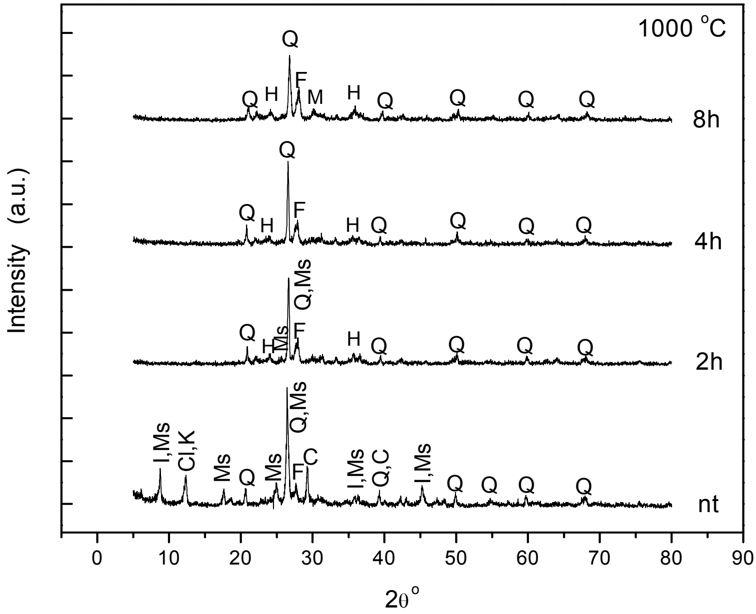

**Fig. 5.** XRD patterns of the not treated raw clay (nt) and the 1000°C-heated samples. Abbreviations: I – Illite, Ms – Muscovite, Cl – Chlorite, K – Kaolinite, Q – Quartz, F – Feldspar, C – Calcite, H – Hematite, M – Magnetite.

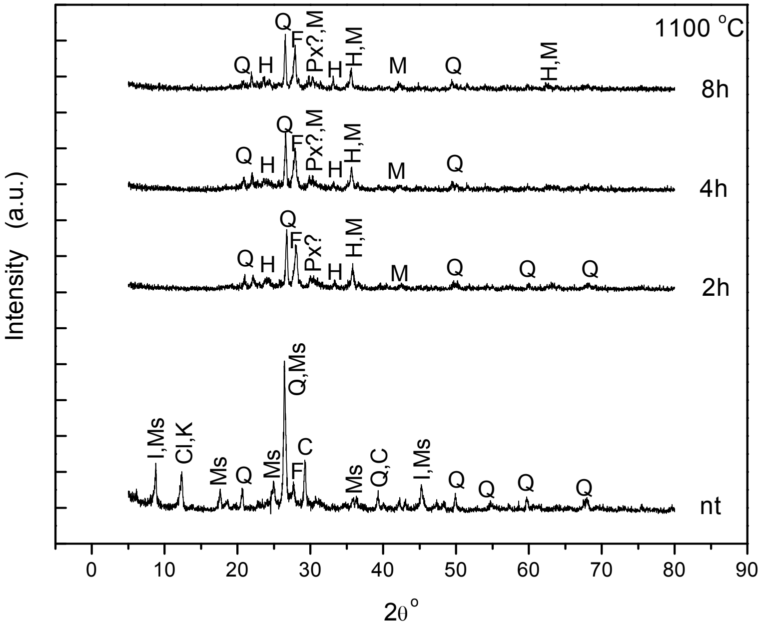

**Fig. 6.** XRD patterns of the not treated raw clay (nt) and the 1100°C-heated samples. Abbreviations: I – Illite, Ms – Muscovite, Cl – Chlorite, K – Kaolinite, Q – Quartz, F – Feldspar, C – Calcite, H – Hematite, M – Magnetite, Px – Pyroxene.

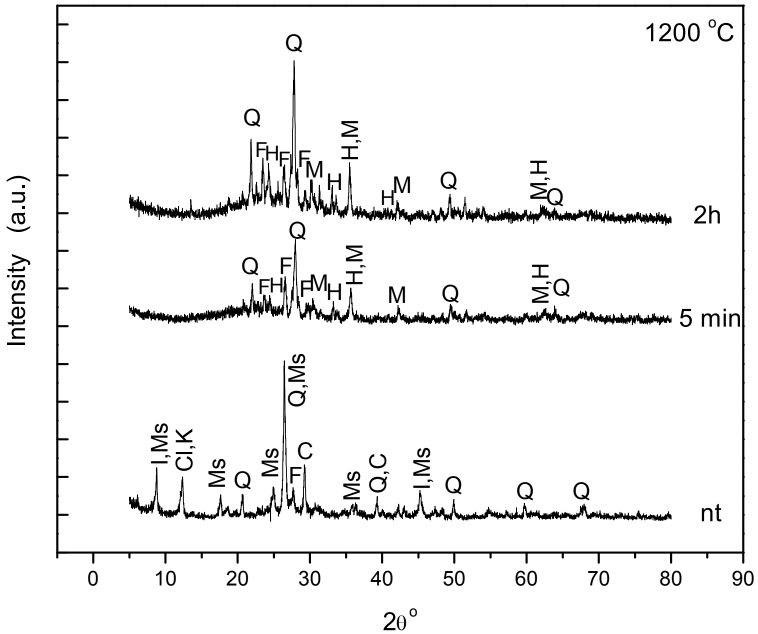

**Fig. 7.** XRD patterns of the not treated raw clay (nt) and the 1200°C-heated samples. Abbreviations: I – Illite, Ms – Muscovite, Cl – Chlorite, K – Kaolinite, Q – Quartz, F – Feldspar, C – Calcite, H – Hematite, M – Magnetite.

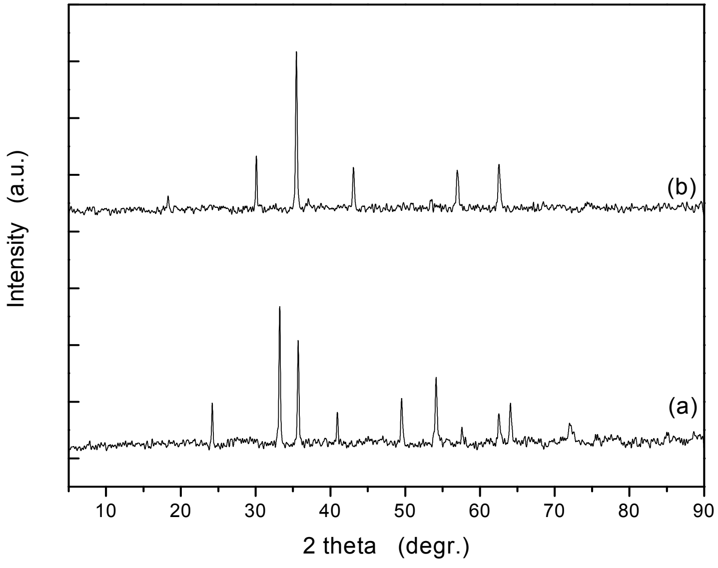

**Fig. 8.** Ideal XRD patterns of hematite (a) and magnetite (b) [from RRUFF ID=R080024, RRUFF ID=R080025].

Hematite on one side, and magnetite/maghemite on the other side –, are generally regarded as responsible for the ceramic red and black colour, respectively [21, 22]. In our samples, one might expect more reddish colours, as the heating was done in a normal atmosphere, i.e. oxidizing conditions. The amount of hematite as identified by XRPD is smaller than the magnetite (± maghemite) and this produces the overall brownish hues. When more magnetite is produced, at 1200°C, the sample changes to a black colour. This requires a progressive reducing atmosphere might be due to the tightly closed oven and the consumption of oxygen during the heating. The formation of a reducing atmosphere by calcite and possible some organic material decomposition might be taken into account as well. Obviously a higher temperature and a long time of heating will lead to the black colour.

## CONCLUSIONS

The heating of Miocene illitic clay samples up to 700-1200°C for different periods of time shows a wide range of physical, structural and mineralogical processes. The density of fired disks has various values, most relevant being its increase at higher temperatures, proportional with the length of heating period. The X-ray diffraction supported the identification not only of primary minerals constituting the clay, i.e. illite + muscovite, quartz, feldspars, calcite and some chlorite and/or kaolinite but also their changes in time, at various heating temperatures. Most of the mineralogical changes show little correlation with the heating time. Exceptions are feldspars, quartz and calcite, with more obvious changes after a longer heating time, i.e. 4h and 8h. The clay minerals are transformed already after 2 hours of heating at any temperature. Among the newly formed phases, hematite and magnetite ± maghemite are responsible for the general brownish hues of the ceramic disks. The black colour can be obtained in a normal oven, only at high temperature, around 1200°C.

## ACKNOWLEDGEMENTS

The present study was supported by the scientific research project UEFISCDI/CNCS ID-2241/2008 in the framework of the Romanian Excellence Research Program.

## REFERENCES

1. B. Fabbri. Appl. Clay Sci., 53, 443 (2011).
2. R.A. Kühnel. Appl. Clay Sci., 5, 155 (1990).
3. W.A. Deer, R.A. Howie, J. Zussman. *An introduction to the rock-forming minerals*. Pearson Prentice Hall, 696 p. (1992).

4. M.R. Stackmeyer. Appl. Clay Sci., 6, 39 (1991).
5. L.P. Meier, R. Nueesch, F.T. Madsen. Jour. Colloid Interf. Sci., 238, 24 (2001).
6. L.Z. Zhu, B.L. Chen. Environ. Sci. Technol., 34, 2997 (2000).
7. L.Z. Zhu, B.L. Chen, X.Y. Shen. Environ. Sci. Technol., 34, 468 (2000).
8. M. Tămăşan, H. Mocuța, C. Ionescu, V. Simon. Studia UBB Physica, 54, 3 (2009).
9. Gr. Răileanu, Fl. Marinescu, A. Popescu. *Geological map of Romania*, 1:200,000 scale, Tg. Mureş Sheet (1968), Geological Inst. Bucharest.
10. M.W. Totten, M.A. Hanan, D. Knight, J. Borges. Amer. Mineral., 87, 1571 (2002).
11. M.P. Riccardi, B. Messiga, P. Duminuco. Appl. Clay Sci., 15, 393 (1999).
12. G. Cultrone, C. Rodroguez-Navarro, E. Sebastian, O. Cazalla, M.J. De la Torre. Eur. Jour. Mineral., 13, 621 (2001).
13. L. Maritan, C. Mazzoli, L. Nodari, U. Russo. Appl. Clay Sci., 29, 31 (2005).
14. C. Ionescu, V. Hoeck, L. Ghergari. Appl. Clay Sci., 53, 466 (2011).
15. C. Ionescu, V. Hoeck. Eur. Jour. Mineral., 23, 6 (2011).
16. M. Hajjaji, H. Mezouari. Appl. Clay Sci., 51, 507 (2011).
17. M.J. Trindade, M.I. Dias, J. Coroado, F. Rocha. Appl. Clay Sci., 42, 345 (2009).
18. P. Duminuco, B. Messiga, M.P. Riccardi. Thermochim. Acta, 321, 185 (1998).
19. A. Khalfaoui, M. Hajjaji, Appl. Clay Sci., 45, 83 (2009).
20. T. Chen, H. Xu, Q. Xie, J. Chen, J. Ji, H. Lu. Earth Planet. Sci. Lett., 240, 790 (2005).
21. M. Maggetti, Ch. Neururer, D. Ramseyer. Appl. Clay Sci., 53, 500 (2011).
22. A.O. Shepard. *Ceramics for the archaeologist*. Carnegie Institute Washington, 414 p. (1976).

STUDIA UBB PHYSICA, LVI, 2, 2011

# SPRING-BLOCK MODELS AND THE MULTI-LANE HIGHWAY TRAFFIC

**JÁRAI-SZABÓ F.**[1]

**ABSTRACT.** A first attempt is presented to adopt the spring-block model of single-lane highway traffic to multi-lane traffic conditions. Simulations on this extended model are performed, and by some case studies the effects of the lane changing behavior on the model system's dynamics are analyzed. Based on this first results, proposal for further investigations are made.

***Keywords:*** *highway traffic modeling; spring-block models.*

## INTRODUCTION

The non-linear and complex nature of the road traffic is strongly affecting our economic and everyday life and it is intensively studied since the last few decades [1-6]. The signs of this complexity may be observed even in the simplest form of traffic that happens on a single highway lane.

Previously, for this simplest idealized form of traffic a three-parameter spring-block model with asymmetric interaction has been developed and studied in detail [7,8]. It was evidenced that, in case of this simplest form of traffic the motion of the first car, the drivers' reaction time and the statistics of driving attitudes govern the motion of the whole queue. The simple free flow structure becomes quite complex if the first car is moving slowly and the differences between the driving attitudes are substantial, or the average reaction time of drivers is increased. In such situations the queue will evolve non-continuously in avalanches, and jams of different sizes will continuously appear and propagate through the system.

By the defined order parameter [8] that focuses on a single car in the row the parameter space of the spring-block model has been explored. From these computational studies we learned, that the model system exhibited non-trivial, critical behavior. A disorder induced second-order phase transition has been observed, separating the free flow phase (with independent block motions) from the congested flow phase dominated by a highly correlated avalanche-like collective motion.

---

[1] *Babeş-Bolyai University, Faculty of Physics, 1 Kogălniceanu str., 400084 Cluj-Napoca, Romania*

Beside of studying this simplest form of traffic, another interesting task would be to study, by the same computational model, the effects of the lane changing behavior on the highway traffic. Unfortunately, such lane-changing situations are quite common, so understanding it and modeling it is extremely important. For this reason our previous spring-block traffic model has been extended to mimic the lane changing behavior of car drivers. Thus, a first attempt of a minimalistic, quasi multi-lane model has been elaborated.

The present work focuses on this extended multi-lane spring-block traffic model. A case study will be presented that highlights the main effects that appear as a consequence of the newly introduced lane-changing behavior. Proposal for further development of the model is made, too.

## SPRING-BLOCK MODELS AND THE MULTI-LANE HIGHWAY TRAFFIC

The used model belongs to the spring-block model family, which has many interdisciplinary applications. The model has been introduced, in its original form, in 1967 by R. Burridge and L. Knopoff [9]. Their primary intent was to explain the empirical law of Guttenberg and Richter [10] regarding the distribution of earthquake magnitudes. The model is built by simple elements: blocks that can slide with friction on a horizontal plane connected in a lattice-like topology by springs. After its first success, this simple model proved to be very useful in describing many phenomena in different areas of science [11-16]. In other words, the model proved to be efficient when it was used to explain complex dynamics or structure formation by collective behavior.

The spring-block approach of the single-lane highway traffic was described in detail in our previous works [7,8]. Accordingly, here only the basic elements of the model and its extension to multi-lane traffic conditions will be discussed in detail.

In the quasi multi-lane spring-block approach a car queue of $N$ cars that moves on a single highway lane is modeled as a chain of blocks of length $L$ dragged by the first block that advances with a constant velocity $v$ (characterized by a drag-step $d_0$). The blocks are connected by springs of equilibrium length $l_0$ and spring constant $k$. These spring interactions model the aim of drivers to keep a certain distance from the car ahead. However, in case of accident-free traffic the car from behind should not have any influence on the front car. Therefore, this distance keeping interaction acts only on the car in behind. In such systems, the action-reaction principle is violated and, in this sense, it cannot be anymore considered as a realistic classical mechanical system.

Another important ingredient incorporated in the model is the drivers' inertia, which indicates how quickly the driver can react to a certain event or how quickly can follow the velocity change of the car ahead. This is introduced via friction forces between blocks and the plane on which they slide. Friction forces are generated randomly and independently for each new position of each block with normal distribution with a fixed mean $<F_f>$ and standard deviation $\sigma$. As a result, both a spatial and temporal disorder is introduced. Spatial disorder means differences in driving styles while temporal disorder means fluctuations of driving attitudes in time. The mean value of the friction force may be connected to the average reaction time of the drivers.

In analogy with real mechanical systems, static and kinetic friction forces are considered denoted by $F_s$ and $F_k$, respectively. Similarly with classical dynamical systems, the maximum possible value of the static friction force is considered to be greater than the kinetic one and their ratio is kept constant $f = F_k / F_s$. By this assumption we include into the model the tendency of drivers to react quicker to an event when the car is in motion.

Of course, in order to ensure accident free traffic that respects the basic traffic rules, some other restrictions have to be considered. So that, a minimum distance between blocks $d_{min}$, and a speed limit (a maximum allowed step-size $d_{max}$) for the blocks inside the row are imposed.

The multi-lane traffic is mapped to a single lane, and only the lane-changing behaviors of drivers are modeled. Accordingly, only the dynamics of cars that move on the studied lane is monitored. In this context, two different events are important to us: when a car is entering, and when a car is exiting the lane. These events may happen at certain traffic conditions with certain probabilities.

On one hand, car-entering events are happening with probability $p_{enter}$, when between two neighboring blocks in the row the distance $\Delta x$ is greater than the length of a block and twice the minimum following *distance:* $\Delta x > L+2 d_{min}$. In such situations one block is added to the row in the center of the free space properly connected by springs to the previous and next blocks. On the other hand, car-exiting events are happening with probability $p_{exit}$, when the headway velocity of a block in the row is smaller than those of the block behind. Then, the second block is removed and the remaining first block is connected to its new previous neighbor.

Beside these lane-changing events, the presence of other lanes with finite number of cars has to be imitated. For this reason, a block storage tank is used which can store a given number of blocks $n_t$. The blocks removed from queue are put into this tank. If its storage limit is reached, then no more car removing events take place. At the same time, the blocks that enter the row reduce the number of blocks in this storage tank. And, of course, if no more blocks are present in the tank, then no car entering events will take place. It is important to note, that at the beginning of simulations the block storage tank is half-filled.

The dynamics of the spring-block chain is simulated following the typical steps of a simplified molecular dynamics simulation with time-step $\Delta t$ valid in case of small drag velocities. Technical details and algorithm tests are specifically described in our previous works [7,8], where a detailed analysis of the model parameters is performed as well.

## SPRING-BLOCK MODELING RESULTS

Our computational study is focusing on what a driver being in the middle of a car row is experiencing. This can be quantified by the statistics of time intervals during which a selected car is not moving (statistics of stop-times). The order parameter $r$, defined and analyzed in our previous work [8], is the ratio of the stop-times standard deviation and the corresponding stop-time average. By this order parameter, the multi-lane modeling results are compared to our previous results for single-lane highway traffic.

In the followings simulation results will be presented for a spring-block chain of length $N = 1000$ blocks. The order parameter is calculated from a statistics of *100 000* stop-times.

Let us now consider a case study with this extended version of the model. The used simulation parameters are:
$L = 1; k = 1; l_0 = 0.3; \Delta t = 1; d_0 = 0.05; d_{min} = 0.3; d_{max} = 1; f = 0.8; n_t = 100$. All parameter values are expressed in simulation units. In this study the car-entrance and car-exit probabilities are considered to be equal $p_{enter} = p_{exit} = 0.01$. The other parameter values $<F_f>$ and $\sigma$ will be varied and noted for each simulation separately.

In the Figure 1 the order parameter and its first derivative is plotted as a function of the disorder level in the system for single-lane ($p_{enter} = p_{exit} = 0$) and multi-lane ($p_{enter} = p_{exit} = 0.01$) traffic conditions. The mean value of friction forces is fixed to $<F_f> = 9$ expressed in simulation force units.

From the Figure 1 it is immediately observable, that in case of multi-lane situations the transition between free-, and congested flow phases becomes less sharp. In addition, there is a more important feature we can learn from this comparison. Specifically, the critical disorder level defined by the inflexion point of the $r$ curves or the maxima of the $dr/d\sigma$ curves will become smaller when the lane-changing behavior is allowed in the model. This first result may be validated by our everyday experience. In case of real traffic situations the lane-changing behavior represents an additional disorder in the system. Accordingly, congested traffic conditions will appear even in case of smaller disorder levels in driving attitudes.

Let us now compare the parameter space maps of single-, and multi-lane traffic models. In Figure 2 the order parameter is represented as a function of the two main parameters of the single-lane model: the mean value of static friction force $<F_f>$ varied between *[0, 16]* and the disorder level $\sigma$ varied between *[0.1, 3.0]*.

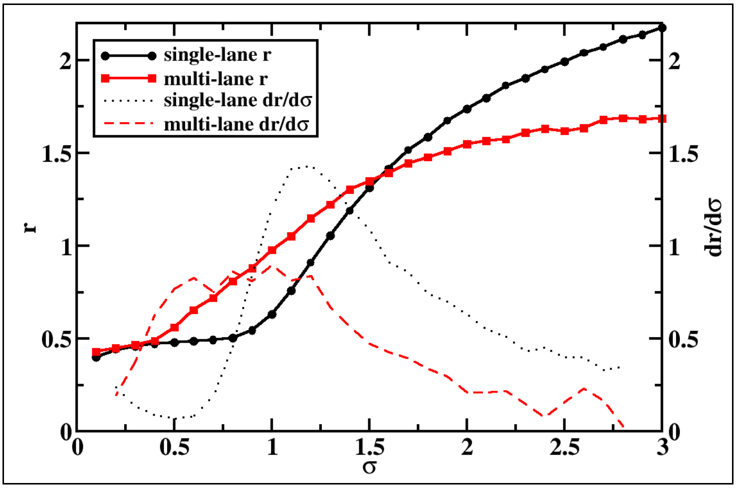

**Figure 1.** The order parameter *r* and its derivative *dr/d*$\sigma$ plotted as a function of the disorder in the system $\sigma$ for single-, and multi-lane traffic models.

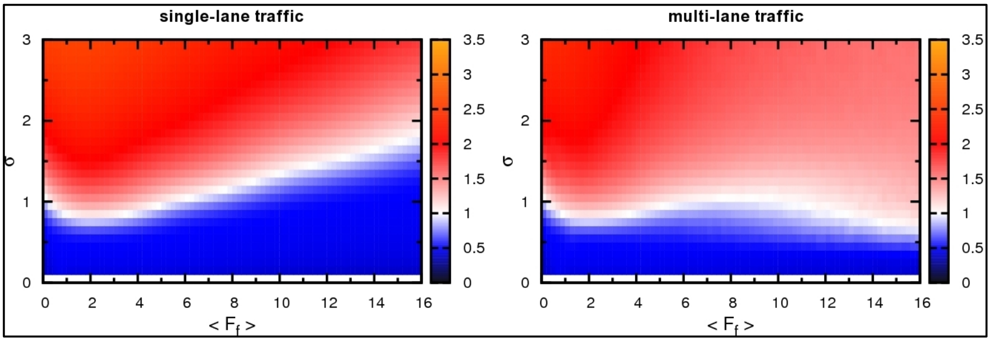

**Figure 2.** Parameter space maps of single-lane (left) and multi-lane (right) traffic models.

Each map contains 2430 data points and each point is calculated from a statistics of 100 000 simulated stop-times. In agreement with our previous case study performed for a single <$F_f$> value, on each parameter map the free flow and jam phases are clearly separated. However, in case of the multi-lane model the size of the free flow phase is reduced. From the maps it is observable, that this effect is important only in case of large <$F_f$> values. In other words, the effect of lane-changing behavior becomes important only in case of long reaction times of drivers.

Another important conclusion arises if one looks at the same point on both maps. Particularly, let us select the point characterized by a large mean value of friction forces $<F_f> = 14$ and a disorder level $\sigma = 1$. At these conditions in case of single-lane approach a free-flow phase is expected. As the lane-changing behavior is turned on, the system evolves to the congested flow phase without the change of any other traffic conditions. This transition may not happen in case of short reaction times of drivers ($<F_f> < 7$). Therefore, the lane-changing behavior affects only traffic systems with longer reaction times. This result may be confirmed again by our driving experience. If we have quick reactions when a car is entering in the front of us from the nearest lane or a car in front of us is exiting the lane, then this reaction (reducing or increasing our headway velocity) should be smaller. In case of small changes in our driving velocity the car that moves in our back should have even smaller reaction. In the contrary, a big change in our headway velocity that should happen as a consequence of a late observation of some events may lead to a complete stop of the cars behind us.

## CONCLUSIONS

In conclusion, inspired from the spring-block modeling of the single-lane highway traffic a first attempt to elaborate a minimalistic one-dimensional asymmetric spring-block model for studying multi-lane highway traffic conditions was presented. The model introduces the car entering and car exiting events, and a fixed capacity car storage tank imitates the presence of other lanes. By computer simulations it was shown that even in case of multi-lane traffic conditions the free and congested traffic flow phases exists. The qualitative comparison of the parameter space maps of single-, and multi-lane traffic models reveals that the lane-changing behavior affects only systems that include elements having long average reaction time. In such situations it is possible to have a free-flow – congested-flow transition induced only by the presence of other traffic lanes. One drawback of this model is that it introduces three new parameters. Accordingly, further investigations are expected in order to clarify the role of these free parameters and to reduce the number of them.

## ACKNOWLEDGMENTS

This work was supported by CNCSIS-UEFISCSU, project number PN II-RU PD404/2010.

## REFERENCES

1. T. Nagatani, *Rep. Prog. Phys.*, 65, 1331 (2002).
2. B.S. Kerner, The physics of traffic, Springer, Berlin, NewYork (2004).
3. D. Chowdhury, L. Santen, A. Schadschneider, *Physics Reports*, 329,199 (2000).
4. D. Helbing, *Rev. Mod. Phys.*, 73, 1067 (2001).
5. S. Maerivoet and B. De Moor, *Physics Reports*, 419, 1 (2005).
6. S. Darbha, K.R. Rajagopal and V. Tyagi, *Nonlinear Analysis*, 69, 950 (2008).
7. Járai-Szabó F., Sándor B., Néda Z., *Cent. Eur. J. Phys.*, 9(4), 1002 (2011).
8. Járai-Szabó F., Néda Z., *Earthquake Model Confirms Traffic Jams Caused by Tiredness*, submitted to *PLOS-ONE* (2011), preprint on arXiv:1111.1803v1 [physics.soc-ph].
9. R. Burridge and L. Knopoff, *Bull. Seism. Soc. Am.*, 57, 341 (1967).
10. B. Gutenberg and C.F. Richter, *Ann. Geophys.*, 9, 1 (1956).
11. K.-t. Leung and Néda Z., *Phys. Rev. Lett.*, 85, 662 (2000).
12. K.-t. Leung, Jozsa L., Ravasz M.and Néda Z., *Nature* 410, 166 (2001).
13. Járai-Szabó F., S. Astilean and Néda Z., *Chem. Phys. Lett.*, 408, 241 (2005).
14. Járai-Szabó F., Néda Z., S. Astilean, C. Farcau and A. Kuttesch, *Eur. Phys. J. E*, 23, 153 (2007).
15. Járai-Szabó F., Horvát E-Á., Vajtai R., Néda Z., *Chem. Phys. Lett.*, 511, 378 (2011).
16. Kovács K. and Néda Z., *Physics Letters A*, 361, 18 (2007).

STUDIA UBB PHYSICA, LVI, 2, 2011

# MONITORING OF COPPER-GLICINE COMPLEX ADSORPTION ON SILVER SURFACE

**D. MANIU[1]*, T. ILIESCU**

**ABSTRACT** The copper-glicine complex adsorption on silver surface was monitored. FT Raman and density functional theory (DFT) calculation have been performed in order to find the optimized structure and compute vibrational spectra of copper-glicine complex. Surface enhanced Raman spectra in silver hydrosol have been recorded. A spectral fluctuation was observed and was explained by thermal effect and by the different local work function of the metal in different sites of adsorption.

***Keywords:*** *SERS, copper-glicine, Raman, DFT*

## INTRODUCTION

Minerals like copper, zinc, iron can chemically bond to natural amino acids resulting chelates. Metal amino acids chelates are compounds which allow the minerals to be carried in with the amino acids during absorption [1, 2]. The amino acids, once released from the metal, can be used to built proteins or provide energy. In recent years metal amino acids complexes have received much attention because they proved to be useful antibacterial and antifungal agents applied against staphylococcus aureus, candida albicans, aspergillus flavus and escherichia coli, nutritive supplies for humans and animals [3].

In order to understand the action of metal amino acids complexes into the human body is very important to know more about the structure and vibrational properties of these compounds. From pharmaceutical studies it is known that each drug is specific to certain human organ in which it is adsorbed on some special centers. The adsorption of the molecules on the metal surface can be considered as a *mimic* of drug adsorption process [4]. Adsorption of the molecules on the metallic surface with nanometer structure give intense Raman spectra (SERS) determined by two main mechanism; electromagnetic and chemical one [5]. SERS has the advantages of chemical specificity, which help to overcome background problems affecting fluorescence spectroscopy in transient signals.

---

[1] *Babes-Bolyai University, Physics Faculty, M. Kogalniceanu 1, 400084 Cluj-Napoca, Romania*
* *corresponding author, e-mail: dana.maniu@phys.ubbcluj.ro*

In the first part of this study we present the vibrational analysis of copper-glicine complex (CuGc) from experimental (FT Raman) and theoretical (DFT calculations) point of view. The second part of this paper is concerned with the adsorption behavior of copper-glicine complex on the silver surface [6].

## EXPERIMENTAL

The complex was prepared following the procedure described in the literature [7]. 2 mMolls of glicine were dissolved in 20 ml distilled water. For deprotonation of amino acid, 0.33 ml 30% NaOH was added. Then 1 mmol of metal solid Cu $(NO_3)_2.2H_2O$ was dissolved in 2 ml of distilled water and added to the deprotonated amino acid solution under stirring it for several minutes. The precipitation was instantaneous and intense blue color was observed. Sodium citrate silver colloid was prepared according to literature [8]. A small amount of $3.\text{mol}L^{-1}$ aqueous solution of CuGc was added to 2 ml colloid. A few droplet of 1.5 $\text{mol}L^{-1}$ KCl solution were added to obtain coagulation of the sol. The final concentration of the sample was $3.10^{-4}$ $\text{mol}L^{-1}$. All measurements were obtained at neutral pH values. No HCl and NaOH solution were added to change the pH.

FT-Raman spectra were recorded using a Bruker IFS 120 HR spectrometer with integrated FRA 106 module and resolution 2-4 $cm^{-1}$. The radiation of 1064 nm from Nd-YAG laser was employed for Raman spectra excitation. 180° geometry was used to collect the scattered light. The SERS measurement were performed on the confocal Raman microscope (Alfa 300R Witec), equipped with a 50X microscope objective. SERS spectra were excited with 532 nm radiation obtained by frequency doubling from Nd-YAG laser.

The molecular geometry optimization and frequencies calculation were performed with the Gaussian 98W software package [9] by using the B3LYP [9, 11] DFT method in conjunction with the split valence-shell 6-31 G(d) basis set [12]. All the calculation has been carried out with the restricted closed shell formalism. We localized all the minima on the potential energy surface on the basis of semi empirical AM1 calculations [13] then the geometry of the lowest energy conformer was subsequently fully optimized with the help of analytical gradient procedure implemented within Gaussian 98W program. The force constants were calculated by analytical differentiating algorithm for completely optimized geometry. Prior to compare the calculated vibrational frequencies with the experimental counterparts, the former have been scaled by appropriate scaling factor recommended by Scott and Radom [14]. For DFT method at B3LYP/6-31 G(d) level, the recommended frequency scaled factors for high and low frequencies are 0.9614 and 1.0013 respectively. To help in mod assignments we are based on the visual inspection of normal modes animated by using Molekel program [15]. The calculated Raman intensities ($S_i$) were converted to relative Raman intensities ($I_i$) using the following relation [16]:

$$I_i = \frac{f(\nu_0 - \nu_i) S_i}{\nu_i [1 - \exp(-(hc\nu_i / kT))]}$$

where $\nu_0$ is the exciting laser wavenumber, $\nu_i$ is the wavenumber of the i-th vibrational mode, *c* is the speed of the light, *h* and *k* is Planck's and Boltzman's constants and T is the temperature.

## RESULTS AND DISCUSSION

### *Theoretical calculations*

Theoretical investigations have been performed on two conformers in order to find the most stable one. The optimized geometries of the conformers calculated at the B3LYP/6-31 G(d) level of theory are illustrated in Fig.1. The most stable conformer was found to be conformer 2 by an energy difference of 49 KJ/mol.

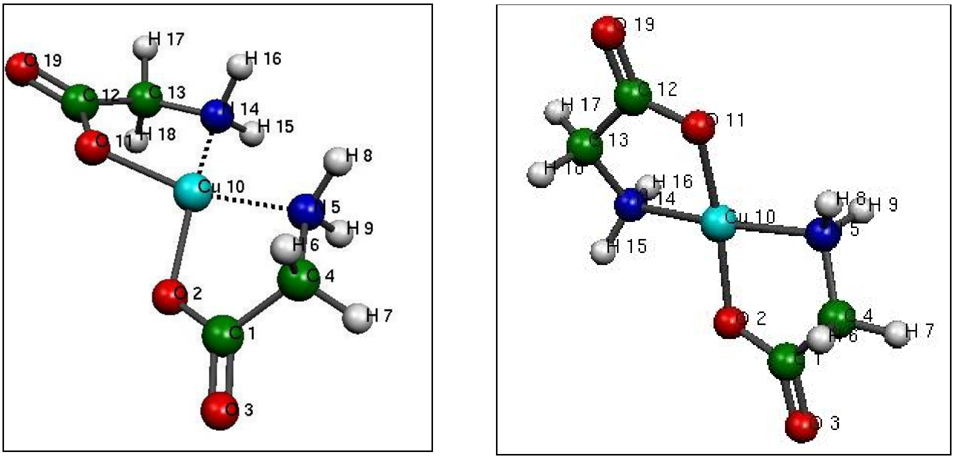

(a) Conformer 1 (b) Conformer 2

**Fig. 1.** Optimized geometry of two conformers of copper-glicine complex at B3LYP/6-31G(d) theoretical level

As can be seen in the Fig. 1, for conformer 2, C, O, and Cu atoms are practically in the same plane. For this conformer the obtained theoretical wavenumber values were found to be in good agreement with Raman data as can be seen in Fig.2. The observed Raman bands with their assignment accomplished with the help of theoretical calculations are presented in Table 1.

The observed disagreement between theory and experiment is a consequence of the anharmonic potential energy surface, the incomplete incorporation of the electron correlation and the incompleteness of the basis set used in the calculation [12, 17]. Nevertheless, as can be seen in Table 1, the theoretical calculations reproduce well the experimental data and allow the assignment of the vibrational modes.

At low frequencies, $CuO_{11}O_{12}$ (see Fig.1b) twisting mode and $CuO_{11}O_{12}$ rocking and oscillation of glicine groups give strong bands at 102 and 231 $cm^{-1}$ respectively. Asymmetric stretching of $CuO_{11}O_{12}$ group and rocking vibrations of $CH_2$ and $NH_2$ groups determine medium Raman bands at 457, 555 and 920 $cm^{-1}$, respectively.

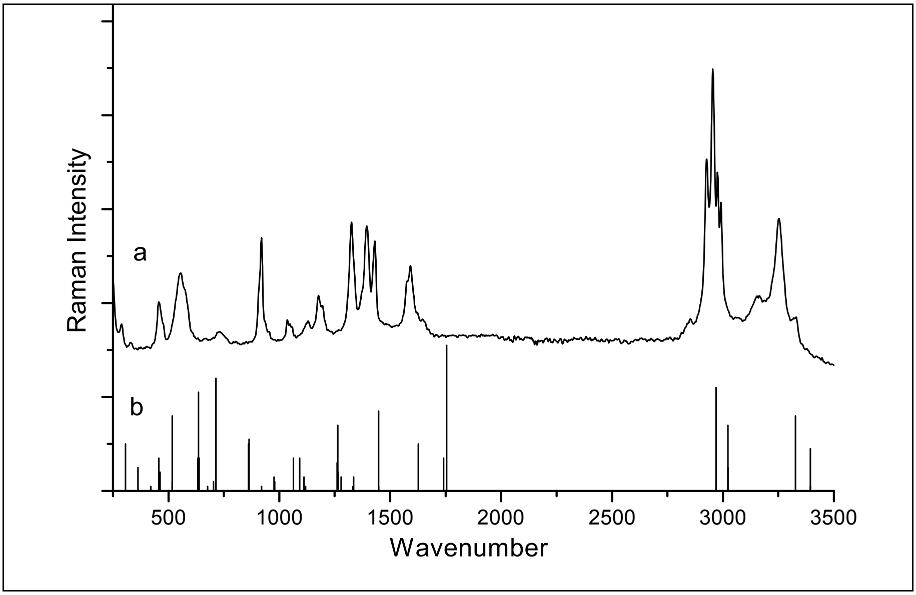

**Fig. 2.** (a) FT Raman spectrum of solid state copper-glicine complex. (b) Theoretical Raman spectrum of copper-glicine complex at B3LYP/6-31G (d) level of theory

Strong band at 1324 $cm^{-1}$ is assigned to the wagging of $CH_2$ and twisting of $NH_2$ groups. Scissoring mode of $NH_2$ group was observed at 1541 $cm^{-1}$ and symmetric and asymmetric stretching modes of $CH_2$ group are located at 2852, 2975 and 2991 $cm^{-1}$. $NH_2$ groups give their symmetric and asymmetric stretching modes at 3253 and 3330 $cm^{-1}$ respectively.

**Table 1.** The experimental (FT-Raman) and calculated (B3LYP/6-31G(d)) wavenumber values (cm$^{-1}$) of copper glicine complex

| Experimental | Calculated | Assignment |
|---|---|---|
|  | 25 | Osc. of glicine group |
|  | 44 | Osc. of $NH_2$ and $CH_2$ groups |
| 87(sh) | 89 | $CH_2(\rho)+NH_2(\rho)$ |
| 102(s) | 98 | $CuO_{11}O_2$ $(\tau)+O_{11}O_{19}(\tau)+O_2O_3(\tau)$ |
|  | 107 | $CH_2(\rho)+NH_2(\rho)$ |
| 125(m) | 115 | $CH_2(\rho)+NH_2(\rho)$ |
| 167(sh,w,) | 166 | $NH_2(\rho)+$ $CuO_{11}O_2(\omega)$ |
| 231(s) | 258 | $CuO_{11}O_2(\rho)$+osc. of glicine groups |
| 289(w) |  |  |
| 329(vw) | 330 | $CuO_2$ $(\nu_s)$+Osc. of glicine groups |
|  | 358 | $CuO_2(\delta)+$ $NH_2(\rho)$ |
| 457(m) | 446 | $CuO_2(\nu_{as})$+CO def. |
|  | 473 | $CH_2(w)+NH_2(w)+$ $C_1C_3$ and $C_{12}O_{19}$ (def) |
|  | 486 | $NH_2(w)+$ $CH_2(w)+$ $C_1C_3$ and $C_{12}O_{19}$ (def) |
|  | 535 | $CH_2(\rho)+NH_2(\rho)$ |
| 555(m) | 539 | $CH_2(\rho)+NH_2(\rho)$ |
| 570(sh) |  |  |
|  | 624 | $CH_2(\rho)+O_{13}C_{12}O_4$ and $O_3C_1O_2$ (o.of p. def.) |
|  | 630 | $CH_2(\rho)+O_{13}C_{12}O_4$ and $O_3C_1O_2$ (o.of p. def.) |
|  | 658 | $NH_2(\rho)$ |
|  | 681 | $NH_2(\rho)$ |
| 731(vw) | 774 | $N_5H_8$ and $N_{14}H_{15}$ (o. of p. def.) |
|  | 801 | $N_5H_8$ and $N_{14}H_{15}$ (o. of p. def.) |
|  | 863 | $C_1C_4$ and $C_{12}C_{13}$ $(\nu)+N_5H_8$ and $N_{14}H_{15}$ (o. of p. def.) |
| 920(s) | 906 | $CH_2(\rho)+NH_2(\rho)$ |
| 1035(vw) | 994 | $C_4N_5$ and $C_{13}N_{14}(\nu)$ |
| 1047(sh.vw) | 1056 | $NH_2(w)$ |
|  | 1061 | $NH_2(w)+C_{13}H_{17}$ and $C_4H_7$ (o. of p./ def.) |
| 1130(vw) | 1108 | $CH_2(\tau)+NH_2(\tau)$ |
| 1176(m) |  |  |
| 1194(sh) |  |  |
|  | 1262 | $C_1C_4$ and $C_{13}C_{12}(\nu)+CH_2(\tau)+NH_2(\tau)$ |
|  | 1266 | $CH_2(w)+C_1O_2$ and $C_{12}O_{19}(\nu)$ |
|  | 1269 | $CH_2(\tau)+NH_2(\tau)$ |
|  | 1270 | $CH_2(\tau)+NH_2(\tau)$ |
| 1324(s) | 1321 | $CH_2(w)+NH_2(\tau)$ |
|  | 1323 | $CH_2(w)+NH_2(\tau)$ |
| 1430(s) | 1443 | $CH_2(\delta)$ |
| 1577(sh) |  |  |
| 1591(m) | 1625 | $NH_2(\delta)$ |
| 1649(sh.w.) |  |  |
|  | 1743 | $C_1O_3$ and $C_{12}O_{19}(\nu)$ |
| 2852(vw) | 2970 | $CH_2(\nu_s)$ |
| 2925(s) |  |  |

| | | |
|---|---|---|
| 2954(vs) | | |
| 2975(s) | 3021 | $CH_2(\nu_{as})$ |
| 2991(s) | 3021 | $CH_2(\nu_{as})$ |
| 3153(w) | | |
| 3253(m) | 3348 | $NH_2(\nu)$ |
| 3330(vw) | 3418 | $NH_2(\nu_{as})$ |

**Abreviations:** w. weak; m. medium; s. strong; v. very; sh. shoulder; δ. Bending; ρ. rocking; τ. twisting; ω. wagging; ν. stretching; s. symmetric; as. asymmetric; def. deformation; osc. oscillation

*Adsorption on silver surface*

SERS spectra of CuGc in silver sol present a strong change in intensity and peak position in time. We analyzed two situations. (a) Spectra were recorded from the bulk of the colloid - a droplet of the colloid and 50X objective were used, and (b) spectra were obtained from the fixed cluster - the colloid was put between two microscope lamellas and 50X objective was focused on the fixed cluster located on the bottom of the sample.

A sequence of 30 SERS spectra with 0.5 s integration time from the bulk colloid is presented in Fig 3. In a previous paper [6] we presented spectra recorded from two fixed clusters with 0.5 s integration time.

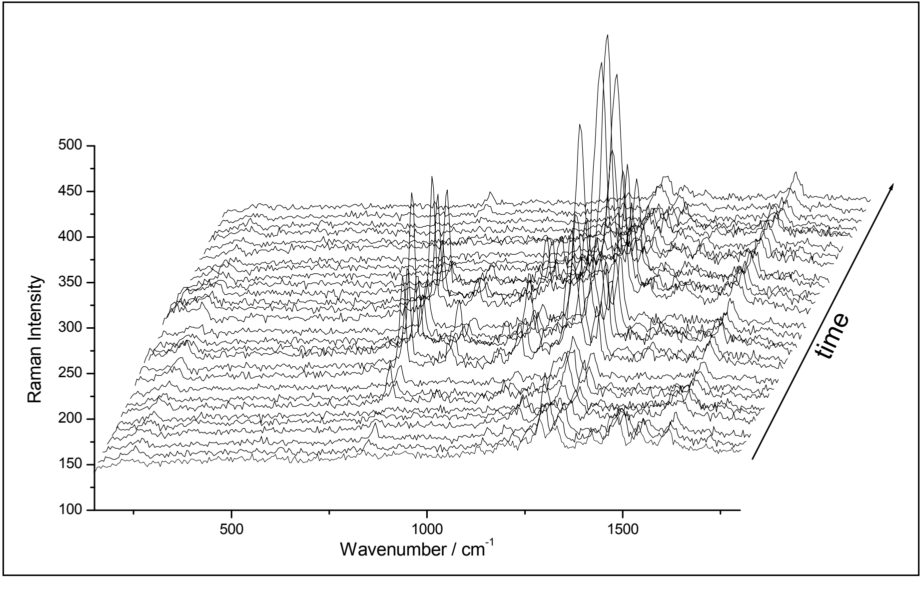

**Fig.3.** A sequence of 30 SERS spectra with 0.5s integration time from bulk silver colloid

In both cases a fluctuation in the peaks position and intensity can be observed especially in sequence obtained from the bulk colloid. Iliescu and all [6] explained these spectral fluctuations as been mainly determined by thermal effect of the light and by the different local work function of the metal in different sites of adsorption. It is known that very intense spectra can be obtained from the ''hotspots'' were the electric field are very large [18].

Excitation line (532 nm) for Raman spectra in our case is in the wing of absorption spectrum of CuGc (Fig. 4). In this case probably we have some contribution from resonant SERS effect. Our attempt to obtain SERS spectra at large power (30 mW) of laser was negative as was presented in previous paper [6]. This confirms that the most probably in our case thermic effect play a very important role in fluctuation of the SERS signal in time.

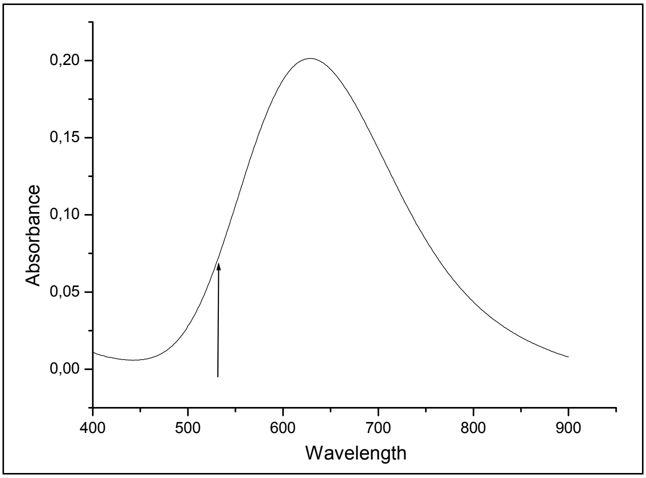

**Fig. 4.** Absorption spectrum of copper-glicine complex.
Arrow show 532 nm excitation line in Raman spectrum.

The change in the peak position of SERS spectra in time, as observed in Fig 3. can be determined by the change of orientation of the molecule in time with respect to silver surface, the molecule being adsorbed and re-adsorbed. Although the concentration in our case is large ($3.10^{-4}$) is possible that only a few number of the molecules to give signal like in the case of single molecule situation. In our case probably the charge transfer (CT) mechanism play an important role in enhancement of the Raman signal. In charge transfer mechanism an electron is transferred from the metal to the empty molecular orbital of the adsorbed molecule or from the occupied orbital to the metal. In this case a process known as ''desorption induced by electron transition'' can be present [19]. This electronic transition induces vibrational excitation in a mode crucial for surface bonding and provide enough energy to that mode to enable desorption. Since our experiments are not carried out under vacuum, the friction exerted on the desorbed molecule by the liquid can force it to re adsorb at the same site from which it was detached or very nearby one.

Fig. 5a present the spectrum as obtained by summing up several spectra from the fixed cluster as obtained in sequence which reveals the main spectral feature of CuGc in solid state (Fig. 5b) (except the change in the peak position and relative intensity specific to SERS phenomenon).

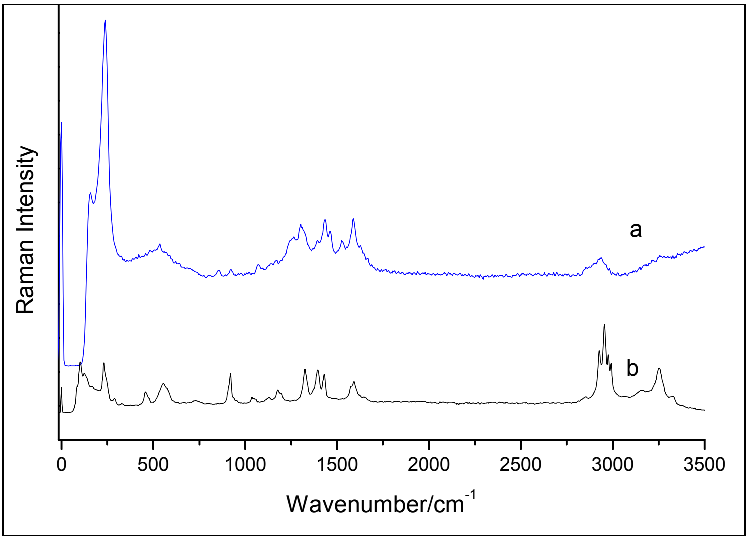

**Fig. 5.** (a) SERS spectrum as obtained by summing 120 SERS spectra of a copper-glicine complex from fixed cluster, recorded in sequence lasting 0.5s between two successive measurements. (b) FT Raman spectrum of copper-glicine solid state (excitation line 1064 nm).

The similitude between the spectra presented in Fig. 5. eliminates the possibility that the changes in SERS spectra to be determined by photodecomposition of the compound and by the fragments obtained by this process.

The adsorption and re adsorption of the glicine complex molecule is a consequence of the weak binding of the molecule to the silver surface. The molecules which have the nitrogen and oxygen in their composition can be attached to the metal surface by these atoms. In copper-glicine molecule the lone pair electrons of nitrogen atoms are involved in the coordination with copper atom and only lone pair of oxygen atoms can attach the molecule top the silver surface, this bond probably being very weak.

The energy of CT resonance depends on the position of the HOMO or LUMO levels of the molecule, but these levels are not expected to fluctuate. The CT energy depends on the local work function of the metal at the molecular adsorption site. The difference between different sites of adsorption probably can be determined by slightly different local work function to extract electron from the metal [19].

## CONCLUSIONS

FT Raman and DFT theoretical calculation on the copper-glicine molecule was performed in order to find the optimized structure and to compute vibrational spectra. The fluctuations in the peak position and intensity of the SERS bands of adsorbed molecule on silver surface were observed. The molecular dynamics of adsorption was discussed and found that crucial contribution in the spectral fluctuation are determined by thermal effect of the light and by the different local work function of the metal in different sites of adsorption.

## ACKNOWLEDGEMENT

This work was supported by by CNCSIS–UEFISCSU, project number PNII-ID_PCCE_129/2008. D. M. also acknowledge the suport of Sectorial Operational Programme for Human Resources Development 2007-2013, co-financed by the European Social Fund, in the frame of project number POSDRU/21/1.5/G/36154.

## REFERENCES

1. R. Bentley, ''Biochemistry and Molec. Biology Education'', **33,** 274, (2005).
2. K. Shoveller, B. Stall, R. Balt, D. Burrin, J. Nutr., **135**, 1609, (2005).
3. M.Z. Iqbal, S. Khurshid, M.S. Iqbal, J. Pak, Med. Assoc., **40**, 221, (1990).
4. C.D. Dryhusrst, ''Electrochemistry of Biological Molecules'' Academic press, New york, p. 472, (1977).
5. R.K. Chang, T.E. Furtak, Eds. ''Surrface Enhanced Raman Scattering'' Plenum press, New York, (1982).
6. T. Iliescu, D. Maniu, S. Astilean, A. Marcu, JOAM - Symposia, **2**, 1, (2010).
7. P. O'Brien, J. Chem. Educ., **59**, 1052, (1982).
8. T.K. Lee, D.M. Meisel, J. Phys. Chem., **87**, 3391, (1982).
9. Gaussian 98, Revision A 7, M.J. Frisch, G.W. Trucks, H.B. Schlegel, G.E. Scuseria, M.A. Robb, J.C. Burat, S. Dapprich, J.M. Millam, A.D. Daniels, K.N. Kudin, M.C. Strain, O. Farcas, J. Tomasi, V. Barone, M. Cossi, R. Cammi, B. Mencucci, C. Pomelli, C. Adamo, S.C. Clifford, J. Ochterski, G.A. Peterson, P.Y. Ayala, Q. Cui,

K. Morokuma, D.K. Molik, A.D. Rabuck, K. Raghavachari, J.B. Foresman, J. Cioslowski, J.V. Ortiz, A.G. Baboul, B.B. Stefanov, G. Liu, A. Liashenko, P. Piskorz, I. Komaromi, R. Gomperts, R.L. Martin, D.J. Fox, T. Keith, M.A. Allaham, C.Y. Peng, A. Nanayakkara, C. Gonzales, M.C. Challacombe, P.M. Gill, B.J. Johnson, W. Chen, M.V. Wong, J.L. Andes, M. Head-Gordon, E.S. Replogle, J.A. Pople, Gaussian Inc., Pittsburgh P. A. (1998).

10. A.P. Brcke, J. Chem. Phys., **98**, 5468, (1993).
11. C. Lee, W. Yang, R.G. Parr, Phys. Rev., B, **37**, 785, (1988).
12. W.J. Hehre, L. Radom, P.V.R. Schleyer, J.A. Pople, ''Ab Initio Molecular Orbital Theory'' Wiley, New York, (1986).
13. M. Dewar, W. Thiel, J. Am. Chem. Soc., **99**, 4499, (1977).
14. A.P. Scott, L. Radom, J. Phys. Chem., **100**, 16502, (1996).
15. Molekel 4.2, P. Flukiger, H.P. Luthi, S. Portmann, J. Weber, SwissCenter for Scientific Computing, Manno (Switzerland).
16. A. Pirnau, V. Chis, O. Oniga, N. Leopold, L. Szabo, M. Baias, O. Cozar, Vibr. Spectrosc., **48**, 2, 289-296. (2008).
17. G. Rauhut, P. Pulay, J. Phys. Chem., **99**, 3093, (1995).
18. R. C. Maher, M. Dalley, E.C. Le Ru, L.F. Cohen, P.G. Etchegoin, H. Hartigon, R.J. C. Brown, M.J.T. Milton, J. Chem. Phys., **121**, 8901, (2004).
19. M. Baia, S. Astilean, T. Iliescu, ''Raman and SERS Investigations of Pharmaceuticals'' Springer-Verlag, Berlin, Heidelberg, p.49, (2008).

STUDIA UBB PHYSICA, LVI, 2, 2011

# EFFECT OF NANODEFECTS INDUCED BY 4F ELEMENTS ON DISSIPATIVE PROCESSES IN SINTERED SUPERCONDUCTORS

**D. MARCONI[1], V. POP[2], C. LUNG[1], A.V.POP[*,1]**

**ABSTRACT.** By using solid state reaction method the (Bi,Pb):2223 single phase superconducting samples were obtained. The influence of partial substitution of Ca by 4f elements (Er, Lu) and Y on structure and purity of 2223 phase is analyzed by XRD measurements. The effect of nanoscale defects induced by 4 f elements on the intergranular dissipation processes is characterized from a.c. magnetic susceptibility function of temperature and a.c. field amplitude. The maximum value of critical current density obtained for a critical $x_c$ value of partial substitution is discussed in relation with the increase of pinning force.

***Keywords:*** *HTS synthesis, nanodefects, X-ray diffraction, a.c. susceptibility.*

## INTRODUCTION

Bi:2223 superconductors have a relatively high $T_c$ around 110K and some advantages of easy formability high chemical stability and nontoxic safety.

Superconductivity of Bi:2223 system may be directly influenced by Cooper substitution in the $CuO_2$, or indirectly by substitution in the Ca or Sr positions (affecting a charge transfer to or from $CuO_2$ planes [1]). Studies of partial substitution of divalent cation Ca by trivalent cations Y or rare earth (Re) ions in Bi:2223 system are in limited number in literature[2-6].These substitutions was found to induce nanodefects which decreases the hole concentration and affect the normal and superconducting properties. The bulk (Bi,Pb):2223 material consists of grains weakly coupled at the grain boundaries by junctions or weak links. The macroscopic critical current density $J_{cJ}$ is limited by the intergranular vortex pinning force at the grain boundaries ($J_{cJ}$ is much smaller than the critical current density $J_{cG}$ inside the grain). The Sm and Yb addition on the bulk Bi:2223 is that the critical current density is seven times higher than that of pure sample [7, 15, 16]. It was fabricated a Bi:2223 cylindrical bulk current lead ($J_c$ higher than 670 A/cm$^2$) for use in cryocooler –cooled superconducting magnets [8].

---

[1] *Faculty of Physics, University Babes-Bolyai, Str. M. Kogalniceanu, No. 1, 400084 Cluj- Napoca, Romania*

[2] *Faculty of Materials Science and Engineering, Department of Physics, Technical University, Bd. Muncii 103-105, 400 641 Cluj-Napoca, Romania.*

* *Corresponding author: aurel.pop@phys.ubbcluj.ro*

Two peaks in the temperature dependence of the imaginary part $\chi$"(T) of the complex a.c. susceptibility reflecting the inter-and intragranular losses can be distinguished in bulk system (Bi,Pb)(Sr,Ba):2223 [9-11]. Intergranular Josephson vortices are assumed to sweep in and out of the weak links network, while Abrikosov vortices move in and out of the superconducting grains, both causing energy losses and giving direct contributions to the imaginary component of a.c. magnetic susceptibility.

In this paper we report the influence of the partial substitution for Ca to 4 f elements (Er, Lu) and Y on the critical current density, the intergrain pinning and the purity of samples in 2223 phase from a.c.susceptibility and X-ray diffraction measurements, respectively.

## EXPERIMENTAL

Polycrystalline samples with nominal composition $(Bi_{1.6}Pb_{0.4})(Sr_{1.8}Ba_{0.2})(Ca_{1-x}R_x)_2Cu_3O_y$ with R=Er,Lu,Y and $0\leq x \leq 0.02$ were prepared by the conventional solid-state reaction. Appropriate amounts of $Bi_2O_3$, PbO, $SrCO_3$, BaO, $CaCO_3$, $R_2O_3$ and CuO were mixed in agate mortar and calcined at 800 $^0$C for 36 hours. The calcinated powder was pressed into pellets and sintered at 845 $^0$C for 200 hours. The pellets were grinding, pressed and resintered for 60 hours at 850 $^0$C. Slabs with thickness 2d=3mm were cut from the sintered samples and used for a.c. susceptibility measurements.

The phase purity was determined by Brucker X-ray diffractometer with Cu-$K_\alpha$ radiation.

The real ($\chi^{'}$) and imaginary ($\chi^{''}$) parts of the a.c. susceptibility were simultaneously collected with a Lake Shore Model 7000 a.c. susceptometer in the temperature range from 77K to 110K, by using frequencies f and a.c. field amplitudes $H_{ac}$ situated in the ranges from 20 Hz to 1000Hz and from 20 A/m to 800 A/m respectively.

## RESULTS AND DISCUSSION

Fig.1 shows the X-ray diffraction pattern for x = 0.00 and x=0.02 Er samples. The results have shown that the sample with x=0.00 has a single (2223) phase.

With increasing x up to x=0.02, peaks corresponding to (2212) phase have bean observed.

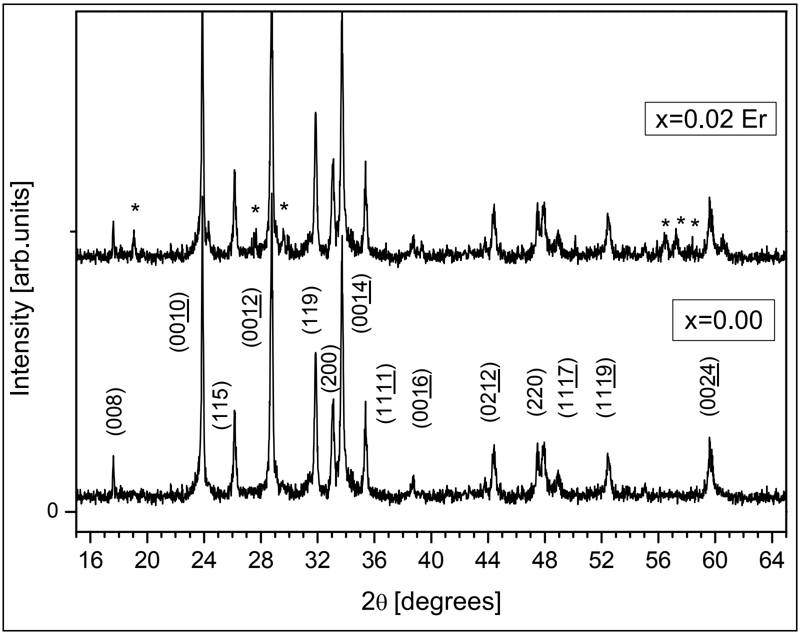

**Fig. 1.** Powder XRD pattern for $(Bi_{1.6}Pb_{0.4})(Sr_{1.8}Ba_{0,2})(Ca_{1-x}Er_x)_2Cu_3O_y$ (x=0.00,0.02 Er) with each peak indexed according to the crystallographic direction that produced it for 2223 phase. Stars show the 2212 phase.

Fig.2 show the temperature dependence of imaginary part $\chi''$ of a.c. susceptibility for x = 0.002 Er, Lu and Y samples in the presence of a d.c. field $H_d$ = 200A/m superposed over the a.c. field $H_{ac}$=400 A/m. $\chi''$(T) exhibit a single peak at temperature $T_p$ indicating a maximum hysteressis losses due to the motion of the intergranular (Josephson) vortices. With increasing the amplitude of alternative field $H_{ac}$, the $\chi''$ signal shifts to lower temperatures. This result shows that with increasing the amplitude of ac field the intergranular coupling decrease. The value of temperature $T_p$ for maximum of $\chi''$ is influenced different by the nature of 4f ions (Er and Lu) and Y respectively.

To estimate the intergranular critical current density $J_{cJ}$ from the$\chi''$ (T) data we used the magnetic formulas for isotropic superconductors of cylindrical geometry in the Bean critical state model [10]. At the temperature Tp, in the frame of the Bean model, the intergranular critical current density is $J_{cJ} = H_{ac} / R$, where R is the radius of cylindrical sample.

The temperature dependence of $J_{cJ}$(T) for Er doped samples are shown in fig.3.

The best fit of the data from Fig.3 is described by: $J_{cJ}(T)= J_{cJ}(0)\ (1-T/T_{p0})^2$

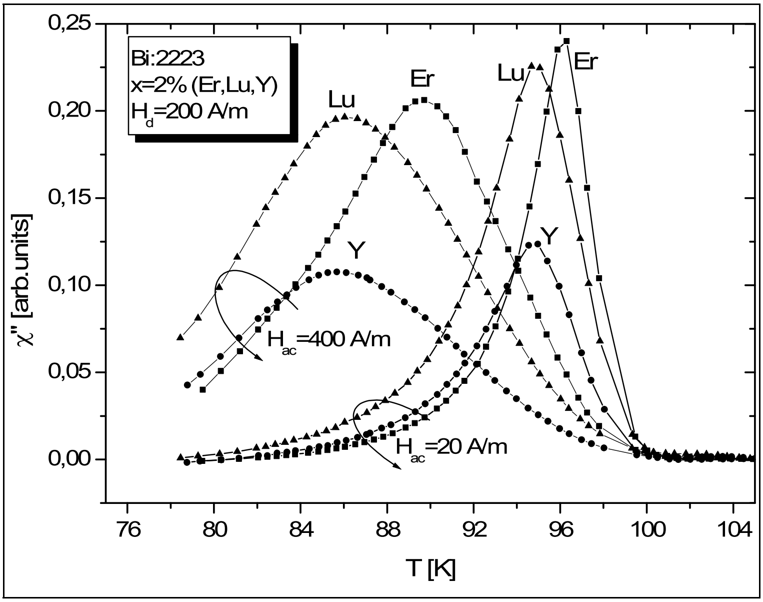

**Fig. 2.** The temperature dependence of the imaginary part$\chi''$ (T) of the complex susceptibility for x= 0.02 Er, Lu and Y for $H_{ac}$ =20 A/m and 400 A/m, respectively

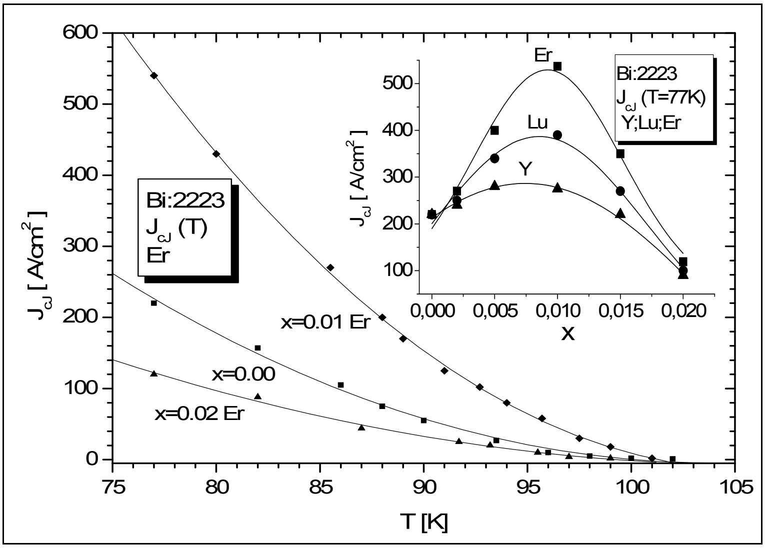

**Fig. 3.**The temperature dependence of intergranular current density for x=0.00; 0.01 and 0.02 Er doped samples. The critical current density at T=77K, $J_{cJ}$(T=77K), function of Er, Lu, Y content x is presented in the insert of figure 3.

This behavior suggest the presence of superconducting-normal – superconducting (SNS) junctions between the grains.

The fitting parameters $J_{cJ}(0)$, $T_{p0}$ and $J_{cJ}(77K)$ are presented in Table 1.

**Table 1.**The fitting parameters of $J_{cJ}(T)$ for Bi:2223 samples with Er.

| Sample Er | $J_{cJ}$ (0) [A/cm$^2$] | $T_{p0}$ [K] | $J_{cJ}$ (77K) [A/cm$^2$] |
|---|---|---|---|
| x=0.00 | 3417 | 105.2 | 220 |
| x=0.005 | 4243 | 105 | 400 |
| x=0.01 | 7428 | 105 | 535 |
| x=0.02 | 1694 | 104.9 | 120 |

The dependence of critical current density at 77K, $J_{cJ}(T=77K)$, as function of Er, Lu and Y content x is presented in the insert of figure 3. Solid lines are the fitting of data by the Gaussian function. As can be seen, $J_{cJ}(x)$ at 77K increases with increasing x up to a maximum around $x_c$ =0.009 Er, $x_c$ =0.005Lu and $x_c$ =0.007 Y, respectively. This new result suggest that a critical low concentration $x_c$ of Er, Lu and Y create pinnig centers at grain boundaries of monophase Bi:2223 samples, which lead to a maximum value of intergranular critical current density. Nd addition in Bi:2223 superconductor lead to the increase of flux pinning and $J_c$, respectively [14]. This behavior is related by the pinning centers created by Nd ions which substitute at the Ca positions.

## CONCLUSIONS

The influence of partial substitution of Ca by Er, Lu and Y on the structural and magnetic properties of (Bi,Pb):2223 bulk superconducting compound were investigated.

XRD shows that only traces of (2212) phase were found by increasing x up to 0.02.

The temperature $T_p$ for the of the imaginary part $\chi''$ (T) of the complex magnetic susceptibility performed at various field amplitudes is different influenced by the concentration of Er, Lu and Y.

The critical current density $J_c(x)$ shows a maximum value for x = $x_c$ near 0.01, and suggest the increase of pinning force at grain boundaries.

The value for the maximum current density at 77K, $J_{cJ}(T=77K)$, is influenced by the nature of ion which substitute Ca.

The temperature dependence of critical current density, $J_{cJ}(T)$, agree by the SNS behavior of grain boundaries.

## REFERENCES

[1] D. Ginsberg, Physical properties of HTS II, Ed.World Scientific (1990) p.511.

[2] N. Nanda Kishore, M. Muralidhar, V. Hari Babu, O. Pena, M. Sergent and F. Beniere, Physica **C204**, 299(1993).

[3] N. Nanda Kishore, S. Satyavathi, M. Muralidhar, O. Pena and V. Hari Babu, Physica **C2235-240**, 1521(1993).

[4] A.V. Pop, Modern Physics Letters **B14,** no.12, pag.447-453(2000).

[5] G. Ilonca, A.V. Pop, T.R. Yang, I.Gr. Deac, C. Lung, R. Stiufiuc, G. Stiufiuc, International Journal of Inorganic Materials **3**, Issue 7, 769-772 (2001).

[6] A. Sedky, Journal of Physics and Chemistry of Solids **70,** 483–488, (2009).

[7] V.G. Prabitha, A. Biju, R.G. Kumar, P.M. Sarun, A.P. Aloysius, U. Syamaprasad, Physica **C433**, 28-36(2005).

[8] M. Ishizuka, J. Sakuraba, Physica **C433**,173-181(2006).

[9] A.V. Pop, R. Deltour, A. Harabor, D. Ciurchea and G. Ilonca, Int. J. Mod. Phys. **B11**, 3461(1997).

[10] A.V. Pop, I.G. Deac, G. Ilonca, D. Ciurchea, V. Pop, Physica **B284-288**, pag. 284-288 (2000).

[11] A.V. Pop, D. Marconi, M. Topan, M. Pop, JOAM, Vol. 10, No. 7, p. 1866 – 1868, (2008).

[12] C.P. Bean, Phys.Rev.Lett.**8**,250(1962).

[13] I.G. Deac, A.V. Pop, G. Ilonca, R. Deltour, Physica **C 341-348**,1451(2000).

[14] R. P. Aloysius, P. Guruswamy and U. Syamaprasad, Supercond. Sci. Technol. **18**, 427(2005).

[15] D. Marconi, G. Stiufiuc and A V. Pop, J. Phys.: Conf. Ser. **153** 012022 (2009).

[16] A.V. Pop, D. Marconi and M. Pop, J. Phys.: Conf. Ser. **150** 052213(2009).

STUDIA UBB PHYSICA, LVI, 2, 2011

# ANNEALING INDUCED TEXTURAL PARTICULARITIES ON $TIO_2$-Au NANOCOMPOSITES

**G. MELINTE[1], M. BAIA[1], V. DANCIU[2], L. BAIA[1,*]**

**ABSTRACT.** Using the sol-gel synthesis method and the supercritical drying procedure we successfully prepared a highly porous $TiO_2$ aerogel – Au nanoparticles composite with open ended cylindrical pores and high specific surface area. $N_2$ sorption measurements were performed in order to understand the effect of thermal treatment on the morphological characteristics of the composite. The porosity and specific surface area significantly decreased (~80%) and the pores network became less connected because of the blocking effect. The thermal treatment also induced the narrowing of the pore size distribution and the entire withdraw of the sample microporosity. However, the heat treated composite remains relatively porous, with a narrow mesopores distribution and a good specific surface area that make them appropriate for further applications.

***Keywords:*** *aerogel, porosity, $N_2$ adsorption, pore distribution, hysteresis.*

## INTRODUCTION

Porous solids with complex internal void space geometries are frequently used in industry as supports for heterogeneous catalysts and as absorbents [1]. Aerogels are a class of highly porous materials that are used or show promise in many key products such as catalysts, chemical absorbents, thermal insulators, sensors, fuel storage, energy absorbers, and aero capacitors [2]. Titanium dioxide ($TiO_2$) aerogels combine the aerogels properties (extremely low densities and very high specific surface areas) [3] with those of $TiO_2$ (high photosensitivity, stability in aqueous media, non-toxic nature, recyclable and inexpensive) [4]. The large bandgap of $TiO_2$ (~3.2 eV) lies in the UV range of the electromagnetic spectrum. This allows only 5–8% of the sunlight that possesses the required energy useable for photocatalysis [5]. Tailoring the bandgap of $TiO_2$ to allow visible light photocatalysis may be accomplished by noble metal (Au, Ag, and Pt) nanoparticles doping [6, 7].

---

[1] *Babeş-Bolyai University, Faculty of Physics, M. Kogălniceanu 1, 400084, Cluj-Napoca, Romania*

[2] *Babeş-Bolyai University, Faculty of Chemistry and Chemical Engineering, Arany Janos 11, 400028, Cluj-Napoca, Romania.* [*] *Corresponding author. E-mail: lucian.baia@phys.ubbcluj.ro*

Gold was widely believed to be a catalytically inactive material for a long time, but this situation changed dramatically with the discovery of the catalytic activity of gold nanoparticles (AuNPs) [8]. AuNPs catalysts have attracted wide attention because of their wide range of applications such as CO oxidation, epoxidation of propylene, water–gas-shift reaction, hydrogenation of unsaturated hydrocarbons, and liquid phase selective oxidation [9]. AuNPs supported on $TiO_2$ aerogels show a high activity in many catalytic processes [10, 11], including the oxidation of CO and NO and the destruction of $SO_2$ [12, 13].

The effective properties (diffusion and reaction properties) of $TiO_2$ aerogels - AuNPs composites are highly dependent on their internal pore structure. Therefore, in order to predict the transport and reaction behavior of these porous solids, the evaluation of the morphological parameters like specific surface area, pore size distribution, pore topology, and pore volume is required [14]. Thus, the purpose of this study was to determine the effect of the thermal treatment on the textural properties (specific surface area, pore size and pore size distribution, pore volume, etc.) of a porous composite based on $TiO_2$ aerogel and AuNPs.

## 1. EXPERIMENTAL

### 1.1. Samples preparation

$TiO_2$ gel was prepared by the one-step sol-gel procedure using titanium isopropoxide, nitric acid, ethanol and water with the 1/0.08/21/3.675 molar ratios. The gel was allowed to age for 21 days. To obtain AuNPs with the mean size of 16 nm the chloroauric acid solution was reduced with sodium citrate. The aged gel was immersed in AuNPs colloidal solution for 3 days. After the immersion the gel was washed with ethanol and maintained in absolute ethanol for 12 hours. Then the gel containing ~16 nm AuNPs was supercritical dried with liquid $CO_2$. The obtained composite will be further denoted as **C**.

The composite **C** was heat treated at 450ºC (30 min) using a two step procedure in order to preserve its porosity: with 1ºC/min up to 140ºC and with 4ºC/min up to 450ºC. The heat treated composite will be further denoted as **C_ht.**

### 1.2. Samples characterization

The nitrogen sorption measurements were performed using a Sorptomatic 1990 equipment. The Brunauer, Emmett and Teller (BET) - 3 parameters model [15] was used to determine the specific surface area. The mean mesopores sizes (MMSs), pore size distributions (PSDs) and cumulative mesopores volumes (CMVs) were find out using the Barrett, Joyner and Halenda (BJH) model [16] applied on both the adsorption and desorption data. The mean micropores sizes and cumulative micropores volumes were establish using the HK model developed by Horvath and Kowazoe [17].

## 2. Results and discussion

The adsorption and desorption isotherms of both as prepared and heat treated $TiO_2$ aerogel – AuNPs composites are presented in **Fig. 1**. Both composites exhibit type IV adsorption isotherms and type H1 hysteresis loops. This type of hysteresis loop is usually associated with open ended tubular pores, but as a consequence of broad variations in pore shape of the mesopore systems, the "tubular" character should be treated with caution. One should note that both hystereses present some features of the H2 type, which prove the interconnectivity of the pores. Moreover, it can be observed that the desorption isotherm of the **C_ht** sample has a horizontal interval between 0.88 and 0.98 relative pressure. This behavior reveals the effect of the thermal treatment on the composite pores topology, the pores being transformed from open ended pores in blocked pores with ink-bottle shape [18]. The horizontal characteristic of the desorption branch is induced by the percolation phenomenon, which can be associated with the decrease of the pore network connectivity in the heat treated composite. The decreasing of the pores connectivity can be caused by a cumulated effect of the pore network shrinkage and the aggregation of AuNPs inside the $TiO_2$ network during the thermal treatment.

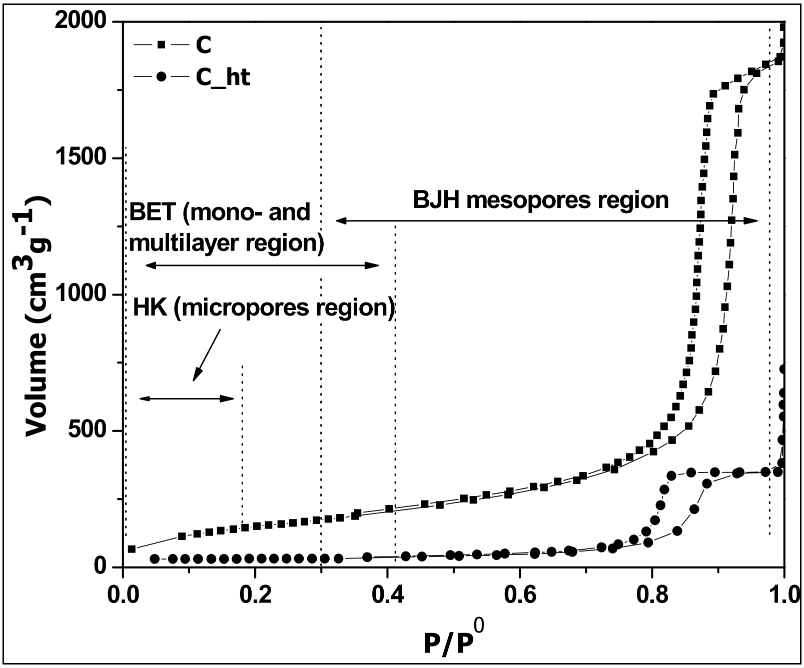

**Fig. 1.** $N_2$ sorption hystereses of the as prepared (**C**) and heat treated (**C_ht**) $TiO_2$ aerogel – AuNPs composites.

The mono- and multilayer region, between 0.05 and 0.4 relative pressure, is used to establish the specific surface area of the composites by applying the BET model. As can be observed (**Fig. 1**) the **C** composite adsorbed in this region a significant amount of nitrogen gas, while for the **C_ht** sample the region is almost horizontal. **Table 1** present the results obtained by applying the BET model on the adsorption data, whereas the fitting procedure is shown in **Fig. 2**. The heat treatment of the composite leads to the decrease of the surface area with 75%, from 550 $m^2g^{-1}$ (sample **C**) to 135 $m^2g^{-1}$ (sample **C_ht**). The $C_{BET}$ parameter, which is also derived from BET measurements, represents the relative strength of adsorption to the surface and it is a useful tool for a qualitative evaluation of the composites hydrophobicity. Smaller $C_{BET}$ value means larger hydrophobicity [20]. As can be seen from **Table 1** the heat treatment induces a major decrease of the sample hydrophobicity. This can be associated with the elimination of the organic components during the thermal treatment from both $TiO_2$ aerogel and AuNPs surface.

**Table 1**. Textural parameters of the as prepared (**C**) and heat treated (**C_ht**) $TiO_2$ aerogel – AuNPs composites.

| Sample | BET surface area ($m^2g^{-1}$) | Mean pore diameter$^{BJH}$ (adsorption) (nm) | Cumulative mesopores volume$^{BJH}$ (adsorption) ($cm^3g^{-1}$) | Mean pore diameter$^{BJH}$ (desorption) (nm) | Cumulative mesopores volume$^{BJH}$ (desorption) ($cm^3g^{-1}$) | Mean micropores diameter$^{HK}$ (nm) | Cumulative micropores volume$^{HK}$ ($cm^3g^{-1}$) |
|---|---|---|---|---|---|---|---|
| **C** | **550<br>(62*)** | **24** | **2.70** | **16** | **2.91** | **1** | **0.21** |
| **C_ht** | **135<br>(337*)** | **15** | **0.57** | **11** | **0.61** | **-** | **-** |

*$C_{BET}$ *parameter*

Fig. 3. presents the differential pore size distributions (dPSD) of the composites obtained from both adsorption **(a)** and desorption branch **(b)** by applying the BJH model and considering a cylindrical pore shape**.** The evaluation of the PSDs from the adsorption data has the advantage that the adsorption phenomenon comprise a pure thermodynamic contribution, while the desorption phenomenon contains not only a thermodynamic effect, but also is influenced by the pore network connectivity (percolation phenomenon). Nevertheless, during the desorption a more defined meniscus of condensed nitrogen exists, which can be associated whith the pore opening. The dPSDs determined from adsorption data shows that the composite **C** has a broad distribution with the pores size between 2 and 35 nm and the mean mesopore diameter (MMD) of 24 nm. After the thermal treatment the distribution becomes narrow with pores size between 5 and 18 nm and the MMD of 15 nm.

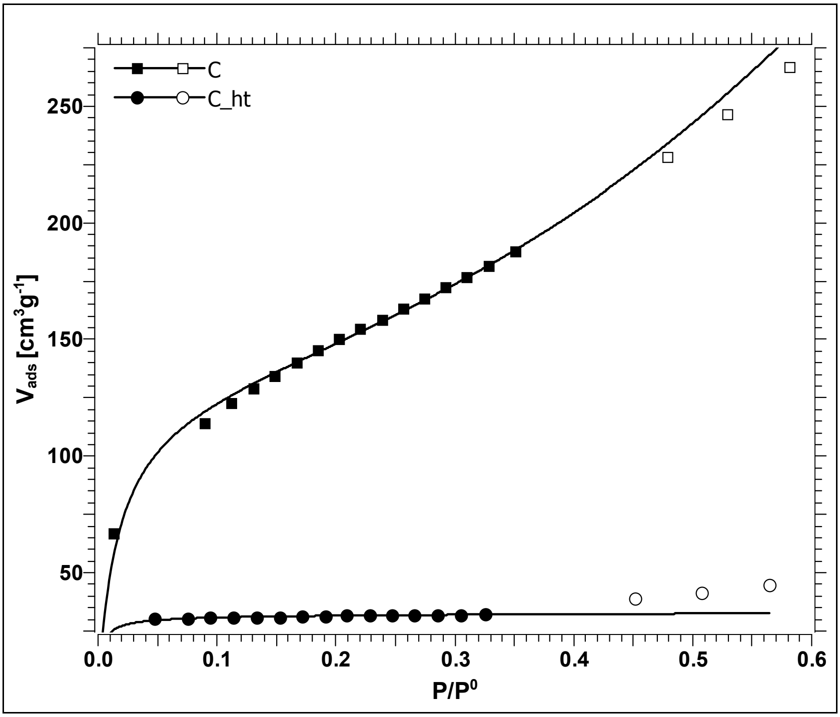

**Fig. 2.** Fitting procedure of the adsorption data in BET 3-parameter model for the as prepared (**C**) and heat treated (**C_ht**) $TiO_2$ aerogel – AuNPs composites.

The desorption data reveal a similar behavior for the dPSDs, after the heat treatment the distribution becoming narrower. However, the MMDs determined from the desorption branch are smaller that those evaluated from adsorption data, 16 nm and 11 nm for **C** and **C_ht** sample, respectively. Moreover, the desorption dPSDs are narrower than the adsorption ones, but this can be an effect of the percolation phenomenon.

Fig. 4. shows the cumulative pore size distributions (cPSDs) of the investigated samples determined from both adsorption and desorption data, by using the BJH model. The values of the cumulative pore volumes (CPVs) are presented in **Table 1** and are approximately the same for both adsorption and desorption data with a slight increase for the desorption branch. The percent of the volume loss during the heat treatment is 79 % for both the adsorption and desorption data. One should note, that the BJH model takes into consideration only the mesopores volume. The micropore cumulative volume is also presented in **Table 1** and was determined by using HK model.

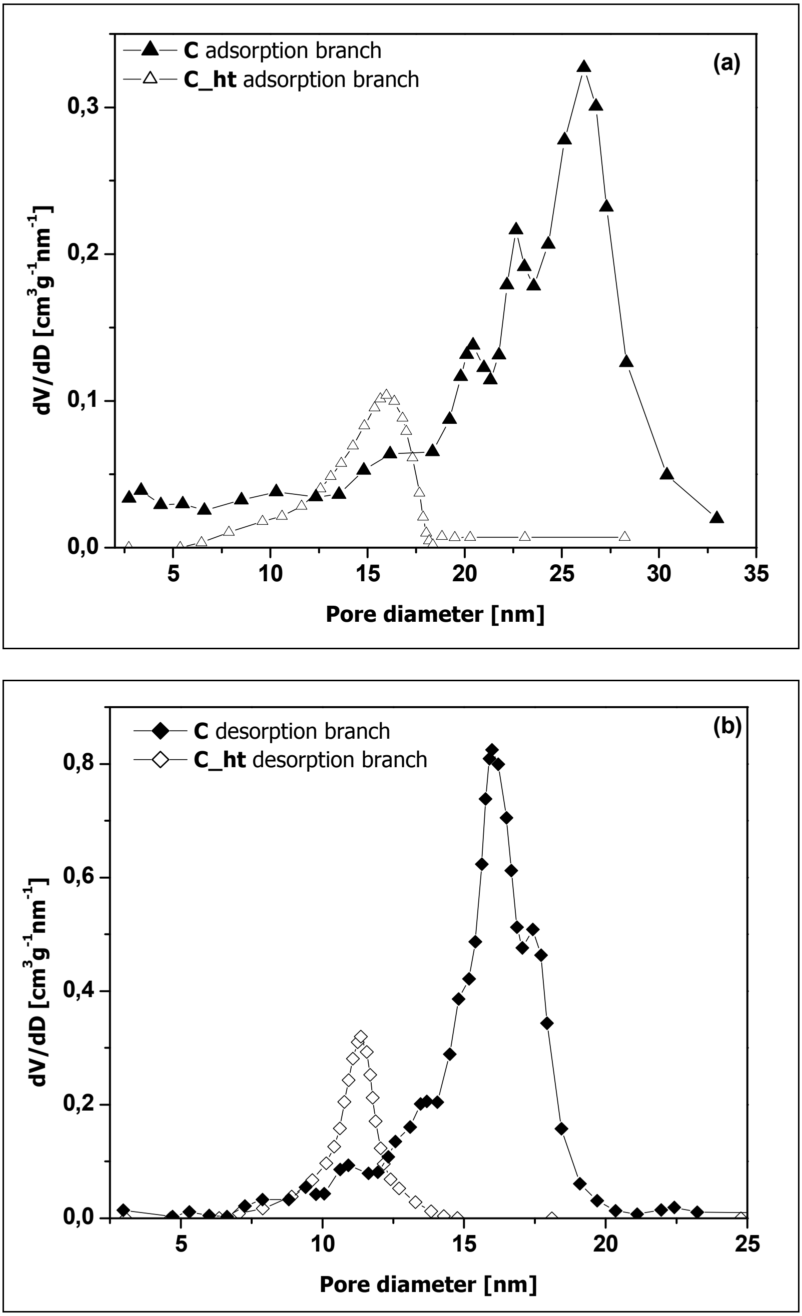

**Fig. 3.** Differential pore size distribution (dPSDs) obtained from adsorption (**a**) and desorption (**b**) data by applying the BJH model.

As can be observed the heat treatment causes the disappearance of the entire microporosity, the model applied being unable to indentify the micropores in the heat treated sample. It is possible that the micropores with a median diameter of 1 nm to collapse during the heat treatment, and thus to become smaller. It is well known that the nitrogen measurements can't detect pores with diameter smaller than 0.7 nm [20]. The total percent of volume loss during the heat treatment (~80%) shows that the porosity of the composite is considerably decreasing during the thermal treatment. However, one should emphasize that despite the morphological changes caused by the applied thermal treatment the composite remains relatively porous, with a narrow mesopores distribution and a good specific surface area.

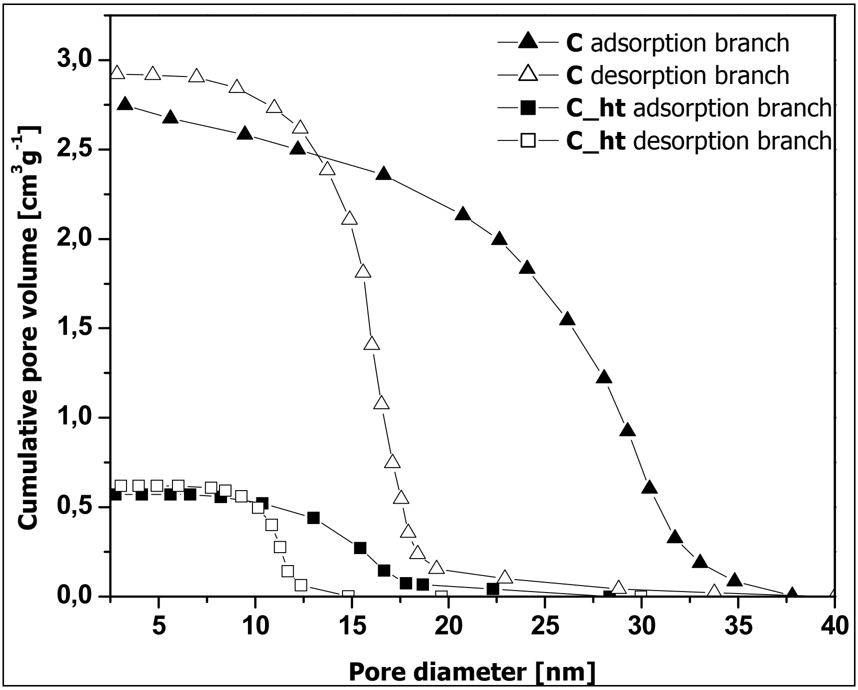

**Fig. 4.** Cumulative pore size distributions (cPSDs) obtained from adsorption and desorption data by applying the BJH model.

## 3. CONCLUSIONS

Throughout of this work we had shown that a highly porous $TiO_2$ aerogel – AuNPs composite with open ended cylindrical pores and high specific surface area was obtained. The heat treatment induced substantial changes in the textural properties of the composite. The porosity and specific surface area drastically decreased (~80%) and the pores network became less connected because of the blocking effect. The thermal treatment also determined the narrowing of the pore size distribution and the entire withdraw of the sample microporosity. Despite this significant morphological changes the heat treated composite remains relatively porous, with a narrow mesopores distribution and a good specific surface area that make them appropriate for further applications.

## ACKNOWLEDGMENTS

This work was supported by CNCSIS-UEFISCSU, project number PN II-RU-TE 81/2010.

## REFERENCES

[1] S.P. Rigby, M.J. Watt-Smith, R.S. Fletcher, J. Catal., 227 (1), 68-76, (**2004**).

[2] K.A. Sunol, S.G. Sunol, Dekker Encyclopedia of Nanoscience and Nanotechnology, Ed. J.A. Schwarz, C.I. Contescu, CRC Press, (**2004)**.

[3] N. Hüsing, U. Schubert, Angew. Chem. Int., Ed. 37, 22-45, (**1998**).

[4] D. Beydoun, R. Amal, G. Low, S. McEvoy, J. Nanopart. Res., 1, 439-58, (**1999**).

[5] S. Buzby, S.I. Shah, Dekker Encyclopedia of Nanoscience and Nanotechnology, Ed. J. A. Schwarz, C. I. Contescu, CRC Press, (**2004)**.

[6] M.A. Barakat, H. Schaeffer, G. Hayes,S.I. Shah, Appl. Catal. B, 57, 23, (**2004**).

[7] W. Li, Y. Wang, H. Lin, et al., Appl. Phys. Lett., 83, 4143, (**2003**).

[8] J.A. Rodriguez, Dekker Encyclopedia of Nanoscience and Nanotechnology, Ed. J.A. Schwarz, C.I. Contescu, CRC Press, **2004**.

[9] M. Haruta, Chem. Rec., 3 (2), 75–87, (**2003**).

[10] L. Baia, L. Diamandescu, L. Barbu-Tudoran, A. Peter, G. Melinte, V. Danciu, M. Baia, J. Alloy Compd., 509, 2672-678, (**2011**).

[11] M. Baia, G. Melinte, L. Barbu-Tudoran, L. Diamandescu, V. Iancu, V. Cosoveanu, V. Danciu, L. Baia, J. Phys.: Conf. Ser. 304 (1), 2059, (**2011**).

[12] M. Haruta, Catal. Today, 36 (1), 153, (**1997**).

[13] J.A. Rodriguez, G. Liu, T. Jirsak, J. Hrbek, Z. Chang, J, Dvorak, A. Maiti, Am. Chem. Soc., 124 (18), 5242, (**2002**).

[14] A.B. Jarzi-Bski, J.W. Lorenc, Chem. Eng. Sci., 50(2) 357-360, (**1995**).

[15] S. Brunauer, P.H. Emmett, E. Teller, J. Am. Chem. Soc., 60, 309, (**1938**).

[16] E.P. Barrett, L.G. Joyner, P.P. Halenda, J. Am. Chem. Soc., 73, 373-380 (**1951**).

[17] G. Horvath, K. Kawazoe, J. Chem. Eng. Japan, 16 (6) 470-475 (**1983**).

[18] J. Rouquerol, F. Rouquerol, K. Sing, Adsorption by Powders and Porous Solids Principles, Methodology and Applications, Academic Press (1998).

[19] M.M. Gerona, Silica aerogels: synthesis and characterization, PhD thesis, Barcelona University, (**2002**).

[20] M. Thommes, Chem. Ing. Tech., 82 (7), 1059-1073, (**2010**).

STUDIA UBB PHYSICA, LVI, 2, 2011

# DETERMINING COEFFICIENTS OF THE $\alpha\vec{v}$ MODEL USING MATLAB SIMULATION OF TRANSVERSAL LOOP OSCILLATIONS WITH RANDOM ELEMENTS

G. MOCANU[1,*], D. MOGA[2], A. MARCU[1]

**ABSTRACT** Our previous work on the theoretical $\alpha\vec{v}$ model regarding transversal oscillations of coronal loops can be tested using a Matlab simulation. The simulation consists of a trajectory of the apex of the loop, with random elements, which mimics the observed pattern displayed by coronal oscillating loops. To this motion, a Kalman filter is applied and a connection between the Kalman filter parameters and the parameters of the $\alpha\vec{v}$ model is discussed. Such a connection is not obvious at this point, but it is nonetheless clear that a Kalman filtering technique may be used in applications designed for real time prediction of coronal loop dynamics.

***Keywords:*** *Solar corona, transversal oscillations, Kalman filter.*

## INTRODUCTION

Technical developments in sensors aimed at the Sun have led to very interesting discoveries and subsequently posed difficult problems for theoreticians. One specific problem concerns the observed rapid damping of transversal oscillations of coronal loops (Aschwanden et al., 1999, Nakariakov et al., 1999). Such oscillations appear after an energetic event, such as a flare and decay very fast, on timescales of just a few minutes. This damping cannot be explained by any theory based on classical viscosity and theoreticians are currently undergoing serious efforts in order to explain and model this behavior. Several theoretical models were proposed to explain the excitation and damping of oscillations, including viscous damping with anomalous low Reynolds number (Nakariakov et al., 1999), damping due to phase mixing (Roberts, 2000), destabilization of magnetic sources in the photosphere and damping due to subsequent relaxation of magnetic field lines (Schrijver and Brown, 2000), damping due to foot point leakage of Alfv´en waves (DePontieu et al., 2001), damping due to resonant absorption (Ruderman and Roberts, 2002), viscous damping due sub resolution scales (Ofman, 2005), excitation

---

[1] *Babes-Bolyai University, Faculty of Physics, 1 Kogalniceanu str., 400084 Cluj-Napoca, Romania.*
[*] *corresponding author e-mail: gabimocanu_ro@yahoo.com*
[2] *Technical University, 15 Daicoviciu str., Cluj-Napoca, Romania*

and damping due to dispersive nature of the magnetized medium inside and outside the loop (Terradas et al., 2005), excitation due to vortex shedding (Nakariakov et al., 2009). The common aspects of these models are the association of a flare event with the excitation and the identification of the oscillation mode as the fast kink mode of a magnetic flux tube (Nakariakov et al., 1999).

We proposed a model that accounts for this observed behavior, (Marcu and Mocanu, 2010), (Mocanu and Marcu, 2010), (Mocanu and Marcu, 2011) but the physical mechanism behind this ”effective” viscosity is not yet clear.

However, since this particular modeling appears to agree very well with observational data we propose that the parameters of the theoretical model may be directly (i.e. during real time observations) linked with parameters characteristic to a Kalman filter. The Kalman filter is a tool specific to applications that track the motion of objects with a large size, such as an aircraft.

The paper is organized as follows: the next section reviews the theoretical model describing the excitation, oscillation and attenuation of transversal motion of coronal loops. Also, a review of the basic assumptions and mathematical implementation of the Kalman filter is presented. Section 3.1 contains a detailed description of the simulation, including the assumptions made. The connection between plasma dynamics and Kalman filter parameters is found and explained in Section 3.2. Conclusions follow in Section 4.

## THEORETICAL REVIEW OF ISSUES INVOLVED

### *Review of the $\alpha\vec{v}$ model*

The configuration under analysis (Fig. 1, Mocanu and Marcu, 2011) consists of a magnetic slab approximating the line tied coronal loop. In a coordinate system fixed to the loop, the structure is aligned with its constant equilibrium magnetic field $\vec{B}_0$ and the $\hat{z}$ axis. The internal and external magnetic fields are of the same order of magnitude and if they are not parallel, they are at least coplanar in the *yOz* plane. The shock wave, moving parallel to the $\hat{x}$ axis, hits the loop and exerts a force $\vec{F}_{sh}$. The response of the external medium to the oscillations of the loop is given through a force of the form $-\alpha\vec{v}$ where $\alpha$ is a constant and $\vec{v}$ is the velocity of the oscillating loop. The linear MHD approximation in a $\beta \to 0$ medium is used, where the internal medium has an equilibrium density stratification of the shape $\rho_0(z) = \rho_{00} f_n(z)$ with $f_n(z) = e^{nz/L}$ where the parameter $n$ stands for a variable scale height along the loop. The force exerted by the shock wave against the loop is described analytically as follows

$$\vec{F}_{sh}(z,t) = F(z,t)\hat{x}\,,$$
$$F(z,t) = F_0 H(\tau - t)\frac{1}{2a\sqrt{\pi}}\exp\left\{-(z-z_0)^2/a^2\right\},$$

where $F_0$ is the energy per appropriate length scale of the fast MHD shock wave, given as $F_0 = \rho_e c\left(v_{Ae}^2 + c_{Se}^2\right)/2a$, $c_{Se}^2$ and $v_{Ae}^2$ are the sound speed and the Alfven speed in the external medium, $c$ is a constant used to determine the amount of energy needed to obtain the observed displacements, $\tau$ is the temporal duration of the interaction, $a$ is the width of the spatial shock and $z_0$ is the impact point along the the loop. Other variables are taken as $\rho_e = d\rho_{00}$, $c_{Se} = 10^5\,m/s$, $v_{Ae} = v_{A0}\sqrt{1/d}$ with $d = 0.1$ being the density filling factor of the loop for coronal conditions.

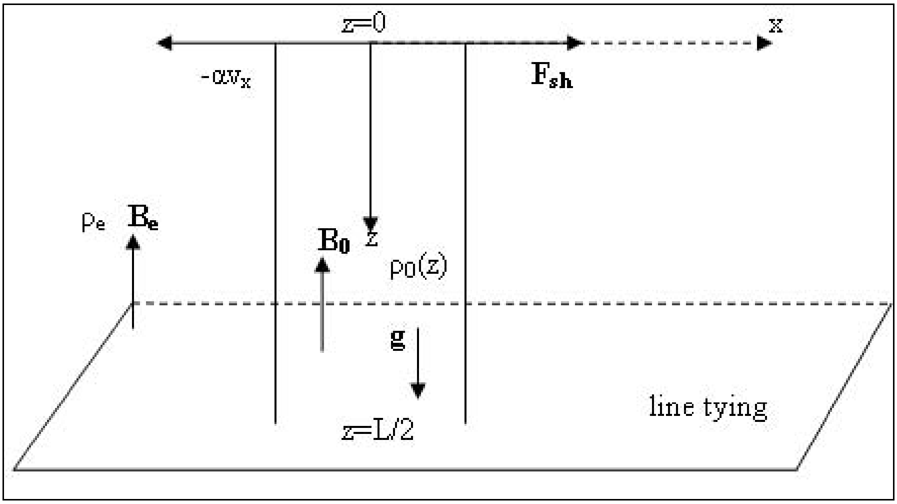

**Fig. 1.** Configuration of the model

The equation of motion can be written for the transversal component of the velocity as

$$v_{A0}^2\frac{d^2\hat{v}_x}{dx^2} + \hat{v}_x\left[f(z)\left(\omega_R^2 - \omega_I^2 + \omega_R\omega_z + g\frac{\omega_R}{\omega_z}k_z\right) - \frac{\omega_R}{\omega_z}g\frac{df}{dz}\right]$$
$$= -\frac{1}{\rho_{00}}\frac{\partial F_{sh}}{\partial t}e^{i\omega_I t}\cos(\omega_R t)$$

where it was assumed that the vertical motion has spectral components $\omega_z$ and $k_z$ and that Fourier decomposition for the transversal motion is possible and is given by $v_x(z,t) = \hat{v}_x(z)e^{i\omega t}$ where, $\omega = \omega_R + i\omega_I$.

The free parameters of the theoretical model are $c$, the energy transmission coefficient, $\omega_I$, the imaginary frequency describing the damping phenomenon of the oscillations and $n$, a parameter describing the importance of the scale height along the loop. These are the parameters that we shall try to correlate with the parameters of a Kalman filter applied to loop oscillations.

### *Review of Kalman filtering*

A motion model is a theoretical structure used to model the dynamics of a moving object. More clearly stated, a motion model assumes a fixed relation between the current position of the object and its past position, velocity and acceleration.

The motion model presented here (Moga et al., 2009) is commonly used for the development of *one dimensional* trackers for estimating position, velocity and acceleration of an aircraft or similar space vehicle moving with constant acceleration perturbed by a zero mean plant noise which accounts for maneuvers and/or other random factors. The positions are sampled uniformly at intervals of $T_s$ seconds and all the measurements are noisy. Two key aspects will be considered: the movement (dynamic model) and the measurement (measurement model).

### Friedland Dynamic Model

Each position coordinate of the object is assumed to be describe by the following equations of motion:

$$x_{n+1} = x_n + \dot{x}_n T_s + \frac{1}{2} a_n T_s^2$$

$$\dot{x}_{n+1} = \dot{x}_n + a_n T_s$$

where: $x_n$ is the position of the object at scan $n$, $\dot{x}_n$ is the object velocity at scan $n$, $T_s$ is the interval between observations (sampling time) and $a$ is the vehicle acceleration at time-step $n$. In this particular motion model, the acceleration is assumed to be a noise characteristic to the process, with zero mean and constant variance ($\sigma_a^2$) and also uncorrelated with its values at other intervals, i.e. the noise has no memory of previous motion. It satisfies the following statistical properties

$$E\{a_n\} = 0, E\{a_n^2\} = \sigma_a^2 = const., \forall n$$
$$E\{a_n a_k\} = 0, \forall n \neq k$$

where $E\{\ \}$ is an operator with the physical meaning of the mean value of a random variable.

For future reference, it is clearer to put equations (1) and (2) in matrix form

$$X_{n+1} = F \cdot X_n + G \cdot a_n \text{, with } X_n = \begin{pmatrix} x_n \\ \dot{x}_n \end{pmatrix},\ F = \begin{pmatrix} 1 & T_s \\ 0 & 1 \end{pmatrix},\ G = \begin{pmatrix} T_s^2/2 \\ T_s \end{pmatrix}$$

where $X_n$ is the object's state vector, $F$ is the transition matrix and $G$ is the input distribution matrix.

**Measurement Equation**

The measurement equation may be written as follows:
$x_m(n) = H \cdot X_n + v_n$, where $x_m(n)$ is the measured position at scan $n$, $v_n$ is the random noise corrupting the measurement at scan $n$, $X_n$ is the true position at scan $n$ and $H = (0 \quad 1)$ is the measurement matrix. Real data acquisition is more or less noisy and this must be taken into consideration. Thus, $v_n$ is introduced to stand for uncertainties inherent to real measurements, such as noise introduced by the sensors. The statistical properties of the measurement noise are assumed to be the same as the ones of the acceleration, $a_n$:

$$E\{v_n\} = 0, E\{v_n^2\} = \sigma_x^2 = const. \equiv R, \forall n,$$
$$E\{v_n v_k\} = 0, \forall n \neq k.$$

Equation (8) states that whatever the instrument records at time step $n$ is related to the real data $X_n$ by a measurement matrix $H$ and corrupted by a measurement noise $v_n$.

**Filtering Equations**

Commonly, it is desirable to obtain an optimum state estimate for the $n^{th}$ sample based on $n$ measurements. It is also of interest to obtain a prediction of the state at moment $n+1$. With this in mind, the filtering equations were implemented as follows:

**Initialization**

The state vector and the error covariance matrix ($\widetilde{P}_0$, see equation (16) below for a formal definition): $\widetilde{P}_0, \widetilde{X}_0$ are initialized.

**Measurement Update**

Compute the Kalman gain:

$$K_n = \tilde{P}_n \cdot H^T \cdot \left(H \cdot \tilde{P}_n \cdot H^T + R\right)^{-1}$$

Update the optimal estimate of the state vector after the measurement, $x_m(n)$ is processed:

$$\hat{X}_n = \tilde{X}_n + K_n \cdot \left(Z - H \cdot \tilde{X}_n\right)$$

Update the error covariance matrix:

$$\hat{P}_n = \left(I - K_n \cdot H\right) \cdot \tilde{P}_n$$

**Time Update**

Predict the state vector:

$$\tilde{X}_{n+1} = F \cdot \hat{X}_n .$$

Predict the error covariance matrix:

$$\tilde{P}_{n+1} = F \cdot \hat{P}_n \cdot F^T + G \cdot Q \cdot G^T ,$$

where $Q = \sigma_a^2$ is the process noise covariance.

For a fixed sampling time the position error can be kept below the sensor error (Moga et al., 2009) if the following relationship between process noise, measurement noise and sampling time is obeyed:

$$\sigma_a T_s^2 < 0.24\sigma_x .$$

## THE SIMULATION

### *The codes and motivation of choices*

The codes are written to find/demonstrate the link between Kalman filtering and oscillation parameters based on observations.

The idea is to apply Kalman filtering to loop dynamics. A real time application would contain the following steps:

1. point an instrument towards the area of interest, namely a coronal loop. The instrument will take frames of the dynamics in that region every $T_s$ seconds.

2. at $n = 0, (t = 0)$ decide which is the region you wish to follow. For loop dynamics this is the apex of the loop and it may be identified as the brightest region in the image (as in Fig. 2).

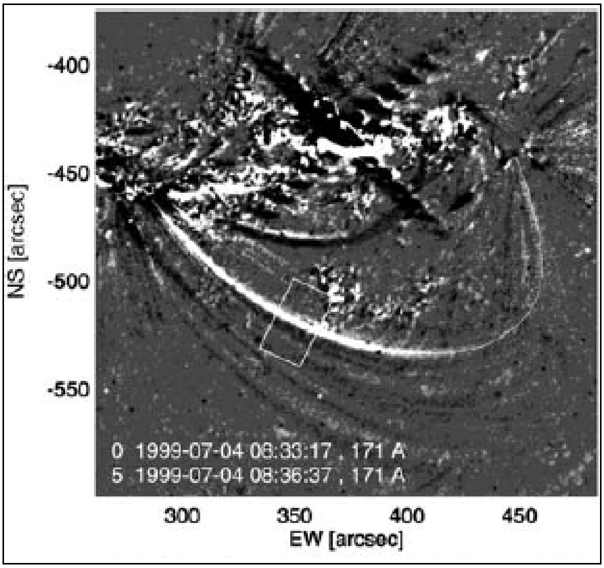

**Fig. 2.** An instance of the observed motion (Aschwanden et al., 1999).

3. for every $n$ (or equivalently at every $t = n \cdot T_s$) measure the position of the region and **predict** the position at $n+1$. This prediction is done based on implementation of the algorithm described in the previous section and on the ability of the Kalman filter to minimize its prediction errors.

However, available observations make it impossible for us to use such an algorithm because a combination between the time cadence ($T_s = 0.74s$) available and the rapid damping of the transversal oscillation leads to insufficiently large input data vectors. Instead, typical loop dynamics was simulated. A Matlab routine was written to simulate the motion of the apex in a damped transversal displacement. This was done by having a square moving on a stochastically determined trajectory and identified and tracked as the object that has a brightness larger than a gray threshold. The stochasticity is included to mimic real measurements when uncertainties are present.

Consider that at step $n$ a frame is taken of the loop. The frame is analyzed and the $x(n), y(n)$ coordinates of the square representing the apex are taken. The vector $Z(n) = [x(n) \quad y(n)]$ is the measurement vector. The process measured includes an intrinsic noise component, with a $\sigma_a$ covariance, to be fixed by the user. The noise introduced by the sensors in the measurement apparatus must also be included, with covariance $\sigma_x$, to be fixed by the user. At this point, $F, G, H, R, Q$ and $Z(n)$ are known. Two updates can be made:

1. Measurement update: based on the measured position $Z(n)$ and the predicted position $\tilde{X}_n$ (predicted at time step $n-1$), an optimum estimate of the position is made, $\hat{X}_n$. Each update has an error covariance matrix associated with it and, similarly to the position, an optimum estimate of the error covariance is made, denoted by $\hat{P}(n)$.

2. Time update: based on the optimum estimate of the position, $\hat{X}(n)$ the prediction for position at time step $n+1$ is made, $\tilde{X}(n+1)$. The error covariance matrix for the $n+1$ time step is also predicted $\tilde{P}(n+1)$.

Two sets of independent routines are needed:

### Simulation of Damped Motion Routines

These routines generate frames where a square changes its position similar to a damped oscillation, with stochasticity included in the trajectory of the square (a short excerpt of how this is done is given in Listing 1). The end result can be seen in the upper part of Figs. 3, 4, 5, 6.

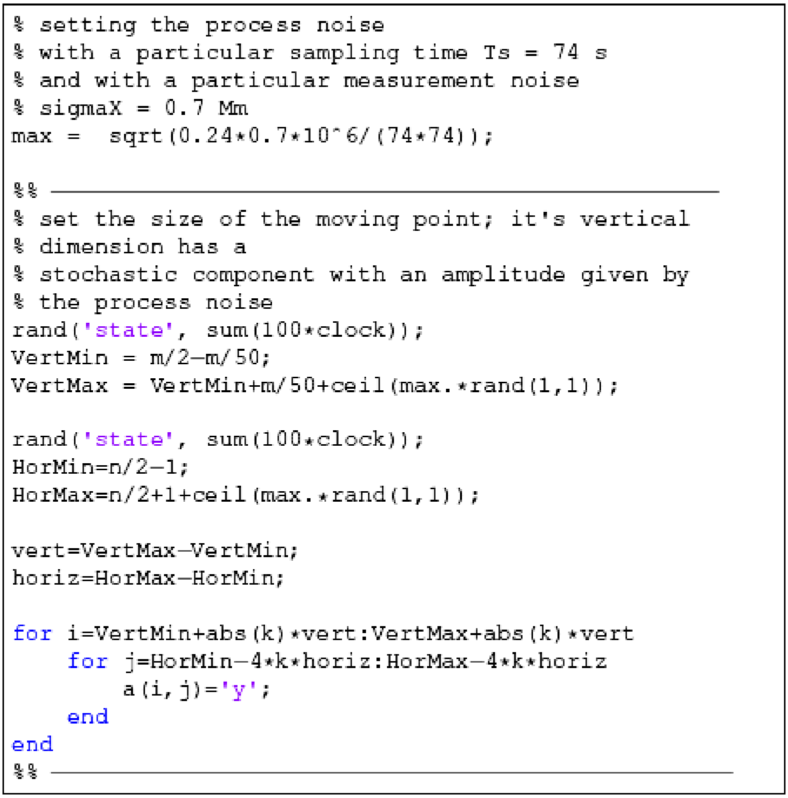

```
% setting the process noise
% with a particular sampling time Ts = 74 s
% and with a particular measurement noise
% sigmaX = 0.7 Mm
max =  sqrt(0.24*0.7*10^6/(74*74));

%%
% set the size of the moving point; it's vertical
% dimension has a
% stochastic component with an amplitude given by
% the process noise
rand('state', sum(100*clock));
VertMin = m/2-m/50;
VertMax = VertMin+m/50+ceil(max.*rand(1,1));

rand('state', sum(100*clock));
HorMin=n/2-1;
HorMax=n/2+1+ceil(max.*rand(1,1));

vert=VertMax-VertMin;
horiz=HorMax-HorMin;

for i=VertMin+abs(k)*vert:VertMax+abs(k)*vert
    for j=HorMin-4*k*horiz:HorMax-4*k*horiz
        a(i,j)='y';
    end
end
%%
```

**Listing 1.** Simulation of the damped motion

### Measurement and Prediction Routines

Taking as an input frames from the previously discussed routines, the following routines use position measurements to estimate and predict the dynamics of the square. They may be applied to real data obtained from solar observations when a suitable input data vector can be extracted from observations.

1. routine that extracts the $(x, y)$ coordinates of the center of mass of an object from an uploaded image. The assumption is made that the image contains only one object that has a brightness larger than a given threshold (see the lower side of Figs. 3, 4, 5, 6).

2. routine that for a given time step performs all the matrix calculations for the measurement and time updates (effectively implements the Kalman filter, see Figs. 7, 8). It outputs the predicted vs. real motion and the error of the filter as a function of the motion step.

Acquisition and interpretation of observational data is complex and the road from image capturing to physical insight is long. In the particular case of the oscillations discussed here, after acquisition the images have been co-aligned by cross correlation to correct for solar rotation and spacecraft pointing jitter (Aschwanden et al., 1999) an input signal is obtained, consisting of an image. The measurement error is due to diffusive boundary of the object and a systematic error is introduced by the background time variability. We consider these effects to be included in the measurement covariance error and we set the numerical value of $\sigma_x$ to be equal to the length of two TRACE pixels (one TRACE pixels maps 350 km at the level of the Solar corona). The sampling time is given by the instrument's temporal cadence and is $T_s = 74s$. Relation (19) was considered to hold for this specific case and was used in order to determine the process noise covariance.

We ran the simulation in order to estimate and predict the dynamics of the square. The output of the experiment is presented graphically, for the onset of the motion, in Fig. 3 for the left hand motion and in Fig. 4 for the right hand motion.

It can be seen from the figures referred above that the filter behaves well when the input vector is large enough. If we apply the same algorithm, but when the motion is close to extinction, the behavior is not so trustworthy (see Figs. 5 and 6), as the input data vector is smaller and the filter does not have time to "learn".

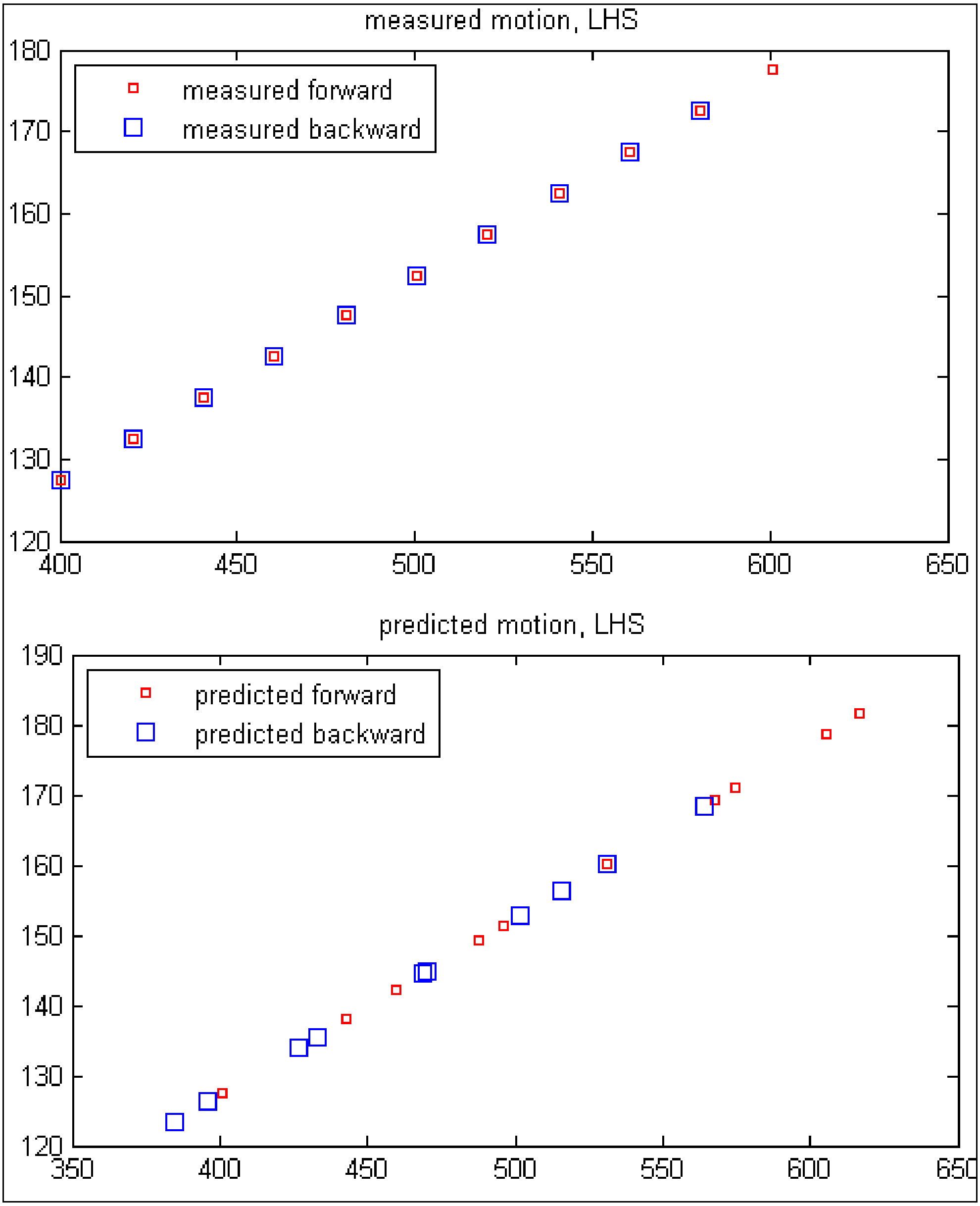

**Fig. 3.** Measured and predicted motion forward and backward for left hand side.

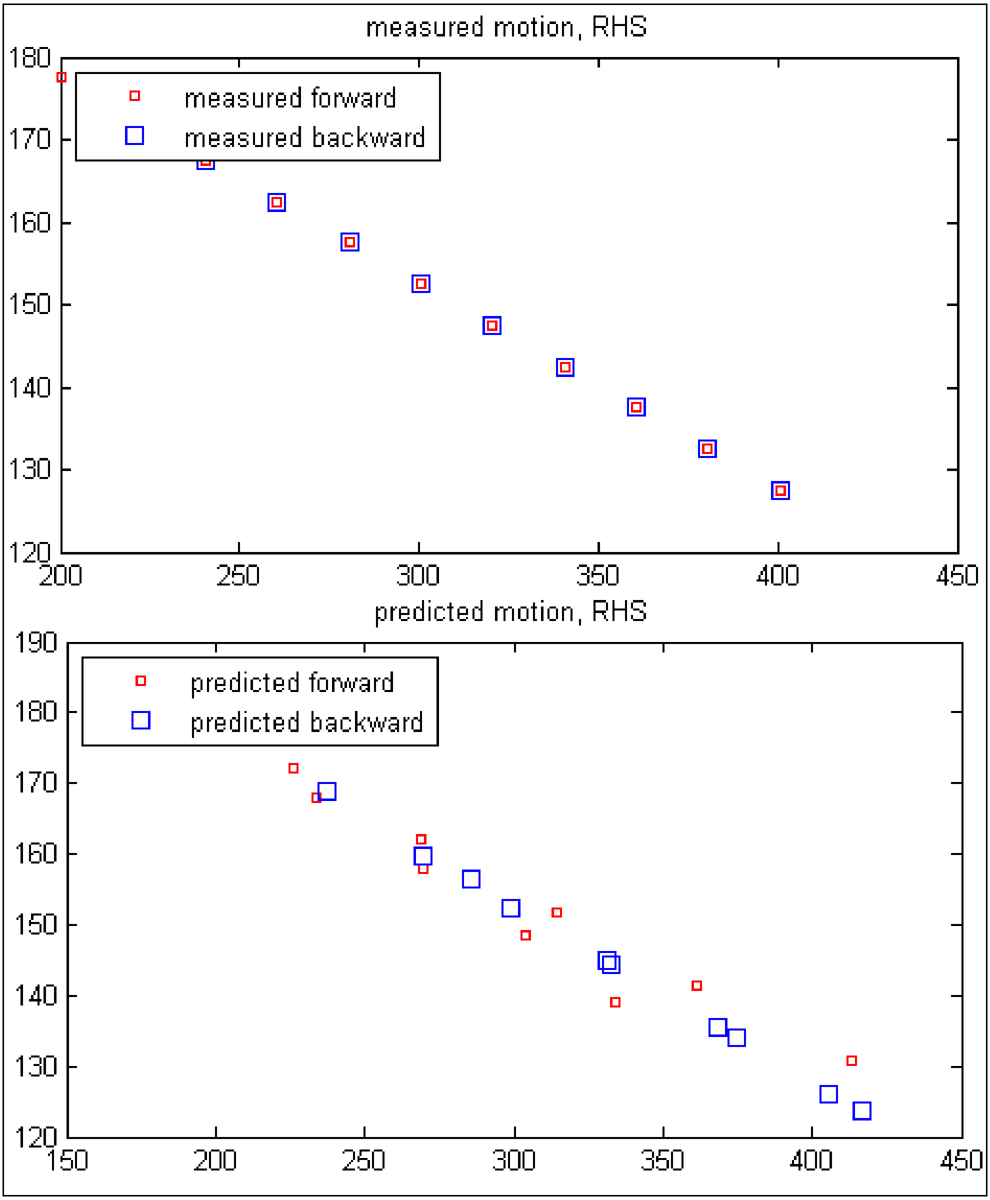

**Fig. 4.** Measured and predicted motion forward and backward for right hand side

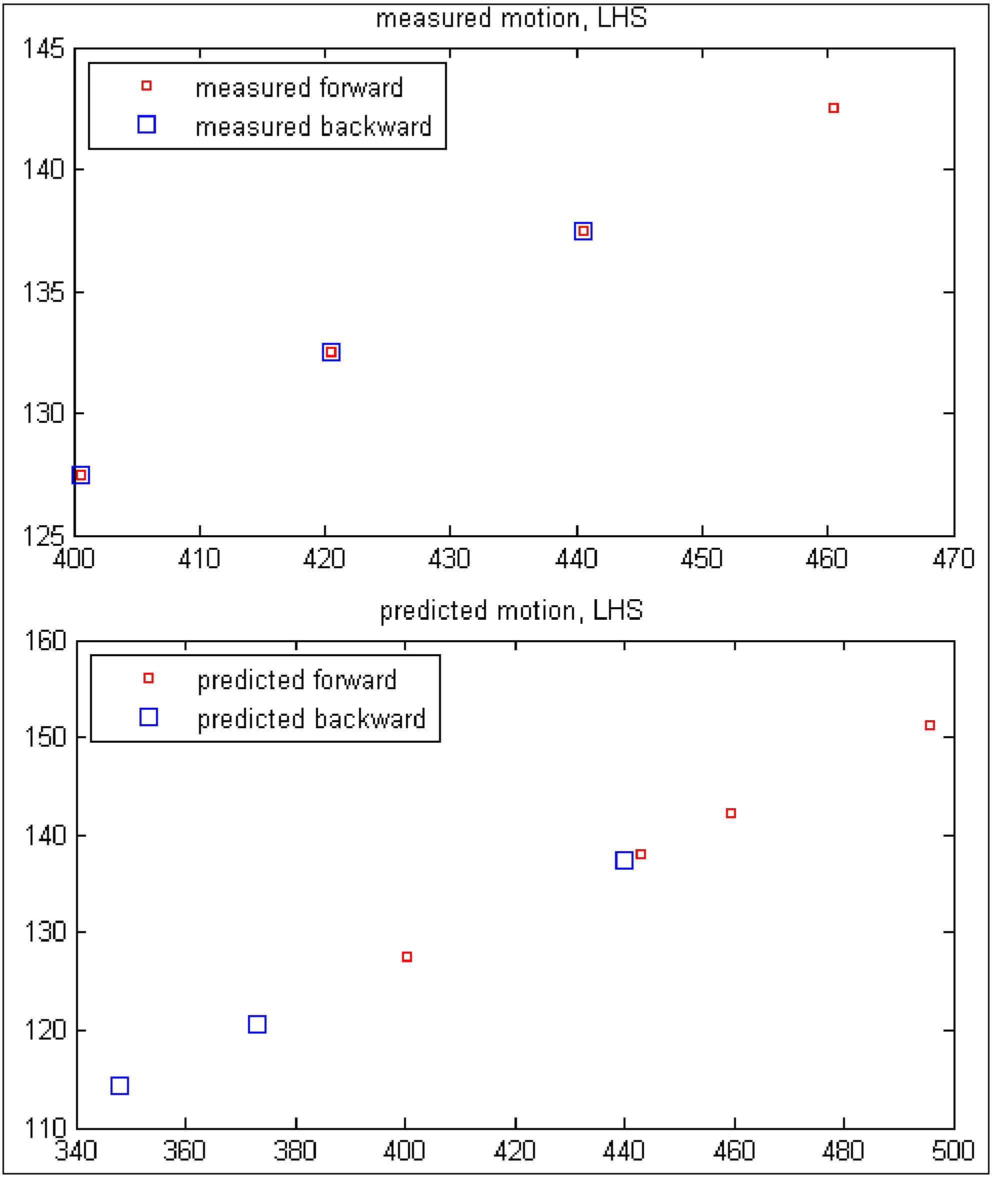

**Fig. 5.** Measured and predicted motion forward and backward for left hand side.

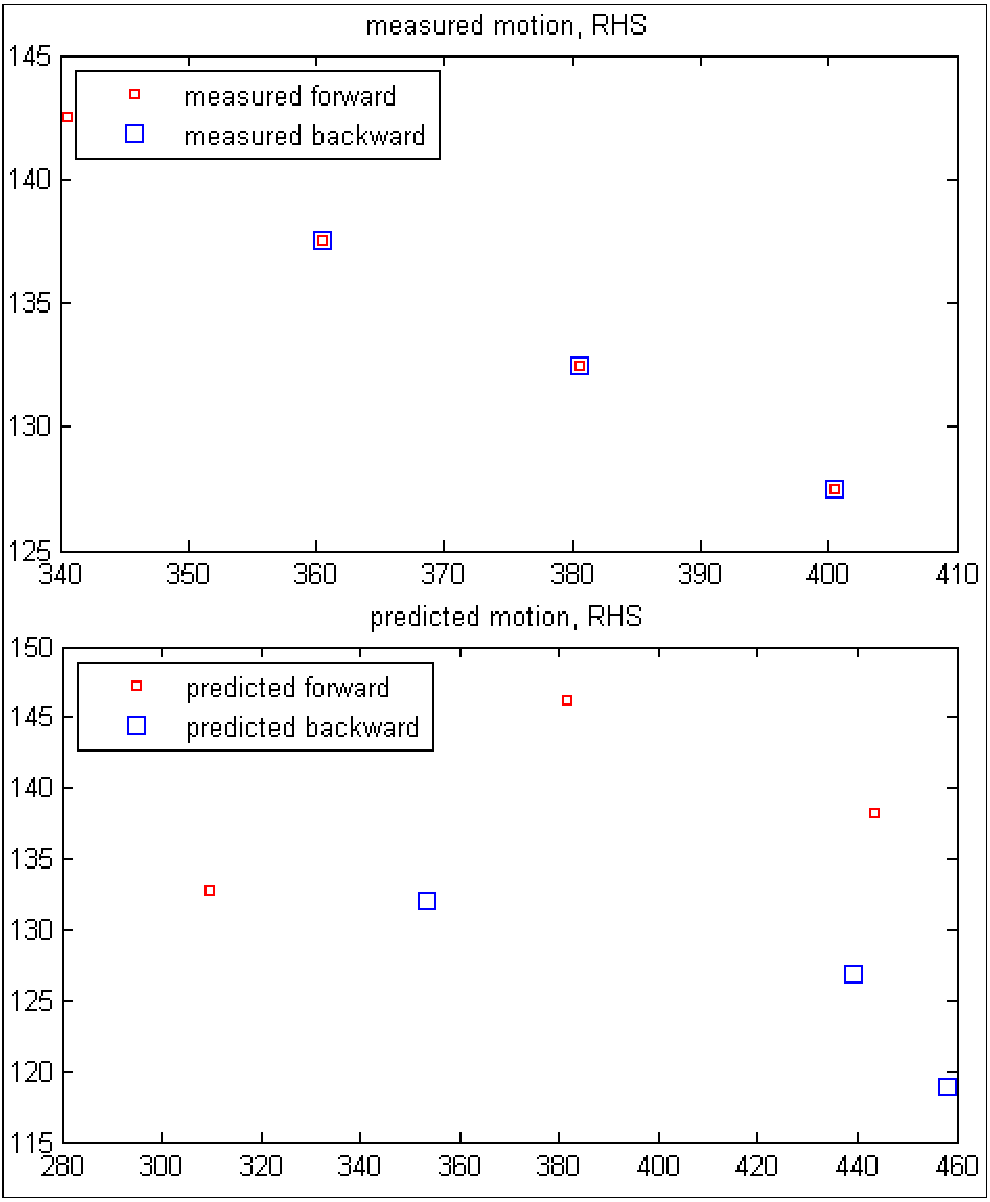

**Fig. 6.** Measured and predicted motion forward and backward for right hand side.

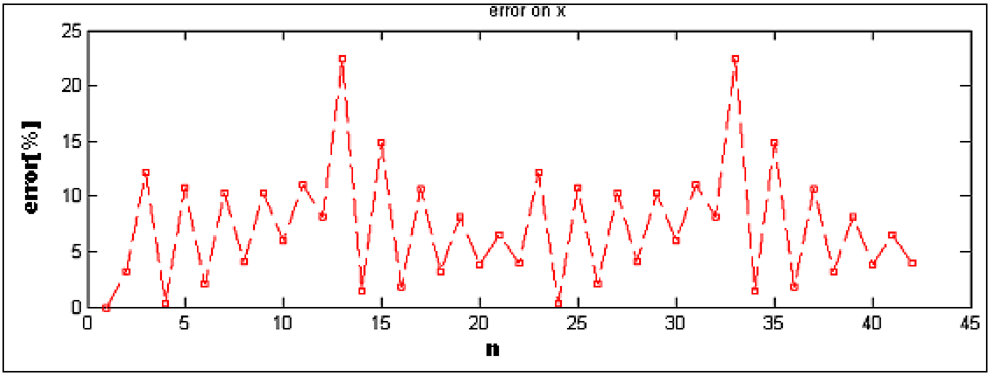

**Fig. 7.** Error in prediction of the $x$ coordinate as a function of motion step.

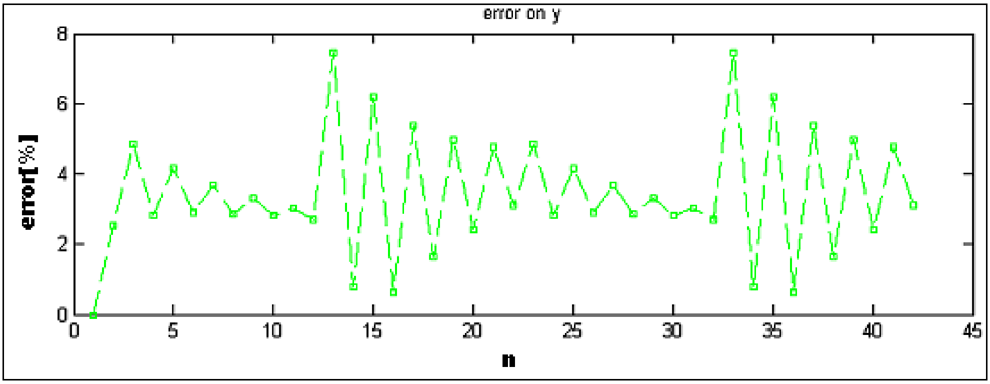

**Fig. 8.** Error in prediction of the $y$ coordinate as a function of motion step.

Another disadvantage, besides the strong dependency of the quality of the prediction on the size of the input data vector is the filter's inability to predict turning points. Turning points are the ones when the amplitude of the displacement changes sign and the restoring force tries to get the apex back in its original position. However, after the turning point, the filter starts "learning" again, and the error in prediction drops accordingly (see Fig. 7 for the error in prediction of next coordinate $x$ and Fig. 8 for the error in prediction of the next coordinate $y$ ).

### Connection between parameters

We propose that there is a connection between the parameters $c$, $n$ and $\omega_I$ and the parameters of the Kalman filter, $K_i$ (Kalman gain at each measurement update $i$) and $P_i$ (error covariance matrix).

After running the simulation many times, the maximum and minimum difference between consecutive time-step Kalman gains is noticed to be constant. This means that the dynamics of the system is such that the maximum adjustment the filter has to perform is constant. We can then say that it depends only on the input parameters, such as the geometrical characteristics of the system and on the amplitude of the allowed stochastic fluctuations.

## CONCLUSIONS

At this point, a Kalman filtering technique does not offer a bijective connection between the parameters of the Kalman filter and those determined by applying the simple line of reasoning offered by the $\alpha\vec{v}$ model.

It can nonetheless prove to be very useful in real-time applications designed for tracking and predicting coronal loop dynamics.

The framework that was obtained may be applied to any motion of a large object with similar geometrical properties that is observed by sensors with similar resolution characteristics. The model thus needs to be refined before we can say that the filter "knows" it is looking at a coronal loop and this is our goal for future work.

## ACKNOWLEDGEMENTS

G.M. acknowledges the financial support of the Sectoral Operational Programme for Human Resources Development 2007-2013, co-financed by the European Social Fund, under the project number POSDRU/107/1.5/S/76841 with the title "Modern Doctoral Studies: Internationalization and Interdisciplinarity".

## REFERENCES

1. Aschwanden, M.J., Fletcher, L., Schrijver, C.J., and Alexander, D. (1999). Coronal loop oscillations observed with the transition region and coronal explorer. *ApJ*, 520(2):880–894.
2. DePontieu, B., Martens, P., and Hudson, H. (2001). Chromospheric damping of alfven waves. *ApJ*, 558(2):859–871.

3. Marcu, A. and Mocanu, G. (2010). Excitation and damping of transversal coronal loop oscillations. *AIP*, 1262:39.
4. Mocanu, G. and Marcu, A. (2010). New approach on the excitation and damping of transversal coronal loop oscillations. *Rom.Rep.Phys*, 62(3).
5. Mocanu, G. and Marcu, A. (2011). Simulation model for transversal loop oscillations: the effects induced by shock waves and opposition of the external medium. *Romanian Astronomical Journal*, accepted.
6. Moga, D., Mocanu, G., and Munteanu, R. A. (2009). *Vision Based Measurement and Control*. Mediamira Science Publishing.
7. Nakariakov, V.M., Aschwanden, M.J., and Doorsselaere, T.V. (2009). The possible role of vortex shedding in the excitation of kink-mode oscillations in the solar corona. *A&A*, 502(2):661–664.
8. Nakariakov, V.M., Ofman, L., DeLuca, E.E., Roberts, B., and Davila, J.M. (1999). Trace observation of damped coronal loop oscillations: Implications for coronal heating. *Science*, 285(5429):862–864.
9. Ofman, L. (2005). Three dimensional mhd models of active region loops. *Adv. Space Res*, 36(8):1572–1578.
10. Roberts, B. (2000). Waves and oscillations in the corona (invited review). *SolPhys*, 193(1-2):139–152.
11. Ruderman, M.S. and Roberts, B. (2002). The damping of coronal loop oscillations. *ApJ*, 577(1):475–486.
12. Schrijver, C.J. and Brown, D.S. (2000). Oscillations in the magnetic field of the solar corona in response to flares near the photosphere. *ApJ*, 537(1): L69–L72.
13. Terradas, J., Oliver, R., and Ballester, J.L. (2005). The excitations and damping of transversal coronal loop oscillations. *ApJ*, 618(2):L149–L152.

STUDIA UBB PHYSICA, LVI, 2, 2011

# VOLATILE AROMA PROFILE OF APPLE JUICE DETERMINED BY GC-MS

G. SCHMUTZER[1,*], Z. MOLDOVAN[1], A. MAGDAS[1], L. DAVID[2]

**ABSTRACT.** Apple juice aroma profile was obtained using the rapid and solvent free solid phase microextraction (SPME) method and a selective and sensitive gas chromatography – mass spectrometry (GC-MS) analytical system. In this paper, the influence of different parameters for headspace SPME is presented. The volatiles (belonging to ester, terpene and alcohol classes) observed in apple juice, obtained from concentrate in Romania, are common compounds in these types of matrices. The total amount of esters, terpenes and alcohols provide important information about the quality of apple juices. The concentration of total esters was found to be low (63 µg/L), which suggests that the aroma recovering process is insufficient. In the paper were identified 12 terpene natural compounds, with odor activities. The high amount of 3-hexen-1-ol found in the sample, is a clear indication that the studied juice is a processed product, not a fresh single strength apple juice.

***Keywords:*** *volatile aroma/flavor profile, apple juice, SPME, GC-MS*

## INTRODUCTION

Apple juice is one of the most common fruit juices in the world and is one of the most important apple products worldwide [1, 2]. The term of apple juice generally refers to the filtered and pasteurized product of pressed apple and the term of natural apple cider to the unfiltered and sometimes unpasteurized apple product. In some places apple cider is referred to an alcoholic beverage, which is also known as hard cider. Commonly, distinction between filtered apple juice and natural apple cider is not clear. In areas of high apple production unfiltered and unclarified fresh apple juice is produced in smaller quantity. The filtered apple juice is produced by complex and expensive equipment in order to obtain large volumes of clarified juice from apple and can be of two types: made from concentrate or not from concentrate (NFC). In the manufacturing

---

[1] National Institute for Research and Development of Isotopic and Molecular Technologies, 65-103 Donath str., 400293 Cluj-Napoca, Romania. [*]corresponding author e-mail: *schmutzer@itim-cj.ro*

[2] *Babeş-Bolyai University, Faculty of Physics, 1 Mihail Kogălniceanu str., 400084 Cluj-Napoca, Romania*

process of apple juice concentrate, by thermal evaporation, the amount of aroma compounds are significantly reduced, therefore the production of apple juice concentrate involves an aroma recovering step [3].

The quality of fruit juice, especially of those made from concentrate, depends on the aroma constituents and concentrations. Apple aroma is a very dilute solution of esters, alcohols, terpenes whose quantities never exceed levels of mg/L in the juice [4], while in single strength apple juices a higher amount is present [3, 5, 6]. The amount and the variety of aroma compounds from single strength juice depend on different factors such as: growing region, climate, cultivator and cultivator practices, maturity of harvest and storage conditions [7]. In the case of filtered and clarified juice the concentrations of volatile compounds responsible for the aroma are additionally influenced by transport conditions and processing technologies.

The objective of this study was to present the volatile compounds profile of Romanian apple juices made from concentrate, using headspace solid phase microextraction (SPME) and the selective and sensitive coupled gas chromatography mass spectrometry (GC-MS) technique.

## EXPERIMENTAL

In this study we analyzed a Romanian apple juice, obtained from concentrate and with sugars addition. 15 ml sample of apple juice spiked with 66 µg/L of 2,4-disec-butylphenol, used as internal standard (IS), was subjected to extraction process of aroma compounds from the fruit juice. The volatile aroma compounds were extracted by SPME technique, using a 75 µm carboxen/polydimethyl-siloxane (CAR/PDMS) and a 65 µm polydimethyl-siloxane/divinyl-benzene (PDMS/DVB) fiber for manual holder. The equilibration and extraction was made at 60 °C under continuous stirring for 30 min.

The GC-MS system was equipped with a HP-5MS capillary column (crossbond 5% diphenyl and 95% dimethyl polysiloxane, having length of 30m, internal diameter of 0.25 mm and film thickness of 0.25 µm). The injector was set at 250 °C and the desorption was made for 2 min. The GC temperature program started from 40 °C, hold 2 min, rise up to 300 °C hold for 10 min with a temperature increasing rate of 10 °C/min. The MS parameters were: electron impact (+) ionization mode, electron energy of 70 eV, source temperature set at 250 °C, emission current at 300 µA, mass range of 50-650 m/z.

The compounds identification was made based on their mass spectra, by comparison with mass spectra from the NIST Mass Spectral Library using the search program NIST MS Search (version 2.0) and also based on rules of ion fragmentation in the mass spectrometer ion source. Quantification of the detected compounds was performed by comparison of their characteristic ion fragment peak areas with the area of the internal standard.

## RESULTS AND DISCUSSION

The extraction of the aroma volatile compounds from samples, using the SPME technique, was chosen for the separation and the concentration of interesting compounds from the complex matrices of commercial apple juice. The major advantages of headspace SPME is the fact that this technique is: rapid, solvent free and rather easy to handle. Moreover, this extraction method enables us to obtain results with high reproducibility [8]. For the optimization of the extraction method, we tested two different combinations of absorption phases: a carboxen/polydimethyl-siloxane (CAR/PDMS) and a polydimethyl-siloxane/divinyl-benzene (PDMS/DVB). The concentration rate that we obtained for CAR/PDMS was lower than for PDMS/DVB, although both fiber types should be suitable to enrich a very wide spectrum of compounds with different polarities. Before the very measurements the fibers were preconditioned according to producer recommendation in the GC injection port under hydrogen flow. The extraction of volatiles from commercially available apple juice was carried out without dilution of the juice and no salt was added, in order to avoid inducing modifications in the studied juice composition.

The time and temperature, during thermostating of the sample, influence the distribution of the analytes between the sample and the headspace of the sample and therefore, have a significant effect on the extraction yield [9, 10]. The extraction was tried at different temperature values: 22°C, 40 °C and 60 °C. The exposure of fiber to the sample headspace was made for 15 and 30 min, after equilibration of the sample during 30 min. The highest extraction yield was obtained for the 60 °C and 30 min sample preparation conditions. After extraction, the charged fiber was immediately transferred to the injection port of the GC-MS system and the compounds were desorbed from the fiber directly into the liner and held for 2 min.

GC-MS system was used to separate and detect the volatile compounds, responsible for the apple juice flavor. The separation of the aroma volatiles on the capillary analytical column was tested using several different temperature program, but the best gas chromatograms were obtain for the temperature sets presented in the experimental part. The determined volatile compound from the studied apple juice can be included in three classes: esters, terpenes and alcohols.

The esters are important flavor compounds naturally occurred in many fruits, having distinctive fruit-like odors. According to Nikfardjam et al. and Heil et al., the total esters are very important for apple juice from concentrate [6, 11]. The highest amount of ester compounds that we found in our apple juice were for isoamyl acetate and n-hexyl acetate. The value determined for the total esters was 63 μg/L, much lower than the lower value proposed by Heil et al. (150 μg/L), for an effective aroma recuperation process for apple juices. The very low value of the total esters suggests that rearomatization of apple juice from concentrate has been insufficient [6, 11].

The GC-MS chromatogram of the volatile compounds from a Romanian apple juice is presented in fig.1. The upper chromatogram from the fig 1, represents the total ion current (TIC) and the lower one represents the chromatogram of selected mass range (in our case m/z=91, characteristic ion fragment for many terpenes). Generally, fruit juices have significant concentrations of terpenes, terpenoids, natural phenols, like flavanols and other, with health promoting effect and often with strong smelling [4]. In our apple juice sample we determined 12 terpene compounds (Fig. 1): α-pinene (1), 3-carene (2), limonene (3), terpinene (4), terpinolene (5), camphene (6), myrcene (7), p-menth-1-en-4-ol (8), terpineol (9), anethole (10), α-damascenone (11) and α-farnesene (12). The concentration of total mean value of terpenes in our sample was 217 μg/L.

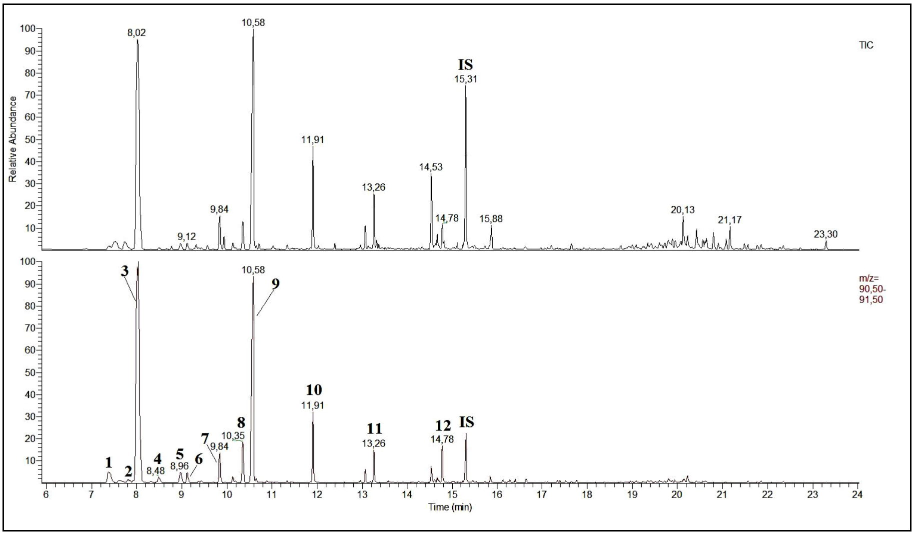

**Fig.1** The total ion current (TIC) chromatogram for volatile compounds from apple juice (upper part) and the m/z=91 ion fragment chromatogram (lower part), with the corresponding identification: α-pinene (1), 3-carene (2), limonene (3), terpinene (4), terpinolene (5), camphene (6), myrcene (7), p-menth-1-en-4-ol (8), terpineol (9), anethole (10), α-damascenone (11) and α-farnesene (12)

One of the main higher alcohols that we determined was 3-hexen-1-ol, which is formed mainly during the unwanted fermentation process [12]. Elss et al. reported that the amount of 3-hexen-1-ol in the apple juice aromas is higher than those found in the single strength apple juice [3], due to the long manufacturing process. In our sample the concentration of 3-hexen-1-ol was 7 μg/L, which is a value characteristic for processed apple juice.

## CONCLUSIONS

In the present study characterization of the volatile compound profile of a Romania apple juice, obtained from concentrated, was made by SPME, GC-MS analytical method. The volatile compounds responsible for the aroma of apple juice were included in three chemical classes: esters, terpenes and alcohols. The value of total esters (63 µg/L) show that the recovery of the aroma compounds in the manufacturing process is insufficient. Terpenes, 12 identified in this paper, are primary constituents of many types of plants, so the presence of these compounds in the juice suggested the fact that the concentrate was obtained from apple fruits. The manufacturing of filtered and clarified apple juice is a long process in which the fermentation cannot be totally prevented. The presence of some higher alcohols in the studied sample reflects this fact.

### ACKNOWLEDGEMENTS

This research was supported by a grant from Unitatea Executiva pentru Finantarea Invatamantului Superior, a Cercetarii, Dezvoltarii si Inovarii (UEFISCDI) of Romania under contract PN II RU TE, contract no. 120/2010.

## REFERENCES

1. W.H. Root, D.M. Barrett, H. Ramaswamy, “Processing fruits – science and technology”, 2nd ed., CRC Press, **2005**, chapter 18.
2. USDA Foreign Agricultural Service, “World Apple Juice Situation”, (2004-2005).
3. S. Elss, C. Preston, M. Appel, F. Heckel, P. Schreier, *Food Chemistry,* 98, 269 (2006).
4. D. Jaros, I. Thamke, H. Raddatz, H. Rohm, *Eur. Food Res. Technol.*, 229, 51 (2009).
5. A.C. Carelli, G.H. Crapiste, J. E. Lozano, *J. Agric. Food Chem.*, 39, 1636 (1991).
6. M.P. Nikfardjam, D. Maier, *Food Chemistry*, 126, 1926 (2011).
7. T.A. Eisele, S.R. Drake, *J. Food Compos. Anal.*, 18, 213 (2005).
8. B. Zierler, B. Siegmund, W. Pfannhauser, *Anal. Chim. Acta*, 520, 3 (2004).
9. A. Steffen, J. Pawliszyn, *J Agric. Food Chem.*, 44, 2187, (1996).
10. J Pawliszyn, “Solid Phase Microextraction – Theory and Practice”, Wieley/VCH, New York, **1997**.
11. M. Heil, V. Ara, *Flüssiges Obst*, 09, 444 (2007).
12. M. Gil, J.M. Cabellos, T. Arroyo, M. Prodanov, *Anal. Chim. Acta*, 563, 145 (2006).

STUDIA UBB PHYSICA, LVI, 2, 2011

# SYNTHESIS AND STABILIZATION OF GOLD NANOPARTICLES BY GELATIN BIOPOLYMER

**SORINA SUĂRĂŞAN[1,2], MONICA FOCŞAN[1], DANA MANIU[2], SIMION AŞTILEAN[1,2]***

**ABSTRACT.** In the present paper we investigated the ability of Gelatin biopolymer to act as both reducing and stabilizing agent in the synthesis of gold nanoparticles (GNPs) with controlled size. The obtained GNPs were characterized by surface plasmon resonance spectroscopy, dynamic light scattering, zeta potential and fluorescence measurements. We found that Gelatin concentration plays an important role in controlling the size of synthesized GNPs. Specifically, a lower Gelatin concentration leads to the formation of larger GNPs in a short time while a higher Gelatin concentration enables the synthesis of smaller GNPs but in a longer time. However, a Gelatin concentration too high prevents the formation of GNPs. Although there are several methods to prepare GNPs, the method presented here is attractive as being completely “green” method to provide in a “one-pot” synthesis both stabilized and biocompatibilized GNPs. The bio-synthesized GNPs can become ideal candidates for biomedical applications.

***Keywords:*** *Gold nanoparticles; Gelatin; Bio-synthesis*

## INTRODUCTION

The study of gold nanoparticles (GNPs) having various sizes and shapes is valuable in order to take advantage of their full potential in biomedical application [1]. During the past years, has been reported the significance of GNPs in drug delivery [2], bioimaging [3] or biodiagnostic [4].

The first conditions that must be accomplished in view of successfully exploiting of GNPs in biological media is to provide them stability and biocompatibility. The classical methods of GNPs synthesis imply the reduction of gold ions by reducing agents such as sodium citrate or sodium borohydride. Subsequently, the GNPs must be encapsulated in different proteins or polymers in order to prevent their aggregation and to provide them biocompatibility. Recently, many studies reported the synthesis of GNPs using amino acids [5],

---

[1] *Nanobiophotonics Center, Interdisciplinary Research Institute on Bio-Nano-Science, Babeş-Bolyai University, T. Laurian 42, 400271, Cluj-Napoca, Romania*

[2] *Physics Faculty, Babeş-Bolyai University, M. Kogalniceanu 1, 400084 Cluj-Napoca, Romania*

[*] *Corresponding author: simion.astilean@phys.ubbcluj.ro*

proteins [6] or biopolimers [7]. These “green” methods of GNPs bio-synthesis make use of non-toxic materials to facilitate the formation of eco friendly nanoparticles. As-synthesized GNPs have improved properties, being already stabilized and biocompatibilized due to protein/biopolymer coating~~.~~

Gelatin is a good candidate for biomaterial assisted synthesis of GNPs due to its amphoteric properties and unique composition containing 18 amino acids in varying amounts depending of collagen sources and processing treatments [8]. Therefore, the aim of this study was to investigate the ability of this natural biopolymer to reduce gold ions and subsequently to produce GNPs. Recently, Gelatin was successfully employed in the formation of silver-gold bimetallic nanoparticles [9] or carboxylic single-walled carbon nanotubes-GNPs composites [10]. In our study, once proved the possibility to synthesize nanoparticles, we investigated the role of Gelatin concentrations in the synthesis of GNPs with different sizes. In order to achieve valuable information about the bio synthesis of GNPs and their size, charge and stability, we successfully used a variety of spectroscopic methods as localized surface plasmon resonance (LSPR) spectroscopy, dynamic light scattering (DLS), zeta potential measurements and fluorescence spectroscopy.

## EXPERIMENTAL

### *Materials*

Tetrachloroauric acid ($HAuCl_4$ $4H_2O$, 99.99%) and Gelatin (Type A) from porcine skin were purchased from Aldrich. Sodium Chloride (NaCl) was purchased from Merck. All chemicals were of analytical grade, and all aqueous solutions were prepared with double distilled water.

### *Sample preparation*

The bio-assisted synthesis of GNPs was performed using Gelatin biopolymer as reducing agent. The Gelatin stock solution (30mg/ml) was heated under continuous stirring at 80°C and mixed with 2mM $HAuCl_4$ at different volume ratios (Gelatin: $HAuCl_4$) as follows: 10:1, 5:1, 2:1 and 1:1. The mixed solution was shaken vigorously for 30 seconds and then incubated at 80 °C.

The stability of as-prepared GNPs was investigated by adding a 1M NaCl solution to the colloidal gold in a volumic ratio of 5:1. For DLS measurements the obtained GNPs were centrifuged once at 10.000 RPM for 5 min to remove the excess Gelatin biopolymer and then redispersed in ultrapure water.

### *Experimental measurements*

The optical absorbance spectra of as-synthesized GNPs were recorded at room temperature using a V-670 UV–Vis-NIR spectrophotometer (Jasco) with a band width of 2 nm. The particle size distribution and zeta potential of the colloidal solutions were measured at 20 $^{o}$C using a Nano ZS90 Zetasizer (Malvern Instruments) equipped with a He-Ne laser (633 nm, 5 mW). The fluorescence spectra were recorded using a Jasco LP-6500 spectrofluorimeter. The emission spectra were recorded with the excitation wavelength set at 295 nm.

## RESULTS AND DISCUSSION

### *Bio-synthesis of GNPs by Gelatin biopolymer*

The nature of Gelatin biopolymer, containing functional groups as $-NH_2$, $-SH$ and $-COOH$, gives them the possibility to reduce the gold ions. Having this in mind, we were interested to investigate the ability of Gelatin to form colloidal gold. It is well known that the amino acids of Gelatin such as lysine, methionine and tyrosine having electron-donating properties enable the reducing of gold ions at room temperature. However, their concentration in Gelatin is too low and therefore, one week is required to form GNPs at room temperature. Another amino acid responsible for the reduction of metallic ions in Gelatin is glutamic acid, but it works as reducing agent only at high temperature [9]. Considering this detail and taking into account the concentration of glutamic acid in Gelatin, we preferred to incubate the Gelatin and $HAuCl_4$ mixed solution at 80 °C in order to synthesize GNPs.

Figure 1 presents the absorption spectra of Gelatin-$HAuCl_4$ solution (1:1 volume ratio) at different stages of the synthesis. In the first minutes (curve a), the UV-Vis absorbance of mixed solution, presents any plasmonic response, indicating that no detectable amount of nanoparticles is formed.

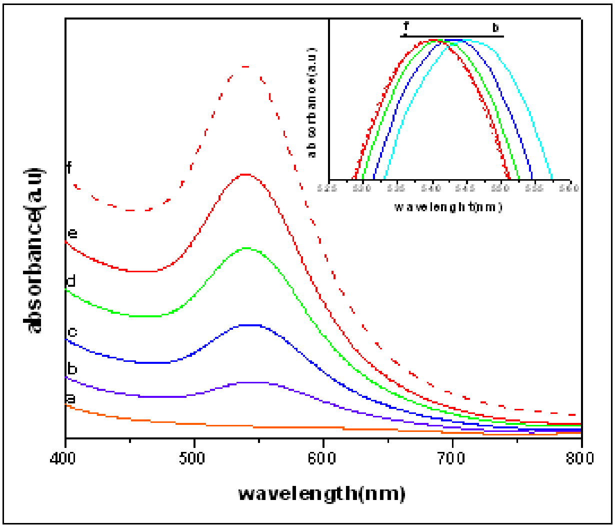

**Fig. 1.** Time evolution of the UV-Vis spectra of GNPs synthesized by Gelatin biopolymer (1:1). Spectra recorded after a) 30 min, b) 60 min, c) 90 min, d) 120 min, e) 150 min f) 180 min. Inset shows the normalized spectra of GNPs for different periods of the formation.

After about 60 minutes we detect a change in the solution color and emergence of a plasmonic band in the absorbance spectra. During incubation at high temperature, we noticed the intensity increase of plasmonic band and the blue-shifting of GNPs peak position (curves c-e). This phenomenon is attributed to continuous reduction of gold ions by the Gelatin which induces the increase of GNPs concentration in time. Moreover, the heating of the solution induces the dissociation of aggregated particles into smaller particles, stabilized by the amine pendant groups of Gelatin backbone [10]. The dissociation of larger particles into smaller particles is reflected by the blue-shift of plasmonic band, detailed in inset of the figure 1 by the normalized spectra of GNPs in different period of the formation. Additionally, the peak position is stable at 540 nm (curves e, f), indicating that the size of GNPs is preserved.

### *The effect of Gelatin biopolymer concentration on the gold nanoparticles size*

In order to take advantage of the Gelatin biopolymer ability to reduce gold ions we study the effect of Gelatin concentration on the synthesis of GNPs. Figure 2 shows the absorption spectra recorded from gold colloids obtained with different Gelatin concentrations. For the solutions with a volumic ratio of 10:1 and 5:1 between Gelatin and $HAuCl_4$ the absence of plasmonic response is observed (curves a, b) accompanied by no change in the color of mixture (inset: the right sample), suggesting that GNPs were not formed. However, by decreasing the concentration of Gelatin we recorded a plasmonic band (curve c) located at 540 nm, corresponding to spherical GNPs. Through an additional decrease in the Gelatin concentration at a ratio of 1:1, we noticed that the shape of plasmonic band is preserved although it shifts to higher wavelength (curve d), indicating the formation of larger spherical GNPs. This shift denotes the modification of the GNPs size [11] and the refractive index from their local environment determined by the Gelatin concentration. The increase of the maximum absorption wavelength of GNPs with the decrease of Gelatin concentration was also reported by Zhang et al. [10].

The formation of GNPs with different sizes as a function of Gelatin concentration is also accompanied by a visual change in the color of the initial mixture from light yellow to purple-red and wine red as seen in figure 2. During incubation at 80 °C, a change in color of solution with 1:1 Gelatin:$HAuCl_4$ ratio is perceived after about 1h, while a similar trend is noticed after a longer time in solution with 2:1 Gelatin:$HAuCl_4$ ratio.

From these results we concluded that the Gelatin concentration is essential in the synthesis of GNPs with different sizes. A lower Gelatin concentration leads to the formation of larger GNPs in a short time while a higher Gelatin concentration enable the synthesis of smaller GNPs but in a longer time. However a Gelatin concentration too high prevents the formation of GNPs.

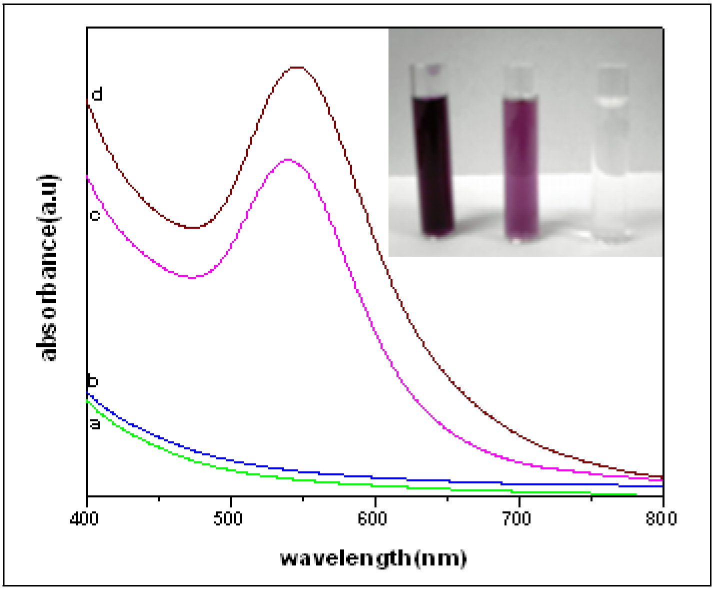

**Fig. 2.** UV-VIS absorption spectra of gold ions and Gelatin biopolymer solutions at different ratio a) 10:1 b) 5:1 and GNPs synthesized by Gelatin biopolymer at different Gelatin concentrations: c) 2:1 d) 1:1 Inset: digital images of Gelatin-$HAuCl_4$ solutions at volumic ratio of 5:1, 2:1 and 1:1

### ***Monitoring the stability of bio-synthesized GNPs by LSPR spectroscopy***

An important problem that should be considered is the stability of bio-synthesized GNPs in biological media. In order to answer at this issue we tested the flocculation behavior of GNPs by mixing 0.1 mL of 1M NaCl solution with 0.5 mL colloidal gold solution synthesized at different Gelatin concentrations. Figure 3 shows the absorption spectra of as-synthesized GNPs, before and after the addition of the aggregation agent. We noticed that, apart from a decrease in the intensity of LSPR band induced by dilution of colloid solution with NaCl, the addition of the salt solution has no significant effect on the plasmonic response. The plasmonic band preserves their shape, which demonstrates the stability of GNPs bio-synthesized using Gelatin. Thereby, we demonstrated that Gelatin has not only an essential role in the synthesis of GNPs but it stabilizes the GNPs, covering their surface and thus preventing the undesired aggregation.

We show here, for exemplification, only the spectra recorded from one colloidal gold solution because the behavior of bio-synthesized GNPs at different Gelatin concentration in the presence of NaCl solution is similar.

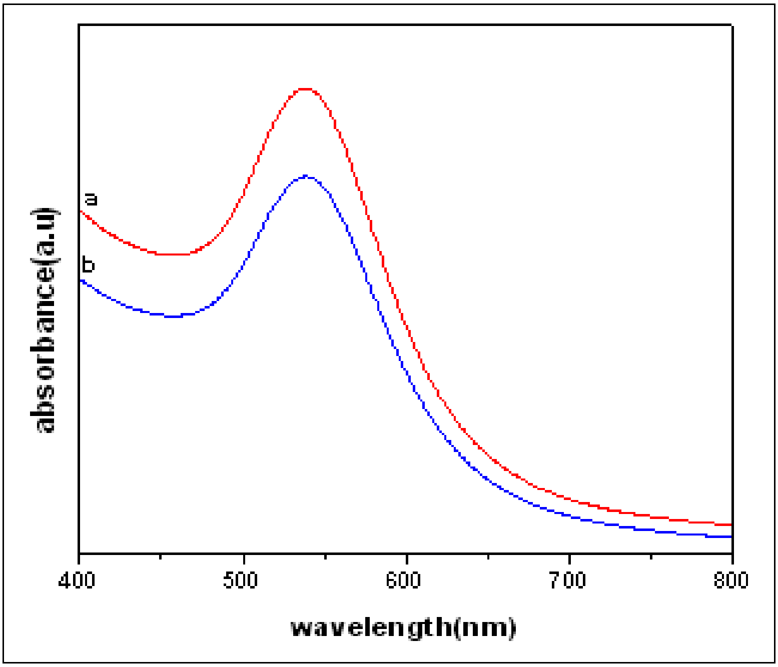

**Fig. 3.** Absorption spectra of GNPs synthesized by Gelatin biopolymer: a) before and b) after the addition of 1M NaCl solution

### *Size distribution and surface charge characterization of nanoparticles*

In order to confirm the synthesis of GNPs having different sizes as a function of Gelatin concentration, we performed DLS measurements on the obtained colloidal solutions. To record information only from the GNPs, we removed the excess of Gelatin biopolymer. DLS data revealed a mean hydrodynamic diameter of GNPs synthesized with lower Gelatin concentration (1:1) equal to 122 nm whereas, for GNPs synthesized at higher Gelatin concentration (2:1) the mean hydrodynamic diameter is 91 nm. These results suggest that a higher Gelatin concentration reduce stronger the gold ions leading to formation of small GNPs, although in a long time, while a lower Gelatin concentration enable the faster formation of larger GNPs. This observation agrees with UV-Vis behavior of GNPs synthesized at different Gelatin concentrations (2:1, 1:1).

According to zeta potential measurements, as we expected, the zeta potential of as-synthesized GNPs has a positive value provided by the Gelatin biopolymer which have a zeta potential of 8.5 mV.

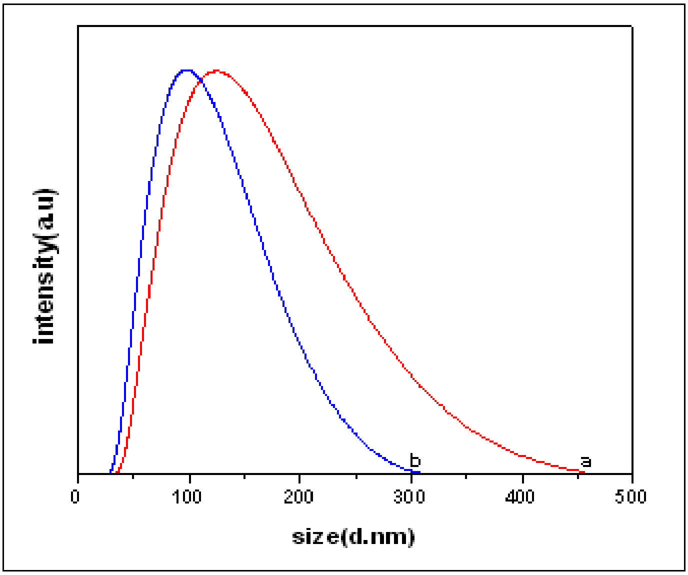

**Fig. 4.** Normalized dynamic light scattering analysis of GNPs synthesized by Gelatin biopolymer at different amounts of Gelatin. Gelatin-$HAuCl_4$ ratio a)1:1 b)2:1

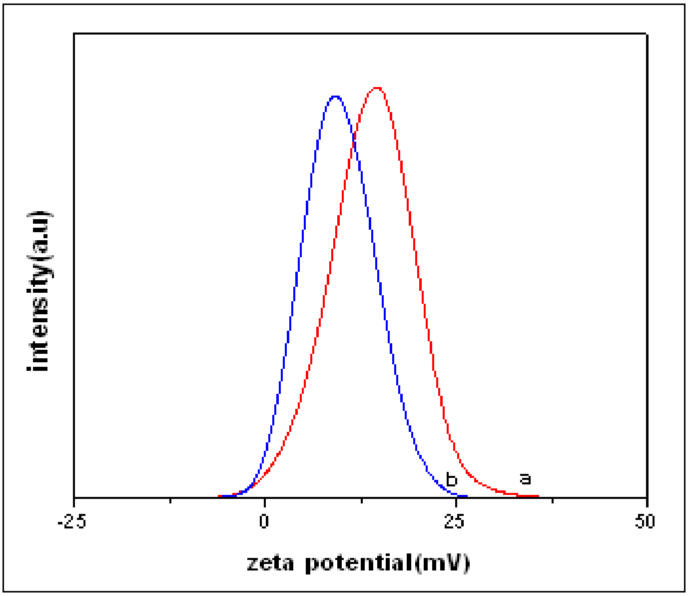

**Fig. 5.** Zeta potential data for GNPs synthesized by Gelatin biopolymer at different amounts of Gelatin: a) 1:1 b) 2:1

During the synthesis of GNPs apart from the reduction of gold ions Gelatin stabilizes the formed GNPs, covering their surface. In this manner, the predominantly $NH_3^+$ groups from Gelatin reach onto the gold particles surface leading to a positive zeta potential. Therefore, GNPs synthesized with higher Gelatin concentration have a zeta potential of 9.68 mV. As we mentioned before, a lower Gelatin concentration enable the formation of larger GNPs. These GNPs presenting a large contact surface area allows the attachment of multiple $NH_3^+$ groups which induce a positive zeta potential of 14 mV.

### *The fluorescence study of Gelatin*

Another method used to monitor the GNPs synthesis is by performing fluorescence measurements. In present study we monitored the fluorescence of Gelatin in the spectral region between 300 nm and 550 nm, which coincide with the pyridinoline fluorescence emission. The Gelatin biopolymer was investigated using for excitation a 295 nm wavelength. As can be seen in figure 6, initially Gelatin exhibits a strong intrinsic fluorescence band centered at 395 nm typical for pyridinoline cross-link [12]. Herein, we monitored the quenching of the Gelatin fluorescence emission induced by synthesized GNPs. Beside from an evident, strong quenching effect, a red-shift and a broadening of fluorescence band was noticed which indicate the synthesize of GNPs having Gelatin biopolymer attached onto their surface.

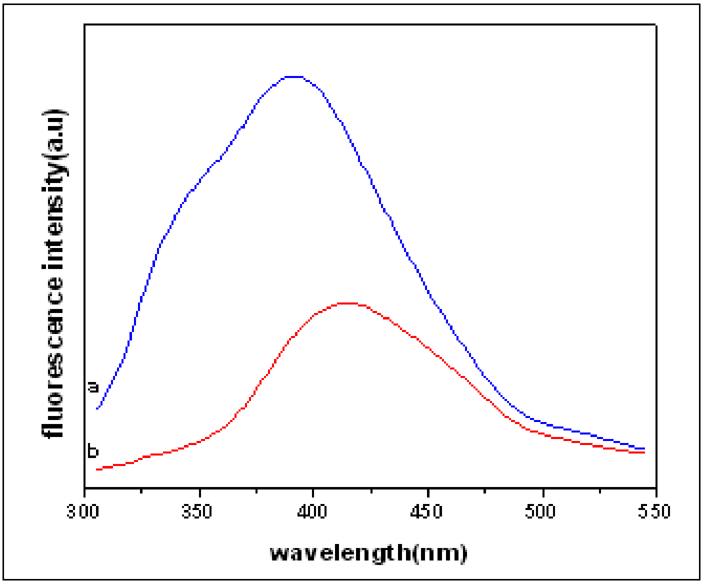

**Fig. 6.** Fluorescence spectra of a) Gelatin biopolymer and b) bio- synthesized GNPs by Gelatin

The quenching mechanism generally arises from static quenching determined by the ground state complex-formed between Gelatin and GNPs during the synthesis of GNPs. Liu et al. [9] observed a similar fluorescence emission assigned to lysine, tryptophan and tyrosine residues from Gelatin. They also showed that GNPs considerably quenching the fluorescence emission in a Gelatin-GNPs solution.

## CONCLUSIONS

The successfully bio-synthesis of GNPs was demonstrated. By employing the ability of Gelatin biopolymer to act as a reducing/stabilizing agent we synthesized GNPs with controlled sizes. We used LSPR spectroscopy, DLS and zeta potential and fluorescence measurements as versatile methods for investigation the formation of GNPs. Additionally, we checked the stability of as-synthesized GNPs in high molarity salted solution. Thanks to their biocompatible nature, the Gelatin bio-synthesized GNPs can be the ideal candidates for biomedical applications.

## ACKNOWLEDGEMENTS

This work was supported by CNCSIS–UEFISCSU, project number PNII_ID_PCCE_312/2008.

## REFERENCES

1. E. Boisselier, D. Astruc, Chemical Society Reviews, 2009, 38, 1759-1782.
2. P.M. Tiwari, K. Vig, V.A. Dennis and S.R. Singh, Nanomaterials, 2011, 1, 31-63.
3. P. Sharma, S. Brown, G. Walter, S. Santra, B. Moudgil, Advances in Colloid and Interface Science, 2006, 123–126, 471 – 485.
4. N.G. Khlebtsov, L.A. Dykman, Journal of Quantitative Spectroscopy & Radiative Transfer, 2010, 111, 1–35.
5. N. Wangoo, K.K. Bhasin, S.K. Mehta, C. Raman Suri, Journal of Colloid and Interface Science, 2008, 323, 247–254.
6. M. Focsan, A.M. Gabudean, V. Canpean, D. Maniu, S. Astilean, Materials Chemistry and Physics, 2011, 129 939– 942.
7. B.A. Rozenberg, R.Tenne, Progress in Polymer Science, 2008, 33, 40-112.
8. V.H. Segtnan, T. Isaksson, Food Hydrocolloids, 2004, 18, 1–11.
9. Y. Liu, X.Liu, X.Wang, Nanoscale Research Letters, 2011, 6:22.

10. J.-J. Zhang, M.-M. Gu, T.-T. Zheng, J.-J. Zhu, Analytical Chemistry, 2009, 81, 6641–6648
11. S.C. Boca, C. Farcau, S. Astilean, Nuclear Instruments and Methods in Physics Research B, 2009, 267, 406–410
12. E. van den Bosch, C. Gielens, International Journal of Biological Macromolecules, 2003, 32, 129–138

STUDIA UBB PHYSICA, LVI, 2, 2011

# VIBRATIONAL AND DFT STUDY OF CALCON AND ITS METAL COMPLEXES

**L. SZABÓ[1,2,*], K. HERMAN[1], N. E. MIRCESCU[1], A. FĂLĂMAŞ[1],**
**L. F. LEOPOLD[3], N. LEOPOLD[1], V. CHIŞ[1]**

**ABSTRACT** This study presents a complete vibrational characterization of 2-hydroxy-1-(2-hydroxy-1-naphthylazo)naphthalene-4-sulfonic acid sodium salt (Calcon) molecule and a method for the identification of metal complexes of Calcon with Al(III), Mn(II), Fe(III) and Cu(II) by employing surface enhanced Raman scattering (SERS). In this work, Calcon was studied by FTIR/ATR, FT-Raman and DFT investigations. Molecular geometry optimization, molecular electrostatic potential (MEP) and vibrational frequencies calculations were performed at B3LYP/6–31G(d) level of theory for the Calcon molecule. Differentiation between Calcon complexes with Al(III), Mn(II), Fe(III) and Cu(II) is demonstrated and characteristic SERS spectral features of each complex are identified.

***Keywords:*** *Calcon; DFT; FTIR; FT-Raman; SERS.*

## INTRODUCTION

Metal ions determination represents an area of interest in several fields, like environmental protection, food safety or clinical diagnostics. Analytical methodologies for direct determination of metal ions were established over the last decades including atomic absorption or emission spectroscopy and mass spectrometry [1]. Although these methods are sensitive and accurate, they require tedious sample pre-treatment and expensive equipment. On the other hand, recently one has seen an increase in the development of optical chemical sensors for heavy metals, because of their easy fabrication, low cost, good selectivity and sensitivity [1-3]. 2-Hydroxy-1-(2-hydroxy-1-naphthylazo) naphthalene-4-sulfonic acid sodium salt (Calcon), with the structure shown in Fig. 1, is a non-selective azo dye, widely used as colorimetric reagent for metal ions spectrophotometric determination, because it forms very stable, water-soluble and highly colored complexes with the vast majority of transition metals [4].

---

[1] *Babeş-Bolyai University, Faculty of Physics, Kogălniceanu 1, 400084 Cluj-Napoca, Romania*
[2] *Nicolae Stăncioiu Heart Institute, Moților 19-21, 400001 Cluj-Napoca, Romania*
[*] *corresponding author e-mail: laszlo.szabo@phys.ubbcluj.ro*
[3] *Department of Chemistry and Biochemistry, University of Agricultural Sciences and Veterinary Medicine, Calea Manastur 3-5, 400372 Cluj-Napoca, Romania*

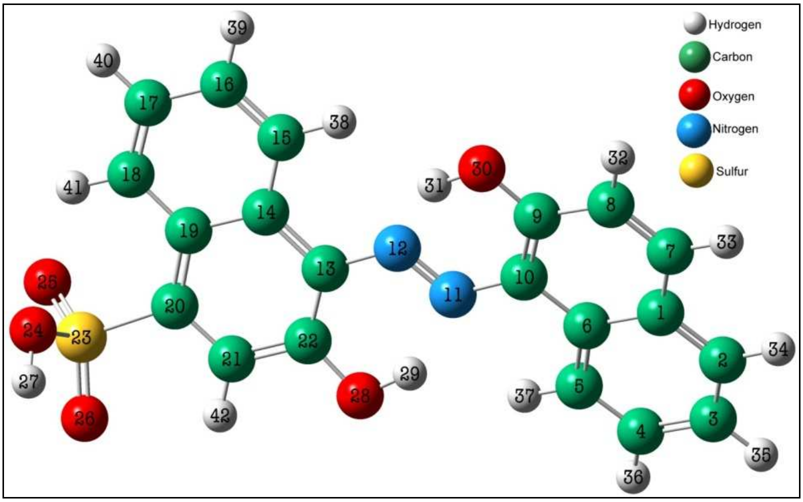

**Fig. 1** B3LYP/6-G(d) optimized geometry of Calcon with atom numbering scheme.

Calcon was used as indicator for the evaluation in a micromethod for the determination of calcium serum and cerebrospinal fluid. The results prove the possibility of using this method in clinical laboratories [5].

A mixture of Calcon and Aliquat 336 was used for the impregnation of a silica gel to be used as chelating sorbent for preconcentration of metals from dilute aqueous solutions as well as for purification of analytical grade sodium and potassium salts from other metals. Calcon was not eluted from sorbent with perchloric and hydrochloric acids. The sorbent was used for preconcentration of traces of some metals from aqueous solutions, for separation of metal ion mixtures by column extraction chromatography and for additional purification of potassium chloride solutions [6].

Surface-enhanced Raman scattering (SERS) offers a suitable alternative to overcome the low sensitivity inconvenience of Raman spectroscopy. When the molecules are adsorbed to rough metal surfaces, the Raman cross section is enhanced several orders of magnitude [7-10]. The potential to combine high sensitivity with the structural information content of Raman spectroscopy makes SERS spectroscopy a powerful tool in a variety of fields.

The determination of metal ions by sensing of 4-(2-pyridylazo)resorcinol -metal complexes using surface-enhanced resonant Raman scattering (SERRS) was reported by Crane et al. [11], whereas Carron et al. [12] used the metal indicator Eriochrome Black T (with a structure similar to Calcon) for SERRS detection of metal ions at ppb level. Previously, in our group, the metal ion determination using 4-(2-pyridylazo)resorcinol and Eriochrome Black T as metal chelating agent and SERS as detection method was reported [13, 14].

In this work, SERS spectroscopy is used in conjunction with quantum chemical calculations in order to characterize the structure, electronic properties and vibrational spectra of the Calcon molecule and its complexes with Al(III), Mn(II), Fe(III) and Cu(II). Thus, the Raman and SERS spectra of Calcon, as well as the SERS spectra of Calcon-Al(III), -Mn(II), -Fe(III) and -Cu(II) complexes, were assigned using DFT calculations at B3LYP level of theory. Calcon complexes with Al(III), Mn(II), Fe(III) and Cu(II) are differentiated by their SERS spectra, each metal complex showing a particular SERS spectral fingerprint.

## EXPERIMENTAL

***Chemicals.*** All chemicals used were of analytical reagent grade. The hydroxylamine reduced silver colloid was prepared according to the previously reported procedure [15]. The pH value of the silver colloid, measured immediately after preparation, was found to be 8. For the metal complexes preparation, the following metal salts were used: aluminium (III) chloride hexahydrate, manganese (II) chloride tetrahydrate, iron (III) chloride hexahydrate and copper (II) sulfate pentahydrate. Calcon and the metal salts were dissolved in doubled distilled water. Calcon complexes with Al(III), Mn(II), Fe(III) and Cu(II) were prepared by adding 1 ml dilutions of $10^{-3}$ M metal salt solution to 1 ml $10^{-3}$ M Calcon solution, obtaining Calcon:metal complexes, Calcon chelating metal ions at 1:1 ratio [4].

***Methods.*** The FTIR/ATR spectrum of Calcon powder sample was recorded at room temperature on a conventional Equinox 55 (Bruker Optik GmbH, Ettlingen, Germany) FTIR spectrometer equipped with a DTGS detector.

The FT-Raman spectrum of Calcon was recorded in a backscattering geometry with a Bruker FRA 106/S Raman accessory equipped with a nitrogen cooled Ge detector. The 1064 nm Nd:YAG laser was used as excitation source, and the laser power measured at the sample position was 300 mW. The FT-Raman and FTIR/ATR spectra were recorded with a resolution of 4 $cm^{-1}$ by co-adding 32 scans.

SERS spectra were recorded using a DeltaNu Advantage 210 Raman spectrometer (DeltaNu, Laramie, WY) equipped with a HeNe laser emitting at 633 nm. The laser power was 4 mW and the spectral resolution of 10 $cm^{-1}$. For all SERS measurements 25 μl of analyte were added to 0.5 ml silver colloid, the final concentration of the metal-complexes in the colloidal solution being $4.8 \times 10^{-5}$ M.

## COMPUTATIONAL DETAILS

Molecular geometry optimizations, molecular electrostatic potential (MEP) distributions and vibrational spectra calculation were performed with the Gaussian 03W software package [16] by using density functional theory (DFT) methods with B3LYP hybrid exchange-correlation functional [17, 18] and the standard 6-31G(d) basis set. No symmetry restriction was applied during geometry optimizations. The vibrational frequencies were computed at the optimized geometries to ensure that no imaginary frequencies were obtained, confirming that they correspond to true minima on the potential energy surfaces.

The calculated Raman activities ($S_i$) were converted to relative Raman intensities ($I_i$) using the following relationship:

$$I_i = \frac{f(\upsilon_0 - \upsilon_i)^4 S_i}{\upsilon_i \left[ 1 - \exp\left( - \frac{hc\upsilon_i}{kT} \right) \right]} \tag{1}$$

where $v_0$ is the exciting laser wavenumber, $v_i$ is the wavenumber of the $i^{th}$ vibrational mode, $c$ is the speed of light, $h$ and $k$ are Planck's and Boltzmann's constants and $T$ is the temperature [19-21].

The computed wavenumbers have been scaled by 0.9614 as proposed by Scott and Radom [22]. The mode assignment is based on the direct comparison between the experimental and calculated spectra by considering both, the frequency sequence and intensity pattern and by comparisons with vibrational spectra of similar compounds [13, 14, 23].

## RESULTS AND DISCUSSION

Experimental FTIR/ATR and calculated IR spectra of Calcon in the 640 $cm^{-1}$ – 1700 $cm^{-1}$ region are shown in Fig. 2, while the most important IR experimental and calculated vibrational modes of Calcon molecule, together with the proposed assignments are summarized in Table 1.

The predicted B3LYP/6-31G(d) theoretical IR wavenumbers are in consistently good agreement with the experimental values. The average of the absolute deviations between experiment and theory is 9.59 $cm^{-1}$, while the root mean square deviation (RMSD) of residuals is 11.54 $cm^{-1}$ (standard deviation (SD) of 10.96 $cm^{-1}$). On the other hand, the normalized RMSD is 1.21%. The largest discrepancy between experiment and theory is observed for the IR bands at 878 and 1048 $cm^{-1}$ (absolute deviation of 42 $cm^{-1}$ and 39 $cm^{-1}$ respectively), corresponding to a normal mode that mainly involves the sulfonic group. This discrepancy can be due to intermolecular hydrogen bonding interactions of the sulfonic group. This statement is sustained by the broad band at 1048 $cm^{-1}$, seen in the experimental FTIR spectrum (Figure 2). Other important deviations are observed for the bands at 739, 811, 1172, 1371 and 1543 $cm^{-1}$.

As shown in Fig.2 and Table 1, the most representative FTIR/ATR bands for the Calcon are the following: 1048 and 1122 cm$^{-1}$, corresponding to the symmetric stretching vibration of the two S=O bonds in the $SO_3H$ group coupled with OH bending in the same group; the broad band centered at 1436 cm$^{-1}$ due to the CC stretching vibrations of the naphthalene rings. The C-C stretching vibrations of the naphthalene rings contribute also significantly to the normal modes corresponding to the IR bands at 1303, 1371, 1410, 1460, 1543, 1593 and 1615 cm$^{-1}$.

The molecular electrostatic potential (MEP) is widely used as a reactivity map displaying most probable regions for the electrophilic attack of charged point-like reagents on organic molecules [24]. As it can be seen in the MEP distribution of the Calcon molecule obtained from DFT calculations depicted in Fig. 3, the negative charge is located mainly on the $SO_3H$ group and on the O and N atoms. Thus when added to the silver colloidal solution, the adsorption of the molecule to the silver surface is supposed to occurs through the $SO_3H$ group. The adsorption through the –N=N– chromophore cannot be completely ruled out but it seems however less probable due to the required necessary deformation of the molecule in order to arrange with the N=N bond in the close vicinity of the silver surface.

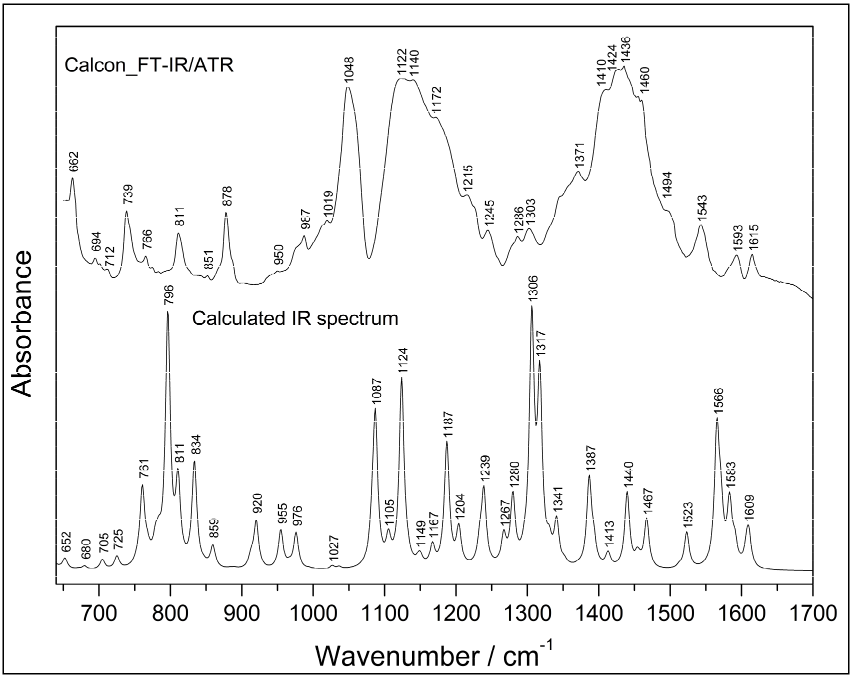

**Fig. 2** Experimental FTIR/ATR (top) and B3LYP/6–31G(d) (bottom) calculated IR spectra of Calcon.

**Table 1.** Selected experimental FTIR/ATR bands (cm$^{-1}$) and B3LYP/6–31G(d) calculated wavenumbers (cm$^{-1}$) of Calcon.

| **Experimental wavenumbers (cm$^{-1}$)** | **Calculated wavenumbers (cm$^{-1}$)** | |
|---|---|---|
| **FTIR/ATR** | **B3LYP*** | **Band assignment** |
| 662 | 652 | ip. ring2 deformation, ρ(SO$_3$H), δ(CH ring2) |
| 739 | 761 | ip. ring2 deformation, υ(SO$_3$H), δ(CH ring2), υ(C20SO$_3$H) |
| 811 | 796 | op. bending CH ring2, ip. ring2 deformation, υ(SO$_3$H) |
| **878** | **920** | **ip. (ring1, ring2) deformation, δ(CH ring1, ring2), υ(C20SO$_3$H)** |
| **1048** | **1087** | **δ(O24H), υ$_s$(SO$_3$H), δ(CH ring1, ring2)** |
| **1122** | **1124** | **δ(O24H), υ$_s$(SO$_3$H)** |
| 1140 | 1149 | δ(CH ring1, ring2) |
| 1172 | 1187 | δ(CH ring1, ring2), υ(C10N11) |
| 1215 | 1204 | δ(CH ring1) |
| 1245 | 1239 | δ(CH ring1, ring2), ip. (ring1, ring2) deformation, δ(O30H) |
| 1286 | 1280 | υ(CC ring1), δ(CH ring1, ring2), υ(N12N11), δ(O30H, O28H), υ(C9O30H) |
| 1303 | 1306 | υ(C10N11), δ(O30H, O28H), υ(CC ring1), δ(CH ring1) |
| 1371 | 1387 | υ(CC ring1, ring2), υ(N12N11), δ(O28H), δ(CH ring1, ring2) |
| 1410 | 1413 | υ(CC ring1), δ(CH ring1), δ(O30H) |
| 1436 | 1440 | υ(CC ring2), δ(CH ring2, ring1), υ(C22O28H) |
| 1460 | 1467 | υ(CC ring1), δ(CH ring1), δ(O30H) |
| 1543 | 1566 | υ$_s$(CC ring2), δ(O30H, O28H) |
| 1593 | 1583 | υ$_s$(CC ring1, ring2), δ(O30H, O28H), δ(CH ring2, ring1) |
| 1615 | 1609 | υ$_{as}$(CC ring1), δ(O30H), δ(CH ring1) |

ν-stretching, ν$_{as}$- asymmetric stretching, ν$_s$- symmetric stretching, δ-in-plane bending, op.-out of plane, ip.-in plane; ring1- naphthalene (C1-C10), ring2- naphthalene(C13-C22)

* scaled values according to Scott and Radom [22].

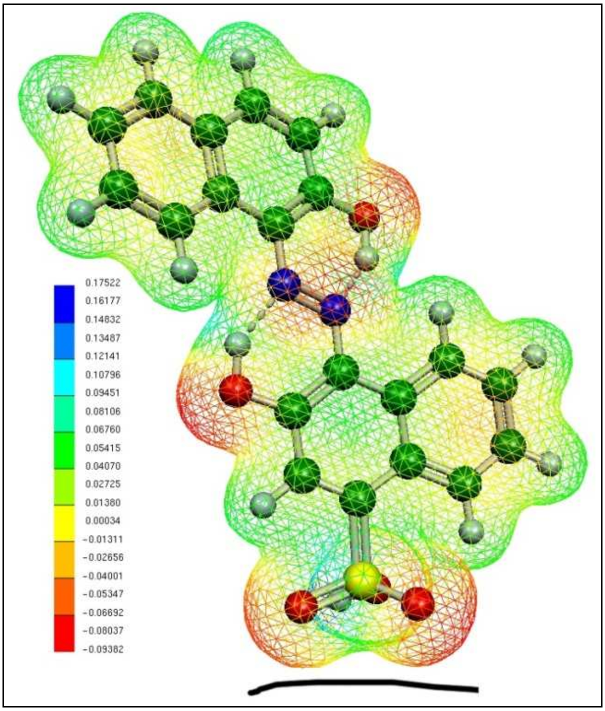

**Fig. 3** B3LYP/6–31G(d) calculated 3D molecular electrostatic potential of Calcon in atomic units (a.u.) mapped on the electronic density isosurface of 0.02 a.u., and schematically view of Calcon adsorption geometry on the silver surface.

It was observed that Raman spectrum of Calcon is overlapped by strong fluorescence emission when the 633 nm laser excitation line was used. Therefore, the FT-Raman spectrum of Calcon was recorded using a Nd:YAG laser, emitting at 1064 nm, from solid polycrystalline sample. This spectrum, together with the B3LYP/6–31G(d) calculated Raman spectrum of Calcon in the 100 cm$^{-1}$ – 1700 cm$^{-1}$ region are shown in Fig. 4.

The assignment of the Calcon FT–Raman bands was performed based on the direct comparison between experimental and DFT calculated bands by considering both, the frequency sequence and the intensity pattern. Table 2 shows the most important FT–Raman bands as well as the B3LYP/6–31G(d) calculated wavenumbers of Calcon with their assignment. The predicted B3LYP/6–31G(d) theoretical wavenumbers are in consistently good agreement with the experimental FT-Raman values. The average of the absolute deviations between experiment and theory is 13 cm$^{-1}$, while the root mean square deviation (RMSD) of residuals is 13.27 cm$^{-1}$ (standard deviation (SD) of 13.27 cm$^{-1}$). On the other hand, the normalized RMSD is 0.96%.

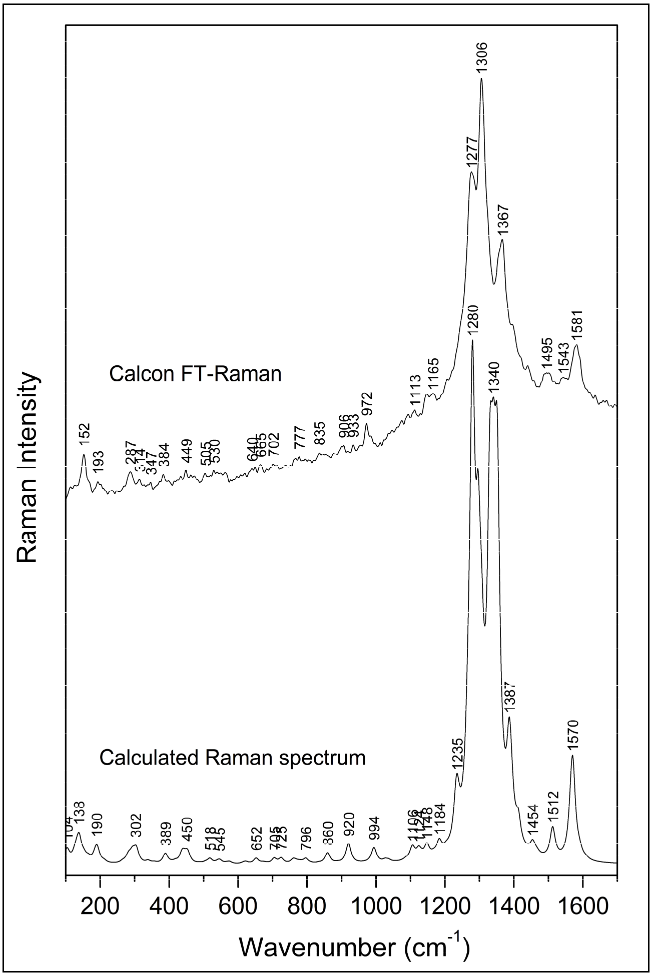

**Fig. 4.** Experimental FT–Raman (top) and B3LYP/6–31G(d) calculated Raman (bottom) spectra of Calcon.

The region between 1000-1600 cm$^{-1}$ presents the most intense Raman bands, with the experimental values: 1277 cm$^{-1}$, assigned to the breathing vibration of the naphtalene ring1 (calculated value 1280 cm$^{-1}$), 1306 cm$^{-1}$ and 1495 cm$^{-1}$, assigned to the bending vibration of the C-O and C-H bonds of the same ring (calculated values 1340 cm$^{-1}$and 1512 cm$^{-1}$ respectively) and 1581 cm$^{-1}$, assigned to the deformation vibration of both naphtalene rings, corresponding to the calculated value 1570 cm$^{-1}$.

A more comprehensive assignment of the Calcon FT-Raman bands is shown in Table 2.

**Table 2.** Selected experimental FT-Raman bands of Calcon and B3LYP/6–31G(d) calculated vibrational modes with considerable Raman intensity.

| Experimental wavenumbers (cm$^{-1}$) | Calculated wavenumbers (cm$^{-1}$) | |
|---|---|---|
| **FT-Raman** | **B3LYP*** | **Band assignment** |
| 193 | 190 | δ(O24H) |
| 384 | 389 | δ(OH, CH) |
| 777 | 796 | δ(CH ring1) |
| 835 | 860 | δ(CH ring1) |
| 906 | 920 | δ(CH ring1), breathing ring2 |
| 972 | 994 | breathing (ring1,ring2) |
| 1113 | 1124 | δ(O24H) |
| 1277 | 1280 | δ(CH ring1), breathing ring2 |
| 1306 | 1296 | δ(OH, CH ring1) |
| 1367 | 1351 | υ(CC ring1, ring2), δ(CH ring1, ring2) |
| 1495 | 1512 | δ(OH, CH ring1) |
| 1581 | 1570 | ring1, ring2 deformation, δ(O30H) |

ν-stretching, $\nu_{as}$- asymmetric stretching, $\nu_s$- symmetric stretching, δ-in-plane bending, op.-out of plane, ip.-in plane; ring1- naphthalene (C1-C10), ring2- naphthalene(C13-C22)
*-scaled values according to Scott and Radom [22].

The Calcon-metal complexes can be differentiated based on their characteristic SERS spectra. Fig.5 presents the SERS spectra of the Calcon-Al(III), -Mn(II), -Fe(III) and -Cu(II) complexes. The SERS spectra of the Calcon-metal complexes show similitudes in the band position, several bands are shifted up to ~ 10 cm$^{-1}$ and the relative intensities of the present vibrational modes are modified. For instance, the band at 1440 cm$^{-1}$ appears strongly enhanced only in the Cu, Mn (1448 cm$^{-1}$) and Al (1408 cm$^{-1}$) complexes with Calcon, not in the Fe one. On the other hand, the band at 1288 cm$^{-1}$ is only present in the complex with Cu and in the one with Fe, at 1285 cm$^{-1}$ and not in the case of Mn and Al. Another characteristic feature, the band at 1236 cm$^{-1}$ present in the Fe complex spectrum, is also notable in the one with Al, at 1245 cm$^{-1}$. Thus, the assignment of the SERS bands of the Calcon-metal complexes is similar. Each of the Calcon-metal complexes SERS spectra shown in Fig.5 present a characteristic spectral fingerprint.

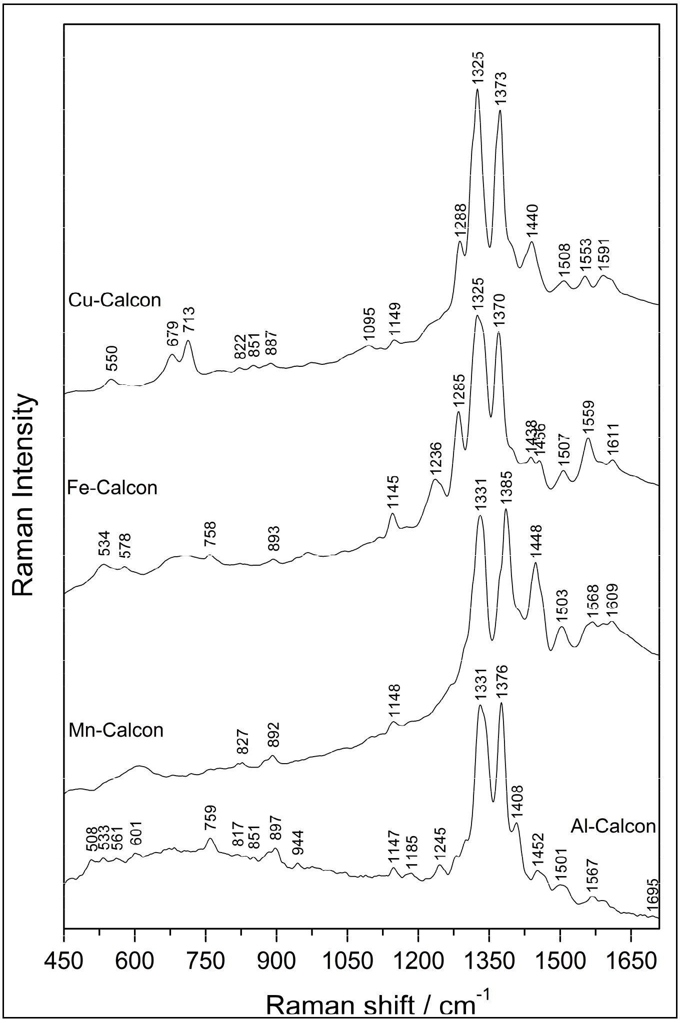

**Fig. 5.** SERS spectra of Calcon–Al(III), –Mn(II), –Fe(III) and –Cu(II) complexes, prepared at Calcon:metal salt molar ratio of 1:1.

Below are given some of the SERS marker bands for each Calcon-metal complex: 1185, 1245, 1331, 1376, 1408, 1452, 1567 cm$^{-1}$ for the Calcon-Al(III); 1148, 1331, 1385, 1448, 1503, 1568, 1609 cm$^{-1}$ for the Calcon-Mn(II); 1145, 1236, 1285, 1325, 1370, 1438, 1507, 1559 cm$^{-1}$ for the Calcon-Fe(III); 1095, 1149, 1288, 1325, 1373, 1440, 1508, 1591 cm$^{-1}$ for the Calcon-Cu(II). The spectral fingerprint of each complex will be further used for the identification of the heavy metal ions.

## CONCLUSIONS

Optimized geometry, molecular electrostatic potential (MEP) and normal modes of Calcon molecule were calculated by theoretical DFT B3LYP/6-31G(d) methods. The FTIR and FT-Raman spectra of Calcon were safely assigned, due to a good match between experimental and DFT calculated vibrational modes.

The calculated MEP distributions indicate for the Calcon molecule the highest electronegativity localized on the $SO_3H$ group, thus, the adsorption to the silver surface is supposed to occur by this group.

Each Calcon-metal complex SERS spectrum shows a characteristic spectral fingerprint, permitting thus a safe discrimination between Calcon-metal ion complexes. Therefore Calcon can be employed for the identification of the heavy metal ions by using SERS method. This study creates perspectives for determining the presence of heavy metal ions in real life samples, e.g. contaminated soils or dairy products.

## ACKNOWLEDGMENT

This work was supported by CNCSIS-UEFISCSU, project number PN II RU PD_445/2010.

## REFERENCES

[1] A.A. Ensafi, M. Fouladgar, Sens. Actuators B, 113 (2006) 88.

[2] P.C.A. Jeronimo, A.N. Araujo, M. Conceicao, B.S.M. Montenegro, Sens. Actuators B, 103 (2004) 169.

[3] P.C.A. Jeronimo, A.N. Araujo, M.C.B.S.M. Montenegro, C. Pasquini, I.M. Raimundo Jr, Anal. Bioanal. Chem., 380 (2004) 108.

[4] Theoretical Basis of Analysis: Complexometric Titrations, Dr. Asif Husain, Lecturer, Dept. of Pharmaceutical Chemistry, Faculty of Pharmacy, New Delhi-**2007**.

[5] Jacques Boxer, Clinica Chimica Acta, 5, 1 (1960) 82.

[6] R. Kocjan, S. Przeszlakowski, Talanta 39, 1 (1992) 63.

[7] G.C. Schatz, R.P. Van Duyne, Electromagnetic Mechanism of Surface-Enhanced Spectroscopy, in J.M. Chalmers, P.R. Griffiths (Eds.), Handbook of Vibrational Spectroscopy, 759 – 774, Wiley, New York, **2002**.

[8] K. Kneipp, H. Kneipp, I. Itzkan, R.R. Dasari, M.S. Feld, Chem. Rev., 99 (1999) 2957.

[9] K. Kneipp, H. Kneipp, H.G. Bohr, Top. Appl. Phys., 103 (2006) 261.

[10] N. Leopold, S. Cîntă Pînzaru, M. Baia, E. Antonescu, O. Cozar, W. Kiefer, J. Popp, Vib. Spectrosc., 39 (2005) 16.

[11] L.G. Crane, D.X. Wang, L.M. Sears, B. Heyns, K. Carron, Anal. Chem. 67 (1995) 360.

[12] K. Carron, K. Mullen, M. Lanouette, H. Angersbach, Appl. Spectrosc., 45 (1991) 420.

[13] N. Leopold, L. Szabó, A. Pîrnău, M. Aluaş, L.F. Leopold, V. Chiş, O. Cozar, J. Mol. Struct., 919 (2009) 94.

[14] László Szabó, Krisztian Herman, Nicolae Leopold, Vasile Chiş, Spectrochimica Acta Part A, 79 (2011) 226.

[15] N. Leopold, B. Lendl, J. Phys. Chem. B, 107 (2003) 5723.

[16] Gaussian 03, Revision E.01, M. J. Frisch, G.W. Trucks, H.B. Schlegel, G.E. Scuseria, M.A. Robb, J.R. Cheeseman, J.A. Montgomery, Jr., T. Vreven, K.N. Kudin, J.C. Burant, J.M. Millam, S.S. Iyengar, J. Tomasi, V. Barone, B. Mennucci, M. Cossi, G. Scalmani, N. Rega, G.A. Petersson, H. Nakatsuji, M. Hada, M. Ehara, K. Toyota, R. Fukuda, J. Hasegawa, M. Ishida, T. Nakajima, Y. Honda, O. Kitao, H. Nakai, M. Klene, X. Li, J.E. Knox, H.P. Hratchian, J.B. Cross, V. Bakken, C. Adamo, J. Jaramillo, R. Gomperts, R.E. Stratmann, O. Yazyev, A.J. Austin, R. Cammi, C. Pomelli, J.W. Ochterski, P.Y. Ayala, K. Morokuma, G.A. Voth, P. Salvador, J.J. Dannenberg, V.G. Zakrzewski, S. Dapprich, A.D. Daniels, M.C. Strain, O. Farkas, D.K. Malick, A.D. Rabuck, K. Raghavachari, J.B. Foresman, J.V. Ortiz, Q. Cui, A.G. Baboul, S. Clifford, J. Cioslowski, B.B. Stefanov, G. Liu, A. Liashenko, P. Piskorz, I. Komaromi, R.L. Martin, D.J. Fox, T. Keith, M.A. Al-Laham, C.Y. Peng, A. Nanayakkara, M. Challacombe, P.M. W. Gill, B. Johnson, W. Chen, M.W. Wong, C. Gonzalez, and J.A. Pople, Gaussian, Inc., Wallingford CT, **2004**.

[17] A.D. Becke, J. Chem. Phys., 98 (1993) 5648.

[18] C. Lee, W. Yang, R.G. Parr, Phys. Rev. B, 37 (1988) 785.

[19] P.L. Polavaru, J. Phys. Chem., 94 (1990) 8106.

[20] V. Krishnakumar, G. Keresztury, T. Sundius, R. Ramasamy, J. Mol. Struct., 702 (2004) 9.

[21] S.D. Williams, T.J. Johnson, T.P. Gibbons, C.L. Kitchens, Theor. Chem. Acc., 117 (2007) 283.

[22] A.P. Scott, L. Radom, J. Phys. Chem., 100 (1996) 16502.

[23] C.F. Leypold, M. Reiher, G. Brehm, M. O. Schmitt, S. Schneider, P. Matousek, M. Towrie, Phys.Chem.Chem.Phys., 5 (2003) 1149.

[24] P. Politzer, D.G. Truhlar, (Eds.), Chemical Application of Atomic and Molecular Electrostatic Potentials, Plenum, New York, **1981**.

STUDIA UBB PHYSICA, LVI, 2, 2011

# THE EFFECT OF THE PROJECTILE'S CHARGE ON THE IONIZATION OF $N_2$ BY ELECTRON AND POSITRON IMPACT

**TÓTH I.**[1], **NAGY L.**[1,*]

**ABSTRACT** Triple differential cross sections for the ionization of molecular nitrogen by electron and positron impact are presented. In case of electron projectiles, the results are in agreement with the experimental data, especially for lower ejected electron energies. Since there are no measurements available for positron projectiles, we compare our results with the corresponding electron cross sections. The comparison shows interesting differences regarding the size and angular distribution of the electron and positron cross sections.

***Keywords*** *electron, positron, ionization, triple differential cross section*

## INTRODUCTION

In the last years a growing interest has been observed for kinematically complete collision phenomena. Such studies provide the most detailed information package about the ionization process, allowing for the tracking of every particle in the system. The physical quantity of interest in these processes is the TDCS (triple differential cross section), which describes the angular distribution of the ejected electron of a given energy, while the momenta of the incident and scattered particles are fixed. The ionization of molecular nitrogen by charged particles is particularly important from the perspective of atmospheric sciences, but is equally important in newly emerging fields like interstellar chemistry.

Experimental and theoretical studies have been performed for the ionization of several molecular targets by electron impact. We mention here only a few studies for simpler targets like $H_2$ [1, 2], $O_2$ [3], $N_2$ [4-6] or more complex structures like $CH_4$ [7], $H_2O$ [8], $C_2H_2$ [9] or $C_4H_8O$ [10]. Similar studies for the ionization of atomic and molecular targets by positron projectiles are less abundant (e.g. Ar [11] and $H_2$ [12-14]), given the relatively low intensities of the projectile's beam in this case.

The present study shows calculations in the framework of the DWBA (distorted-wave Born approximation) method for positron impact ionization of molecular nitrogen and a comparison of the results with the corresponding

---

[1] *Babes-Bolyai University, Faculty of Physics, 400084 Cluj-Napoca, Romania.*

[*] *E-mail: lnagy@phys.ubbcluj.ro*

electron TDCSs, in order to identify the effects of the projectile's charge on the cross section. Our electron impact ionization TDCS were recently published [16] and were compared with the relative experimental data and the theoretical results of the FBA-TCC (first Born approximation-two-center continuum) and M3DW-OAMO (molecular three-body distorted-wave coupled with an orientation-averaged molecular orbital approximation) models, presented in [6].

## THEORETICAL DETAILS

Since the theoretical background for the calculation of the TDCS for a molecular target was described previously in detail [15, 16], here we present only the main stages of the theoretical treatment. In the framework of the DWBA method the TDCS for the ionization of a given molecular orbital may be written in the following form

$$\frac{d^3\sigma}{d\hat{k}_f d\hat{k}_e dE_e} = 2(2\pi)^4 \frac{k_f k_e}{k_i} |t|^2 . \tag{1}$$

Here, $k_f$, $k_e$ and $k_i$ are the wave-vectors of the scattered, ejected and incident particles, respectively. $E_e$ is the energy of the ejected electron, $t$ stands for the transition matrix element of the system. The transition matrix element may be expressed as shown below

$$|t|^2 = |t_d|^2 + |t_{ex}|^2 - |t_d||t_{ex}| . \tag{2}$$

In case of positron impact ionization there is no exchange interaction between the outgoing particles, therefore $t = t_d$ . The direct and exchange terms may be expressed as

$$t_d = \left\langle \phi_f(\vec{r}_1)\phi_e(\vec{r}_2) \middle| -\frac{Z}{r_{12}} \middle| \phi_b(\vec{r}_2)\phi_i(\vec{r}_1) \right\rangle \tag{3}$$

$$t_{ex} = \left\langle \phi_e(\vec{r}_1)\phi_f(\vec{r}_2) \middle| -\frac{Z}{r_{12}} \middle| \phi_b(\vec{r}_2)\phi_i(\vec{r}_1) \right\rangle , \tag{4}$$

where in the exchange term the position vectors of the outgoing electrons are exchanged relative to the direct term. In the expression (3) of the direct transition matrix element $Z = \pm 1$ is the charge of the projectile, $r_1$ and $r_2$ are the position vectors of the projectile and active electron, respectively. $r_{12}$ stands for the distance between the projectile and the active electron. The wavefunctions of the continuum states, $\phi_f, \phi_e$ and $\phi_i$, are expanded into partial wave series in order to separate the radial and orbital parts. The initial, bound state of the active electron is denoted by $\phi_b$ , which is a multi-center Gaussian-type wavefunctions. The Gaussian-type wavefunction for a molecular orbital is constructed as a linear combination of the constituent atomic wavefunctions, while the atomic wavefunctions are expressed in terms of contracted Gaussian primitives. In order to simplify the calculations, we expand the multi-centre initial wavefunction into a series of the Legendre polynomials,

$$\phi_b = \sum_{l_b} c_{l_b}(r_2, R_0) P_{l_b}(\cos\omega). \tag{5}$$

Here, $c_{l_b}$ are the expansion coefficients. We expand also the interaction term between the projectile and the active electron into the multipole series. These expansions are then used to calculate the direct and exchange transition matrix elements, similarly as in [15] and [16].

Since in the experimental setup the measurements are usually not performed for a fixed orientation of the molecular target, we average the TDCS over all orientations of the molecular axis.

The TDCSs are determined within the TS* (Total Screening) model. In this model we neglect the influence of the ejected electron on the scattered one. Both final state free particles move in the same potential field, i. e. in the spherically averaged potential of the residual ion as shown below for electron and positron projectiles.

$$V_e = -V_{nuclei} + V^{-}_{electrons} \tag{7}$$

$$V_f = \mp V_{nuclei} \pm V^{-}_{electrons} \tag{8}$$

Above, we assume that the scattered particle is the faster one. Here, $V_{nuclei}$ and $V^{-}_{electrons}$ stand for the spherically averaged potential of the nuclei and the residual electrons, respectively. It may be noted that the averaging method employed here was described elsewhere [17]. However, we briefly describe the averaging method of the nuclear potential, since it is necessary for the discussion of the obtained result. We have "rotated" the molecule around the center of mass in all possible directions. By this procedure the nuclear charge is uniformly distributed on the surface of a sphere with a radius $R = R_0/2$, $R_0$ being the average internuclear distance.

## RESULTS AND DISCUSSION

We have calculated TDCSs for the ionization of the molecular nitrogen by electron and positron impact. The TDCSs were calculated for the outer valence orbitals ($3\sigma_g$, $1\pi_u$, $2\sigma_u$) and for the inner $2\sigma_g$ orbital of the nitrogen molecule. The ionization potentials corresponding to these molecular orbitals are: 15.6 eV, 16.7 eV, 18.75 eV and 37.9 eV, respectively. The TDCSs were calculated for the kinematical conditions given in [6], that is, for a scattering angle of –6 degrees and for $E_f$ = 500 eV, where $E_f$ is the energy of the scattered particle. In our study we have investigated the angular distribution of the ejected electron for 37 eV, 74 eV and 205 eV energies. Since the chosen kinematics correspond to a large recoil ion momentum, which suggests a strong participation of the recoiling ion in the ionization process, we have calculated TDCSs also for an enhanced residual ion–ejected electron interaction by introducing an adjustable parameter, which modulates the nuclear potential created by the nuclei.

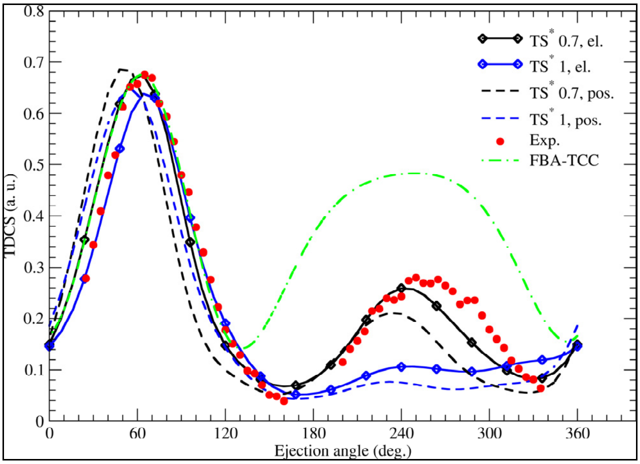

**Fig. 1.** Weighted sum of the TDCSs corresponding to the outer orbitals of $N_2$ for electron and positron impact ionization at $E_e$ = 37 eV.

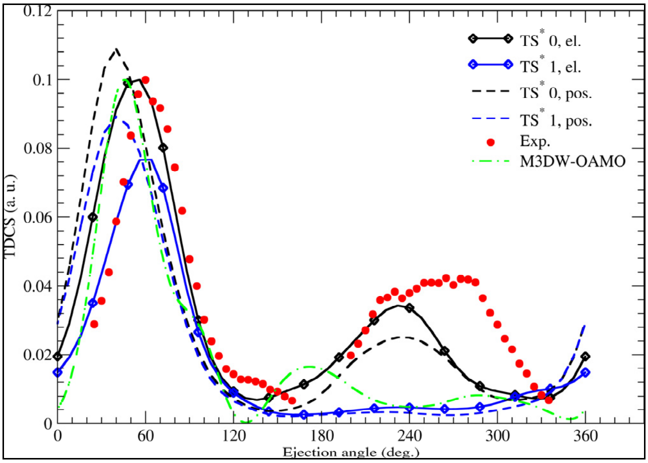

**Fig. 2.** Same as Fig. 1, but for $E_e$ = 74 eV.

This parameter represents the fraction of the original radius of the sphere on which the nuclear charge is located after the averaging process of the nuclear potential. By decreasing this parameter, we obtain a stronger nuclear potential and consequently an enhanced residual ion – ejected electron interaction, which may lead to a more pronounced recoil peak in the TDCS. This adjustable parameter is represented by a number in the figure legends. For example, 0.7 means 0.7 × $R$. On every figure the experimental data, the results of the FBA-TCC and M3DW-OAMO models are normalized at the binary peak maximum to one of our TDCSs, which corresponds to the best value of the adjustable parameter. According to [6] the outer orbitals, $3\sigma_g$, $1\pi_u$, and $2\sigma_u$, could not be resolved at the chosen energy resolution, therefore the experimental data represents a weighted sum of these orbitals with relative efficiencies of 1, 0.78 and 0.32, respectively.

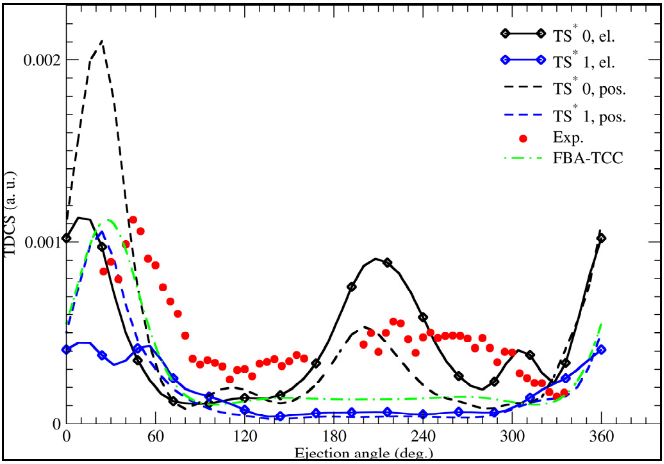

**Fig. 3.** Same as Fig. 1, but for $E_e$ = 205 eV.

Figures 1-3 present the weighted sum of the TDCSs for the outer orbitals in case of electron and positron projectiles. We observe that for all energies considered in this study the positron cross sections are higher at the binary peak, while in the region of the recoil peak the electron TDCSs are higher. This behavior is more pronounced for higher ejected electron energies, while at 37 eV the electron and positron cross sections show almost identical values, especially in case of the binary peak maximum. Further, it may be observed that in case of positron projectiles, the binary peak of the TDCS is shifted to smaller ejection angles relative to the TDCSs obtained for electron projectiles, except for the highest ejected electron energy, where the (TS*, 0) model shows an opposite behavior. The higher values for positron projectile at the binary region may be the effect of the attraction between the scattered positron and the ejected electron, which increases the probability of ejection in the binary region. The shift of the TDCS toward lower angles in case of positron projectiles may be related to the post collision interactions between the outgoing particles. In this particular case, the positron projectile pulls the ejected electron toward the forward direction, causing the shift of the TDCS to lower ejection angles. We note that a similar behavior was observed previously also for molecular hydrogen [14]. It seems that at the highest energy this is not true. It may be that at this energy, the shift of the electron cross section toward lower angles relative to the positron cross section is the effect of the more pronounced exchange effects between the two outgoing electrons.

Concerning the agreement of the electron TDCSs with the experimental data, we may state that for the lowest ejected electron energy, the agreement is very good in case of the (TS* 0.7) model. This model gives the correct recoil-to-binary peak ratio, while the FBA-TCC model provides a higher ratio than the experimental one. At 74 eV, in figure 2 the agreement between our (TS* 0) and the experimental data is good, although the calculated TDCS is slightly shifted to lower angles relative to the experimental one. Nevertheless, this model reproduces correctly the experimental recoil-to-binary peak ratio, while the M3DW-OAMO model shows a lower and a very different recoil peak compared to the experiment. This ratio is higher in case of the (TS* 0) model for electrons ejected at 205 eV than the experimental one and the binary peak is shifted to lower ejection angles compared to the measured binary peak. For all energies, the (TS* 1) model for electron projectiles gives correctly the position of the binary peak. At the highest energy, this model shows a split of the binary peak, which is not showed by the other models. Since there are no experimental points for angles lower than 25 degrees, this prediction of our model cannot be verified.

We note here that by increasing the ejected electron energy, we had to increase also the nuclear potential. This was achieved by decreasing the value of the earlier introduced adjustable parameter. In this way, we have obtained also the recoil peak of the TDCS. However, the position of the binary peak is reproduced correctly for all energies by the (TS* 1) model, which works with the unmodified, spherically averaged potential of the target. Although there are no experimental data for positron TDCSs, we may observe a similar behavior of our models in case of the opposite charges of the projectile. In both cases the (TS* 1) shows no recoil intensity at all, while the increased nuclear potential leads to the appearance of the recoil peak in case of the other models employed here.

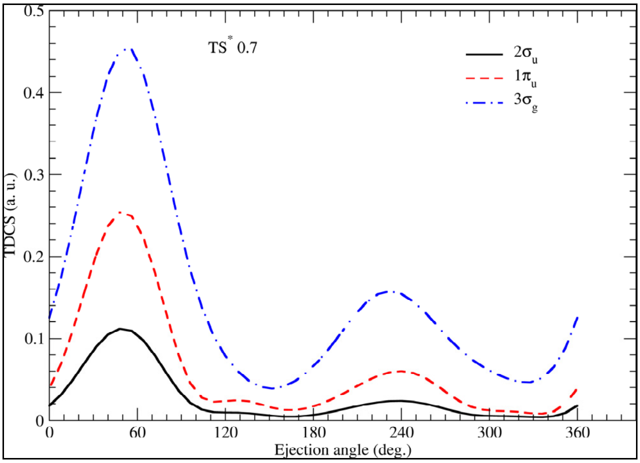

**Fig. 4.** TDCSs for the ionization of the outer orbitals of $N_2$ by positron impact in case of the (TS* 0.7) model and for $E_e$ = 37 eV.

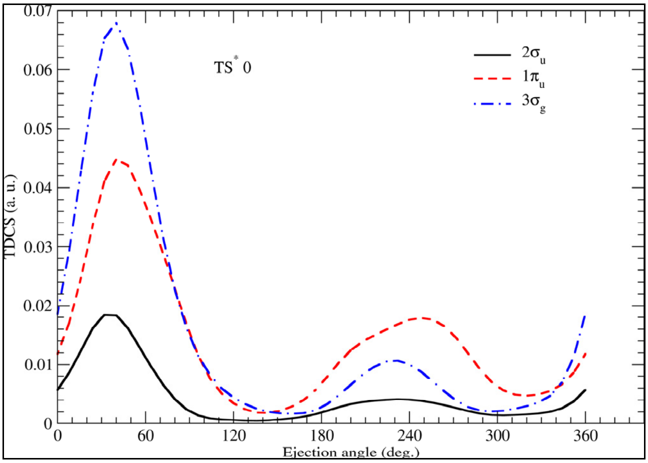

**Fig. 5.** Same as Fig. 4, but for the (TS* 0) model and $E_e$ = 74 eV.

In figures 4 – 6 we present the TDCSs for the outer orbitals separately and for the best values of the adjustable parameter. At 37 eV, in figure 4 we observe that the cross section corresponding to the $3\sigma_g$ orbital shows the highest values, followed by the TDCS of the $1\pi_u$ orbital and finally the $2\sigma_u$ orbital, which means that the shape and size of the weighted sum of the TDCSs is largely determined by the $3\sigma_g$ orbital. In figure 5, for an ejected electron energy of 74 eV, one may observe a similar situation at the binary peak, but at the recoil region the dominant term comes from the $1\pi_u$ orbital. Figure 6 shows a similar situation as figure 4, that is, the main contributor to the weighted sum of the outer valence orbitals is the $3\sigma_g$ orbital.

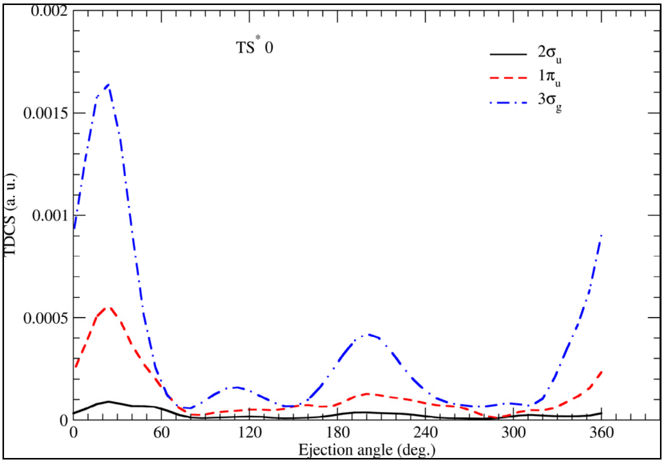

**Fig. 6.** Same as Fig. 4, but for the (TS* 0) model and $E_e$ = 201 eV.

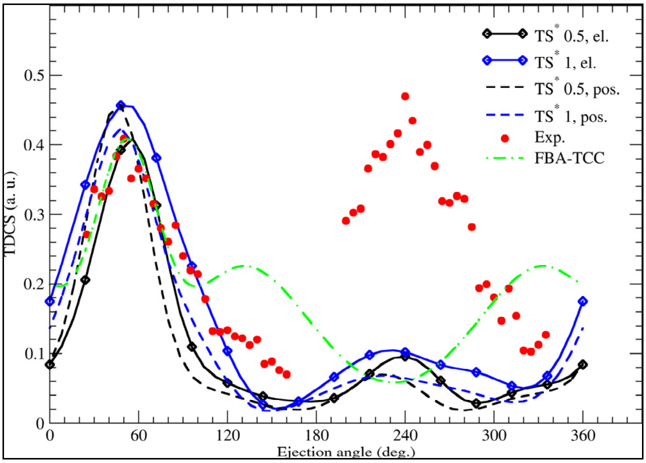

**Fig. 7** TDCSs for the ionization of the inner orbital of $N_2$ by electron and positron impact. $E_e$ = 37 eV.

Our results for the inner $2\sigma_g$ orbital are presented in figures 7 - 9. The most striking observation in case of electron impact ionization is the large recoil intensity of the experimental TDCS, which suggests a strong nuclei-ejected electron interaction and consequently an important role of the recoiling ion in the ionization process. This behavior is not reproduced by any of our models. However, we have obtained recoil intensity for all ejected electron energies considered here, while the FBA-TCC and the M3DW-OAMO model show a minimum at this region for lower energies of the ejected electron. The position of the binary peak is given relatively correctly by all the employed models. It seems that for the inner orbital, our spherically averaged potentials are not suitable when describing the recoil process. The proximity of the nuclei and the two-center nature of the target suggest a more complex and stronger interaction between the ejected electron and the residual ion than our models are able to reproduce.

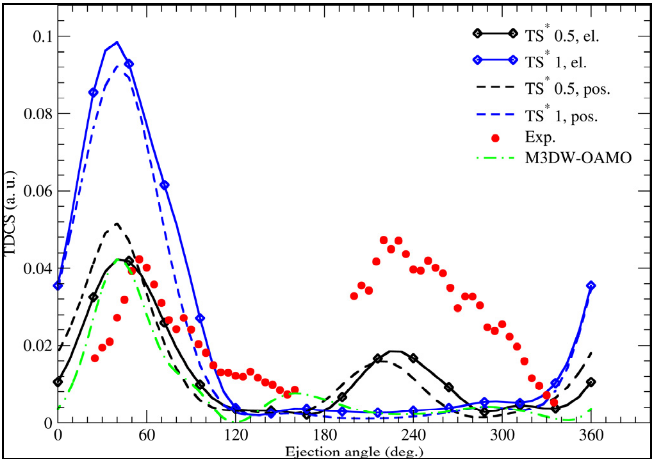

**Fig. 8** Same as Fig. 7, but for $E_e$ = 74 eV.

The positron and electron cross sections show similarities but also differences compared to the outer orbitals. At 37 eV and 74 eV, our (TS* 0.5) models behave similarly as found earlier for the weighted sum of the outer orbitals, that is, the positron cross sections are higher at the binary peak than the electron cross sections, while at the recoil peak the opposite is true. We also found that the positron TDCSs are shifted to lower angle values relative to the electron cross sections at these energies. Nevertheless, the (TS* 1) model gives smaller binary peaks for positron projectiles compared to the electron case. At the highest energy of the ejected electron, both the (TS* 0) and the (TS* 1) models provide smaller binary peak values for the positron TDCS relative to the electron TDCS. However, for all energies, the recoil peak of the electron TDCS is higher than the corresponding peak of the positron TDCS.

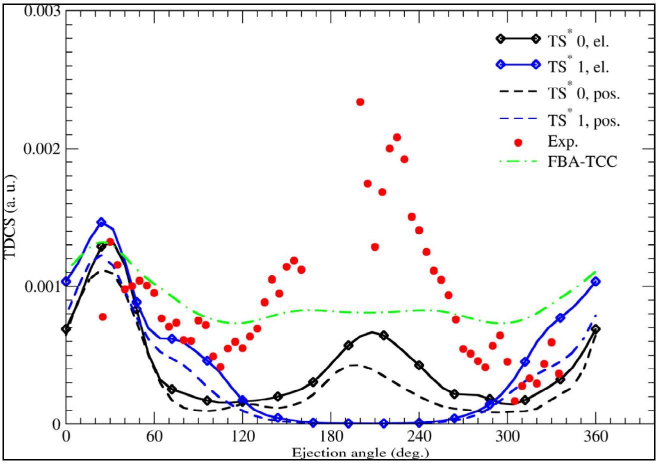

**Fig. 9** Same as Fig. 7, but for $E_e$ = 205 eV.

## CONCLUSIONS

We have determined triple differential cross sections for the ionization of the nitrogen molecule by electron and positron impact. Our calculations were performed in the framework of the DWBA model. The cross sections were obtained within a simple ionization model, named TS*, in which we have employed spherically averaged nuclear and electronic potentials in order to calculate the radial wavefunctions of the incident, ejected and scattered particles. The experimental data in case of the ionization by electron projectiles are given for a large ion recoil momentum, which means a strong participation of the recoiling ion in the ionization process. In order to counterbalance the effect of our spherically averaged potentials used in our model, we have performed TDCS calculations also for an enhanced nuclear potential. In this way we have obtained a stronger nuclei-ejected electron interaction, which led to the appearance of the recoil peak of the TDCS. By this method, we have obtained a good agreement with the experimental data (the weighted sum of the TDCS for the outer molecular orbitals), especially for lower ejected electron energies, while for the highest energy, the TDCS is shifted toward lower ejection angles relative to the experimental TDCS. This shift may be the effect of the post collision interaction between the outgoing particles.

The comparison of the electron and positron TDCSs has shown that the positron cross section is usually higher at the binary peak than the electron cross section, while at the recoil peak the opposite situation is true. However, we found an exception at the highest electron energy considered in this study and in case of the inner orbital of the molecule. In this case the attraction of the positron on the electron may not be enough to counterbalance the effect of the strong potential created by the nearby centers of the molecular target in order to pull the electron in the forward direction. We also found that especially for lower electron energies, the positron cross sections are shifted to smaller ejection angles relative to the electron TDCSs. This behavior may be explained by considering the post collision effects between the outgoing particles. In this particular case, the positron pulls the ejected electron toward the forward direction, leading to the shift of the TDCS.

## ACKNOWLEDGEMENTS

This work was possible with the financial support of the Sectoral Operational Programme for Human Resources Development 2007-2013, co-financed by the European Social Fund, under the project number POSDRU 89/1.5/S/60189 with the title "Postdoctoral Programs for Sustainable Development in a Knowledge Based Society". (I. Tóth)

This work was supported by a grant of the Romanian National Authority for Scientific Research, CNCS - UEFISCDI, project number PN-II-ID-PCE-2011-3-0192 (L. Nagy)

## REFERENCES

1. O. Al Hagan, C. Kaiser, D. Madison, A. J. Murray, Nature Phys., 5, 59–63 (2009).
2. E.M. Staicu Casagrande et al, J. Phys. B: At. Mol. Opt. Phys., 41, 025204, (2008).
3. J. Yang, J.P. Doering, Phys. Rev. A, 63, 032717 (2001).
4. J.P. Doering, J. Yang, Phys. Rev. A, 60, 2176–81 (1999).
5. A. Naja, E.M. Staicu Casagrande, A. Lahmam-Bennani, M. Nekkab, F. Mezdari, B. Joulakian, O. Chuluunbaatar, D.H. Madison, J. Phys. B: At. Mol. Opt. Phys., 40, 3775–83 (2007).
6. A. Lahmam-Bennani, E.M. Staicu Casagrande, A. Naja, J. Phys. B: At. Mol. Opt. Phys., 42, 235205 (2009).

7. A. Lahmam-Bennani, A. Naja, E.M. Staicu Casagrande, N. Okumus, C. Dal Capello, I. Charpentier, S. Houamer, J. Phys. B: At. Mol. Opt. Phys., 42, 165201 (2009).
8. D.S. Milne-Brownlie, S.J. Cavanagh, B. Lohmann, C. Champion, P. A. Hervieux, J. Hanssen, Phys. Rev. A, 69, 032701 (2004).
9. L. Avaldi, R. Camilloni, G. Stefani, Phys. Rev. A, 41, 134 (1990).
10. C.J. Colyer, S.M. Bellm, B. Lohmann, G.F. Hanne, O. Al Hagan, D.H. Madison, C. G. Ning, J. Chem. Phys., 133, 124302 (2010).
11. O.G. de Lucio, S. Otranto, R.E. Olson, R.D. DuBois, Phys. Rev. Lett., 104, 163201 (2010).
12. Á. Kövér, G. Laricchia, Phys. Rev. Lett., 80, 5309-5312 (1998).
13. J. Fiol, R.E. Olson, J. Phys. B: At. Mol. Opt. Phys., 35, 1173–1184 (2002).
14. Á. Benedek, R.I. Campeanu, Nucl. Instrum. Methods B 266, 458-461 (2008).
15. I. Toth, L. Nagy, J. Phys. B: At. Mol. Opt. Phys., 43, 135204 (2010).
16. I. Toth, L. Nagy, J. Phys. B: At. Mol. Opt. Phys., 44, 195205 (2011).
17. I. Toth I, R.I. Campeanu, V. Chi□, L. Nagy, Phys. Lett. A, 360, 131–4 (2006).

STUDIA UBB PHYSICA, LVI, 2, 2011

# UV VIS BEHAVIOR OF DOPED PVA $TiO_2$ MEMBRANES UNDER GAMMA IRRADIATION

**L. UDRESCU[1], E. DINTE[2], C. V. POP[1], T. STEFAN[1], M. TODICA[1,*]**

**ABSTRACT.** The UV-VIS absorption properties of PVA-$TiO_2$ composite materials $\gamma$ irradiated were investigated in function of concentration of $TiO_2$ and the dose of radiation. The UV absorbance of unirradiated samples increases with the concentration of $TiO_2$. Important modifications of this property appear after $\gamma$ irradiation.

***Keywords:*** *PVA, $TiO_2$, gamma irradiation*.

## INTRODUCTION

In the last decades the Poly (vinyl alcohol) (PVA) is one of the most used polymers in pharmaceutical industry as matrix for the active medical drugs, due to its high hydrophilic properties, good film forming by solution casting, compatibility with the biological tissues and high biodegradability [1, 2]. One of the requirements frequently asked to these materials is the good protection against UV radiation. PVA provides only a weak protection in the domain 290 nm, but inclusion of some inorganic materials provides high absorbance in desired domains of the light spectrum. $TiO_2$ is one of the inorganic fillers widely used for this purpose due to its chemical stability in contact with the biological liquids, high refractive index, hydrophilicity, UV resistance. In addition, $TiO_2$ is a very good antibacterian product. During the medical applications, especially in the skin care, the polymeric matrix may be deliberately or accidentally exposed to gamma radiation. Such high energy radiation can have strong effects on the microscopic structure of the polymer such as ionization of the atoms, chain scission or cross-linking, crystallization and local order arrangement. Frequently these processes are followed by modifications of some physical properties like the microstructure or the refractive index.

Our interest was the observation the behavior of the initial polymeric matrix and of the composite material PVA – $TiO_2$ before and after different doses of gamma radiations. The observations were made by UV-VIS.

---

[1] *Babeş-Bolyai University, Faculty of Physics, 1 Kogălniceanu str., 400084 Cluj-Napoca, Romania.*
** corresponding author e-mail: mihai.todica@phys.ubbcluj.ro*

[2] *University of Medicine and Pharmacy, Faculty of Pharmacy, Cluj-Napoca, Romania*

## EXPERIMENTAL

PVA was chosen because its solubility in water and capacity to form aqueous gels. For ours studies we used PVA membrane with 20% polymeric concentrations, obtained from aqueous PVA gels. The gels were obtained by mixing the polymer with distilled water, at constant temperature $55^0$ C, during 3 hours, until a homogeneous dispersion of polymer is obtained. Then the $TiO_2$ was added to these gels in different concentrations 1%, 10%, 20%, and the components were mixed many hours at room temperature. Then the composition was displayed on a glass plate and kept 24 hours in dark, at room temperature, until the water evaporates. These samples were analyzed in their original state and after gamma exposure. The gamma exposure was realized with $^{60}$Co source with the flux 5,6 Gy/h, different time intervals corresponding to 739 Gy, 1478 Gy and 2200 Gy doses [3]. For all the samples the UV VIS investigation was done with Jasco V-670 system with scan speed 200 nm/min, UV VIS bandwidth 2 nm, and NIR bandwidth 8 nm.

## RESULTS AND DISCUSSION

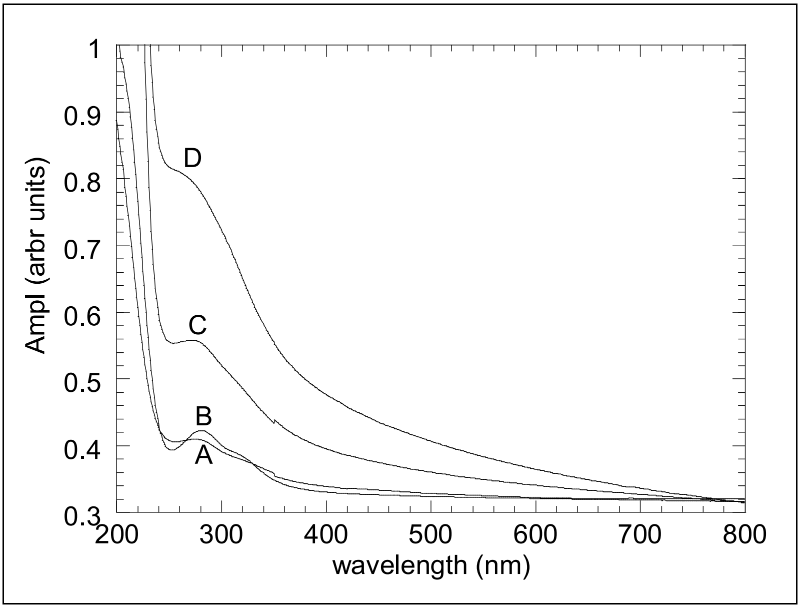

**Fig. 1.** The UV-VIS absorption spectra for the un doped membrane and membranes with different content of $TiO_2$, before irradiation: the un doped membrane (curve A); composite membrane with 1% $TiO_2$ (curve B); composite membrane with 10% $TiO_2$ (curve C); composite membrane with 20% $TiO_2$ (curve D)

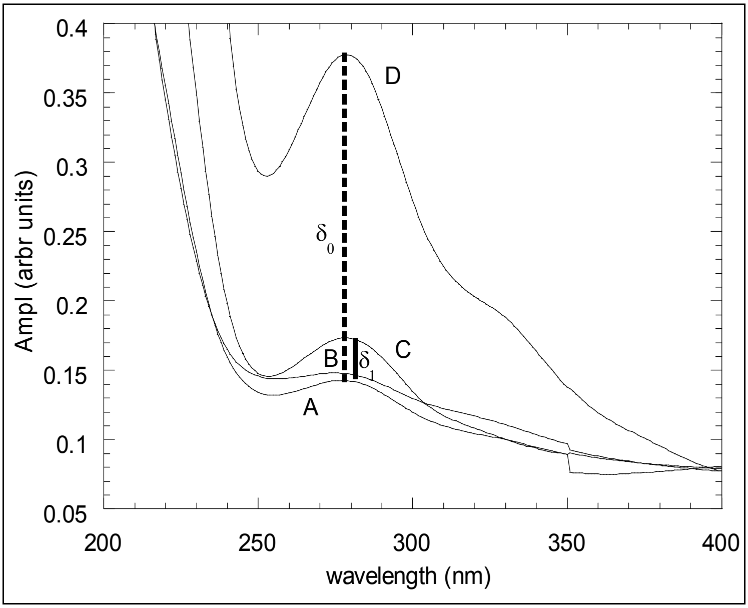

**Fig. 2.** The UV-VIS absorption spectra for the un doped membrane and membranes with different content of $TiO_2$, before and after irradiation: the un doped membrane before irradiation (curve A); PVA membrane with 1% $TiO_2$ before irradiation
(curve B); with 1% $TiO_2$ after irradiation (curve C); the un doped membrane after irradiation (curve D)

Due to its affinity towards water, PVA can form aqueous gels with different polymeric concentration. The absorption coefficient of the light depends on the polymer-water concentration of the initial gel [4]. In previous work we analyzed this dependence and we shown that shape of the absorption UV-VIS spectra is similar for a large domain of polymeric concentration, the only difference being the amplitude of the absorption peak [5]. For medical application the most suitable sample corresponds to the polymeric concentration of the initial gel 20%, and for this reason we limited our study to this system. The absorbance is very weak in the wavelength range 600-400 nm, followed by a continuous increase in the domain 350-250 nm, with a maximum at 285 nm. Containing only single bonds, the PVA membranes would be expected to absorb radiation only in the far UV region (120-200 nm). The presence of the peak at 285 nm must be explained taking into account the morphology of local structure and the residual water content determined by the method of preparation of PVA polymer. PVA is obtained by hydrolysis or partial hydrolysis of polyvinyl acetate [6]. Thus the absorption band at 285 nm may be assigned to $\pi \rightarrow \pi^*$ transition of the carbonyl groups (C=O) associated with ethylene unsaturation (C=C) of the type – $(CH=CH)_2CO$ –. The existence of carbonyl functionalities is probably due to residual acetate groups remaining after hydrolysis of polyvinyl acetate or oxidation during manufacturing [7, 8, 9]. The chemical reaction is accompanied by formation of water molecules from the components resulting from the chemical reaction of polymerization. Knowing the important absorbance of water in the UV domain, we can explain the presence of absorption peak at 285 nm by the existence of some amount of water in the PVA membranes.

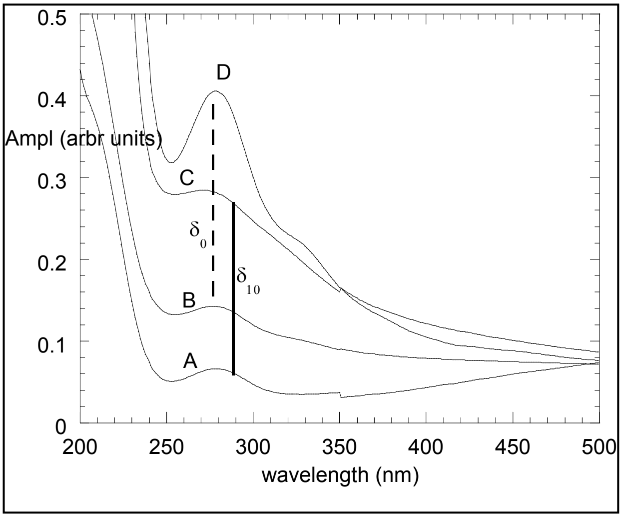

**Fig. 3.** The UV-VIS absorption spectra for the un doped membrane and membranes with different content of $TiO_2$, before and after irradiation: membrane with 10% $TiO_2$ after irradiation (curve A); the un doped membrane before irradiation (curve B); with 10% $TiO_2$ before irradiation (curve C); the un doped membrane after irradiation (curve D)

Inhancement of the absorption in UV is obtained by addition of $TiO_2$. The shape of the absorption spectra of the composite membranes is similar with that of the pure PVA membranes without supplementary absorption peaks but the amplitude of the absorption peaks increases continuously with the amount of $TiO_2$ (Fig 1). At 1% $TiO_2$ concentration, the contribution of $TiO_2$ filler to the absorbance is very small and the spectra of composite and of pure PVA membranes are practically identical. At 10% $TiO_2$ concentration, the amplitude of the peak is more than two times greater, and at 20% $TiO_2$ concentration this amplitude is more than three times greater than the amplitude of pure PVA (the amplitude is measured from the baseline). This fact demonstrates clearly the contribution of $TiO_2$ to the absorption property. Similar effect was observed previously in the other systems, i.e. tacrolimus - $TiO_2$ [10]. Then we irradiated all the samples, the PVA pure membrane and the composite samples, at different doses of $\gamma$ radiation, and we measured the absorbance in the UV-VIS domain. For pure PVA membrane, the UV absorbance increases continuously with the dose of radiation [11]. The possible explication is the breaking of OH and C-OH bonds of PVA with the apparition of $H^+$ and $OH^-$ ions and formation of water molecules [12]. This process is followed by the scission of the chain with respect the reduction of length of the polymeric chains. The resulting water is trapped in the polymeric matrix that is equivalent with the increase of amount of residual quantity of water in the polymeric matrix. As we shown in previous works, the absorbance in UV domain increases with the amount of residual water in PVA membranes [11]. This effect is determined by the high absorbance of water in UV domain.

The PVA – $TiO_2$ composite samples with 1% $TiO_2$ show similar behavior, but the increase of UV absorbance for this concentration of $TiO_2$ after irradiation is less important than for PVA membrane. For instance, the difference between the amplitude of the absorption peak of the irradiated and un irradiated doped membrane is $\delta_1 \sim 0{,}05$, whereas the same difference for the un doped membrane is $\delta_0 \sim 0{,}20$ (Fig. 2). Some mechanisms may to be considered to explain the UV absorption for this concentration of $TiO_2$: a) the increase of the UV absorbance determined by $TiO_2$; b) the breaking of the chains with the apparition of new molecules of water; c) evaporation of residual water trapped in the PVA matrix. At this concentration of $TiO_2$, the effect of nanoparticles on the absorbance is limited. We can see this fact from figure 1, where the spectra of pure PVA and PVA + 1% $TiO_2$ before irradiation are very close. If $TiO_2$ should not absorb $\gamma$ radiation and all the flux of radiation should interact with PVA polymeric chain, then the spectrum of composite material after irradiation should be similar to those of the pure PVA after irradiation. However these spectra are very different, the absorbance of composite material after irradiation being reduced compared with the absorbance of pure PVA after irradiation (Fig. 2). That means that the amount of new water molecules appeared in the composite material after irradiation is less than the quantity of water appeared in pure PVA after irradiation. We can conclude that the $\gamma$ radiation is absorbed by $TiO_2$. Then the flux of $\gamma$ radiation which interact with the PVA macromolecules is reduced, the effect of breaking of polymeric chain with apparition of new water molecules, is reduced, and as we shown previously, the samples with low water content absorbed less the UV radiation. We can conclude that the irradiation of composite samples, PVA + $TiO_2$, is equivalent with the reduction of water content of PVA pure membranes. Or, on other words, the irradiation of pure PVA membrane is equivalent with the increase of concentration of $TiO_2$ of unirradiated composite membranes. Similar reduction of the UV absorbance of composite materials was observed for all the samples, but the difference between the amplitude of the absorption peak of unirradiated sample and of irradiated one, increases with the concentration of $TiO_2$. At 10% $TiO_2$, this difference is $\delta_{10}$ ~ 0,21, being smaller than the corresponding difference of the pure PVA, $\delta_0$ ~ 0,35, and the amplitude of the absorption peak of unirradiated composite is smaller than the amplitude of irradiated pure PVA (Fig. 3). At 20% $TiO_2$ this difference is $\delta_{20}$ ~ 0,4 as the same order of magnitude than $\delta_0$, but the absorbance of unirradiated composite sample is greater than the amplitude of pure PVA irradiated (Fig. 4).

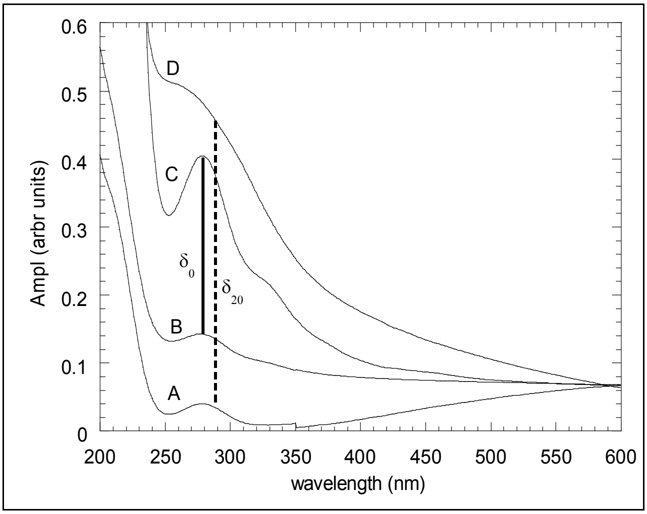

**Fig. 4.** The UV-VIS absorption spectra for the un doped membrane and membranes with different content of $TiO_2$, before and after irradiation: membrane with 20% $TiO_2$ after irradiation (curve A); the non doped membrane before irradiation (curve B); the un doped membrane after irradiation (curve C); with 20% $TiO_2$ before irradiation (curve D)

In PVA-$TiO_2$ composite, materials, the UV absorption is determined by $TiO_2$ nanoparticles and water molecules contained in the polymeric matrix. The irradiation affects mainly the quantity of water by two mechanisms, apparition of new water molecules from the breaking of the chains and evaporation of residual water contained in the polymeric matrix. The two mechanisms have contrary effects, the increase of absorbance in UV domain when new water molecules appear and reduction of UV absorbance when the water evaporates. As the concentration of $TiO_2$ increases, the absorption of $\gamma$ radiation by $TiO_2$

nanoparticles is greater, and the quantity of water resulting from the breaking of polymeric chain is reduced in comparation with the samples with low $TiO_2$ content. From here results a reduction of UV absorbance. Other effect is the evaporation of the existing residual water during the irradiation. But the samples with high $TiO_2$ concentration contain small quantities of water, so that the evaporation determined by $\gamma$ irradiation leads to rapid depletion of water molecules. This effect is accompanied by reduction of UV absorbance.

In such samples the evaporation in the dominant mechanism that explains the reduction of UV absorbance after $\gamma$ irradiation. This effect is more pronounced at high concentration of $TiO_2$, where the amount of residual water is small (Fig. 4).

## CONCLUSIONS

The UV-VIS absorbance of PVA-$TiO_2$ membranes, before irradiation increases continuously with the concentration of nanoparticles. After $\gamma$ irradiation the UV-VIS absorbance of pure PVA membrane increases. This behavior is determined by the breaking of the polymeric chain and apparition of new water molecules. At low $TiO_2$ concentration (i.e. 1%) we observe similar behavior. As concentration of $TiO_2$ increases, i.e. 10% and 20%, the absorbance after $\gamma$ irradiation decreases. Two mechanisms explain this behavior, the strong absorption of $\gamma$ radiation by $TiO_2$ nanoparticles with effect the reduction of $\gamma$ flux interacting with the polymeric chain, and second, the evaporation of residual water trapped in the polymeric matrix under $\gamma$ irradiation.

At high concentrations of $TiO_2$ the evaporation exceeds the apparition of new water molecules from the breaking of the polymeric chains that explains the important reduction of the UV absorbance of these samples after $\gamma$ irradiation.

## ACKNOWLEDGMENTS

This work was supported by CNCSIS-UEFISCU; project number PNII-IDEI ID_1157/2008

## REFERENCES

1. R. Chandra, R. Rustgi, *Prog. Polym. Sci.*, 23, 1273 (1998).
2. E. Chiellini, A. Corti, S. D'Antone, R. Solaro, *Prog. Polym. Sci.*, 28, 963 (2003).
3. C. Ivascu, A. Gabor, O. Cozar, L. Daraban, I. Ardelean, *J. Mol. Struct*. 993 1-3, 249 (2011).

4. D. Lopez, I.F. Cendoya, J. Torres, C. Tejada, J. Mijanagos, *Appl. Polym.,82*, 3215 (2001).
5. L. Udrescu, C.V. Pop, T. Stefan, M. Todica, *Studia UBB Physica*, LVI, 1 (2011).
6. C.C. De Merlis, D. R. Schoneker, *Food Chem. Toxicol*., 41, 319 (2003).
7. K.A.M. Abd El-Kader, S.F. Abdel Hamied, *J. Appl. Polym. Sci*., 86, 1219 (2002).
8. R. Jayasekara, I. Harding, I. Bowater, G.B.Y. Christie, G.T. Lonergan, *Polym. Test.*, 23, 17 (2004).
9. W.H. Eisa, Y.K. Abdel-Moneam , Y. Shaaban, A.A. Abdel-Fattah , A.M. Abou Zeid, *Mater. Chem. Phys.,* 128, 109 (2011).
10. M. Todica, L. Udrescu, *Cent. Eur. J. Phys*., 9, 6 (2011).
11. M. Todica, L. Udrescu, S. Simon, *Cent. Eur. J. Phys* (submitted).
12. N.V. Bhat, M.M. Nate, M.B. Kurup, V. A. Bambole, S. Sabharwal, *Nucl. Instrum. Meth. B,* 237, 585 (2005).